NORTHWESTERN UNIVERSITY

Methods and Mechanisms for Per- and Polyfluoroalkyl Substance (PFAS) Removal and Degradation

A DISSERTATION

SUBMITTED TO THE GRADUATE SCHOOL
IN PARTIAL FULFILLMENT OF THE REQUIREMENTS

for the degree

DOCTOR OF PHILOSOPHY

Field of Chemistry

By

Brittany Trang

EVANSTON, ILLINOIS

September 2022

Abstract

Per- and polyfluoroalkyl substances (PFAS) are man-made compounds containing multiple carbon–fluorine bonds. The unique properties of this strong bond simultaneously make PFAS useful for a number of industrial and consumer applications, toxic to living organisms, and difficult to remediate. Because the pervasive pollution of water sources with PFAS occurs at low parts-per-trillion or parts-per-billion PFAS concentrations, specially formulated adsorbents with high PFAS affinity are needed to remediate contaminated drinking and wastewater. However, until recent years, the factors affecting adsorbents' affinity for PFAS were unclear. Here we present one example of a PFAS adsorbent, based on β-cyclodextrin, that was intended to determine whether fluorophilicity plays a role in PFAS adsorption. As the PFAS adsorbent field has come to a better understanding of how to adsorb anionic PFAS, the next problem to surmount has become the question of what to do with PFAS-containing waste streams, whether wastewater, filtration retentate, contaminated filter media, aqueous film-forming foam (AFFF), contaminated soil, or other PFAS-related waste. PFAS degradation technologies, still in their infancy, have to this point mostly focused on easily scalable methods of injecting large amounts of energy into the PFAS-containing system. Significantly, the relevant degradation mechanisms are neither well-understood nor well-controlled. Here, we present a method that both degrades and defluorinates PFAS without speciating the PFAS into a distribution of intermediate-length fluorocarbon compounds. This method can degrade some PFAS compounds at temperatures as low as 40 °C. Computational investigations of the mechanism revealed a previously unrecognized defluorination pathway mediated by hydroxide-driven fluoride elimination. Systematic variations in the characterized byproducts support the computational results. This method is extended from the original

perfluorocarboxylic acid substrates to branched perfluoroether carboxylates, and might be further extended to other classes of PFAS as methods to activate the headgroups of compounds such as perfluorosulfonic acids are developed. Other strategies for the continuation of this degradation work are also presented.

Acknowledgments

First, I would like to thank the Lord, because my decision-making skills are not the best (see: being very qualified for two wildly different career paths and double-majoring myself into a conundrum right up until the end of my PhD) and through what can only be described as divine intervention, it was very clear that I had to attend Northwestern. I feel so lucky (#blessed) to have attended grad school at Northwestern for many reasons (not in the least because I didn't know it would be convenient to be located in the same state as my parents during a worldwide pandemic) and I have lived and learned and grown so much during my time in Chicagoland in so many ways that I was not able to foresee for myself. I am grateful to get to be praising the Lord for his faithfulness through mostly good times, but there have been tough times throughout not just my grad school years but the rest of my life where I am grateful to depend upon Him despite my own perpetual shortcomings. 1 Timothy 1:15.

One of the things I still feel unbelievably lucky for is my advisor, Will Dichtel. A grad student from another advisor's group told some prospective students at a recent visit weekend, "You have to choose what's important to you in an advisor and prioritize that because there will be other things you'll just have to decide you're okay with," and I realized how fortunate I am to not feel like I had to compromise on anything with Will. I was recently struggling to sum up why I think Will is such a great person to have as a mentor and settled on, "Even when I disagree with him, I still trust him," and the labmate I was discussing this with wholeheartedly agreed. The scientific community has recognized Will's ability to produce quality science and realize blue-sky ideas, but his humility (such as referring to the awards he has won as "awards for all group members past and present"), his integrity (such as deciding to not publish Chapter 2 of this thesis

as a paper even though we could well have brushed aside its hidden shortcomings), his care for his grad students and postdocs as people (from shutting down the lab a week before Northwestern did at the beginning of the pandemic to answering a 1:30 am call from me when my roof was leaking), and his recognition that his role as an advisor is to get his students wherever they want to go ("If you think you want to go into science writing," he told me when I first applied for the AAAS Mass Media Fellowship, "this is what you need to get your foot in the door. Get the fellowship and we'll talk about what happens after that") make him a truly great person and advisor and I am so thankful to have gotten to learn from him.

Though I'm grateful to have been advised by Will, we all know that most of the teaching and learning in a research group comes from other group members. I would like to thank Leilei Xiao, my mentor, for teaching me all of the weird characterizations our group does and instilling in me a sense of rigor and precision. I apologize for not understanding what I was doing as a first- or second-year. I'd like to thank Max Klemes, my longtime lab neighbor and informal mentor, for teaching me to read the Wikipedia page for a chemical before using it because the hazards are more clear on Wikipedia than when reading the MSDS, for teaching me about how so many things work, giving me good advice on my projects, and inspiring me to cook with more beans and sweet potatoes. I'd like to thank my labmate and cohort-mate Luke Skala for being the best coworker and most fun friend I could have asked for in grad school. As I look back on the five years we've worked together, I realize that the times I have felt the most competent, especially in the early years, were when I was discussing science with you. (That sounds like a burn but it's not supposed to be; whoops.) I'd like to thank Anna Yang and Leslie Hamachi for their informal mentorship and kind friendship as I discussed my projects and my grad school struggles with them. Thanks to Zhi-

Wei Lin for being the most hardworking mentee; working with you caused me to stop and think about lab work and grad school differently. I hope you've learned something from me and can't wait to see how your PhD journey turns out. I'd like to thank the classic K366 office lineup—Austin Evans, Ben Elling, Ioannina Castano, Luke Skala, Jeremy Swartz—for the good times and the singalongs; I miss those days and you all. Thanks to the newer K366 additions—Chloe Pelkowski and Clover Moisanu—for being such good and fun friends that I don't want to leave you!

Thanking the Dichtel group would not be complete without thanking Tory Helgeson, who has managed many chartstring complications, told me how to fix my tax-exempt errors while ordering food for group meeting (RIP group meeting food), ordered every single material I needed for my entire PhD, gave me lots of encouragement and advice, and (as I've been writing this I've realized it is impossible to list or express how many things Tory does and how integral he is to our group; Will, if you're reading, please hire someone to help Tory.)

One of the perks of becoming a senior grad student is that you work with the core facilities staff so much that they start to trust you and will help you do unconventional measurements or will trust you with using the instruments. Thanks to Saman Shafaie for all the mass spec help and for finally teaching me the difference between ESI and APCI, Arsen Gaisin for all the LCMS help for the (surely) thousands of PFOA adsorption samples I've run over the years, Charlotte Stern for running my CHNS samples fresh out of the vacuum oven, Yongbo Zhang for helping me develop so many specialized ^{19}F NMR methods and being patient with me every time I needed an error explained, Yuyang Wu for teaching me and troubleshooting NMR with me, Neil Schweitzer for

the GCMS help at REACT, and Rebecca Sponenburg for being the most unbelievably helpful and patient facilities staff member and doing everything for me at QBIC.

I wouldn't have decided to go to grad school if it weren't for the great research experiences I had in undergrad. I'd like to thank Kevin Click, my grad student mentor at Ohio State, for teaching me everything I know. Obviously I have learned a lot more since then, but grad school has made me realize how well you trained me as an undergrad and I'm thankful to have had such a good background to build upon. I'd like to thank Matti (Schulz) Dowds and Nate Hohman as well for the excellent research experiences you provided during my summer internships.

As I mentioned earlier, I ended up being qualified to not only be a research scientist at the end of my PhD, but also a science reporter. I owe so much to Patti Wolter at Medill for introducing me to my favorite piece of writing ever, "The Really Big One," and the idea of narrative structure; teaching me basic journalism skills; and answering every single panicked email I had throughout my job search. I'd like to thank Tom Koetting, my editor at the Milwaukee Journal Sentinel, for taking a chance on me and teaching me so much about journalism. I hope to have a portion of your masterful perspective one day. Thanks also to all the editors and reporters at the MJS who affirmed my writing was good and encouraged me to be a reporter; your words have really stuck with me.

I'd also like to thank the people outside my professional life who have kept me going through grad school. I'm so glad to have a community through Evanston Bible Fellowship, particularly in my Ethos community. To Ben and Jenny Cook, thanks for always opening your home and family to me. To Janae Mann and Josh & Kristina Graham—for the rest of my life, I will remember riding out the pandemic on the social lifeline of blankets set six feet apart in the Grahams' backyard. And to the rest of my Ethos group (too many to name here), I have been

inspired by you and encouraged by you and will miss you dearly. I'd also like to thank my college friends from H2O especially (Diane Gress, Lindsay Gifford, Robbie Freeman, Colin Gay, and many others); I so much value the time we've spent on the phone and the time you all have put into maintaining/building a long-distance friendship with me.

Finally, I'd like to thank my parents. I'm not sure how I would have managed the last five years logistically without you, but more than that, thank you for instilling a lifelong curiosity within me and supporting me even when you're worried about me. No matter how old I get, I still find myself looking to you for reassurance and am thankful you're my parents.

Table of Contents

Contents

List of Tables, Illustrations, Figures, and Graphs

1. Introduction to PFAS Contamination, Adsorption, and Destruction

1.1. Abstract

Per- and polyfluoroalkyl substances (PFAS) are man-made compounds containing multiple carbon – fluorine bonds, which endows them with certain advantageous properties leveraged in many industrial processes and consumer products. However, exposures to even low concentrations of PFAS have been linked to negative health effects such as liver damage, high cholesterol, reduced immune responses, low birth weights, and several cancers. These compounds have accumulated in municipal water supplies and polluted an increasing number of communities due to their widespread use in industrial processes and consumer products. Strategies for removing and remediating PFAS in waste, ground, and drinking waters have been developed in recent years, but questions still remain about how adsorbent properties contribute to the PFAS adsorption process and many emerging PFAS degradation techniques suffer from high energy consumption, inefficient degradation, and questionable scalability. Here, we give an introduction to PFAS compounds and the state of the PFAS field in both academic research and the United States' federal and state regulations for these compounds. Then, we give an overview of PFAS adsorption approaches, PFAS degradation approaches, and conclude with a summary of present challenges and opportunities in PFAS remediation research.

1.2. PFAS Background

Per- and polyfluoroalkyl substances (PFAS) are persistent, bio-accumulative man-made substances containing multiple carbon–fluorine bonds (Figure 1.1). PFAS definitions from different organizations differ, including "Organic chemicals containing 'at least one fully fluorinated carbon atom,'" such as is used for PFAS-related legislation in several states; or "a structure that contains the unit R-CF_2-CF(R′)(R″), where R, R′, and R″ do not equal "H" and the carbon-carbon bond is saturated (note: branching, heteroatoms, and cyclic structures are included)," as defined by the U.S. EPA Office of Pollution Prevention and Toxics; as well as several other more- and less-inclusive definitions, which have important implications for whether fluorine-containing pharmaceuticals, for example, would be subject to future regulations by being included in the PFAS family (*1*). In general, PFAS refers to the more highly fluorinated PFAS molecules, which because of their hydrophobic and lipophobic nature, thermal stability, chemical inertness, good surfactant qualities when combined with polar headgroups, and many other unique properties bestowed upon them by their strong, highly polarized C – F bonds, are used in products such as pizza box linings, compostable takeout bowls, stain-resistant fabric coatings, and fire-fighting foams. PFAS are further used as processing aids in industrial processes, such as those used to make fluorine-containing polymers for paints, coatings, and non-stick polytetrafluoroethylene pans, the most famous of which is marketed as Teflon.

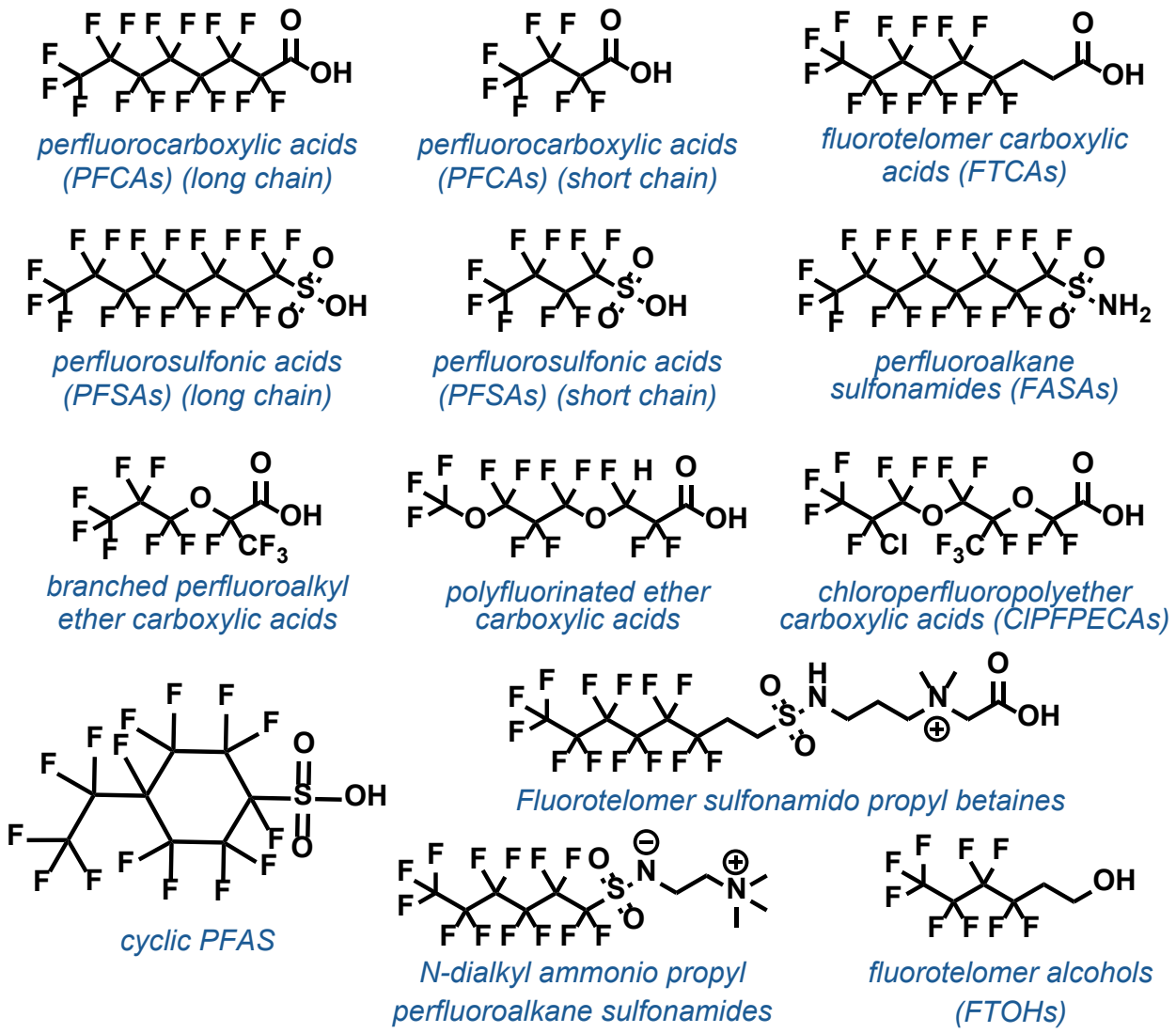

Figure 1.1 Example structures for a selection of PFAS compound subclasses.

Though PFAS compounds are useful, they are at the center of a growing public health crisis. PFAS have been associated with several negative health effects, such as kidney damage (*2*), liver damage (*3*), low birth weights (*4*, *5*), thyroid disease, high cholesterol, reduced immune responses (*6*), several kinds of cancers (*7*), and are probable causes of many other health problems (*8*, *9*). Multi-billion-dollar lawsuits against chemical manufacturers (*10–12*) who exposed people to PFAS without their knowledge or consent have been filed on behalf of just some of the 98% of

Americans who have measurable amounts of PFAS in their blood (*13*). Though people can contact PFAS through directly using products that contain PFAS (*14*, *15*) or air-distributed PFAS pollution (*16–18*), PFAS leaching through soil to or directly discharged into water sources is currently the primary concern in the field. Recent estimates conclude that over 60% of Americans now have detectable PFAS in their tap water, 18 million–80 million of which have 10 ng/L ("parts per trillion," or ppt) or higher concentrations of PFAS in their water (*19*) (Figure 1.2).

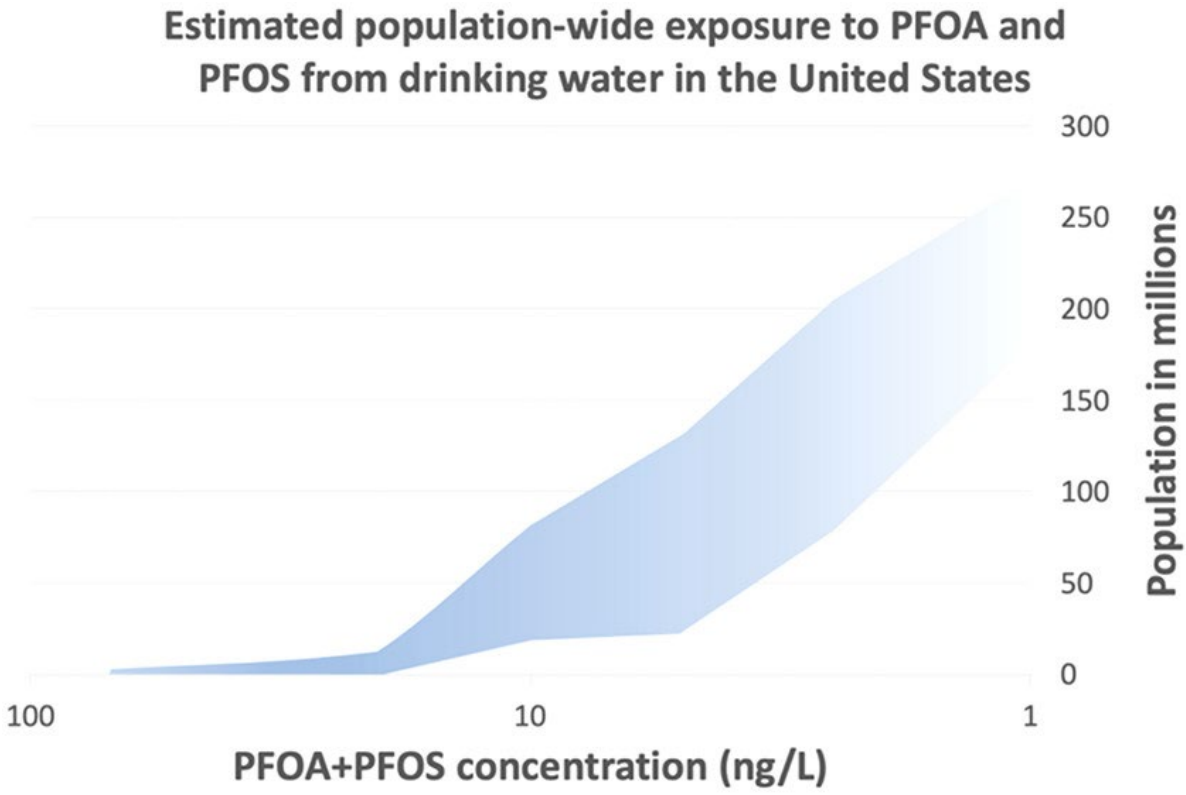

Figure 1.2 Estimated population-wide exposure to PFOA and PFOS from drinking water in the United States. Reprinted with permission from (*19*). Copyright 2020 American Chemical Society.

As of the time of writing, the United States does not regulate PFAS in drinking water. However, in 2021, the US EPA announced its determination to develop a national primary drinking water regulation for legacy PFAS compounds perfluorooctanoic acid (PFOA) and perfluorooctane sulfonate (PFOS) as a result of the regulatory determination for the Contaminant Candidate List 4

(CCL4) process (*20*). Both of these maximum contaminant levels are forthcoming sometime within the next year or two. In lieu of federal regulation, several states have passed PFAS standards much lower than the 2016 EPA advisory level of 70 parts per billions (ppb) for PFOA and PFOS combined (*21*). For example, Michigan has passed guidelines restricting PFOA to 8 ppt and PFOS to 16 ppt. However, the compound-by-compound approach, often termed the "whack-a-mole" approach to regulation, will ultimately fall short as new PFAS compounds are constantly introduced. In a win for PFAS regulation advocates, in 2021, the entire PFAS pollutant family was added to the draft CCL5 to potentially be regulated as a class. However, it remains to be seen whether the pollutant class will be broken into subclasses or garner a drinking water regulation at all (*22*).

On June 15, 2022, the EPA updated the lifetime health advisory limits for PFOA and PFOS, as well as announced health advisories for perfluorobutane sulfonic acid (PFBS) and hexafluoropropylene oxide (HFPO) dimer acid and its ammonium salt (referred to as "GenX chemicals") (*23*). In contrast to the 70 ppt advisory issued for PFOA and PFOS in 2016, the new limits for the legacy PFAS compounds essentially communicated that there is no safe limit for PFOA. The new health advisory limit for PFOA is 0.004 ppt, 17,500 times below the 2016 advisory level. This new, very low level introduces the parts-per-quadrillion ("ppq"; picogram/L) term to common usage in the PFAS vernacular. The EPA pointed out that they came to this conclusion based on health studies even though the agency, and the field in general, cannot currently detect concentrations of PFAS as low as single ppq, which underscores the extreme toxicity of these compounds. The agency lowered the limit for PFOS to 0.02 ppt (3,500 times lower than the 2016 advisory limit) and named advisory limits for PFBS and GenX at 2,000 ppt (2 ppb) and 10 ppt,

respectively. In a press release accompanying the health advisory limit announcement, the EPA stated that they expect to announce their national primary drinking water regulations for PFOA and PFOS by fall 2022 and that "As EPA develops this proposed rule, the agency is also evaluating additional PFAS beyond PFOA and PFOS and considering actions to address groups of PFAS," which indicates that class- or subgroup-based regulations may become reality. In the meantime, it remains to be seen how the new, lower PFAS limit guidelines will practically impact local water utilities and state-level regulations who were using limits previously thought to be protective.

For a more comprehensive overview of the challenges currently facing the PFAS field, see Evich et al.'s recent review in *Science* (*24*).

1.3. PFAS Adsorption Technologies

Despite legislation and resolutions by state and federal governments to limit PFAS use and regulate their cleanup (*25–27*), these compounds are still found in high concentration in wastewater, groundwater, and soil (*28*, *29*). In this work, we focus on issues pertaining to PFAS in water rather than in air or soil. PFAS' exceptionally stable C – F bonds (*30*) make these compounds resistive to environmental degradation (*31*, *32*), so they must be physically removed to lower their presence in water supplies. While other removal strategies such as reverse osmosis or nanofiltration are possible, these strategies produce a retentate in which PFAS are concentrated, which require further remediation to fully decontaminate (*24*). Additionally, these methods require higher capital costs on a point-of-use level, as well as more infrastructure (*33*). Rather, we see adsorption onto filter media as a potentially cost- and energy-efficient method for PFAS removal. While the subsequent disposal or treatment of contaminated filter media also has to be taken into account, we address this issue in section 1.5.

1.3.1. Activated Carbon

Granular activated carbon's (GAC) low price, wide availability, and reasonable capacity (*34*) make activated carbon a very popular treatment method for removing PFAS in drinking water on municipal scales (*35*, *36*). Activated carbons (ACs) can be produced through the pyrolysis or other activation of carbonaceous materials such as coconut shells, peat, lignin, rice hulls, etc. to form an adsorbent with a large surface area and varied pore size distribution ranging from micro- to meso- and macro-pores (Figure 1.3). These activated carbon particles are largely composed of graphitic sheets of polycyclic aromatic hydrocarbons, with the surface functionalities often dominated by oxygen-containing species unless otherwise designed or modified with heteroatoms (*37*, *38*). Adsorption on activated carbon has been attributed to three main mechanisms: van der Waals/π–π dispersion interactions between hydrophobic molecules and the aromatic carbon surface; electron donor-acceptor complexes, such as between a carbonyl oxygen on the carbon surface and aromatic compound acceptors; and hydrogen bonds, such as between -OH groups on the carbon surface and adsorbates containing -NH or -OH groups (*38*). Due to its non-specific interactions with adsorbates, activated carbon has a low affinity for PFAS (*39*, *40*), especially at the low ppt concentrations at which PFAS is often found. This low affinity makes GAC ineffective at meeting the desired ppt contaminant limits now being set or considered by state and federal environmental agencies (*21*, *27*, *41*, *42*). Additionally, though activated carbons have so far been the industrial and municipal micropollutant adsorbent of choice, ACs are highly affected by the natural organic matter (NOM) and other matrix constituents found in soil and groundwater, as NOM is large enough to block pores and adsorption sites from adsorbates (*43*, *44*). Though ACs are often a cost-effective treatment and can be modified to increase adsorption of specific micropollutants (*45*), adsorbents that are not fouled by NOM and also have high PFAS affinity are needed.

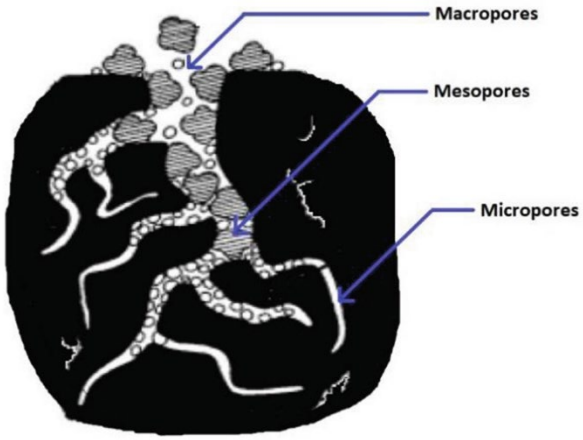

Figure 1.3 Schematic structure of an activated carbon with macro-, meso- and micro-pores illustrated. Reprinted by permission from Springer from reference (*46*). Copyright 2020.

1.3.2. Ion-Exchange Resins

Ion-exchange resins have been explored for the removal of anionic PFAS in particular (*47*). Ion-exchange resins (IX) contain charged groups, often acids or bases, anchored to a polymeric resin, often polystyrene. These charged groups have counterions that readily exchange with the target ion when the waste stream is passed through, leaving the target ion stuck to the resin; in the example of a resin designed to target anionic PFAS, such counterions could include chloride or iodide (*48*). While such resins remove PFAS from waste streams more efficiently than GAC (*49*), they have several susceptibilities, including specificity for only one polarity of PFAS, slow adsorption kinetics, inefficient removal of short-chain PFAS, and complicated end-of-life scenarios for both PFAS-bound single-use resins and the PFAS-contaminated brine solutions from regenerable resins (*47*, *50*).

1.3.3. Specialty Polymers

In recent years, several specialty polymers have been investigated for PFAS remediation; many have cited a synergistic effect between hydrophobicity/fluorophilicity and electrostatics for efficient PFAS uptake. In 2020, Kumarasamy and Manning et al. studied methacrylate-based ionic fluorogels for PFAS adsorption (*51*) (**Figure 1.4**). By varying the amounts of fluorinated linker,

amine-containing linker, quaternization of the amine linker, and substitution of a non-fluorinated linker, the authors showed that the materials' good affinity for PFAS (>90% uptake for PFCAs longer than 6 carbons, all PFSAs tested including PFBS, and GenX at 100 ppm adsorbent, 1 ppb PFAS, 2 h in spiked wastewater; see **Figure 1.4C**) appeared to stem from a synergistic effect from the combination of fluorous monomer and quaternary amine incorporation. When the gels were composed entirely of fluorous methacrylate monomer, the material displayed low adsorption of PFAS besides PFOA. As the amine content increased, the adsorption of all PFAS generally increased (**Figure 1.4A**). With the quaternization of the amines, adsorption of the PFAS was high and similar for all amine loadings. However, when a hydrogenated linker was used instead of the fluorinated linker at 20 – 30 wt% amine or ammonium moiety, uptake was low to negligible, leading to the suggestion of a synergistic effect between fluorous and electrostatic interactions for PFAS uptake (**Figure 1.4A, B**). However, it is difficult to distinguish between fluorophilic and hydrophobic interactions specifically and on a practical level, the integration of fluorous functionalities in a PFAS adsorbent is expensive and less than ideal.

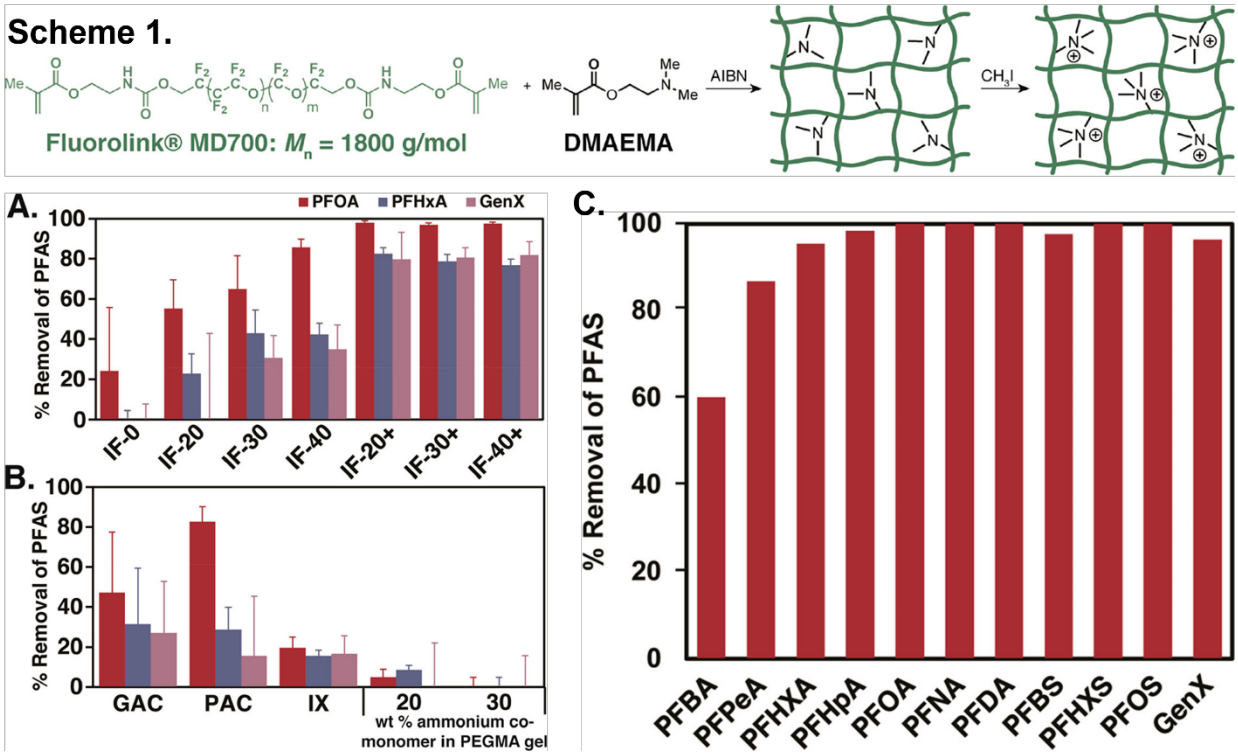

Figure 1.4 Scheme 1. Polymerization and Quaternization of Ionic Fluorogels. (A) Equilibrium PFAS removal by ionic fluorogels with amine (**IF-*X***) or ammonium (**IF-*X*+**) groups where *X* = 0, 20, 30, or 40 wt %. (B) Equilibrium PFAS removal by GAC, powdered activated carbon (PAC), ion exchange resin (IX), and PEGMA gels with 20 or 30 wt % ammonium comonomer. Water constituents, 200 mg/L NaCl and 20 mg/L humic acid; pH = 6.4; [sorbent] = 10 mg/L; $[PFAS]_0$ = 1 μg L^{-1} each; equilibrium time, 21 h. Error bars: standard deviation of 3 experiments. (C) Removal of PFASs after 2 h by **IF-30+** from settled water collected at the Sweeney Water Treatment Plant in Wilmington, NC. TOC = 1.3 mg/L; pH = 6.2; [sorbent] = 100 mg/L; $[PFAS]_0$ = 1 μg/L each. Adapted from (*51*). Copyright 2020 American Chemical Society. Further permissions related to the material excerpted should be directed to the ACS.

More recently, Liu et al. reported a porous aromatic framework (PAF) functionalized with quaternary amines of different chain lengths, thus imparting different hydrophobicities to the porous framework (*52*). The optimized PAF examined in the paper, PAF-1-NDMB (functionalized with N,N-dimethylbutylamine groups), showed a PFOA saturation uptake capacity of over 2000 mg/g, which the authors claimed was a record. In addition to a very high adsorption capacity, the adsorbent showed faster kinetics and longer breakthrough times compared to other adsorbents it was benchmarked against, including decafluorobiphenyl-cyclodextrin polymer (DFB-CDP), an activated carbon (specific formulation not specified in the manuscript), and the original

unfunctionalized PAF-1. The authors used the inferior uptake of control PAFs functionalized with trimethyl amine (electrostatic interactions only) and sodium ethoxide (hydrophobic interactions only) to support the hypothesis that a synergistic effect between the two functionalities, along with "efficacious functionalization" contributed to the adsorbent's superior performance.

However, the use of an ethyl-functionalized control seems inadequate to test the hydrophobic effect of a butyl-functionalized structure. If an increased hydrophobicity were key in increasing the adsorption capacity of the polymer as the authors claimed, such a butyl-functionalized polymer might have outperformed PAF-1-NDMB in the adsorption isotherm (Figure 7f in the study), where the ethyl-functionalized control performs only slightly worse than PAF-1-NDMB, ruining the synergistic hypothesis.

Additionally, the authors use spectroscopic evidence from infrared spectra and NMR spectra to support their argument that hydrophobic and electrostatic interactions are observed; however, the solid-state ^{19}F NMRs (likely noise assigned as peaks; the ^{19}F DP MAS NMR spectrum of PFOA should be much more defined and in the correct shift region around -80, -115 – -130 ppm, as in reference (*53*)) and carbon NMRs (the authors did not fluorine-decouple when they collected their ^{13}C NMR spectrum and incorrectly assign the PFOA carboxylic acid carbon around 170 ppm as the alkyl C1 – C7 carbons and assign a noise peak in the wrong region, around 70 ppm, as the carbonyl peak instead) are poorly collected and incorrectly analyzed and should not be used as evidence in support of any hypothesis.

The PAF can be regenerated for later reuse, but needs to be regenerated with a 1:1 MeOH:saturated NaCl solution. The necessity of using a high salt concentration to regenerate the adsorbent suggests that the adsorbent is largely operating by an ion-exchange/electrostatic

adsorption mechanism. In addition to not having reliable evidence for the reasons underlying the adsorbent's high capacity, the lowest initial concentration of PFAS the study examined was 166 ppb, precluding any study of the adsorbent's affinity, which would be key in any study of PFAS removal at environmentally relevant concentrations (< 1 ppb, preferably in the hundreds of ppt range) and would truly provide useful evidence for the adsorption mechanism.

1.3.4. Natural and Bio-derived Adsorbents

In contrast to the specialty structures described above, modified natural substances such as clays, polysaccharides, and other materials have been investigated as greener, low-cost PFAS adsorbents. Natural and surface-modified clays have been developed for this purpose (*54*); however, the hydrophilic nature of the OH-functionalized natural clay surface presents several difficulties. Clays have a pH-dependent surface charge and can be negatively charged, precluding them from binding anionic PFAS electrostatically. The hydrophilic surface also cannot attract the fluorinated PFAS chains through hydrophobic interactions. Short-chain PFAS also desorb easily from the clay surface, making short-chain PFAS adsorption difficult. Surface modifications can give the clays properties more amenable to PFAS removal, but the expensive and potentially toxic nature of such modifications is also a concern. Biochar, in which organic matter is carbonized but not activated as for activated carbon, presents a lower-cost alternative to ACs (*55*). Other bio-derived materials have been investigated for PFAS adsorption, including quaternized cotton, aminated rice husks, and molecularly imprinted chitosan beads (*56*, *57*). The leading candidates for PFAS removal based on modified bio-derived material commonly contain either naturally occurring amines or are functionalized with amines to increase the electrostatic uptake of anionic PFAS (*50*, *57*). In addition to these bio-derived adsorbents, another major category of bio-derived PFAS adsorbents

is the wide variety of cyclodextrin-based polymers (*56*), which will be discussed in the next section.

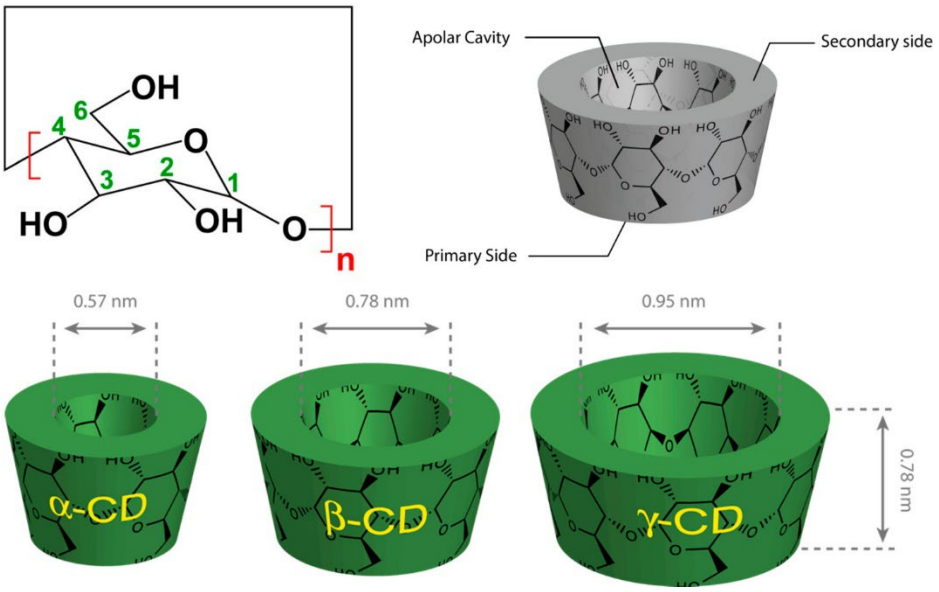

Figure 1.5 Top: Functional structural scheme of α-CD (n = 6), β-CD (n = 7), and γ-CD (n = 8). Bottom: Geometric dimensions of cyclodextrins. Reprinted with permission from (*58*). Copyright 2014 American Chemical Society.

1.3.4.1. Introduction to β-CD

Cyclodextrin (CD) is a glucose macromolecule derived from starches such as corn or potato starch (*58–61*). The most common cyclodextrins are α-, β-, and γ-cyclodextrin, which are composed of six, seven, and eight glucose molecules, respectively (Figure 1.5). Much of the literature focuses on beta-cyclodextrin (β-CD). The fourteen secondary hydroxyls of the seven β-CD glucose monomers form a hydrophilic "secondary" face, while the seven primary hydroxyls form a slightly smaller-circumference "primary" face (Fig. 1A – C), giving cyclodextrin its tapered cup shape. The carbons lining the interior pore of the macrocycle form a hydrophobic cavity that has a strong affinity for forming host – guest complexes with organic molecules such as perfluorooctanoic acid (PFOA; binding constant $K_{assoc} = 5.00 \times 10^5 \pm 0.10\ M^{-1}$, Figure 1D) (*62*). While this supramolecular property has mainly been explored for encapsulating pharmaceutical agents or molecules for

personal care or consumer product applications, this strong host – guest chemistry has also been applied for water remediation (*63*, *64*). Because native β-CD is soluble in water, several β-CD-based cross-linked polymers have been developed to insolubilize the cyclodextrin and adsorb micropollutants from water (*63*, *65–67*). Early cyclodextrin polymers (CDPs) focused on aliphatic crosslinkers, especially epichlorohydrin (*63*, *65*), as well as isocyanates, aldehydes and carboxylic acids (*65*, *66*, *68–71*). However, these polymers did not show clear performance improvements over ACs (*72*), likely because of their low surface areas and slow kinetics (*63*), limiting their utility.

1.3.4.2. History of Dichtel Group β-CD Polymers

In 2016, our group reported the first porous cyclodextrin polymer (TFN-CDP), which was synthesized using an aryl linker, tetrafluoroterephthalonitrile (TFN) (*67*). This rigid linker frustrated the packing of the polymer and opened up pores (S_{BET} up to 263 m^2/g) that led to improved kinetic performance, wherein the polymer could achieve near-equilibrium bisphenol A removal within 10 seconds (BPA, 0.1 mM; 1 g/L adsorbent; Figure 1.6). Our group and collaborators reported several subsequent cyclodextrin polymers (*73–78*) as well as several studies on how CDP properties affect micropollutant uptake (*76*, *78–82*) in the following years. In particular, three studies are of note. Two of them were conducted prior or concurrent to the work presented here; the third was developed after the work presented in chapter 2.

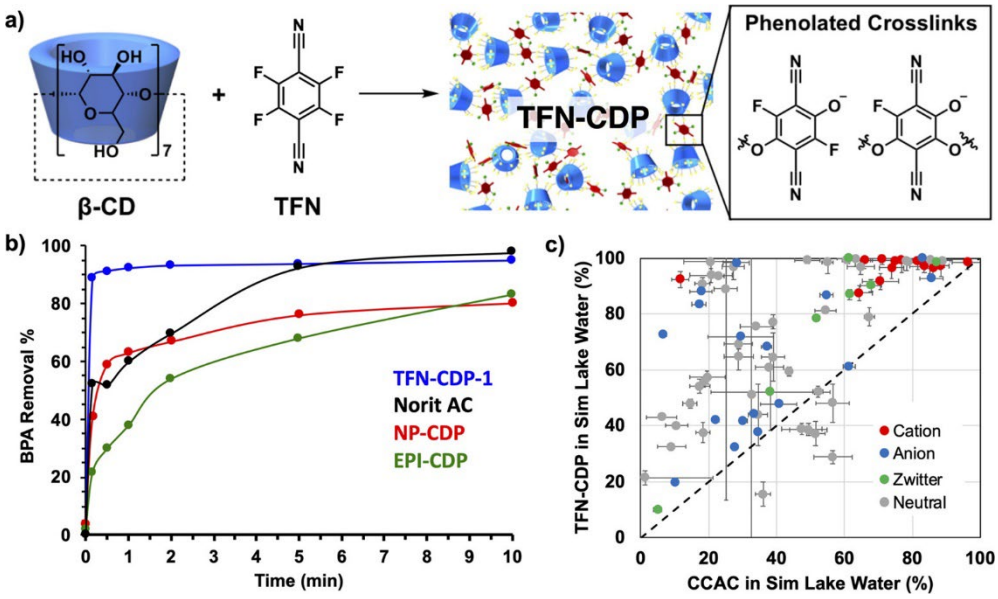

Figure 1.6 (a) **TFN-CDP-1** synthesis yields a high-surface-area cyclodextrin polymer, but there is a side reaction that leads to phenolated cross-links. (b) Bisphenol A removal kinetics show that the porous **TFN-CDP-1** has superior kinetics when compared to Norit activated carbon and nonporous cyclodextrin polymers cross-linked by TFN (**NP-CDP**) and epichlorohydrin (**EPI-CDP**) ($[BPA]_0$ = 22 mg L^{-1}, [adsorbent] 1 mg mL^{-1}. (c) Flow-through removal of 83 different micropollutants in simulated surface water ($[MP]_0$ = 1 μg L^{-1}, [adsorbent] = 1 mg loaded on to a membrane, [Humic acid] = 20 mg L^{-1}, [NaCl] = 200 mg L^{-1}, 8 mL total) shows that adsorption on **TFN-CDP-1** is not inhibited by matrix constituents, whereas adsorption on coconut shell activated carbon is inhibited. Reprinted with permission from (*72*). Copyright 2020 American Chemical Society.

Though the TFN-CDP polymer demonstrated good removal of several organic micropollutants, it displayed low affinity for PFOA. This finding was unexpected given that the affinity constant for the β-CD⊂PFOA inclusion complex is quite high (5 x 10^5, (*62*)). Later studies concluded that phenolation of the cross-linkers of TFN-CDP gave the polymer a negative surface charge that repelled the also-negatively-charged PFOA molecules, which are deprotonated at neutral pH (*74*, *75*). To develop a CDP with high affinity for PFAS, we synthesized an aryl-linked CDP using decafluorobiphenyl cross-linkers (*73*). The resulting polymer, DFB-CDP, showed high PFOA removal, adsorbing >90% of the PFOA from a 1 ppb PFOA solution at an adsorbent loading of only 10 ppm. However, the DFB-CDP was non-porous and showed very slow kinetics (~2 h to equilibrium at 200 ppb PFOA, 400 ppm polymer; >>5 h to equilibrium at 1 ppb PFOA, 10 ppm polymer). Additionally, when tested against a panel of PFAS of varying chain lengths, the PFAS

removal increased as the chain length increased, leading us to believe that the DFB-CDP PFAS removal mechanism was mainly through a hydrophobic or fluorophilic effect. Though DFB-CDP was less prone to phenolation than TFN-CDP, the polymers still carried a negative surface charge (*74*). As our subsequent studies showed that charge could also modulate PFAS uptake (*74*, *83*), we sought to make a positively charged polymer.

By post-synthetically modifying TFN-CDP, we were able to transform the nitrile groups on the TFN crosslinker into primary amines, which are protonated at neutral pH. These positively charged groups imparted an overall positive surface zeta potential to the polymer and presented a strong electrostatic attraction for the anionic PFAS (*76*). When tested for a panel of PFAS of varying chain lengths at a loading of 1 ppb of each PFAS and 10 ppm of adsorbent, uptake of almost all PFAS was over >90%, and short-chain PFBA (perfluorobutanoic acid; four carbons long) uptake improved to over 80% even at the short timepoint of 30 minutes of contact time (Figure 1.7).

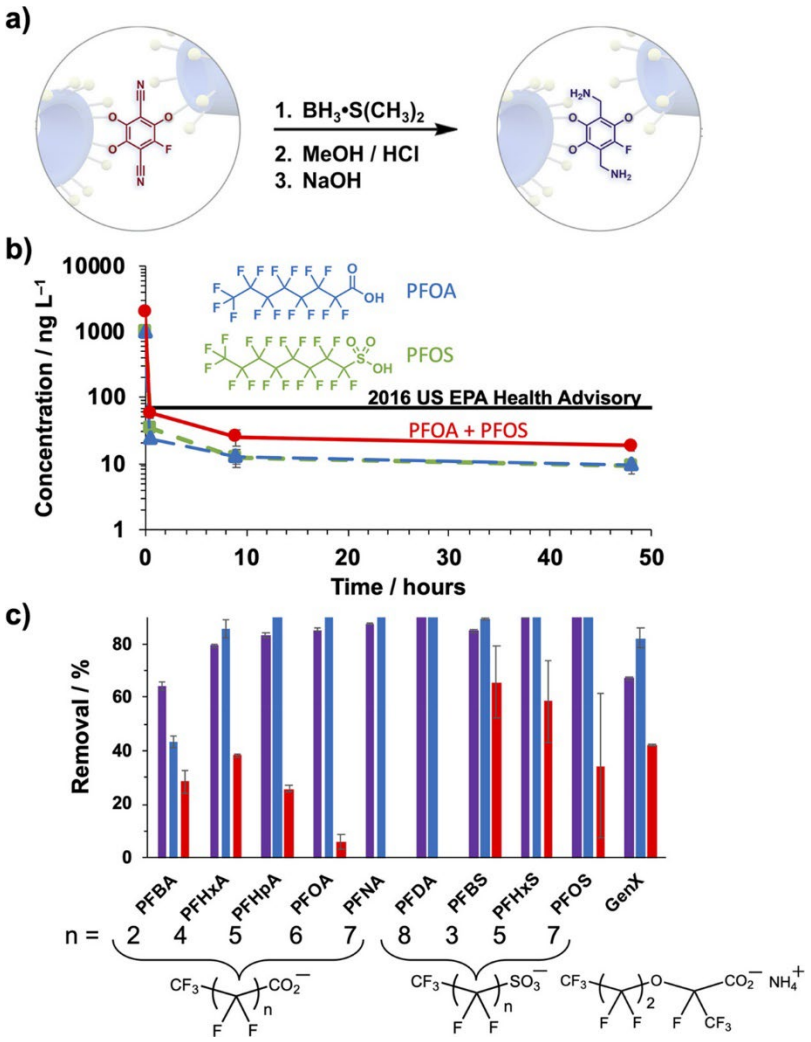

Figure 1.7 (a) Synthesis of **Amine-CDP** from **TFN-CDP**. (b) Removal of PFOA (green short dashed line), PFOS (blue long dashed line), and the combination of PFOA and PFOS (red solid line) as a function of time, demonstrating that the combined concentration of PFOA + PFOS is reduced from 2000 ng L^{-1} (1000 ng L^{-1} each) to below 70 ng L^{-1} within 30 min by 10 mg L^{-1} of **Amine-CDP**. (c) PFAS removal by **Amine-CDP** (purple), powdered AC (blue), and granular AC (red) with 30 min of contact time ($[PFAS]_0$ = 0.5 µg L^{-1}; [CDP] = 10 mg L^{-1}). Reprinted with permission from (*72*). Copyright 2020 American Chemical Society.

Having shown that both charge and hydrophobicity contribute to PFAS removal, we wanted to further study the interplay between these two factors. However, the CDPs we had so far explored were synthesized through S_N2 substitutions that were regiochemically random and prone to phenolation side reactions. CDPs with different properties were made empirically and were not well-controlled. Instead, we developed a new mode for CDP synthesis by modifying the

cyclodextrin to contain a styrene moiety at the thiolated primary alcohol position. By reacting this styrene handle with radically polymerizable monomers, we were able to develop a well-controlled, highly modular platform that was much more amenable to investigating different polymer properties' effect on PFAS uptake (*78*) (Figure 1.8). We incorporated a cationic quaternary ammonium cross-linker into the polymer network using this method and studied the uptake of a panel of different PFAS in both nanopure water and 1 mM sodium sulfate (Figure 1.9). In nanopure water, uptake of 1 ppb PFAS at 10 ppm cationic CDP adsorbent was relatively high with PFCAs with chain lengths longer than 5 carbons at >80% removal, both long- and short-chain PFSAs at >90% removal, and short-chain PFBA at ~55% (Figure 1.9). However, when testing the polymer adsorption in 1 mM sodium sulfate, the uptake of all PFAS dropped. PFBA was barely removed, but the removal increased with increasing chain length for both PFCAs and PFSAs, with the long-chain PFCAs achieving 40 – 60% removal and the long-chain PFSAs achieving removal between 60 – 80% (Figure 1.9). These results showed the effects of the two different removal mechanisms. Because of its short hydrophobic chain, PFBA is removed chiefly through cationic interactions rather than hydrophobic interactions, as evidenced by the drop in removal when sodium sulfate ions disrupted the electrostatic attractions between the adsorbent and adsorbates. However, the reduced-but-not-erased removal of the long-chain PFAS in high ionic strength conditions showed that these compounds are removed by a combination of electrostatic and hydrophobic interactions.

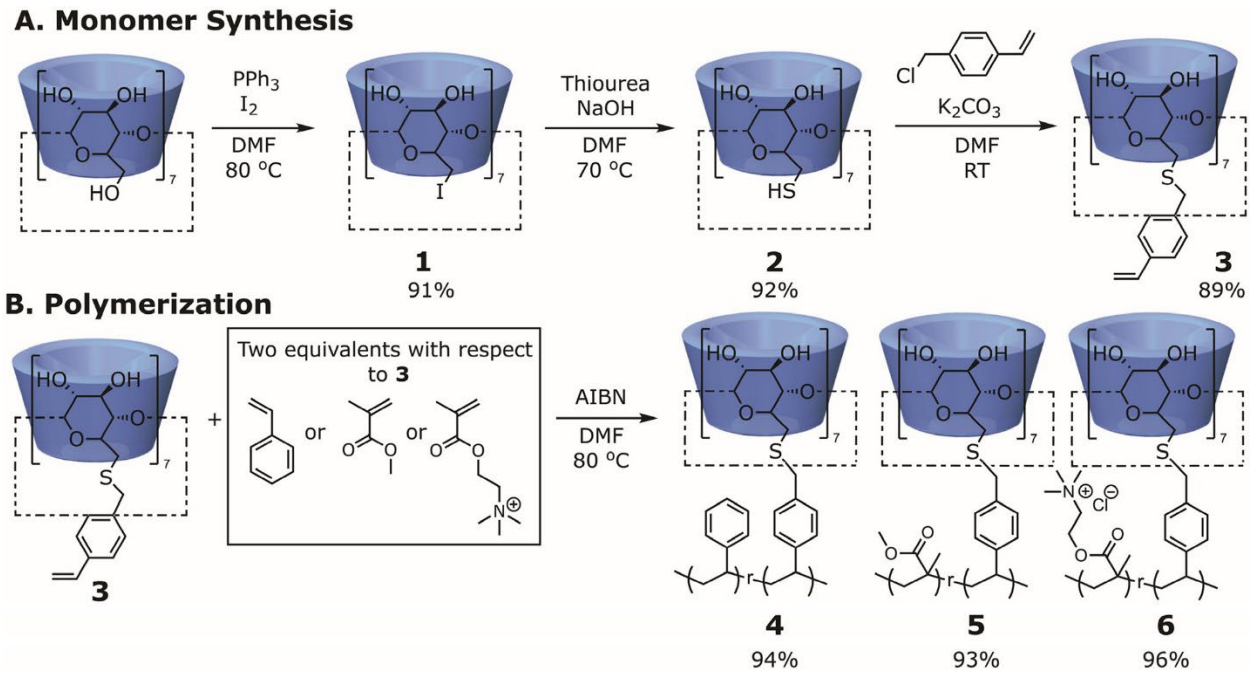

Figure 1.8 Synthetic Scheme of Styrene-Functionalized Cyclodextrin Monomer and Polymers. Reproduced from reference (*78*) under a CC BY-NC-ND 2.0 license.

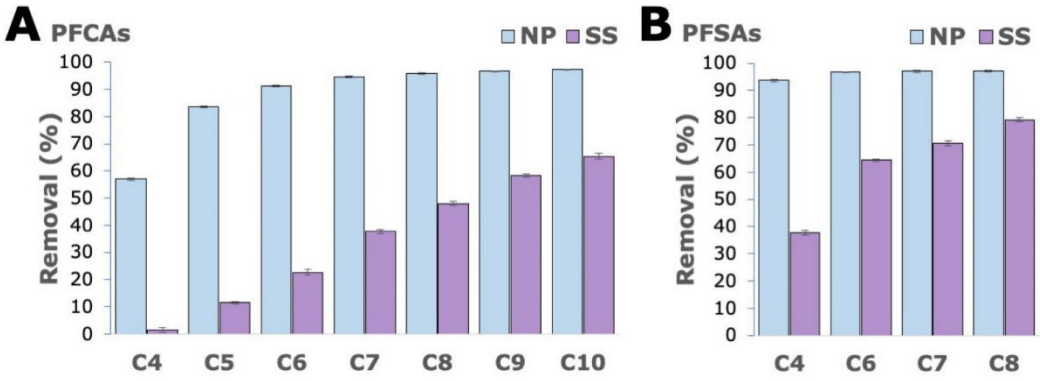

Figure 1.9 Removal of 1 μg L^{-1} PFCAs and PFSAs by 1 mg L^{-1} **6** in nanopure water (NP, blue bar) and 1 mM Na_2SO_4 (SS, purple bar) after 48 h of contact time. The *x*-axis denotes PFASs of different chain lengths. For example, C4 refers to PFBA for (A) and PFBS for (B). Reproduced from reference (*78*) under a CC BY-NC-ND 2.0 license.

1.4. PFAS Destruction Technologies

As mentioned above, properly disposing of PFAS-laden filter media is an important step in fully remediating PFAS and ensuring that PFAS does not leach from the filter materials and re-pollute the environment. To both enable the regeneration of spent filter media and degrade

PFAS in-situ, several PFAS destruction techniques have been explored. Below, we summarize the most popular approaches. For a more detailed review of these processes, see reference (*84*).

1.4.1. Incineration

Incineration is the most widely used method of PFAS degradation, both for disposing of PFAS-containing AFFF and for regenerating activated carbons with adsorbed PFAS. Incinerating PFAS adsorbed onto activated carbons is difficult, requiring temperatures of 700 – 1000 °C to achieve PFAS mineralization (*85–87*). Even at those conditions, studies suggest that fluorocarbon greenhouse gases such as CF_4 or C_2F_6 are being released during incineration (*86–88*). Furthermore, the incomplete incineration of PFAS-contaminated activated carbons in ineffective incinerators has resulted in PFAS being discharged into the air and further contaminating communities near incinerators (*16*).

1.4.2. Hydrated electrons/ UV–sulfite

Several degradation approaches aimed at treating PFAS in water use UV-generated hydrated electrons to degrade PFAS (*89–95*). The hydrated electrons can be generated from water or from chemicals such as iodide or indole under UV irradiation. Several studies from Bentel et al. studied a degradation system using sulfite, one of the most popular electron generators. Bentel et al.'s 2019 work (*89*) was one of the first PFAS degradation studies to examine the distribution of byproducts in detail to attempt to support a degradation mechanism. The major findings of the study were that, firstly, PFCA degradation is highly affected by the direct linkage of the perfluoroalkyl moiety to the carboxylic acid headgroup. Experiments conducted with telomeric PFCAs (FTCAs) and computational investigations showed that PFCAs with H/F exchange at the positions closest to the carboxylic headgroup had a higher bond dissociation energy (BDE) and thus were more recalcitrant. Secondly, the authors found evidence for the oft-proposed

decarboxylation-hydroxylation-elimination-hydrolysis ("DHEH") pathway (*89*, *96*, *97*) in their finding that trifluoroacetic acid (TFA) degraded at the same rate that its fluoride recovery increased, and its fluoride recovery was 100%. Experiments with difluoroacetic acid and trifluoroacetic acid showed that TFA could not have defluorinated through oft-proposed successive H/F exchanges, but rather that all three fluorines were displaced at once, as would occur in the DHEH pathway. Bentel et al. concluded that side reactions that reductively replaced alpha and beta fluorines with hydrogen were responsible for a buildup of recalcitrant PFAS byproducts and thus for the decreased defluorination efficiency compared to the degradation of the parent PFCA compounds, i.e., the disappearance of the original PFCAs without quantitative inorganic fluoride recovery. A follow-up study focusing on perfluoroethercarboxylic acids (PFECAs) noted that short fluorinated sections between ether bonds was desirable, as the BDEs of the fluorines adjacent to oxygens were higher and thus less prone to H/F exchange, and these compounds had higher overall defluorination because C–O bond cleavage tended to defluorinate the adjacent fluorines regardless of BDE (*90*). A second follow-up study focused on the same degradation reaction at pH 12 and noted that the ability of the hydrated electrons to cleave C–F bonds seemed elevated at high pH, leading to more substrates following the desired DHEH pathway but also increasing possible pathways for H/F exchange, particularly in the example of TFA.

In a third follow-up study, Liu, Bentel, et al. used an oxidation-reduction-oxidation sequence to near-quantitatively degrade PFCAs, FTCAs, fluorotelomer sulfonates (FTSAs), and perfluorosulfonic acids (PFSAs). By oxidizing the FTCAs and FTSAs with potassium persulfate and sodium hydroxide at 120 °C in a pressure cooker, they were able to transform these PFAS

into PFCAs. Using the previously developed high-pH UV-sulfite treatment method, they transformed the PFCAs (and PFSAs) into either mineralized PFAS or a mixture of H/F-exchanged PFCAs. An additional post-oxidation step, following the same procedure as the first oxidation, oxidized the H-rich residual compounds and cleaved the remaining C–F bonds to finish the degradation, showing the promise of complementary destruction methods determined by understanding the degradation mechanisms active in each degradation strategy.

1.4.3. Chemical oxidants/Persulfate

Persulfate, as used by Liu, Bentel, et al. in the previous oxidation-reduction-oxidation example, is a common PFAS oxidant. While heat-activated persulfate can degrade PFOA into shorter-chain PFAS and some fluoride (*98*), it is much less effective for PFSAs, hypothesized to be because the sulfonate head group has a lower electron density compared to carboxylic head groups, leading to a decreased susceptibility to oxidation by sulfate free radicals (*84*). Additionally, UV–persulfate systems are inhibited by matrix constituents of real water, which leads to further degradation inefficiencies. A study by Lutze et al. showed that while PFCAs can technically be degraded by sulfate radicals, other matrix constituents react more rapidly with $SO_4^{2-}\bullet$ than PFCAs do, and that PFCA degradation with persulfate took five orders of magnitude more energy than to degrade atrazine pollutant (Figure 1.10) (*99*). The authors suggested that sulfate radical processes should not be used to degrade PFAS because of how the intensely energy intensive the process is.

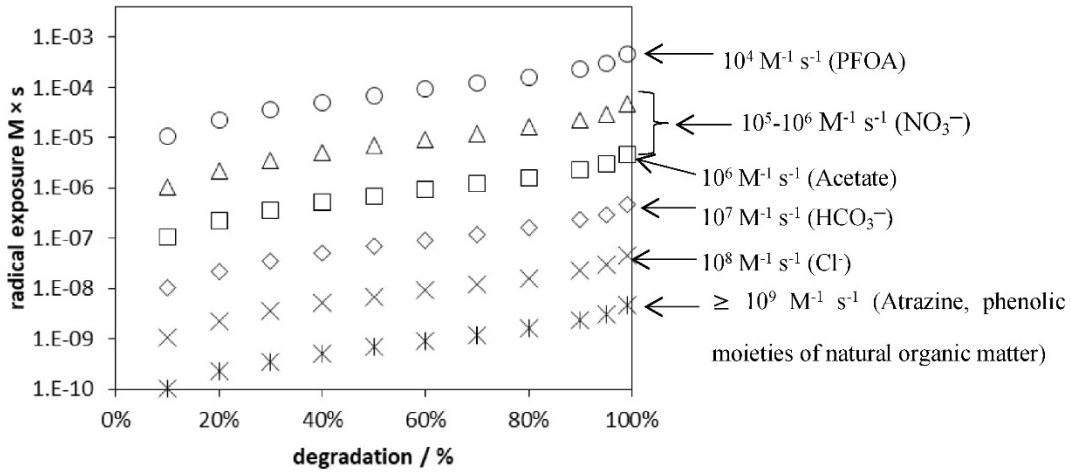

Figure 1.10 Radical exposures necessary for the degradation of compounds calculated on the basis of second order rate constants. Reproduced with permission from (*99*), copyright 2018 Elsevier.

1.4.4. Chemical reductants/Vitamin B_{12}.

Though less common than chemical oxidation, chemical reduction processes have also been investigated for PFAS degradation. Such approaches have included using the cobalt-containing vitamin B_{12} catalyst with reductants such as Ti(III) citrate, zero-valent zinc, or sulfide (*100–102*). These approaches were able to induce PFOS degradation, but were only effective on branched PFOS rather than linear PFOS, mostly affecting the alkyl chain (resulting in H/F exchanged byproducts) rather than cleaving the C–S bond. One study attributed this to "the inability of L-perfluoroalkyl sulfonates to complex with VB12 and not an activation energy issue that can be overcome by stronger reductants/catalysts."

For both oxidation and reduction, advanced oxidation/reduction processes have been developed in which different activation methods, such as ultrasound, UV light, microwaves, or electron beams are combined with chemical reductants/oxidants to generate radicals that aggressively react with contaminants (*84*).

1.4.5. Plasma

In contrast to traditional oxidation/reduction schemes, degradation via plasma allows PFAS to be simultaneously oxidized and reduced, with oxidation hypothesized to occur through hydroxyl radicals and reduction hypothesized to occur through aqueous electrons as well as plasma constituents (*84*). Experiments suggest that plasma-based PFAS degradation is less sensitive to the matrix constituents of wastewater because plasma–PFAS interactions take place at the water–plasma interface rather than the bulk water. While studies show high efficiencies for plasma degradation, there is a lack of clarity for the degradation mechanism and many short-chain PFAS are detected (*103*), in line with the low fluoride recovery from this method, which ranged from 27–62% when the PFOA concentration was near zero in two different studies (*103*, *104*). This destruction method also has the potential to produce gas-phase byproducts that are harder to trap and characterize. A large portion of the fluorine balance was missing from the studies of liquid-state organic fluorine, inorganic fluoride, and volatile organofluoride, leading authors to ascribe >20% of the fluorine for PFOA and >40% of the fluorine for PFOS as being adsorbed to the reactor (*103*).

1.4.6. Ball-milling

PFAS can be mineralized by mechanochemically milling PFAS powders with reactants—usually alkaline hydroxides—under conditions of extreme energy input by physical impact in a ball mill (*105–107*). However, ball-milling PFAS destruction methods appear to be very dependent on the specific milling conditions, which may vary depending on the model of ball mill, size of the container, size of milling balls, and overall energy intensity/energy dose (*105*, *106*). Additionally, different studies find different efficacies for different reagents—one study found that only KOH was competent for PFAS degradation, while another study found that NaOH was also competent

for some PFAS destruction, while another study found that CaO was competent for PFAS degradation, while another study found that CaO was not the optimal reactant for PFAS degradation (*105–107*). Additionally, while studies were generally able to account for stoichiometric amounts of sulfate relative to the amount of PFSAs destroyed, they were not able to account for the full stoichiometric balance of fluoride relative to destroyed PFAS. Ateia et al. found evidence via solid-state ^{19}F NMR spectroscopy for some C_xF_x species being created during the milling process, which might account for the sub-stoichiometric fluoride recovery (*105*). While the mechanism of PFAS degradation has been suggested to be a stepwise "flake-off" mechanism in which carbons "flake off" of the perfluorocarbon structure as either stoichiometric CO, CO_3^{2-}, or formate (*106*, *107*), characterization of the degradation products by Ateia et al. suggest that there is one equivalent of formate formed per molecule of PFAS destroyed, with the rest of the carbons going to carbonate. This suggests a mechanism other than the stepwise "flake-off" mechanism suggested elsewhere in the literature, but does not immediately suggest an alternate mechanism.

1.4.7. Electrochemical degradation

There are several modes of electrochemical treatment of PFAS. Direct electrolysis degrades contaminants directly at the electrode, while indirect electrolysis produces oxidizing agents at the electrode that diffuse to degrade contaminants in the bulk solution. Electrochemical degradation has been investigated with several electrode compositions, including Ti/RuO_2 and Ti/SnO_2-Sb-Bi (*108*, *109*), but the most-studied electrode material is boron-doped diamond (*84*, *110*). While degradation on boron-doped diamond was able to achieve near-quantitative disappearance of the starting PFBS, PFHxS, and PFOS, the fluoride recovery based on the amount of PFAS degraded was only 66% and several shorter-chain PFCAs were detected; in the degradation of a mixture of

PFCAs and PFSAs, the concentration of PFCAs after degradation was higher than their initial concentration (*110*). Generally, electrochemical PFAS degradation suffers from high energy consumption, the formation of toxic byproducts from other matrix constituents in real water, electrode issues such as mass transfer and fouling, and the lack of cost-effective and scalable electrode materials (*111*, *112*).

1.4.8. Supercritical water oxidation

A PFAS degradation method that has recently come to prominence is supercritical water oxidation (SCWO), which brings water to above 374 °C and 22.1 MPa in the presence of an oxidizing agent that might be as simple as ambient oxygen. In a test of three industrial, proprietary SCWO methods (*113*), AFFF was treated at temperatures around 590 – 595 °C, for two methods with air as the oxidizer, and for all methods with alkaline base added, ostensibly to neutralize any hydrofluoric or sulfuric acid generated. The PFAS in the AFFF influent was characterized by HPLC-MS/MS prior to treatment but was not treated with a total oxidizable precursor assay or analyzed for total organic fluorine, meaning that only specific PFAS were quantified and any unknown PFAS outside of those specifically tested for were excluded from the analysis. All three SCWO methods were able to reduce the amount of quantified PFAS by 99.9% after treatment. However, the Battelle Annihilator^{TM} SCWO system was the only one tested for fluoride recovery, and the amount of fluoride detected after degradation far exceeded the predicted amount of fluorine based on the quantified initial amount of PFAS—the predicted stoichiometric amount only accounted for 27% of the found amount of fluoride, showing that the AFFF contained many PFAS structures that were unaccounted for in the targeted quantification of influent. This problem precluded proper quantification of how much of the PFAS was mineralized. Additionally, the authors noted that the effluent concentrations of PFAS quantified in the targeted post-analysis

were still above the EPA's drinking water health advisory of 70 ppb, so SCWO treatment of AFFF-impacted water might need to undergo further treatment by cycling the effluent through the degradation multiple times or by a method such as reverse osmosis to create potable water.

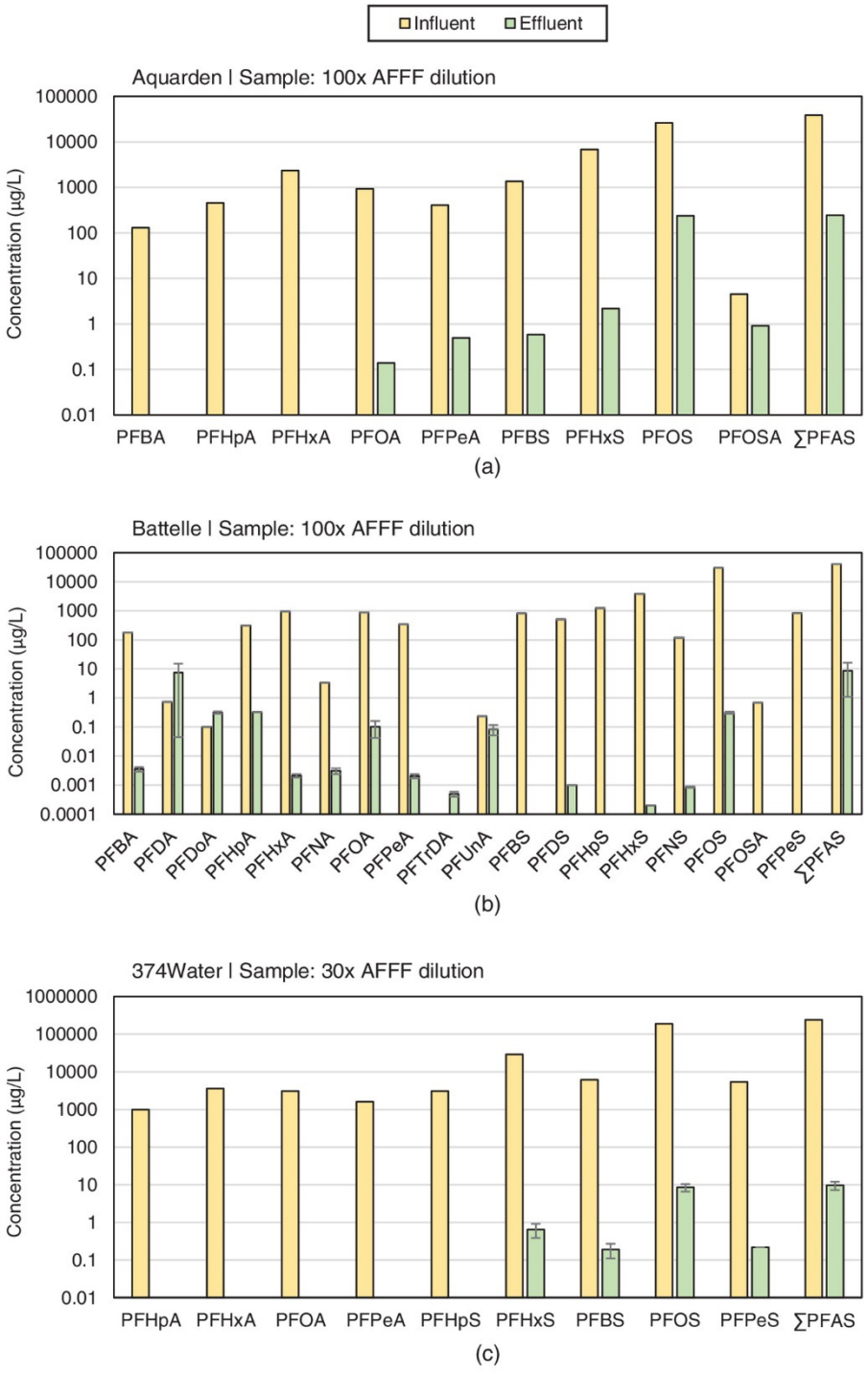

Figure 1.11 PFAS quantified in the influent or effluent of the SCWO experiments performed by (a) Aquarden | sample: 100×100× AFFF dilution; (b) Battelle | sample: 100×100× AFFF dilution; and (c) 374Water | sample: 30×30× AFFF dilution. PFAS are organized alphabetically by detected carboxylic acids and then sulfonic acids. Refer to the supplemental materials for a full list of analyzed PFAS. Reproduced from (*113*). Copyright 2022 American Society of Civil Engineers.

1.4.9. Hydrothermal alkaline treatment

Another recent promising method for PFAS destruction is hydrothermal alkaline treatment (HALT). Higgins, Strathmann, and co-workers screened several different amendments for PFAS degradation efficiency under subcritical hydrothermal conditions (heating water to 200–374 °C and 2–22 MPa) and found that basic amendments, particularly sodium hydroxide, promoted the degradation and defluorination of PFOS (*97*). Treatment at 50 mg/L PFOS, 2.5 M NaOH, 350 °C, and 16.5 MPa for 90 min gave >80% defluorination and total disappearance of the initial PFOS. Small amounts of smaller-chain PFCAs were detected after the reaction, confirming that sulfonate head cleavage does occur in the shortening mechanism, which was proposed to be the DHEH mechanism, though a balanced step for the decarboxylation-to-perfluoroalcohol step was not proposed. This method was later used to degrade AFFF, where the initial organofluorine concentration was determined by ^{19}F NMR spectroscopy and the concentration of fluoride ion after treatment accounted for 110 ± 5% and 105 ± 4% of the total fluorine content for the first and second AFFF samples, respectively. “To the best of our knowledge,” the authors wrote, “this is the first treatment method, other than incineration, (*86*, *114*) demonstrating near-complete defluorination of concentrated AFFF in a short time, and suggests its potential as an alternative technology for the disposal of unused AFFF stockpiles.” However, this author would contend that references (*86*, *114*) do not test the degradation of AFFF and do not actually show complete defluorination of PFAS, though HALT technology is indeed promising for PFAS removal.

1.4.10. Proposed PFAS Destruction Mechanisms

Most PFAS degradation studies either do not propose a mechanism, propose a mechanism that is not chemically balanced, or do not offer any experimental evidence to support their proposed mechanism (see **Table S3.1**). This tendency has led to several misconceptions about the active

degrading species in PFAS destruction experiments, especially in conditions where reactive oxygen species have been ascribed as the active agents. The work of Alvarez and co-workers has been key in dispelling some of these myths, especially in regards to the effectiveness of •OH and superoxide (*115–117*).

However, the most popular proposed mechanism for PFCA chain-shortening and degradation is the decarboxylation-hydroxylation-elimination-hydrolysis ("DHEH") pathway (*89*, *96*, *97*), shown in **Figure 1.11**. In the DHEH mechanism, photolysis, photoredox (*96*), hydrated electrons (*89*, *94*), radical-initiated decarboxylation (*118–120*), or other similar reaction first decarboxylates the PFCA, leaving a reactive perfluorocarbon chain. This reactive species is often proposed to be a radical, but depending on the method of decarboxylation could be a carbanion stabilized by the intense electron-withdrawing character of the perfluoro-functionalized chain. This reactive perfluorocarbon chain reacts with water, hydroxylating it to an unstable perfluoroalcohol, which quickly eliminates HF, leading to an acyl fluoride. The perfluoroacyl fluoride is hydrolyzed by water, leading to another HF elimination and the formation of a chain-shortened perfluorocarboxylic acid one carbon shorter than its starting length, which can again be decarboxylated and chain-shortened (*89*, *96*, *97*). Through this mechanism, PFCAs (and de-sulfonylated perfluorosulfonic acids) can completely decompose and mineralize to carbon dioxide and fluoride.

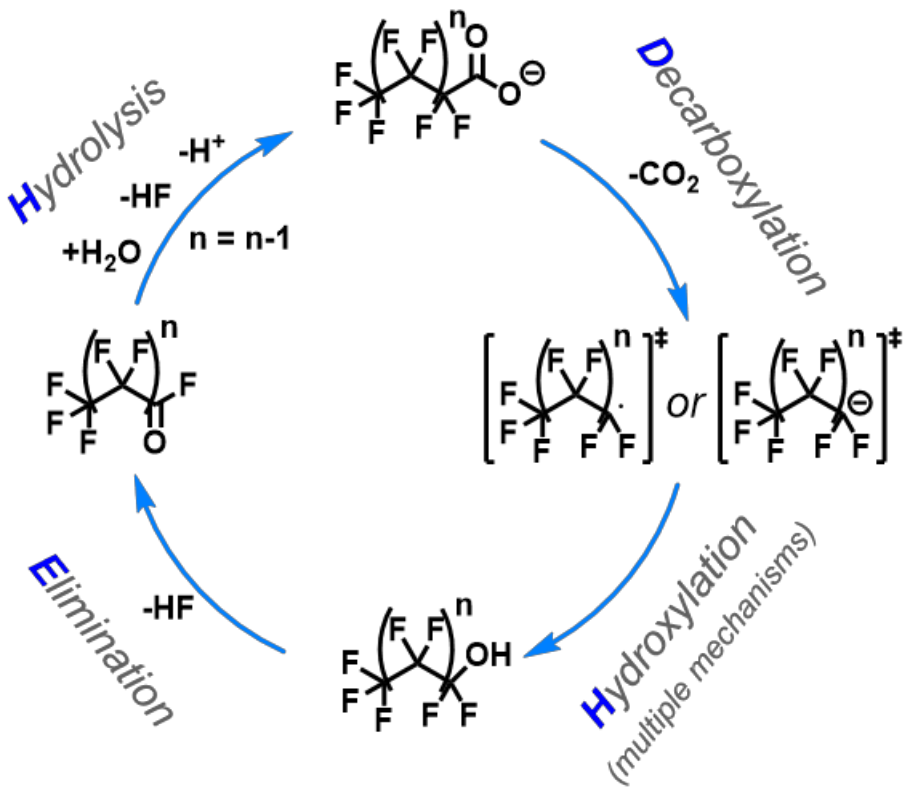

Figure 1.12 Overview of the decarboxylation - hydroxylation - elimination - hydrolysis mechanism. Content adapted from (*89*).

However, as Bentel et al. point out in their studies (*89–91*), in practice, not all PFCA molecules move cleanly through this pathway. In a reductive environment (such as is present in a hydrated electron, electrochemical, or advanced reduction process), the lower-energy C – F bonds alpha to the carboxyl or in the middle of long perfluoro chains can be reductively exchanged with hydrogens, leading to telomeric PFAS with higher recalcitrance to degradation. Bentel et al. estimate from their study of the degradation of $CF_3CF_2COO^-$ that there is a 75% probability for the first degradation step to be H/F exchange rather than the decarboxylation that would lead to the DHEH pathway (*89*). As H/F-exchanged byproducts build up, the number of PFAS molecules available to go through the DHEH pathway decreases, leading to low mineralization efficiencies and a high concentration of diverse, partially hydrogenated PFAS.

This is one of the main reasons why current "brute force" degradation methods predicated on injecting large amounts of untargeted energy are inadequate to effectively address the PFAS pollution problem.

1.5. Current Challenges and Future Opportunities in PFAS Remediation Research

The discovery that cationic polymers are generally effective for adsorbing anionic PFAS has greatly advanced the emerging PFAS adsorbent field (*50*, *51*, *74*, *76*, *81*). However, other components of PFAS adsorption properties have yet to be studied, including the difficult-to-discern difference between hydrophobicity and fluorophilicity in PFAS adsorbents (*51*, *121*) and whether cationic CDP adsorbents adsorb entirely on the charged cross-linker sites, like an IX resin, or contribute to adsorption by complexing the hydrophobic PFAS molecules in the cyclodextrin cup (*68*, *121*). Both of these components are key considerations for designing efficient future adsorbents and especially determining whether cyclodextrin is necessary in cationic PFAS adsorbents.

As PFAS destruction is a newer field than PFAS adsorption, there are presently several opportunities for improving PFAS destruction. Firstly, essentially all of the currently studied PFAS destruction methods are not specifically targeted to PFAS and require high amounts of energy to essentially break bonds non-specifically via great force. As Bentel et al. have detailed, relying on non-specific reactions to degrade PFAS can create conditions that result in unwanted side reactions, such as H/F exchange, that result in more recalcitrant byproducts (*89*). Because the agents that degrade PFAS can also react with other components of real water matrices, these non-specific interactions can also increase the amount of energy needed to degrade PFAS and decrease degradation efficiency (*99*). Developing PFAS degradation strategies that specifically take into

account fluorocarbons' reactivity will increase the efficiency of degradation methods. Further, the mechanism of PFAS destruction is not well-studied, well-supported, or well-understood, and investigations detailing the reactivity of PFAS under various degradation conditions will provide useful insight for improving these methods.

Secondly, many PFAS destruction strategies focus on remediating PFAS in-situ in wastewater. This confers many disadvantages on these methods; PFAS occurs at dilute concentrations in wastewater, often at parts-per-billion or parts-per-trillion levels. The vast amount of water leaves plenty of opportunity for degradation agents to be quenched before they reach the dilute PFAS molecules. Matrix constituents such as salts or NOM can also decrease the degradation effectiveness, and the large volumes of water that need to be treated by this method necessitate scaling the degradation methods up by several orders of magnitude, at which they become either prohibitively expensive or decrease in efficiency because of reactor effects (*84*). Instead, using treatment trains—or the "separate, concentrate, destroy" method (*122*)—in which adsorption or filtration first separates the matrix constituents from the PFAS and also concentrates the PFAS into a smaller volume for destruction—will drastically decrease the electrical energy per order of magnitude (E_{EO}) necessary for total PFAS degradation and will enable solvents other than water to be used in degradation reactions. The effectiveness of such treatment trains has already been studied and has been shown to decrease the E_{EO} by one or more orders of magnitude (*48*). Treatment approaches that integrate both the treatment train approach with degradation methods that are more specific to PFAS have the potential to be very effective for PFAS destruction.

2. Aryl Ether Cross-Linked Cyclodextrin Polymers Through Sulfonyl Transfer Reaction

2.1. Abstract

The seven-membered glucose cyclic macromolecule beta-cyclodextrin (β-CD) contains a hydrophobic cavity that makes it a high-affinity host molecule for a wide variety of organic guest molecules. Cyclodextrins have been used to trap organic micropollutants and are promising for water remediation applications; however, the cyclodextrin molecule itself is soluble in water, limiting its practical use. To solve that problem, many insoluble cross-linked β-CD polymers have been synthesized. In 2016, our group reported the synthesis of a decafluorobiphenyl-linked cyclodextrin polymer (DFB-CDP) crosslinked via nucleophilic aromatic substitution that showed >90% removal of perfluorooctanoic acid (PFOA) in water. PFOA is a persistent environmental contaminant at the center of a growing public health crisis. Similar β-CD polymers show no affinity for PFOA, so the mechanism of PFOA trapping in DFB-CDP remains unknown. To probe the possibility that DFB-CDP's high affinity for PFOA is caused by favorable fluorophilic interactions mediated by its fluorine-rich crosslinker, we wanted to use a similar biphenyl linker to synthesize a fluorine-free polymer. However, eliminating the electron-withdrawing fluorines means the cross-linking reaction can no longer be conducted by nucleophilic aromatic substitution. To access the desired non-fluorinated polymer, we developed a new cross-linking polymerization based on a mesyl transfer reaction. The resulting biphenyl polymer (BP-CDP) initially showed no affinity for PFOA compared to the previous DFB-CDP polymer, indicating that DFB-CDP's fluorines likely contributed to its high affinity to PFOA. However, over time, the polymer's performance deteriorated, making the results inconsistent and unsuitable for scientific conclusions.

Subsequent reports did investigate aryl hydrocarbon-linked polymer synthesis and adsorbent properties and their conclusions are presented here.

2.2. Introduction

Although useful and important, household cleaners, personal care products, pharmaceuticals, pesticides, and industrial chemicals can introduce harmful compounds into the environment when allowed to contact water sources (*123*, *124*). Some of these micropollutants have negative health or ecological impacts and the full ramifications of releasing thousands of these compounds into our environment are not fully understood. Because these micropollutants are present at very low concentrations in water, they are often difficult to remove effectively with conventional water treatment methods such as activated carbon filters (*39*, *40*, *125*). This especially applies to per- and polyfluoroalkyl substances (PFAS). Recently, cross-linked polymers containing beta-cyclodextrin (β-CD) (*65*) have shown great promise for micropollutant removal due to β-CD's high affinity for hydrophobic molecules, including PFAS compounds (*53*, *62*, *126*, *127*). Early cyclodextrin polymers were commonly linked through linear chains formed by reaction with epichlorohydrin (*63*, *128–130*) or with urethanes formed from isocyanates (*66*, *69*), but our group has demonstrated that aromatic cross-linkers show faster uptake kinetics and better fouling resistance compared to activated carbons (*67*, *73*).

Though the majority of cyclodextrin-based networks incorporate the same β-CD hosts, it has become clear that the structure of the crosslinking groups has a profound impact on the selectivity, affinity, and kinetics of micropollutant removal (*66*, *67*, *73*, *74*). Quantitative structure-activity relationship (QSAR) models have investigated which properties are important for micropollutant uptake within these networks (*131*); expanding the library of cross-linkers will increase the utility of these machine-learning-based analyses. However, among aryl-ether-based

cyclodextrin materials, crosslinkers have so far been limited to electron-poor monomers capable of two or more nucleophilic aromatic substitutions (S_NAr) (*67*, *73–75*).

We recently developed a β-CD polymer cross-linked with decafluorobiphenyl linkers (DFB-CDP; Figure 2.1A) that shows a high affinity for PFOA. Its Langmuir affinity coefficients (K_L) are on the order of 2.2 x 10^5 M^{-1} and it can reduce PFOA concentrations from 1 part per billion (ppb) to <10 ppt (*73*), lower than the 2016 EPA advisory limit of 70 ppt (*42*). Though we hypothesize that an attractive fluorous interaction between the DFB aryl fluorines and the PFOA alkyl fluorines is responsible for this polymer's high affinity for PFOA (*132*, *133*), there is no specific experimental evidence to support this hypothesis for our polymer system. Understanding why some β-CD polymers bind PFOA strongly while others do not is a key question for further improving adsorbent performance (*73*, *134*).

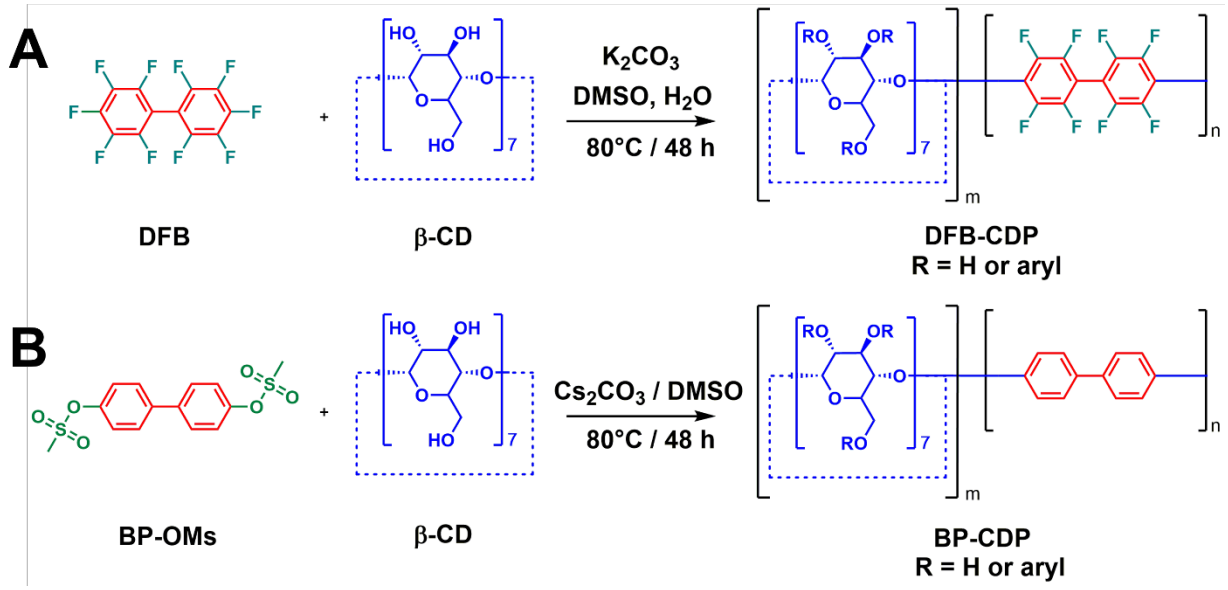

Figure 2.1 Synthesis schemes for DFB-CDP (A) and BP-CDP (B).

One way to probe this hypothesis is by synthesizing a polymer that is isostructural to DFB-CDP except for the fluorines. However, our group has historically only synthesized β-CD polymers

through a nucleophilic aromatic substitution (S_NAr) cross-linking polymerization in which the fluorines on the linkers create an electron-deficient aryl ring that deprotonated cyclodextrin alcohols can attack to form a bond. Removing the fluorines from the linker makes the aryl linkers insufficiently electron-deficient to undergo the S_NAr polycondensation. To make an isostructural non-fluorine-containing DFB-CDP analogue (Figure 2.1B), new chemistry is needed.

S_N2 and Friedel-Crafts-based polymerizations for incorporating aryl moieties into cyclodextrin polymers have been developed (*135–137*), but none of these approaches can attach the cyclodextrin directly to the aryl ring via ether linkages that impart rigidity and stability to the polymer. Polymerizations of functionalized cyclodextrins are an option (*136*, *137*), but these methods are likely to be expensive or perturbative of the cyclodextrin's binding characteristics. To incorporate non-electron-poor aryl monomers into a β-CD polymer network, we hypothesized that sulfonyl transfer, as reported by Sach and co-workers for molecular compounds, might be suitable for cross-linking cyclodextrins through aryl ether linkers (*138*) (Figure 2.2). Here we report three poly(aryl)ether networks containing β-CD synthesized by mesylate transfer etherification and their uptake of model pollutant bisphenol A (BPA). This synthetic approach significantly broadens the scope of aromatic cross-linkers available for CD polymers and other structures.

2.3. Results and Discussion

The initial report of sulfonyl transfer etherifications (*138*) provided four distinct sets of optimal conditions for various substrates and did not explore either carbohydrate functionalization or polymerization. Therefore, we explored conditions to maximize the reaction efficiency for our preferred monomers (Figure 2.2). The previous study employed four different bases: sodium *tert*-butoxide (NaOtBu), cesium carbonate ($Cs_2CO_{3)}$, sodium hydride, and lithium *tert*-butoxide

(LiOtBu). We explored the etherification of BPA dimesylate with *n*-butanol, which serves as a model for β-CD's primary hydroxyl groups, in the presence of each base (Figure 2.3).

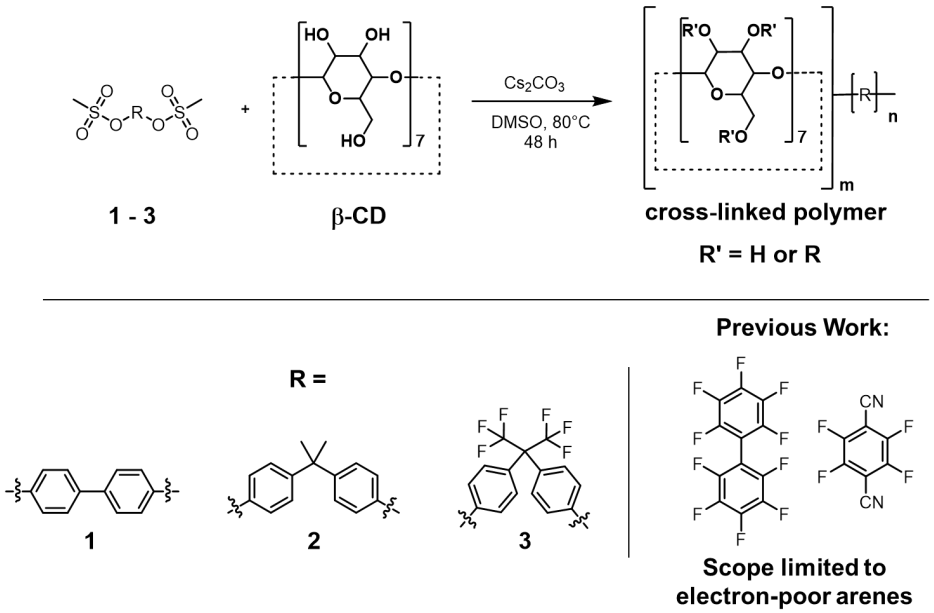

Figure 2.2. Mesylated linkers can be incorporated into β-CD polymers by sulfonyl transfer reaction. Previous cyclodextrin polymers were limited to linkers with electron-withdrawing substituents that could undergo nucleophilic aromatic substitution (*67*, *73*).

The four bases were evaluated in a model reaction between BPA dimesylate **2** and *n*-butanol. LiOtBu (Figure 2.3, middle chromatogram, green) provided the desired dibutyl ether product (peak B) with only minor evidence of under-alkylation and other side products, as assessed by gas chromatography mass spectrometry (GC-MS). Cs_2CO_3 (top chromatogram, red) showed evidence of incomplete etherification, including the monosubstituted side product C and monosubstituted side product D. NaOtBu (bottom trace; blue) gave di-substituted product B, side-product C, as well as two prominent unidentified side products (Figure 2.3). Both LiOtBu and Cs_2CO_3 show the desired bond-forming process with the absence of unwanted side reactions.

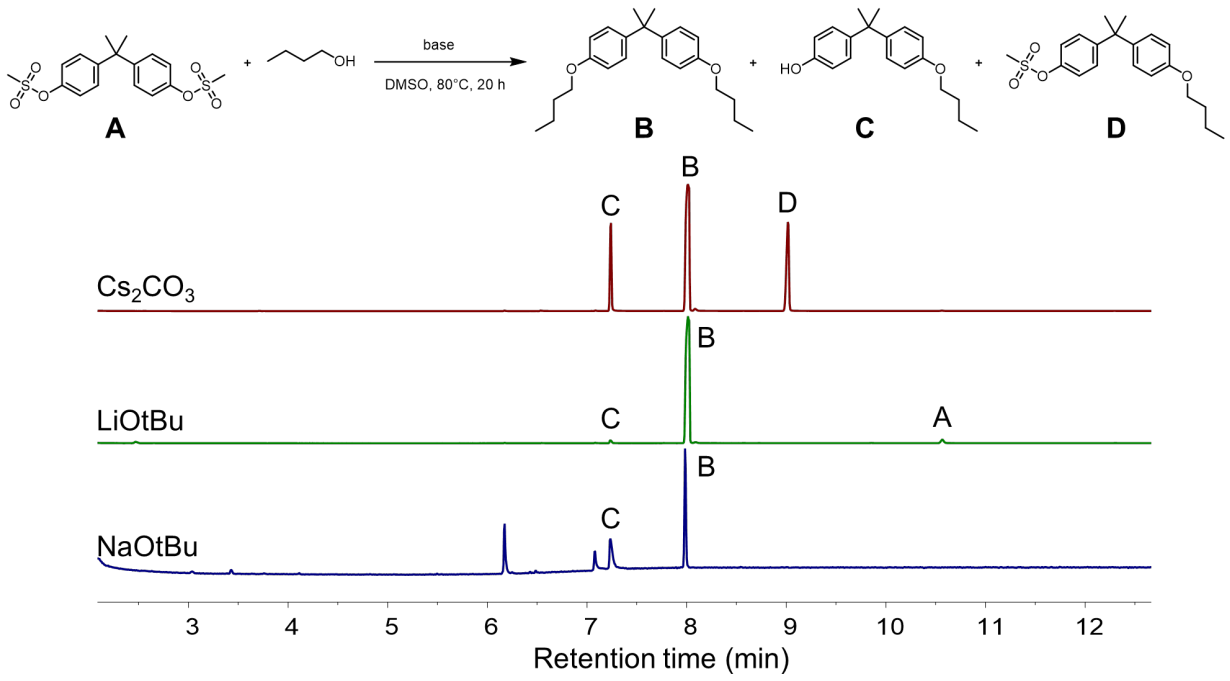

Figure 2.3. Base study. Lithium tert-butoxide reaction proceeds cleanly to disubstituted product, cesium carbonate gives distribution of three products, and sodium tert-butoxide gives two products as well as additional unidentifiable side products.

Having established the desired reactivity in model compounds, we evaluated the sulfonyl transfer etherification reaction's ability to polymerize aryl dimesylates and β-CD. These polymerizations required further optimization of the concentration, dimesylate : β-CD ratio, and amount of base to obtain insoluble, cross-linked products. The polymerizations were evaluated based on the yield of insoluble polymer following workup using successive washes in water, tetrahydrofuran (THF), and CH_2Cl_2. Polymerizations that produced only soluble products were considered inefficient and were not evaluated further. An insoluble polymer powder was obtained in good yield (71 wt%, as compared to the mass of the monomers less the mesylate groups; see chapter appendix) using a dimesylate : β-CD : base ratio of 6 : 1 : 24 at 0.4 M (with respect to β-CD) at 80 °C for 48 hours. Using a β-CD concentration of 0.1 M rather than 0.4 M in β-CD produced more soluble oligomer than insoluble polymer (Table 2.1, entries 2 – 3). Using a 3 : 1

dimesylate-to-cyclodextrin feed ratio rather than a 6 : 1 ratio gave a lower yield of 20% polymer (Table 2.1 entry 4 vs. entry 6). We also found that the amount of base must scale with the linker equivalents in a 4 : 1 ratio (Table 2.1, entries 3 – 6). While 12 base equivalents were sufficient for polymer formation with 3 linker equivalents, and likewise 24 base equivalents with 6 linker equivalents, 12 equivalents of base with 6 equivalents of linker gave products that were insoluble in DMSO/H_2O but solubilized upon washing with THF. Under the optimized conditions, reaction entry 6 afforded a light brown, insoluble, amorphous powder (**BP-CDP**).

Table 2.1. Systematic investigation of base, concentration, and dimesylate : β-CD : base ratios. The optimized reaction (entry 6) uses 0.4 M β-CD, 6 equiv linker, 24 equiv Cs_2CO_3 heated in DMSO at 80 °C for 48 hours.

Entry	[β-CD] (M)	Base	R	Ar : β-CD : Base	Result
1	0.1	LiOtBu	BPA	3 : 1 : 12	0%
2	0.1	Cs_2CO_3	BPA	3 : 1 : 12	sol. products
3	0.4	Cs_2CO_3	BPA	3 : 1 : 12	33% yield
4	0.4	Cs_2CO_3	BP	3 : 1 : 12	20% yield
5	0.4	Cs_2CO_3	BP	6 : 1 : 12	sol. products
6	0.4	Cs_2CO_3	BP	6 : 1 : 24	71% yield
7	0.4	Cs_2CO_3	BPA	6 : 1 : 24	61% yield
8	0.4	Cs_2CO_3	BPAF	6 : 1 : 24	55% yield

BP-CDP was characterized by N_2 adsorption, Fourier-transform infrared spectroscopy (FT-IR) and solid-state cross-polarization magic angle spinning NMR (CP-MAS NMR; Figure 2.4). N_2 adsorption measurements showed that the polymer was non-porous (see chapter appendix). FT-IR and CP-MAS NMR show the incorporation of both biphenyl and β-cyclodextrin peaks from the biphenol/biphenyl dimesylate linker and the pure β-cyclodextrin, while the S=O FT-IR stretch (1369 cm^{-1}) and mesyl carbon NMR peak (37.47 ppm) from the original monomer are not present in the spectra of the final polymer.

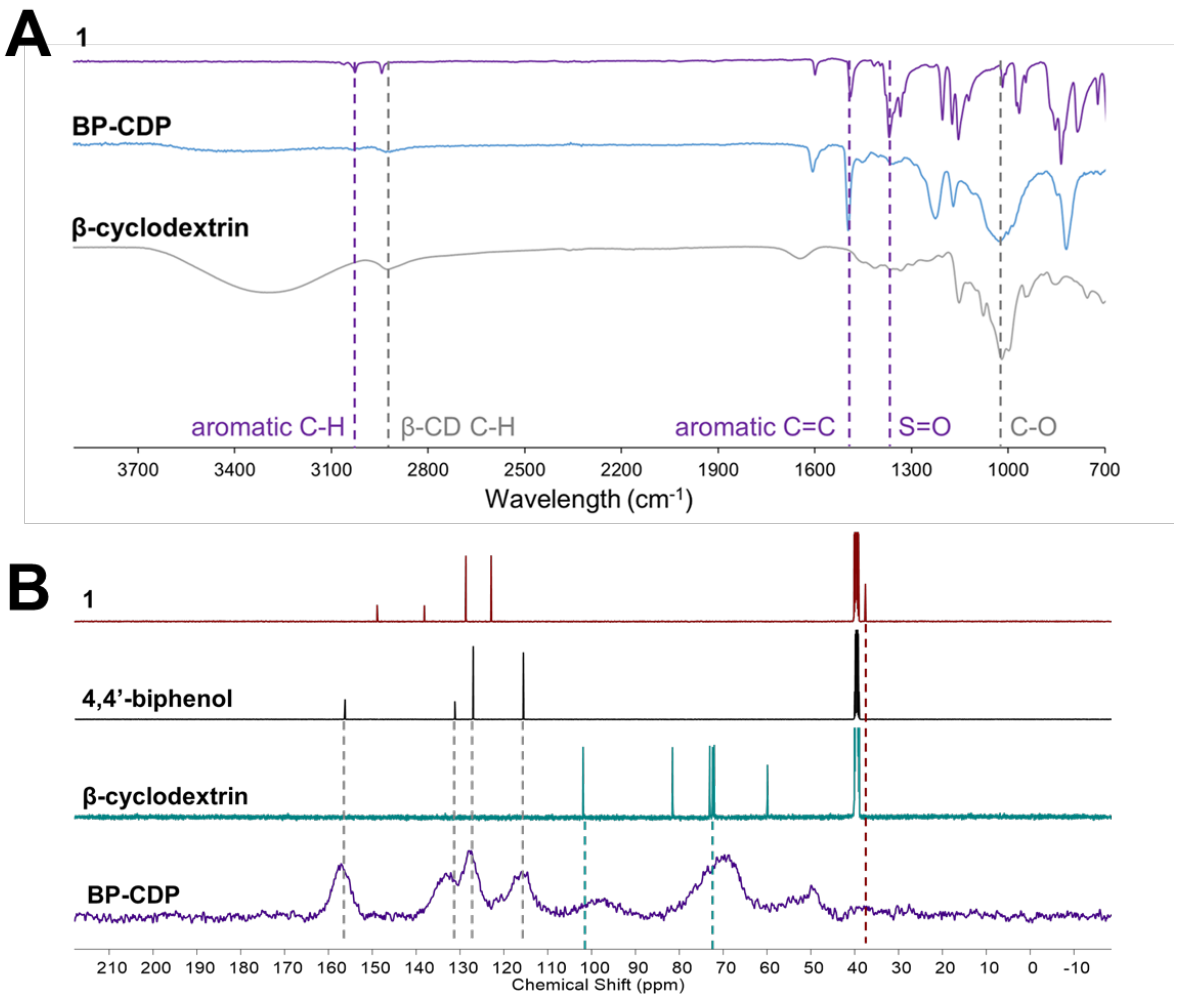

Figure 2.4. Polymer characterization of BP-CDP. A) FT-IR spectrum shows that both the biphenyl linker (1; top, purple) and β-CD (bottom, gray) stretches have been incorporated into the BP-CDP polymer (middle, blue). B) Solid-state CP-MAS ^{13}CNMR (bottom spectrum; 600 MHz, 10k spinning rate) is consistent with the presence of both β-CD and biphenyl groups and also does not show evidence of the mesyl group at 37 ppm.

However, combustion elemental analysis shows that even after extensive Soxhlet extraction with water or methanol, there is still residual sulfur content within the polymer (Table S 2.2), which can be attributed to residual mesylates from mesylate transfer and incomplete condensations, according to the mechanism proposed by Sach and co-workers (*138*). To determine where these mesylates are within the polymer, we conducted a model experiment where we replaced the mesylated biphenyl with a mono-functional mesylated phenol (compound **4**; see

chapter appendix) that could not cross-link the cyclodextrins and would instead provide discrete molecular products that could be characterized by solution methods. Matrix-assisted laser desorption/ionization mass spectrometry (MALDI-MS) of the model reaction product shows several peaks that correspond to the mass of variously-substituted cyclodextrins plus an incompletely transferred mesyl group (see Figure S 2.1). This model study shows that mesylates can be incorporated into the polymer via attachment to the cyclodextrin ring, as well as to a biphenyl group that undergoes a single etherification reaction. However, the incidence of both of these situations is relatively low, given that combustion elemental analysis indicates less than one mesylate per cyclodextrin present in the polymer (0.88 residual mesylates per β-CD) and ~8 biphenyl substitutions per cyclodextrin ring (see Table S 2.2). Furthermore, FT-IR and CP-MAS ^{13}C NMR spectroscopies show the do not show evidence for mesyl groups above their respective detection limits.

The optimized mesylate transfer etherification conditions successfully polymerized β-CD with two other polyfunctional phenol monomers, bisphenol A and bisphenol AF (**2** and **3**, Figure 2.2; Table 2.1, entries 7 and 8). The combustion elemental analysis, FT-IR, and CP-MAS NMR for **BPA-CDP** and **BPAF-CDP** were consistent with the expected structures (see chapter appendix.) Although the yields of these polymers were modest (61% and 55%, respectively), no further optimization of the reaction efficiency was attempted for these substrates. These findings indicate the generality of this method for forming polymer networks, while noting that additional exploration of reaction conditions may be necessary prior to scale-up of for using precious substrates.

All of the polymers showed pollutant removal ability, as shown in Figure 2.5. The polymers' uptake properties were tested in a bisphenol A (BPA) batch adsorption study where 1 g/L polymer was stirred in 0.1 mM BPA in a glass scintillation vial. After 24 hours, an aliquot was syringe-filtered and the residual pollutant concentration was analyzed, showing BPA removal. **BP-CDP** showed the highest removal, around 80%, while **BPA-CDP** and **BPAF-CDP** showed lower removal around 50 – 60%. The lower uptake from **BPA-CDP** and **BPAF-CDP** could potentially arise from the gem-dimethyls and gem-di(trifluoromethyls) in the BPA and BPAF linkers, which potentially could occlude the cyclodextrin pore and hinder micropollutant access. However, the potential that these materials show for micropollutant removal, especially with judicious choice of linker, indicates that the sulfonyl transfer method could be used to make polymers from a variety of linkers for improved micropollutant removal and for structure – function studies.

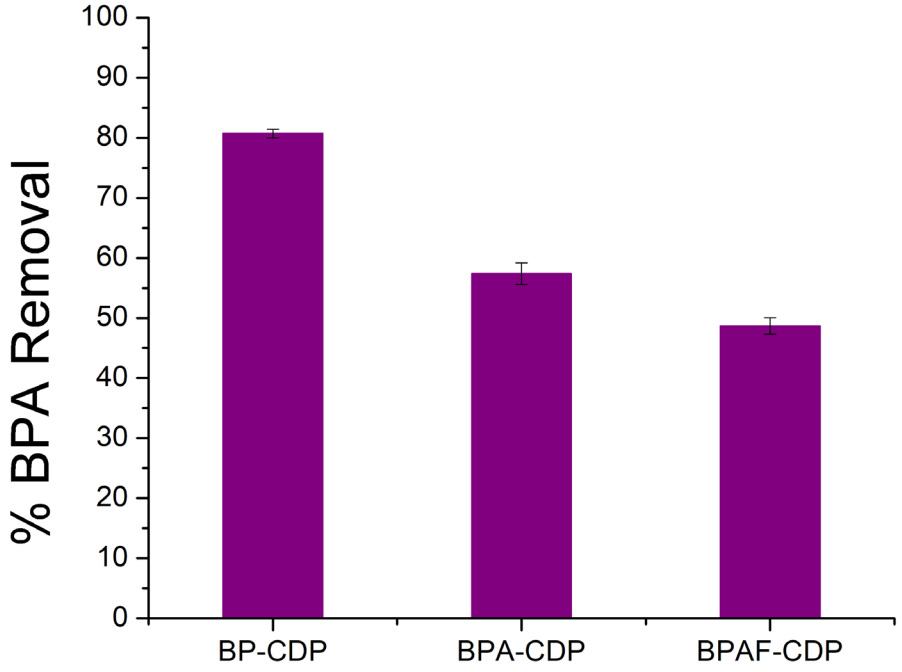

Figure 2.5. Batch BPA removal by polymers made with linkers **1 – 3** at 0.1 mM BPA and 1 g/L polymer in MilliQ water, stirred for 24 hours.

To examine the hypothesis that fluorophilic interactions dominate the PFOA uptake mechanism in the DFB cyclodextrin polymer, we synthesized a variety of DFB-CDPs in an effort to match as many properties as possible with the BP-CDP. In past studies, we found that the surface charge of a polymer (as measured by its zeta potential) affects their micropollutant uptake performance (*75*, *134*). Most of the polymers we have studied have a negative zeta potential, which is correlated with reduced PFOA affinity (*134*). We also found that the surface area of the polymer affects the kinetics of micropollutant uptake but does not affect the equilibrium removal (*75*). To create a comparison between polymers that are as isostructural as possible, we sought to match all of these parameters as well as the cross-linking density. In Table 2.2 are listed values for all of these parameters for BP-CDP and a corresponding DFB-CDP.

Table 2.2. Matched DFB-CDP and BP-CDP polymer properties.

	DFB-CDP	**BP-CDP**
Surface Area (m^2/g)	Non-porous	Non-porous
Zeta Potential (mV, 10 mM phosphate buffer)	-23.0 ± 1.6	-23.8 ± 5.3
Zeta Potential (mV, 5 mM calcium chloride)	-11.7 ± 0.8	-10.3 ± 0.7
Linkers per BCD	4.7	4.8
Residual OMs per BCD	-	0.9

While the BPA uptakes of these two polymers are similar, their PFOA uptakes are very different (Figure 2.6). We performed BPA uptake at 2.8 parts per million (ppm) BPA and 1000 ppm polymer (*67*) and looked at the equilibrium uptake after 20–22 h. Both polymers removed around 90% of the BPA from water under these conditions. However, at 0.2 ppm PFOA and 400 ppm polymer, the equilibrium PFOA uptake of the DFB-CDP (23.5 h) was again over 90%, whereas the BP-CDP took up, within error, zero PFOA (4.1 ± 4.6 %). These results show that

eliminating aryl fluorines in the polymer structure has a profound impact on its PFOA uptake and that the fluorines are likely the major factor making DFB-CDP effective at adsorbing PFAS.

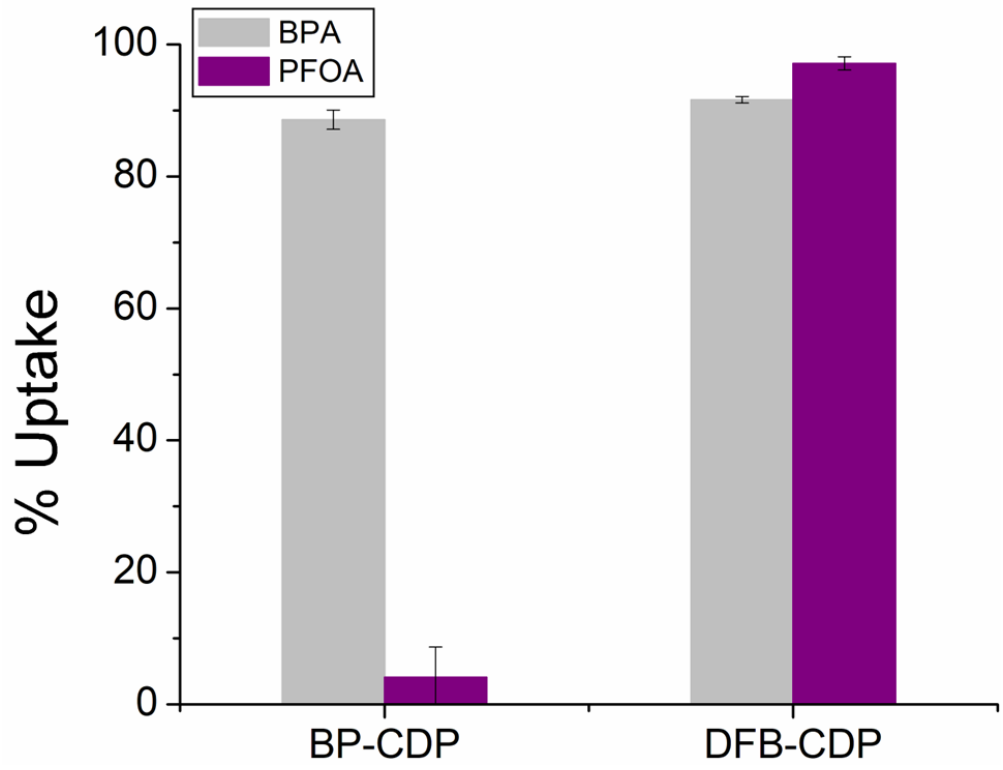

Figure 2.6. PFOA and BPA uptake of BP-CDP and DFB-CDP. PFOA uptake conducted at 0.2 ppm PFOA, 400 ppm polymer, 23.5 h in MilliQ water. BPA uptake conducted at 2.8 ppm BPA, 1000 ppm polymer, 20 – 22 h in MilliQ water.

2.4. Inconsistencies in Results

While preliminary studies seemed to indicate that 1) this synthetic method was good for synthesizing polymers with non-electron-withdrawing aryl substituents and 2) the presence of fluorines in the linker greatly affected the PFOA uptake, several inconsistencies in subsequent results convinced us that these conclusions were incorrect.

Firstly, though we measured high PFOA uptake in the DFB-CDP, as had been reported previously, and low PFOA uptake in the BP-CDP, results from our collaborators showed different performance from the polymers. The polymer synthesis dates and test dates used for make Figure 2.6 above are listed in Table 2.2. In April 2019, a PFAS panel of 10 different PFAS

compounds conducted by collaborators at Cornell showed that within error, both BP-CDP and DFB-CDP had the same PFAS uptake characteristics, both adsorbing ~65% of the PFOA at 1 ppb PFAS mix and 10 ppm polymer conditions.

Table 2.3 DFB-CDP and BP-CDP polymer properties, synthesis date, and test date.

Polymer + Analyte	Synthesis Date	Batch + Uptake Experiment #	Uptake Date
DFB PFOA	Dec 2018	018-0 from BBT-02-022+024	Jan 2019
DFB BPA	Jan 2019	026-651 from BBT-02-033	Feb 2019
BP PFOA	Dec 2018	014 from BBT-02-022+024	Jan 2019
BP BPA	Sep 2018	146 from BBT-01-095+115	Oct 2018

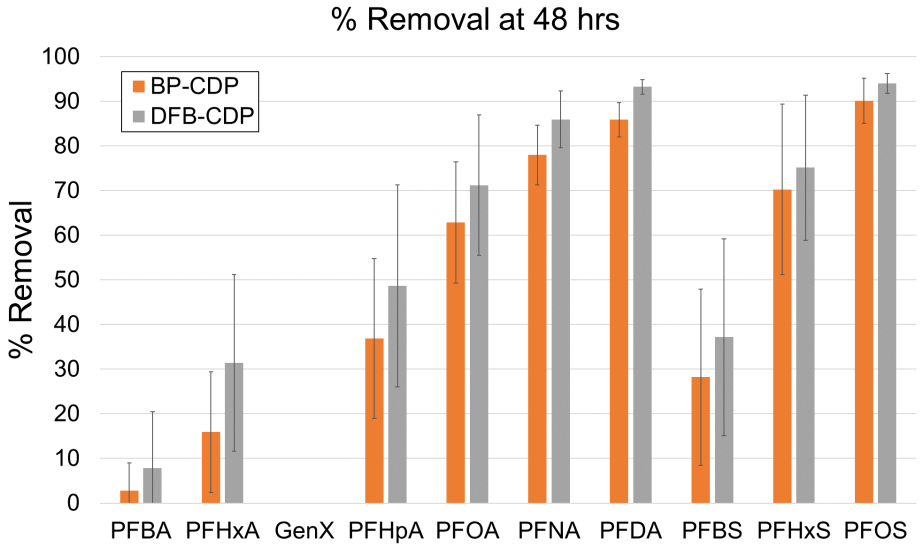

Figure 2.7. PFAS panel of 10 different PFAS, April 2019. 10 ppb of each PFAS in a mixture, 10 ppm polymer. BP-CDP batch 02-014, DFB-CDP batch 02-026-651.

The result showing that both polymers had similar PFAS uptake properties was unexpected based on our preliminary adsorption experiments. Hypotheses as to why the results were different than expected included 1) a polymer mix-up, 2) differences between the preliminary 200 ppb PFOA / 400 ppm polymer experiment and the lower-concentration PFAS panel, 3) errors introduced in the adsorption preparation method, or 4) the possibility that non-removal of PFOA

is the outlier result and that PFOA removal should be expected, especially at these low concentrations.

A polymer mix-up was ruled out and a single-point experiment was conducted at Northwestern at the 1 ppb PFOA / 10 ppm polymer conditions to affirm whether the PFAS panel results should be expected at low PFAS and polymer loadings. As shown in Figure 2.8, even at low loadings, the 1 ppb adsorption experiment conducted at Northwestern showed different PFOA adsorption behavior from the two polymers, which did not agree with the PFAS panel results.

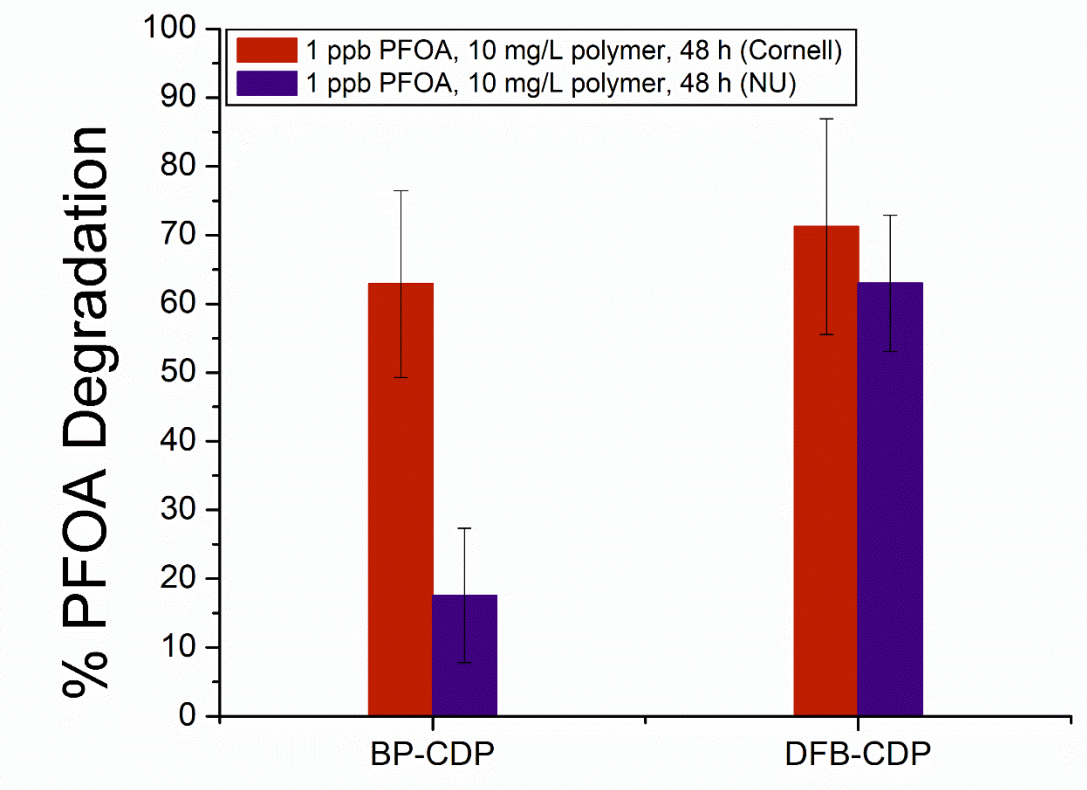

Figure 2.8. Results of 1 ppb PFOA, 10 ppm polymer, 48 hour equilibration adsorption studies conducted at Cornell (red, extracted from PFAS panel) and Northwestern (purple).

In late June, three independent experimental methods for the PFAS panel were validated at Cornell. All three showed that DFB-CDP and BP-CDP exhibited similar performance. One of the methods was chosen and repeated for a fourth time with an additional polymer of known

performance as a control. This test showed that DFB-CDP and BP-CDP still exhibited similar performance (Figure 2.9)—however, in contrast to the April PFAS panel, both polymers exhibited poor PFAS removal (~10%), which could not be explained except for a mistake in the first PFAS panel measurement (very unlikely) or polymer degradation.

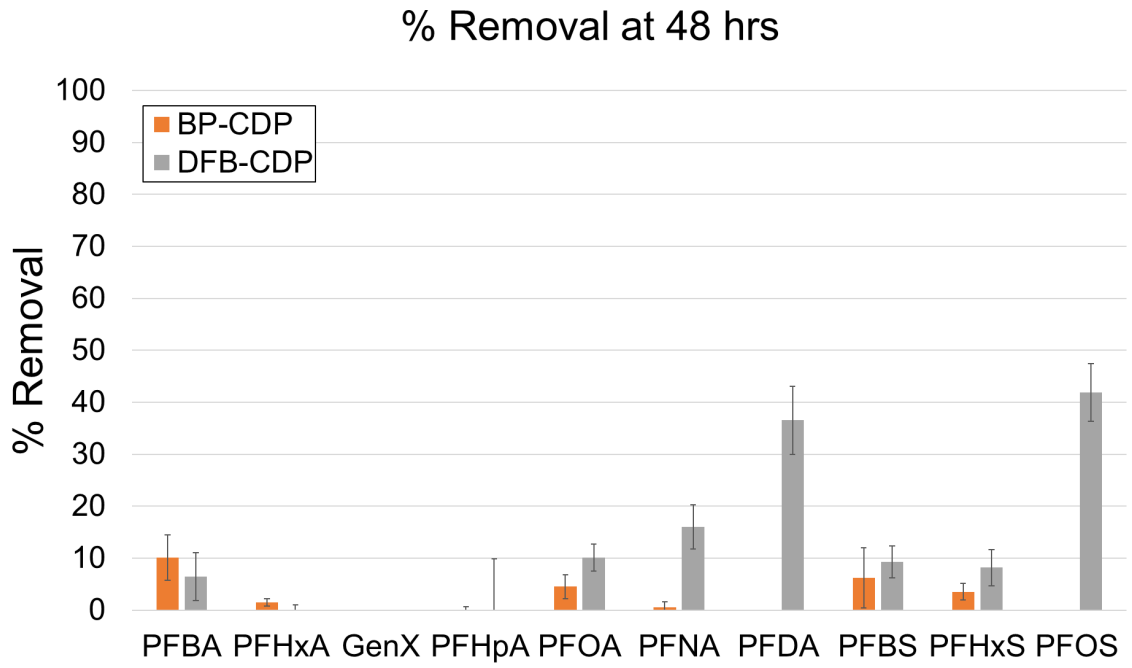

Figure 2.9. PFAS panel of 10 different PFAS, June 2019. 10 ppb of each PFAS in a mixture, 10 ppm polymer. BP-CDP batch 02-014, DFB-CDP batch 02-026-651.

An 83 micropollutant panel was recorded near the same time as the second PFAS panel to determine the overall uptake characteristics of the BP-CDP, especially in relation to the DFB-CDP polymer, but because of the evidence for degradation, no conclusions were ultimately drawn from the panel (Figure 2.10).

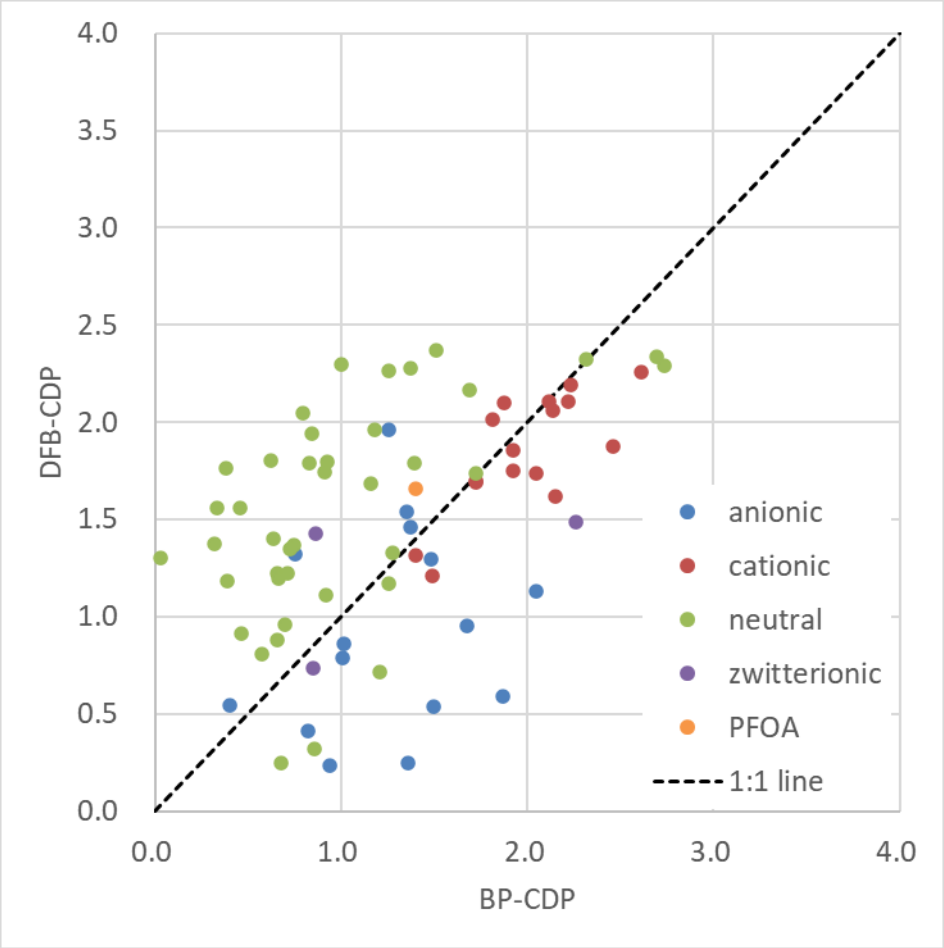

Figure 2.10. 83 micropollutant panel with BP-CDP affinity (KD) on the x-axis and DFB-CDP affinity on the y-axis. 25 mg/L polymer; 2 ug/L each MP; 1 hour contact time.

The polymers were shipped back to Northwestern for re-characterization to determine whether there was detectable degradation. Only infrared spectroscopy of the two polymers were taken because no reference solid-state NMRs were taken of the original polymers; neither was IR of the exact DFB-CDP batch taken because it was assumed the DFB-CDP was similar to all other previously synthesized DFB-CDPs. The IR spectra of BP-CDP had no noticeable differences with the original spectrum (Figure 2.11), but the DFB-CDP spectrum had peaks around 3000 cm^{-1} and 1000 cm^{-1} that looked different than the spectra of several other DFB-CDPs (Figure 2.12).

However, it is unknown whether those differences were present in the original polymer since no IR spectra were taken of the original batch before the polymer was shipped.

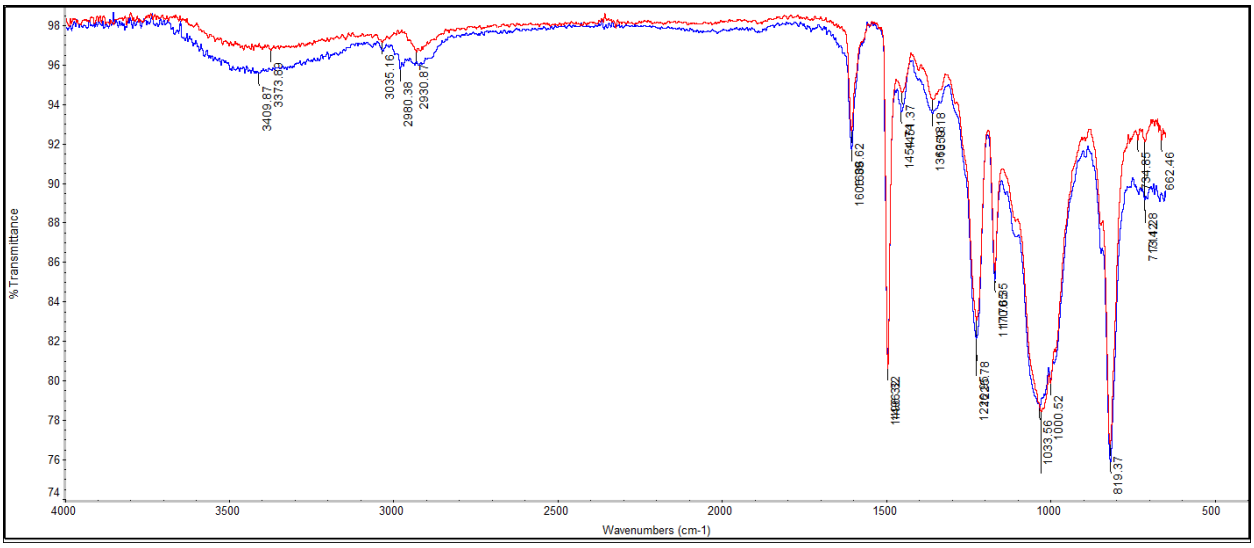

Figure 2.11. Infrared spectrum of original and returned BP-CDP

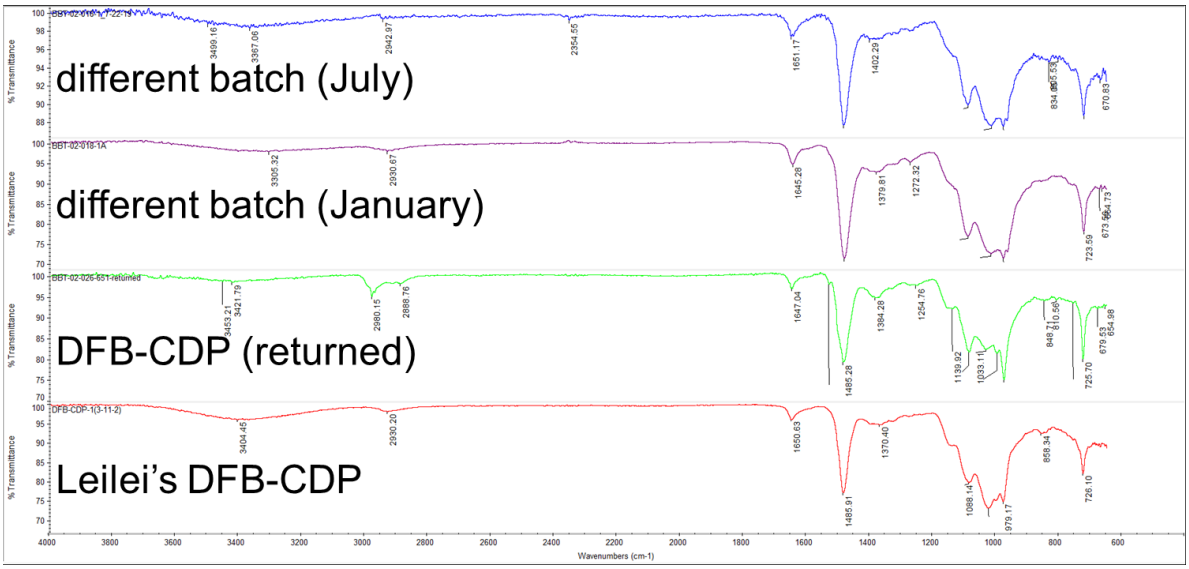

Figure 2.12. Infrared spectrum of sample that was shipped back from Helbling group at Cornell and the sample that stayed at Northwestern.

Equilibrium adsorption of the returned polymers were evaluated at two different adsorption conditions. At 200 ppb PFOA and 400 ppm polymer, both the returned polymers and

newly synthesized polymers performed similarly, with both old and new DFB polymers adsorbing >90% of the PFOA, and both of the BP polymers adsorbing <10% (Figure 2.13).

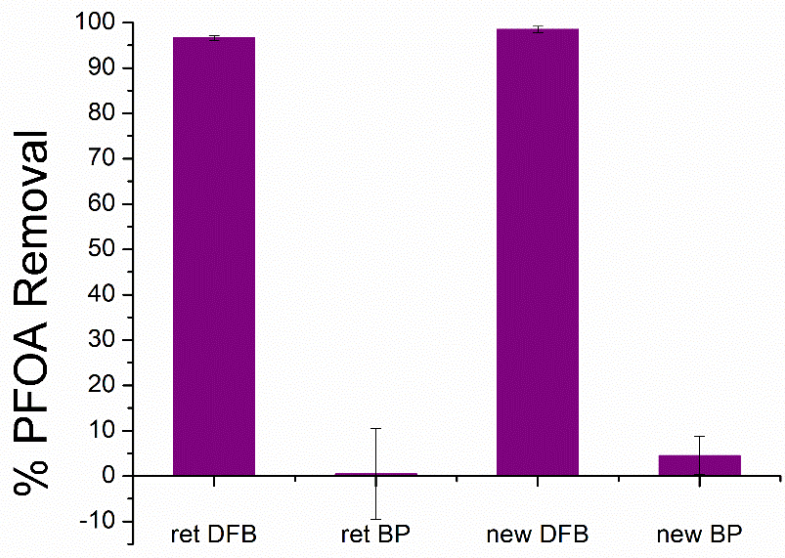

Figure 2.13. PFOA uptake from various polymers at 0.2 mg/L PFOA, 400 mg/L polymer, 23.5 hours. From left to right: BBT-02-026-651 (DFB, returned), BBT-02-014 (BP, returned), BBT-02-088-651 (DFB), BBT-02-084 (BP).

However, at adsorption conditions of 1 ppb PFOA and 10 ppm polymer, the adsorbents showed decreased performance. Adsorption taken in October 2019 (Figure 2.14) showed that both the DFB-CDP that was left at Northwestern and the same batch of DFB-CDP, which had been shipped to Cornell and back, showed the same low PFOA adsorption (~20%) as a batch that had been synthesized in July 2019. (The performance of the July 2019 DFB polymer was not well-characterized when it was freshly synthesized due to the HPLC instrument being down.) Both the BP-CDP that had been sent to Cornell and a BP-CDP batch that had been synthesized in July 2019 showed low removal of PFOA as well. Since the performance of the polymers contradicted both literature and previous performance, we decided to abandon comparisons between the two polymers, surmising that the polymers must have degraded.

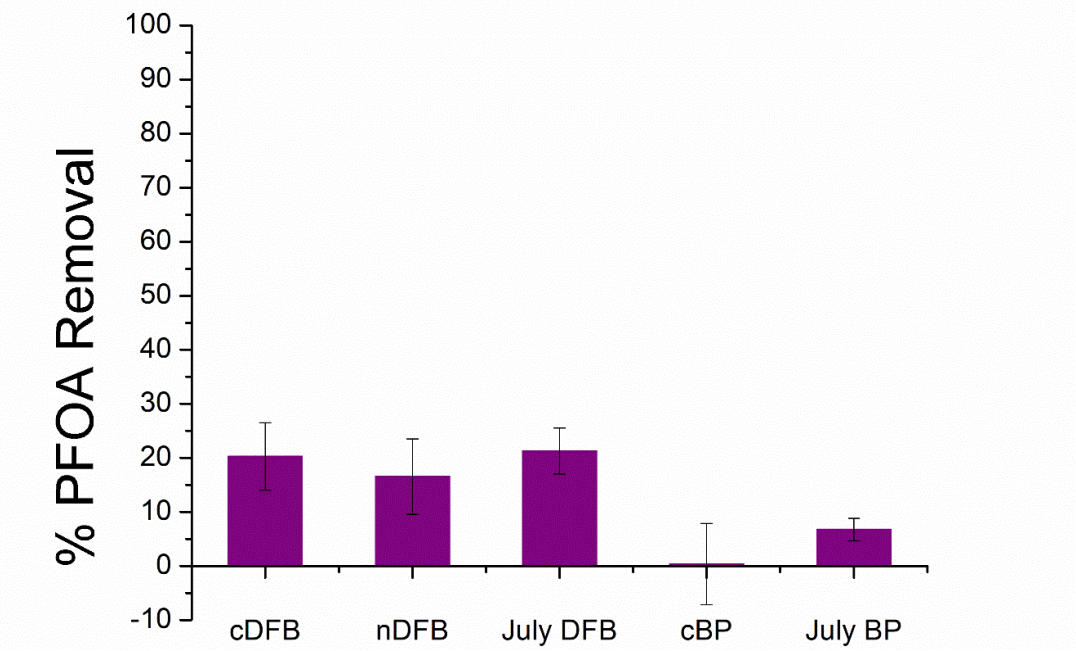

Figure 2.14. PFOA uptake from various polymers at 1 ppb PFOA,10 mg/L polymer, 24 h. old DFB (Helbling, 02-026-651), old DFB (unsent 02-026-651), new DFB (02-088), old BP (Helbling 02-014), new BP (02-084).

Thinking that the synthesis of the polymer was still legitimate, we attempted to write a paper demonstrating the utility of the mesyl-transfer synthesis and using BPA as a model micropollutant to demonstrate adsorption. However, kinetic BPA uptake experiments taken in November 2019 and February 2020 showed vastly different results (Figure 2.15), again confirming that some sort of degradation process was taking place and affecting polymer performance. Based on these observations, we entirely abandoned the mesyl transfer project as determining the cause of the degradation was unlikely to be fruitful on a reasonable timescale.

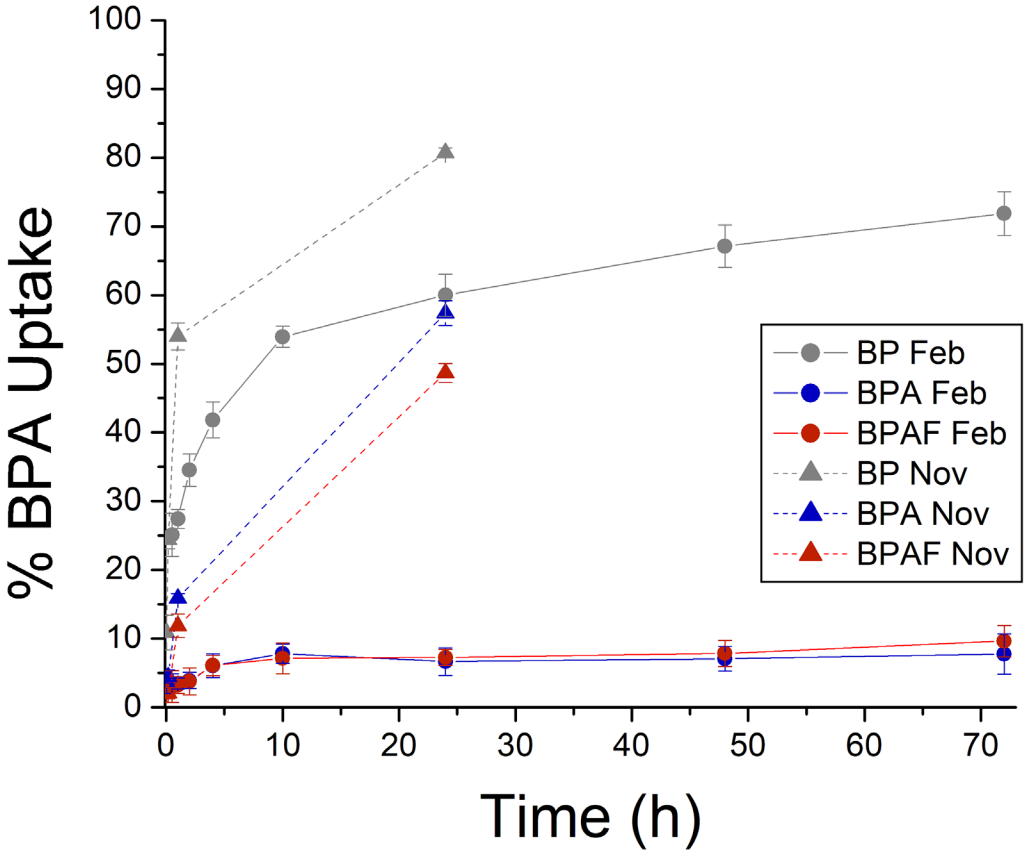

Figure 2.15. BPA uptake of several polymers synthesized through mesyl transfer at conditions of 1 mM BPA, 1 g/L polymer.

2.5. Similar Studies and Their Conclusions

Subsequent studies have been published in recent years that have accomplished various aspects of what the present study was trying to achieve. Below are selected summaries of literature studies and the relevance of their results.

In 2020, Phillips et al. used chemistry similar to the sulfonyl transfer reaction described above to make a linker-less polymer. By using methanesulfonic acid as both solvent and catalyst, they linked cyclodextrins directly to each other and bypassed the need for a separate cross-linking molecule (*139*). The resulting polymer was not porous (< 10 m^2/g) but showed a high capacity for BPA adsorption (Q_{max} = 388 mg/g) and fast kinetics for BPA and methylene blue adsorption. The

polymer was also selective for micropollutants that fit inside the β-CD pore, as it did not uptake rose Bengal, Congo red, or rhodamine B. While the polymer showed selectivity and better performance over α-CD and polymerized glucose controls, the polymer did not perform as well as GAC for adsorbing the dyes tested. As the authors acknowledge, "[I]t is important to note that the kinetics are limited by diffusion, morphology, and particle size, so these measurements may not be completely representative of an intrinsic chemical property of the material." As with kinetics, many other properties of the material would be affected by the porosity or the orientation/steric hindrance of the cups within the linker-less polymer, making it difficult to assess the properties that could be attributed to the linker-less nature of the polymer when comparing it against a cyclodextrin polymer with a crosslinker.

The polymer platform that Phillips et al. offers is interesting for probing the overall effect of crosslinkers and addressing why molecules such as PFOA have a lower binding constant with β-CD in a network than with free, solution-phase β-CD. However, this mesyl-mediated polymerization study did not offer any study of polymer degradation; it is unclear if the authors saw similar performance degradation in this polymer network and if the performance degradation in the biphenyl polymer studied in this chapter derived from the mesyl-transfer polymerization or some other aspect of the polymer.

Synthesis of a multi-phenyl polymer similar to the biphenyl CD polymer was achieved by Tu et al. (*137*) by benzylating β-cyclodextrin to varying amounts, then cross-linking the cyclodextrins using 4,4′-bis(chloromethyl)-1,1′-biphenyl and α,α′-di-chloro-p-xylene via a Friedel-Crafts alkylation to create a "hyper-crosslinked" cyclodextrin polymer. Using a benzylated cyclodextrin synthesized using a 7:1 ratio of benzyl bromide to cyclodextrin, a polymer with a

surface area of 1445 m^2/g was formed. The authors subsequently tested the adsorption of four model pollutants; 3-phenylphenol, 2-naphthol, p-nitrophenol, and 4-cholorophenol; and benchmarked the hyper-crosslinked polymer against GAC and a non-porous epichlorohydrin-linked CD polymer. Tu et al. largely found that the adsorption mechanism was hydrophobic in nature, as more-hydrophobic adsorbates adsorbed better than more hydrophilic adsorbates, adsorption at pH above the pKa of the adsorbates resulted in decreased adsorption, and adsorption in ethanol:water mixtures decreased with increasing ethanol composition. They proposed that the hydrophobic crosslinkers, combined with the hydrogen-bonding alcohols on the cyclodextrin, provided an amphiphilic environment for adsorption. However, addition of salt did not change the adsorption of any of the adsorbates, leading to questions about the nature of the adsorption mechanism.

The Friedel-Crafts polymerization method Tu et al. used should be a sufficient alternative to the mesyl transfer method described in this study. If the polymer were synthesized using only α,α′-di-chloro-p-xylene crosslinkers at a similar substitution density to the DFB polymer, the resulting network should be similar enough to draw broad conclusions about the fluorophilic nature of the PFOA adsorption mechanism in multi-phenyl based polymers, despite the fact that the crosslinkers in the Friedel-Crafts polymer would not have ether linkages and would effectively be three phenyl units long instead of two, as in the decafluorobiphenyl polymer.

Most recently, Choudhary et al. performed atomistic molecular dynamics simulations to computationally investigate the factors contributing to ammonium perfluorooctanoate adsorption onto cyclodextrin-based polymers (*121*). Their simulations of PFOA-NH_4 adsorption onto DFB-CDP showed that most PFOA molecules were not adsorbed in the cavities of the CDs, but instead

were adsorbed onto the cavities formed by the DFB linkers. The authors additionally calculated a potential of mean-force of 2.2 kcal/mol as the free energy barrier to PFOA entering the CD cavity, concluding that the "primary adsorption mechanism does not involve PFAS-CD inclusion complex formation." Evidence for a fluorophilic effect in DBF-CDP's adsorption mechanism was bolstered by changing the PFOA adsorbate for an octanoic acid adsorbate, which decreased the efficiency of adsorption from 78% to 23%, and by exchanging the DFB linkers for BP linkers, which reduced the number of PFOA molecules adsorbed onto the surface to 50%. Further, the authors noted that "the PFOA surfactants that are adsorbed on the network have their fluorinated tails oriented primarily perpendicular to the network, indicating no preferential hydrophobic interaction with BP linkers." The authors also proposed that electrostatic charge was fundamental in PFOA adsorption; though for most of the simulations NH_4^+ was allowed to electrostatically adsorb onto the alcohols of the cyclodextrin, in a simulation where the dipole of the CD alcohols were set to zero and thus the ammonium ions did not adsorb, the PFOA removal efficiency dropped to 60%. The improved adsorption with the cationic proxy was used to corroborate experimental findings that charges within the polymer network modulate ionic PFAS adsorption (*51*, *76*, *134*).

Choudhary et al.'s work gives quantitative insight into the factors affecting adsorption in the polymer and does suggest that there is a fluorophilic contribution to the adsorption process, as demonstrated by changing the adsorbate to octanoic acid and changing the linker to biphenyl. However, the conclusion that none of the adsorption occurs through encapsulation in the β-CD cavity seems erroneous, given that β-CD and PFOA have an experimentally determined binding constant of $5.00 \pm 0.10 \times 10^5$ (*62*) and the calculated barrier to complexation was only 2.2 kcal/mol. No such barrier calculations were conducted for adsorption to the linker sites for comparison and

it stands to reason that there indeed is a balance between the three adsorption processes (inclusion, fluorophilic, electrostatic).

2.6. Conclusions

Aryl-ether-cross-linked β-cyclodextrin polymers were formed via a sulfonyl transfer reaction. The new polymerization method was used to synthesize polymers from three different linkers, all of which exhibited micropollutant binding activity that shows the promise of materials made by the sulfonyl transfer polymerization method. Unlike past polymerizations, which were limited to electron-poor linkers that could undergo nucleophilic aromatic substitution, this sulfonyl transfer polymerization allowed electron-rich aryl linkers to be incorporated into ether-linked β-cyclodextrin polymers. This simple reaction vastly widens the available library of linkers, allowing β-cyclodextrin polymer properties to be changed and studied systematically. For example, this reaction was used to synthesize a biphenyl-crosslinked CDP, which was used to probe fluorophilic interactions in PFOA uptake. However, irregular and inconsistent results led both the fluorophilic study and subsequently the synthesis method to be abandoned, given that all of the polymers appeared to be degrading over time and determining the source of the degradation would likely be time-consuming and unfruitful.

2.7. Acknowledgements

We thank Charlotte Stern at Northwestern University's IMSERC facility for assistance with elemental analysis and Dr. Casey Ching, Dr. Yuhan Ling, and Prof. Damian Helbling at Cornell University for trace micropollutant uptake analysis.

Funding: BBT is supported by the National Science Foundation Graduate Research Fellowship Program (DGE-1842165). This work made use of the IMSERC at Northwestern University, which has received support from the NIH (1S10OD012016-01 / 1S10RR019071-01A1), Soft and Hybrid

Nanotechnology Experimental (SHyNE) Resource (NSF ECCS-1542205), the State of Illinois, and the International Institute for Nanotechnology (IIN).

2.8. Chapter 2 Appendix

Materials:

All chemicals and reagents purchased from Sigma-Aldrich and used as received, with the exception of dimethylsulfoxide (DMSO), which was dried over 4Å activated molecular sieves from Fisher.

For uptake experiments, aliquots filtered through cellulose acetate filters (Macherey-Nagel CHROMAFIL Xtra CA-20/13, 0.2 um pore size, 13 mm diameter)

Instrumentation:

NMR: Liquid-state NMRs taken on a 500 MHz Bruker Avance III equipped with a CryoProbe 5mm DCH w/ Z-Gradient, or a 500 MHz Bruker Avance III HD system equipped with a 5 mm TXO Prodigy probe. Solid-state ^{13}C CP-MAS NMR taken on a 400 MHz Bruker Avance III HD with a Bruker 4 mm HX probe, spinning at 10 kHz.

MALDI: MALDI spectra acquired on a Bruker AutoFlex-III MALDI-TOF using a 2,5-dihydroxybenzoic acid matrix dissolved in methanol.

HRMS: High-res mass spectrometry taken on Agilent 6220 TOF coupled to a 1200 Agilent HPLC binary pump, wellplate sampler, thermostatted column compartment, and UV detector. The TOF HRAM mass accuracy was 2 ppm using IRM and resolution was 16,000 at an m/z of 1,522.

Micropollutant Uptake Quantification: HPLC-MS performed on Bruker AmaZon-X equipped with an Agilent ZORBAX Eclipse Plus C18 Narrow Bore RR 2.1 x 50 mm 3.5-Micron column (part number 959743-902) running an isocratic method of 50% of 0.1% formic acid in acetonitrile and 50% of 0.1% formic acid in H_2O at a flow rate of 0.4 mL/min for 3 minutes. Elution monitored by area of 280 nm UV trace.

General Procedure for Batch Micropollutant Uptake: 6 mg polymer added to 20 mL glass scintillation vial. 6 mL 0.1 mM BPA solution added to vial along with PTFE-coated egg-shape magnetic stirbar. Vial sonicated for ~20 seconds, then sample stirred at 500 RPM. 0.9 mL aliquots taken with micropipette, then syringe filtered through cellulose acetate filters into glass GC vials. Area of 280 nm UV trace from HPLC integrated to calculate remaining BPA concentration.

Micropollutant percent removal was calculated as per equation S1 in Xiao et al, 2017 (*73*).

General Procedure for PFAS Panel Micropollutant Uptake Experiments: The experiments were conducted at 1000 ng L^{-1} of PFASs and 10 mg L^{-1} of CDP in 15 mL Falcon tubes on a rotary tumbler at 23 °C. Each experiment was conducted in 10 mL of nanopure water, and triplicate tubes were sacrificed at 30 minutes, 9 hours, and 48 hours. The contents of each sacrificed tube was filtered with a 0.45 μm cellulose acetate filter (Restek), spiked with a mixture of 7 isotope labelled internal standards, and measured by means of LC-MS. Control experiments to account for PFAS losses were performed at the same condition except for the addition of adsorbents. All experiments were performed in triplicate.

Affinity Experiments: Experiments to estimate affinity (KD) of each MP and PFAS were performed in 125 mL glass (MPs) or polypropylene (PFASs) Erlenmeyer flasks with magnetic stirbars on a multi-position stirrer (VWR) with a stirring rate of 400 revolutions per minute (rpm) at 23 °C. Experiments were performed at adsorbent doses of 25 mg L^{-1}. The MPs and PFASs were spiked to generate an initial concentration of each adsorbate of 2 μg L^{-1}. Samples were collected in 8 mL volumes at 1 hour and filtered through a 0.22 μm PVDF (MPs) or cellulose acetate (PFAS) syringe filter (Restek). Control experiments to account for other MP losses were performed under

the same conditions with no addition of adsorbent. All experiments (including controls) were performed with triplicates. See Klemes et al. and Ling et al. for more details (*76*, *80*).

Surface Area: Nitrogen adsorption isotherms taken on a Micromeritics ASAP 2420. Each sample (20-30 mg) degassed at 100 °C until the off-gas pressure was 0.2 μg Hg/min or less, then backfilled with nitrogen before analysis. The nitrogen isotherms were then measured by incremental exposure to nitrogen up to 1 atm while the sample was cooled in a liquid nitrogen bath.

FT-IR: Infrared spectra taken using a Nicolet iS10 FT-IR spectrometer with a zinc selenide ATR crystal.

Elemental analysis: CHNS combustion elemental analysis performed at Northwestern IMSERC facility on an Elementar Vario EL cube with a combustion tube at 1100 °C, reduction tube at 850 °C, and a 90 second O_2 dosing at 30 seconds into analysis.

For fluorine-containing samples, CHN, F, and S analysis was performed at Robertson Microlit Laboratories. CHN analysis determined on a Perkin-Elmer Model 2400 CHN Analyzer using high-purity helium as a carrier gas, 99.9% oxygen as a combustion gas at approximately 950 °C. Fluorine elemental analysis determined by ion-specific electrode, F-ISE (Orion). Sulfur content determined by titration.

2.8.1. Synthetic Procedures and Materials Characterization

General Procedure for Linker Mesylation:

2.5 g aryl alcohol added to flame-dried roundbottom flask + stirbar. Dichloromethane (DCM) added (0.09 M in aryl alcohol), suspension sonicated (note: not all of the aryl alcohol dissolves). Triethylamine (1.1 eq per alcohol) added, solution became clear. Solution cooled in ice, then vent needle added and mesyl chloride (1 eq per alcohol) added dropwise. Solution may become cloudy or become slightly colored upon addition of mesyl chloride. Vent needle removed, ice bath let melt, reaction stirred at room temperature overnight. After overnight stir, reaction vented, then extracted 3x with saturated $NaHCO_3$, organic fractions combined, dried with $MgSO_4$, rotovapped to produce white powder.

Alternative workup for substrates that are less soluble in DCM (BP-OMs): After overnight stir, solid filtered off, DCM rotovapped down to give white powder. All powders combined, washed with 200 mL $NaHCO_3$ saturated solution, then 150 mL water. White solid dried on high vac overnight, column in DCM if necessary.

General Procedure for Polymerization:

Beta-cyclodextrin (227 mg, 1 eq), mesylated linker (6 eq), Cs_2CO_3 (1.56 g, 24 eq) added to flame-dried roundbottom + stirbar. Solids stirred at 500 RPM, vessel purge-degassed 3x with nitrogen, then 0.5 mL sieve-dried DMSO (0.4 M) added to make a clumpy white paste. Reaction heated to 80°C for 48 h under positive N2 pressure. After 48 h, reaction is a hard brown solid. Solid broken up with spatula and removed from flask with help from DI water and 1 M HCl, ground with mortar and pestle, and neutralized with 1 M HCl (6-7 mL) until it stopped producing bubbles. Solid transferred to 50 mL centrifuge, filled with 45 – 50 mL H_2O, centrifuged.

Supernatant decanted, 45 mL water added, stirred for at least 10 minutes, centrifuged, water decanted. Repeated twice more with tetrahydrofuran (THF) and twice with DCM, or until supernatant was clear for each solvent. Solid transferred to packet made of filter paper and enclosed in a teabag, then Soxhlet extracted for 2 days in water, soaked overnight in methanol, and dried with supercritical CO_2. BP-CDP, BPA-CDP, and BPAF-CDP were all non-porous with surface areas at or below 30 m^2/g.

"Adjusted yield" calculated based on mol of linker, but using molar mass of [linker minus mesyl groups] because the final network will in theory not incorporate the mesyl groups, thus making the theoretical yield a much lower mass than the raw mass-in-mass-out yield.

Procedure for Model Reaction between 4 and β-CD:

Mesylated phenyl **4** (345.3 mg, 2 mmol), beta-cyclodextrin (229.6 mg, 0.2 mmol), and Cs_2CO_3 (1.3033 g, 4 mmol) were added to a flame-dried round-bottom flask equipped with a stirbar. The contents were purge-degassed three times, then molecular-sieve-dried DMSO was added (0.5 mL). Heated to 70 °C for 5 days (not necessary; reaction should be complete after overnight heating). MALDI taken from reaction crude diluted in dimethylformamide.

BP-OMs linker (1). The general procedure for linker mesylation was run using 4,4'-dihydroxybiphenyl on a 1.5 g scale to yield 3.85 g (91.5%) of a white powder.

^{1}H NMR ($CDCl_3$, 500 MHz) δ 3.19 (s, 6H), 7.39 - 7.36 (m, 4H), 7.60 - 7.57 (m, 4H)

^{13}C NMR ($CDCl_3$, 500 MHz) δ 37.70, 122.67, 128.91, 139.32, 149.00

IR (ATR) 3027 (aromatic C-H), 2944 (C-H), 1599 (aromatic C=C), 1489 (aromatic C=C), 1369 (S=O), 1203 (C-O)

HRMS: calculated m/z: 342.02, found m/z: 365.0137 [M+Na]

BPA-OMs linker (2) The general procedure for linker mesylation was run using bisphenol A (2,2-bis(4-hydroxyphenyl)propane) on a 1.5 g scale to yield 2.06 g (74.6%) of a white powder.

^{1}H NMR (DMSO-d_6, 500 MHz) δ 1.66 (s, 6H), 2.36 (s, 6H), 7.28 - 7.25 (m, 4H), 7.35 - 7.32 (m, 4H) (aromatic product peaks overlap with chloroform peak, so deuterated DMSO was chosen instead)

^{13}C NMR ($CDCl_3$, 500 MHz) δ 30.95, 37.54, 42.83, 121.76, 128.52, 147.35, 149.45

IR (ATR) 3030 (aromatic C-H), 2972 (C-H), 2934 (C-H), 2876 (C-H), 1502 (aromatic C=C), 1360 (S=O) **HRMS**: calculated m/z: 384.07, found m/z: 407.0597 [M+Na]

BPAF-OMs linker (3) The general procedure for linker mesylation was run using bisphenol AF (4,4'-(hexafluoroisopropylidene)diphenol) on a 1.5 g scale to yield 3.491 g (93.4%) of a white powder.

^{1}H NMR ($CDCl_3$, 500 MHz) δ 3.21 (s, 6H), 7.34 - 7.30 (m, 4H), 7.44 (d, 4H)

^{13}C NMR ($CDCl_3$, 500 MHz) δ 38.06, 64.34 - 63.93 (t), 122.12, 122.80 (small), 125.08 (small), 132.15, 149.60

^{19}F NMR ($CDCl_3$, 500 MHz) δ 67.00 (referenced to hexaflurobenzene)

IR (ATR) 3047 (aromatic C-H), 2955 (C-H), 1601 (aromatic C=C), 1504 (aromatic C=C), 1368 (S=O)

HRMS: calculated m/z: 492.01, found m/z: 515.0036 [M+Na]

PhOMs model compound (4) The general procedure for linker mesylation was run using phenol on a 2.33 g scale to yield 4.2868 g (quantitative yield) of light yellow-orange crystals. Later sublimed under high vac at 50 °C to give clear crystals.

^{1}H NMR (DMSO-d6, 500 MHz) δ 3.14 (s, 3H), 7.31 - 7.28 (m, 2H), 7.35 - 7.32 (tt, 1H), 7.45 - 7.41 (m, 2H)

^{13}C NMR ($CDCl_3$, 500 MHz) δ 37.48, 122.14, 127.56, 130.18, 149.42

IR (ATR) 3039 (aromatic C-H), 2942 (C-H), 1587 (aromatic C=C), 1352 (S=O)

HRMS: calculated m/z: 172.02, found m/z: 173.0266 [M+H]

BP-CDP polymer. The general procedure for polymerization was run using compound **1** to yield 292.7 mg of a light brown powder (70.9% adjusted yield when accounting for loss of sulfonyl groups).

CHNS elemental analysis (found): 61.06% C, 5.52% H, 1.61% S.

See **Table S2.1** below for information on BP-CDP polymers synthesized at different temperatures.

Table S2.1. Adjusted yield and elemental analysis of BP-CDPs synthesized at different temperatures. Averages of triplicate measurements, except for the 80 °C trial, which is an average of duplicates because of an outlier measurement.

	adjusted % yield	avg %C	avg %H	avg %S	BP/BCD	OMs/BCD
80 °C	71%	61.06	5.52	1.61	3.84 +/- 0.48	0.88 +/- 0.08
100 °C	74%	61.72	5.87	1.12	3.11 +/- 0.49	0.54 +/- 0.08
120 °C	81%	60.75	5.64	0.71	3.35 +/- 0.43	0.36 +/- 0.03
140 °C	71%	60.31	5.56	0.81	3.43 +/- 0.15	0.42 +/- 0.02

BPA-CDP polymer. The general procedure for polymerization was run using compound **2** to yield 284.6 mg of a light brown powder (61.4% adjusted yield when accounting for loss of sulfonyl groups).

CHNS elemental analysis (found): 63.55% C, 6.53% H, 3.23% S. See Table S 2.2 for analysis.

BPAF-CDP polymer. The general procedure for polymerization was run using compound **3** to yield 325.3 mg of a light brown powder (54.8% adjusted yield when accounting for loss of sulfonyl groups).

CHNSF elemental analysis (found): 52.13% C, 3.59% H, 3.70% S, 17.48% F See Table S 2.2 for analysis.

Table S2.2. Elemental analysis of **BP-CDP**, **BPA-CDP**, and **BPAF-CDP**. Averages of triplicate measurements, except for the 80 °C trial, which is an average of duplicates because of an outlier measurement.

	avg %F	avg %C	avg %H	avg %S	Linker/BCD	OMs/BCD
BP-CDP	-	61.06	5.52	1.61	3.84 +/- 0.48	0.88 +/- 0.08
BPA-CDP	-	63.55	6.53	3.23	3.43 +/- 0.09	1.81 +/- 0.06
BPAF-CDP	17.48	52.13	3.59	3.70	3.35 +/- 0.03	2.5 +/- 0.05

2.8.2. Elemental Analysis Data Interpretation

Deconvoluting a carbon-and-hydrogen-containing linker from a carbon-hydrogen-oxygen-containing cyclodextrin using only carbon/hydrogen/nitrogen/sulfur data is challenging. Herein we describe the method used to calculate both the mesyl-to-cyclodextrin ratios and the linker-to-cyclodextrin ratios.

First, 1 g of each sample was assumed, so that the percentages of each element were converted into grams, eg 60% C = 0.060 g C. These masses were then converted to moles of each element.

Next, one mol of carbon and three moles of hydrogen were subtracted for each mol of sulfur, assuming the presence of $-O_3S-CH_3$ for each sulfur. The moles of carbon and hydrogen, with the carbon and hydrogen corresponding to the remaining mesyl groups subtracted out, are denoted *adjC* and *adjH*. (Note that this method does not at any point rely on the number of oxygens; therefore, the oxygens on the mesyl groups do not matter, nor does it matter whether the oxygen connecting the mesyl to the linker or cyclodextrin is counted toward the mesyl or cyclodextrin.)

Because each carbon and each hydrogen now comes from either the cyclodextrin or the biphenyl linker, we can now write two equations with two unknowns and algebraically solve for the moles of β-cyclodextrin and moles of linker in each sample. Using 42 carbons and 70 hydrogens for each β-cyclodextrin, 12 carbons and 8 hydrogens for every “biphenyl” in the network, and assuming di-substitution and therefore 2 hydrogens lost for every biphenyl incorporated into the network:

a = *mol β-CD*

b = *mol BP*

$$C = 42a + 12b = adjC$$

$$H = 70a + 8b - 2b = adjH$$

$$b = \frac{adjH - 70a}{6}$$

$$a = \frac{adjC - \frac{12}{6}adjH}{42 - \frac{12 \times 70}{6}}$$

Because *adjH* and *adjC* are measured quantities, we can very easily solve for the moles of β-CD and moles of biphenyl. Using the moles of sulfur as the moles of residual mesyl groups, we can divide by the moles of β-CD to find out linker-to-cyclodextrin and mesyl-to-cyclodextrin ratios.

Because the BPAF polymer has fluorines that are much more reliably detected than hydrogen, the following equations were used:

$$a = mol\ BCD$$

$$b = mol\ BPAF$$

$$C = 42a + 15b = adjC$$

$$H = 70a + 8b - 2b = adjH$$

$$F = 6b$$

$$\frac{F}{6} = b$$

$$a = \frac{adjC - 15(\frac{F}{6})}{42}$$

Note that entering the same data for BPAF-CDP into the analogous equation as worked out for the BP-CDP polymer will give a different result, though both equations are perfectly valid. Because the F number precisely defines the moles of linker present, it limits the possibilities for the CDP number to the solution for *a* when *b* = F/6 is plugged into either the H equation or the C equation. Because the H number is more subject to variability due to any adsorbed water in the polymer, the C equation was chosen to determine the linker/CD ratio for the BPAF polymer. By contrast, the equation that uses only the C and H numbers relies on both the carbon number and the hydrogen number to produce both the moles of linker and the moles of cyclodextrin, introducing more variability.

Mathematically, the BPAF provides 3 equations with 2 variables, one of which is a flat line when graphed (b = F/6). This line defines the moles of linker present; the intersection of this line with the line created by the graphed C equation or the line created by the H equation will give the same number of moles of linker (b) but slightly different numbers of moles of cyclodextrin (a), depending on the variability of the measurements. However, the intersection of the C and H lines will have both a different x-coordinate and a different y-coordinate than their intersection with the F line (unless the experimental numbers are very accurately determined), giving a different number of linker and cyclodextrin moles than the F & C intersection or the F & H intersection. In the case of the BP-CDP and BPA-CDP polymers, the C – H solution is the only solution we have, but with the introduction of the heteroatom in BPAF-CDP, we can determine the cross-linking density with a higher amount of certainty.

2.8.3. MALDI, HNMR, CNMR, SSNMR, FT-IR Spectra

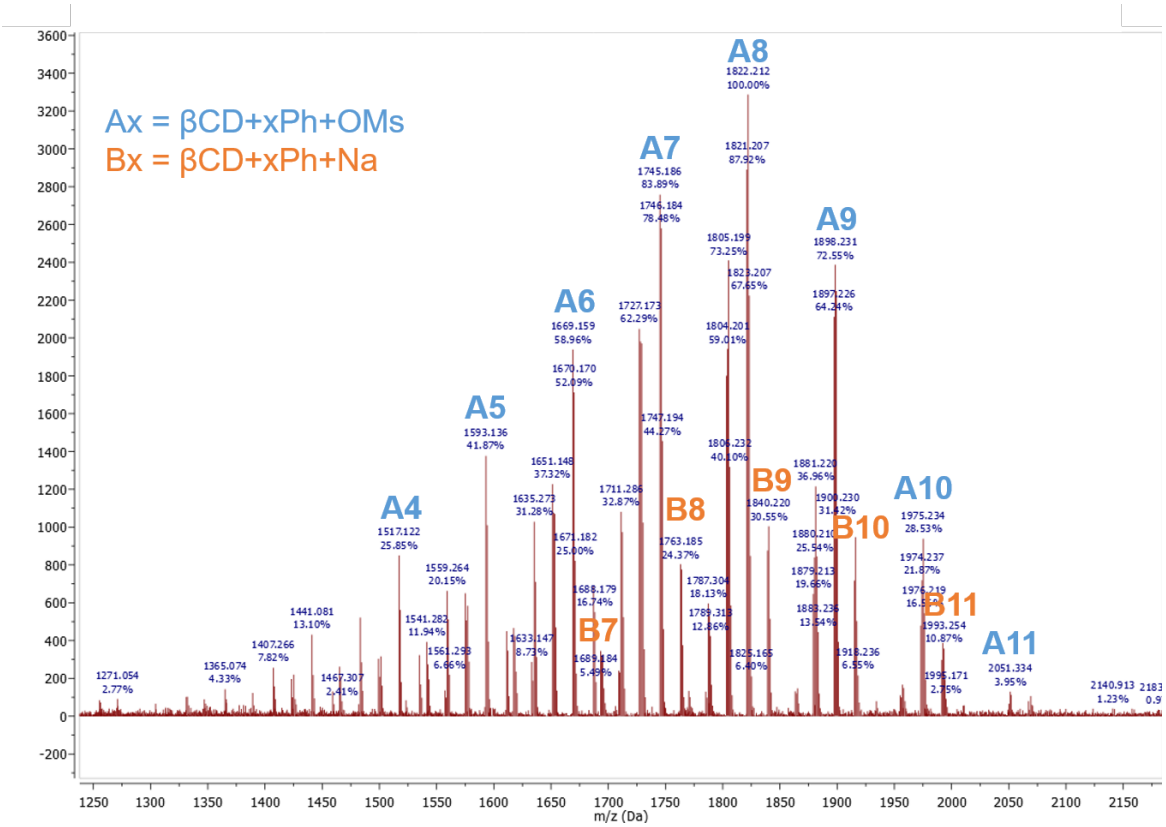

Figure S2.1. MALDI mass spectrum of test reaction between Ph-OMs (4) and β-cyclodextrin. Peaks labeled Ax indicate mass of cyclodextrin plus x phenyl groups plus a mesyl group. Peaks labeled Bx indicate mass of cyclodextrin plus x phenyl groups plus a sodium ion. Other peaks were unidentifiable.

2.8.4. ^{1}H NMR Spectra

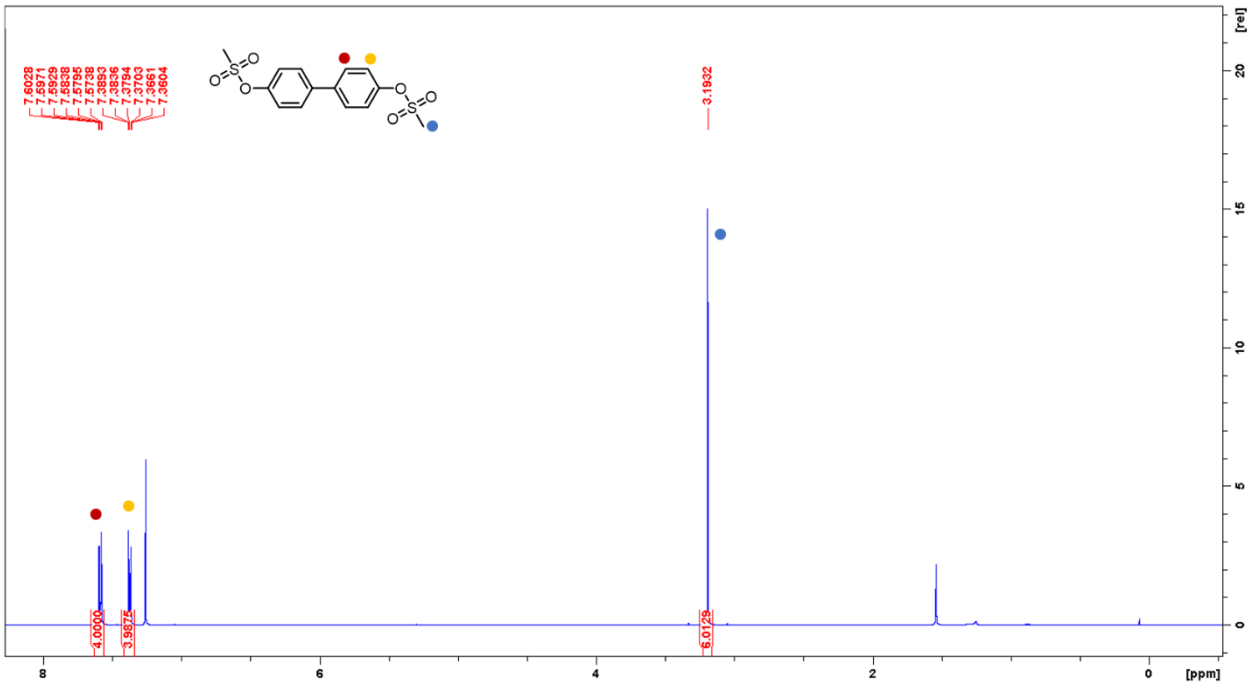

Figure S2.2. ^{1}H NMR spectrum of compound **1**.

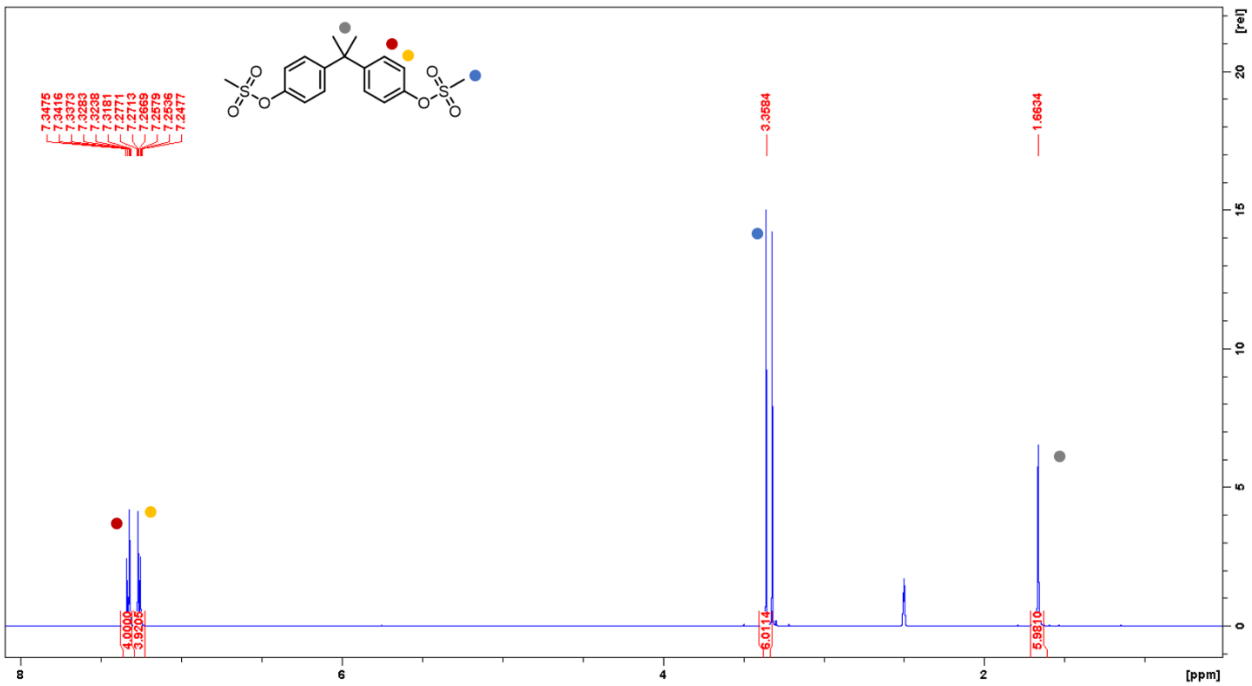

Figure S2.3. ^{1}H NMR spectrum of compound **2**.

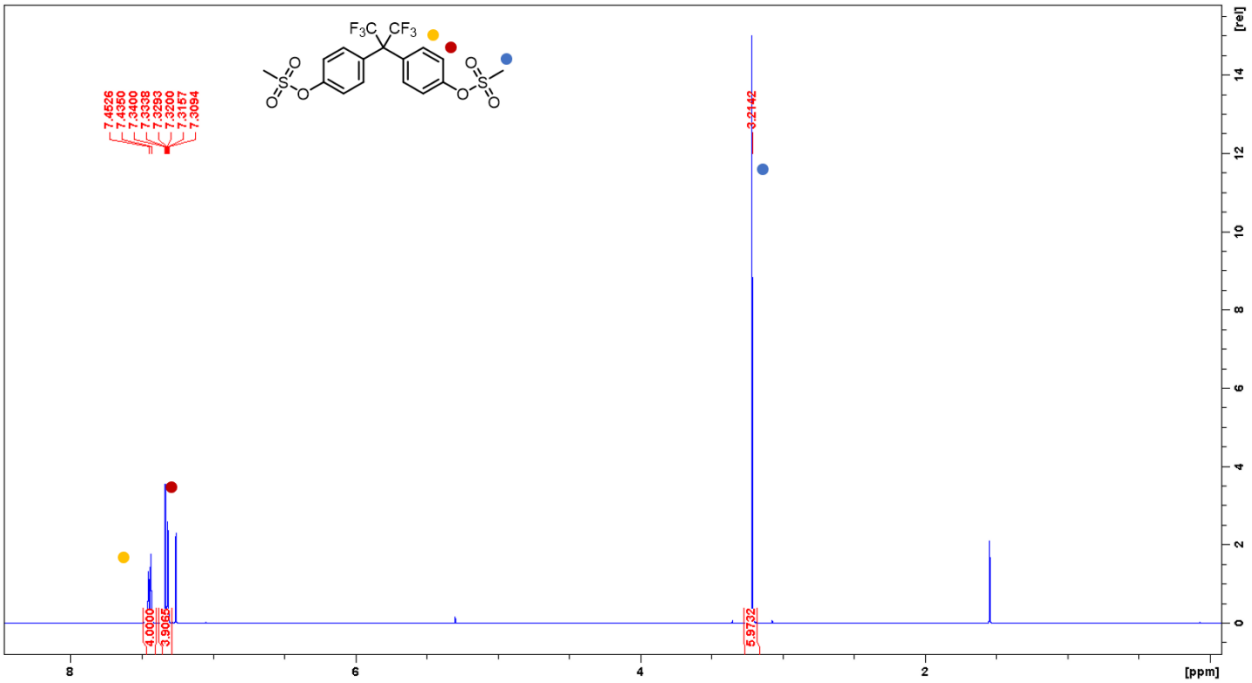

Figure S2.4. [1]H NMR spectrum of compound **3**.

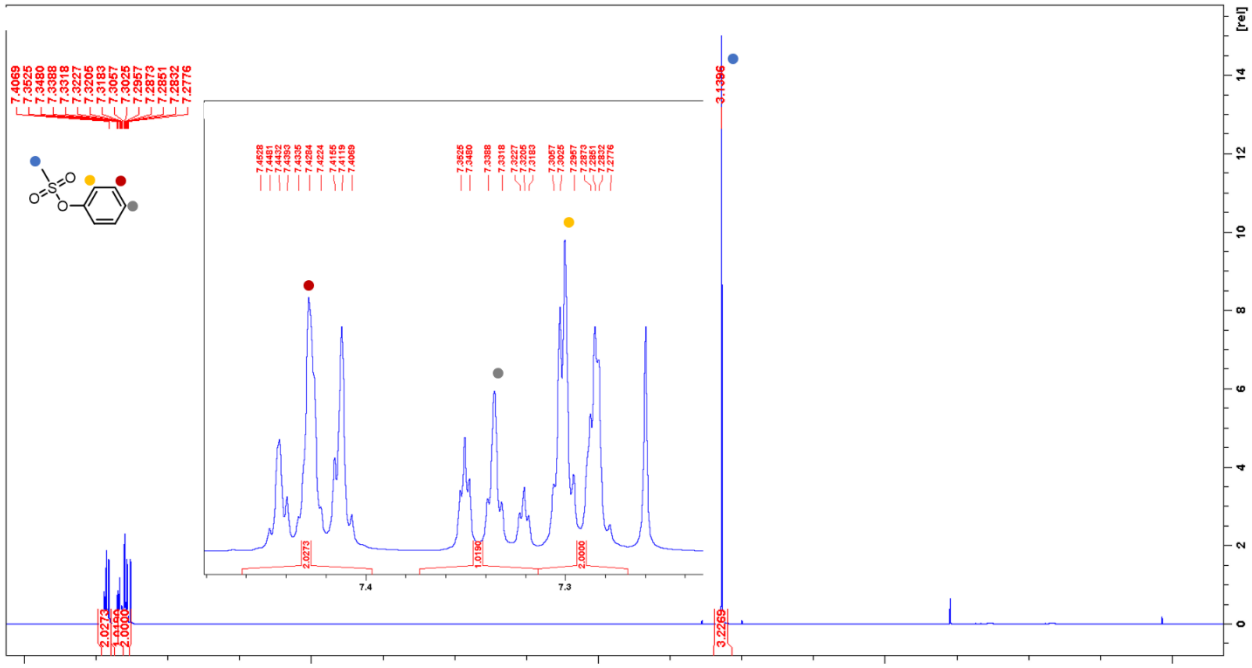

Figure S2.5. [1]H NMR spectrum of compound 4, aromatic peaks inset.

2.8.5. ^{13}C NMR Spectra

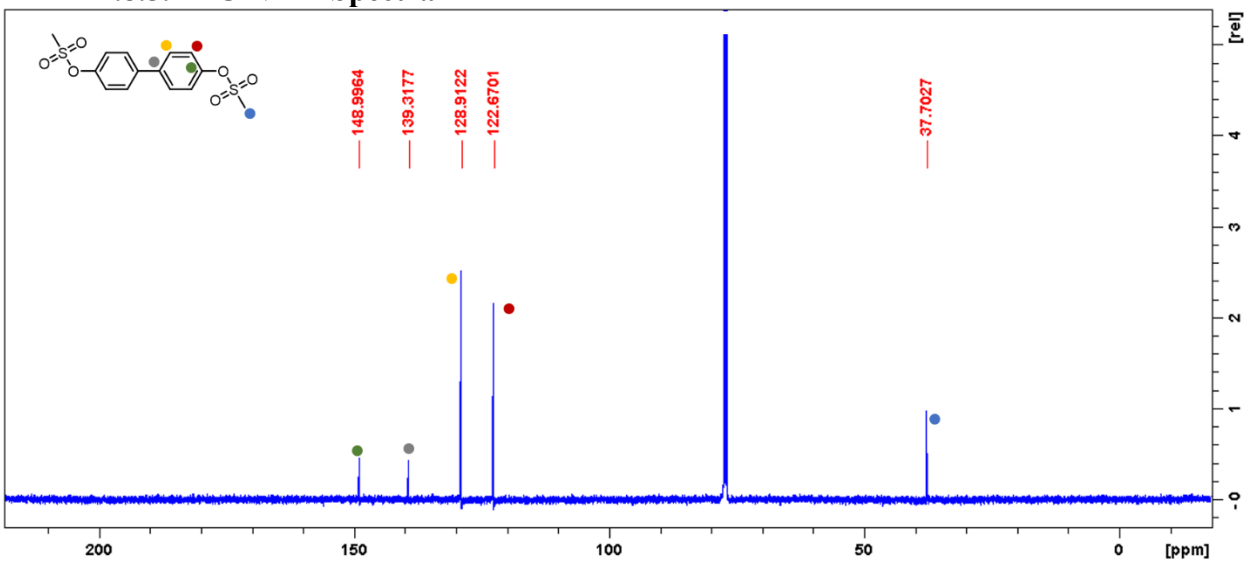

Figure S2.6. ^{13}C NMR spectrum of compound **1**.

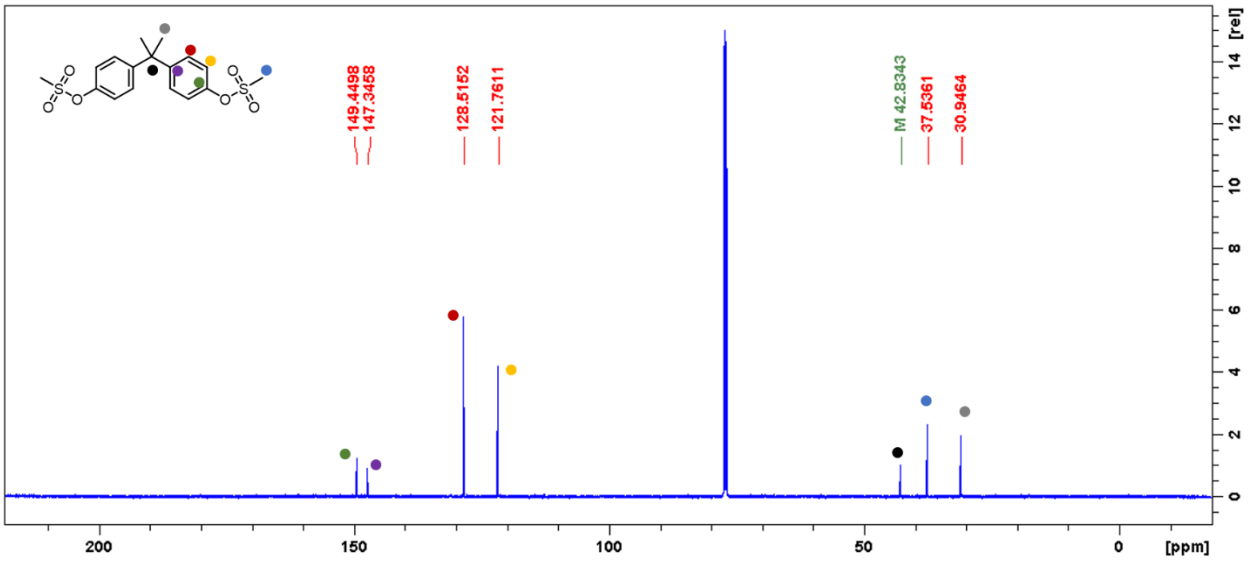

Figure S2.7. ^{13}C NMR spectrum of compound **2**.

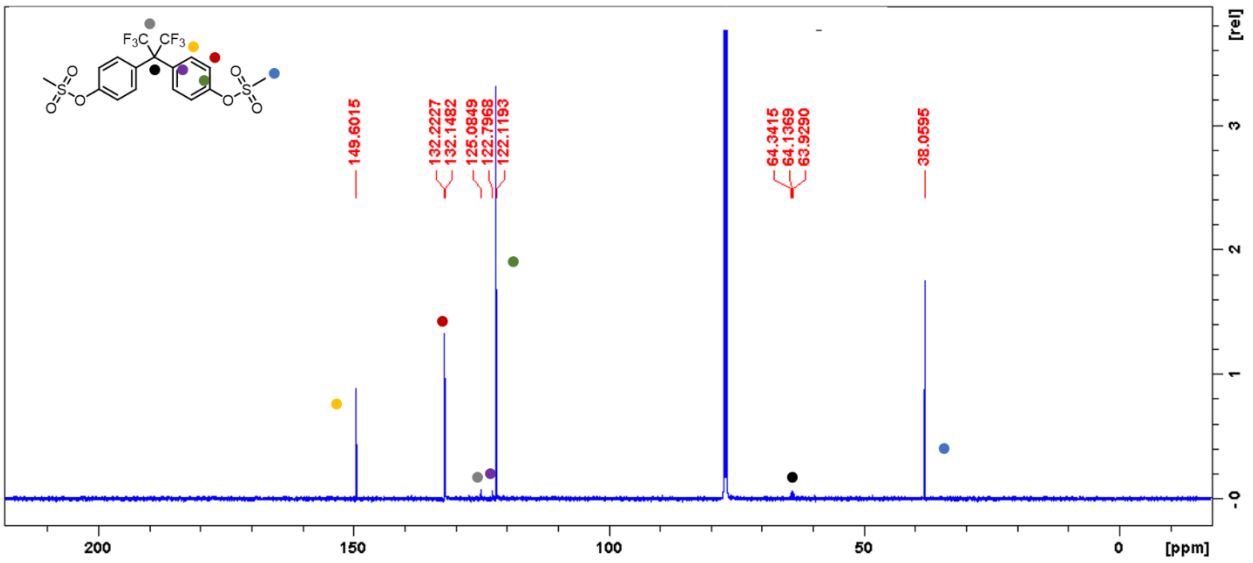

Figure S2.8. ^{13}C NMR spectrum of compound **3**.

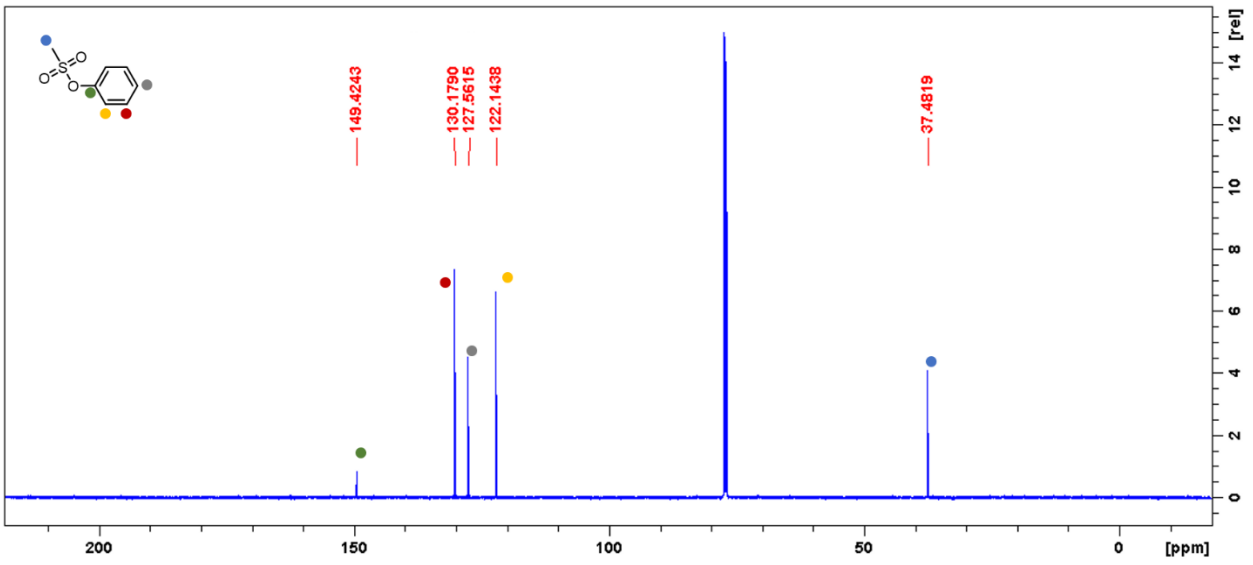

Figure S2.9. ^{13}C NMR spectrum of compound **4**.

2.8.6. ^{19}F NMR Spectrum

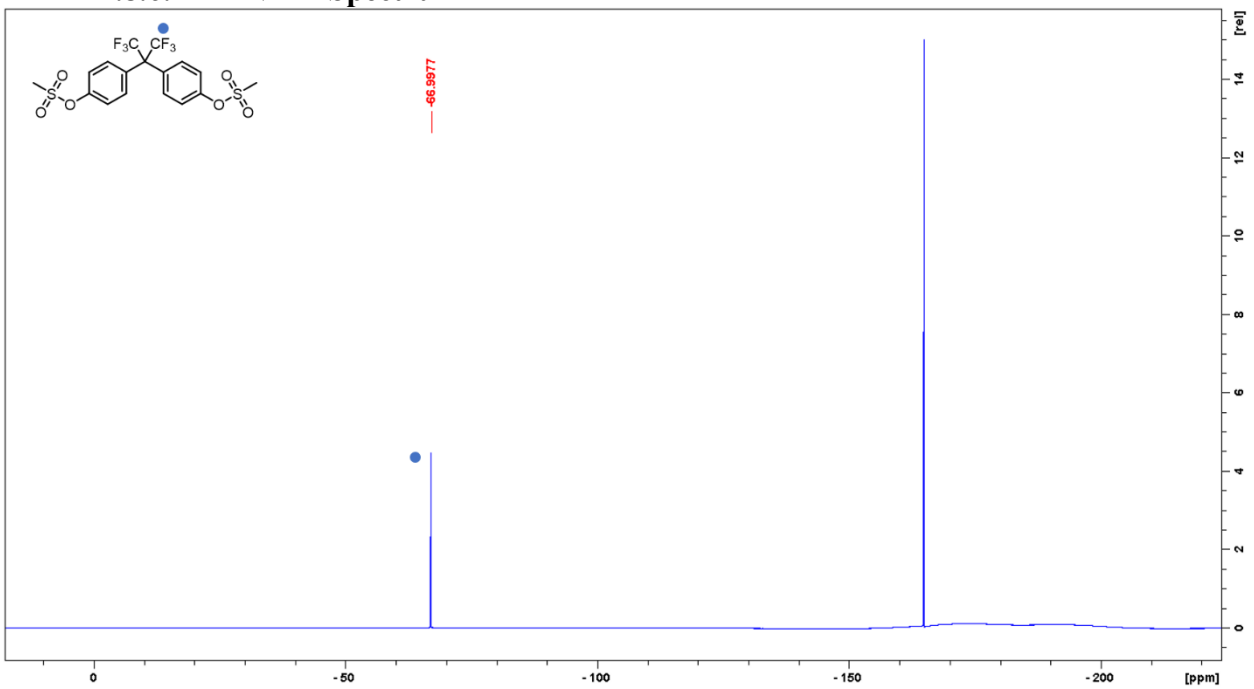

Figure S2.10. ^{19}F NMR spectrum of compound **3**.

2.8.7. Solid-state ^{13}C CP-MAS NMR spectra

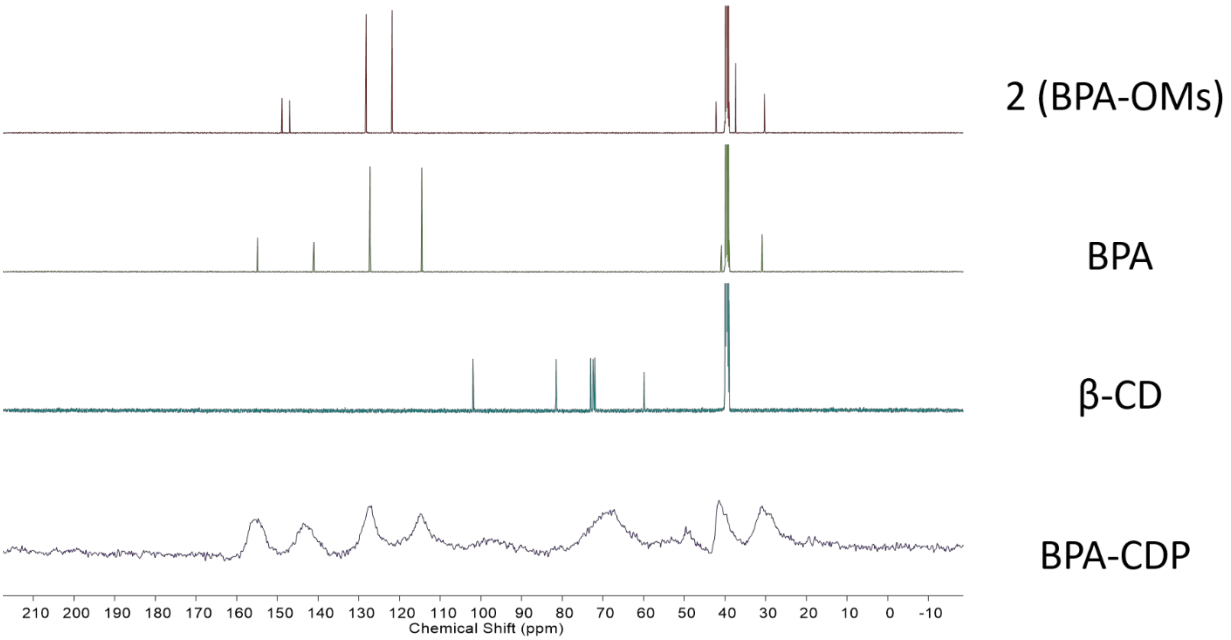

Figure S2.11. Solid-state CP-MAS ^{13}C NMR spectrum of BPA-CDP (bottom), Liquid-state ^{13}C NMR spectra of β-cyclodextrin (second from bottom), bisphenol A (second from top), and mesylated linker **2** (top) in DMSO-d_6.

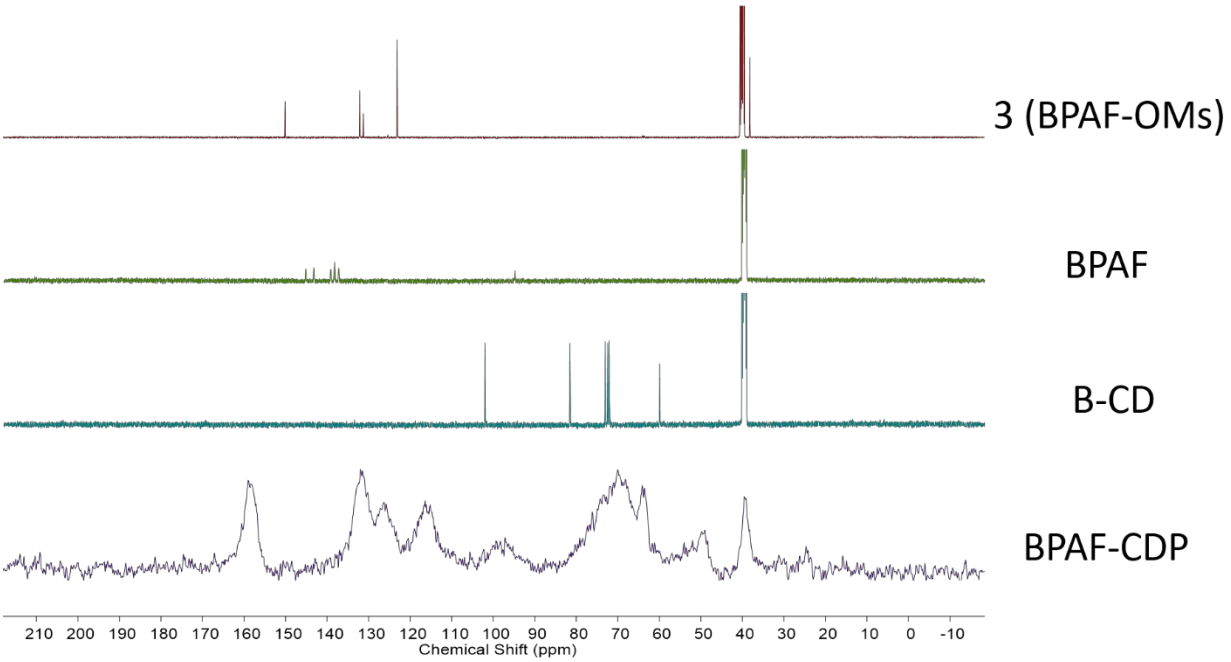

Figure S2.12. Solid-state CP-MAS ^{13}CNMR of BPAF-CDP (bottom), Liquid-state ^{13}CNMR spectra of β-cyclodextrin (second from bottom), bisphenol AF (second from top), and mesylated linker 3 (top) in DMSO-d6.

2.8.8. Infrared Spectra

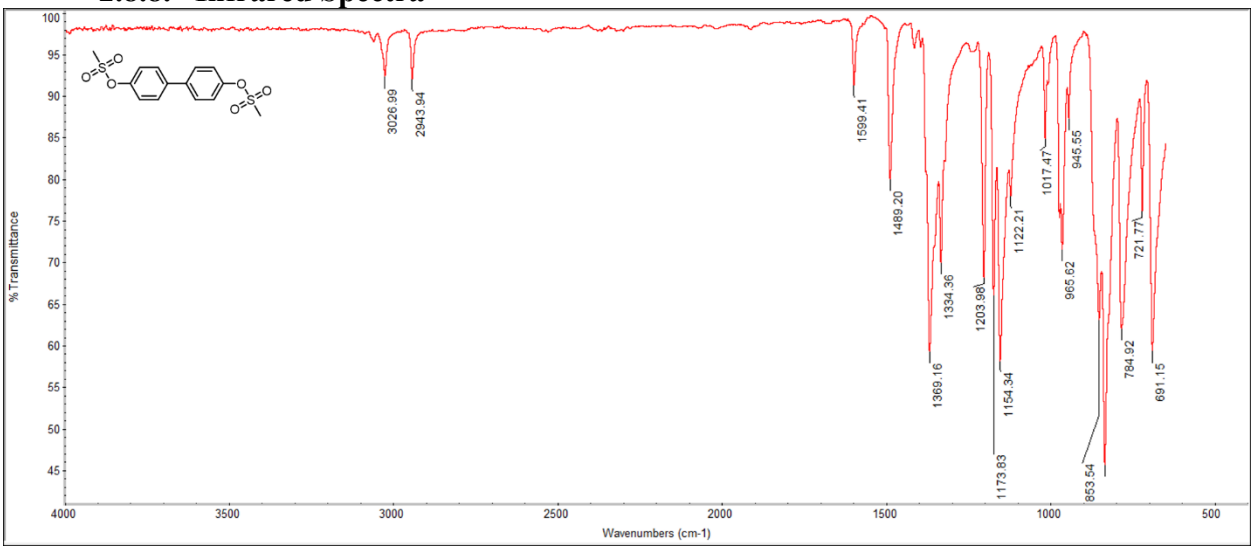

Figure S2.13. FT-IR spectrum of compound **1**.

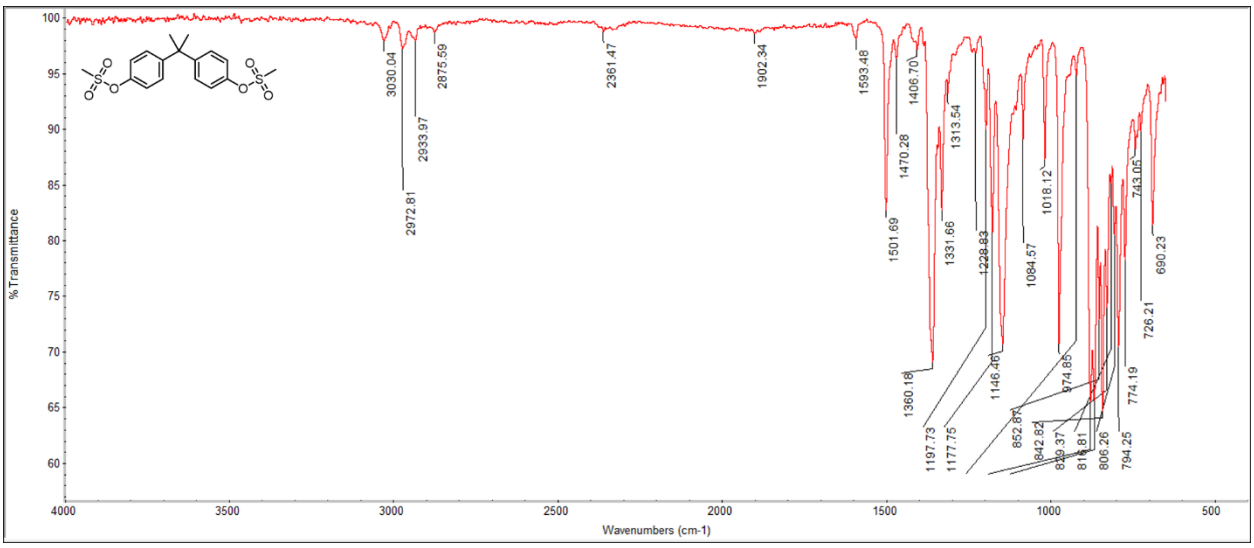

Figure S2.14. FT-IR of compound **2**.

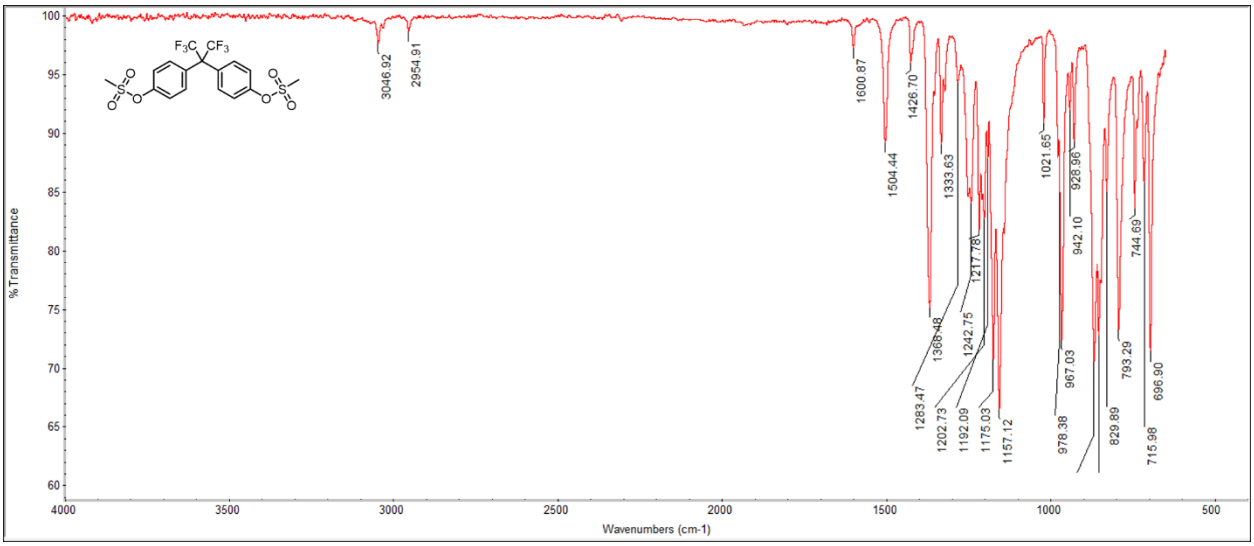

Figure S2.15. FT-IR of compound **3**.

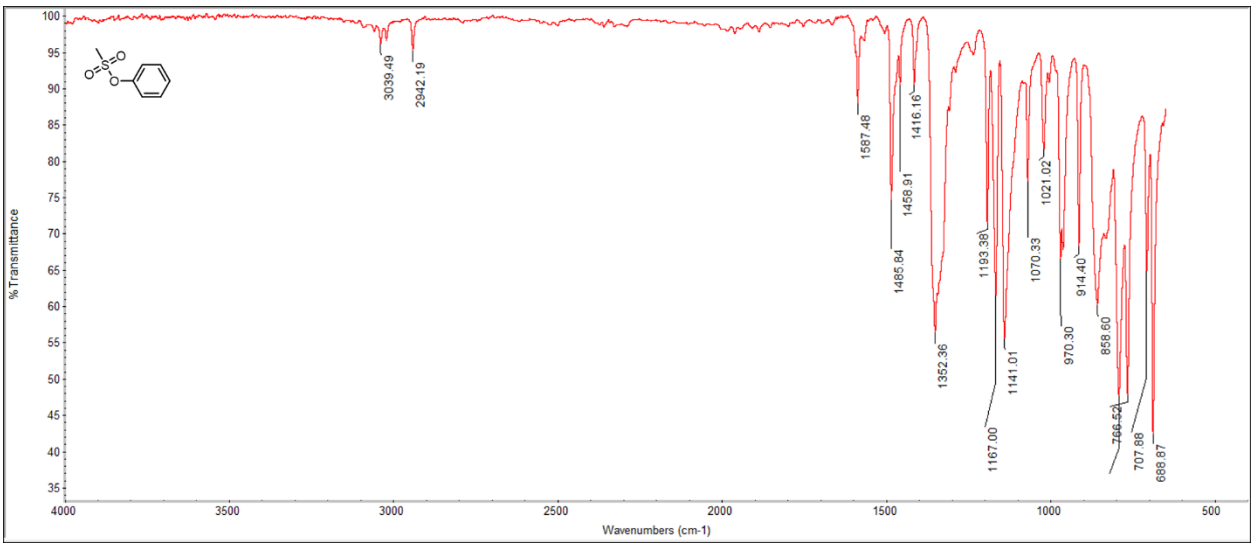

Figure S2.16. FT-IR of compound 4.

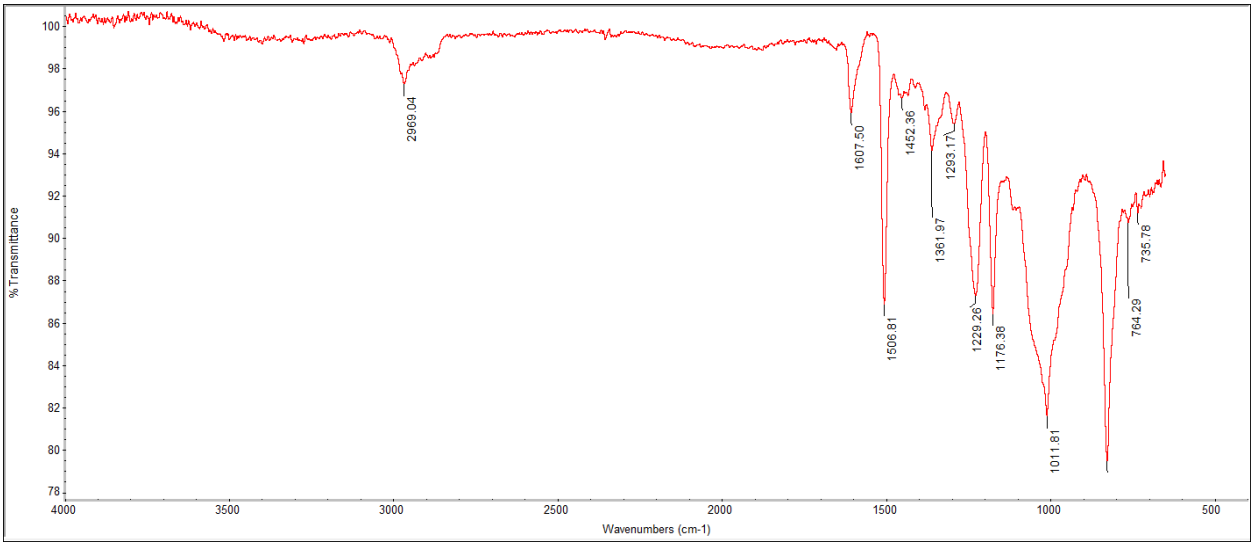

Figure S2.17. FT-IR of **BPA-CDP.**

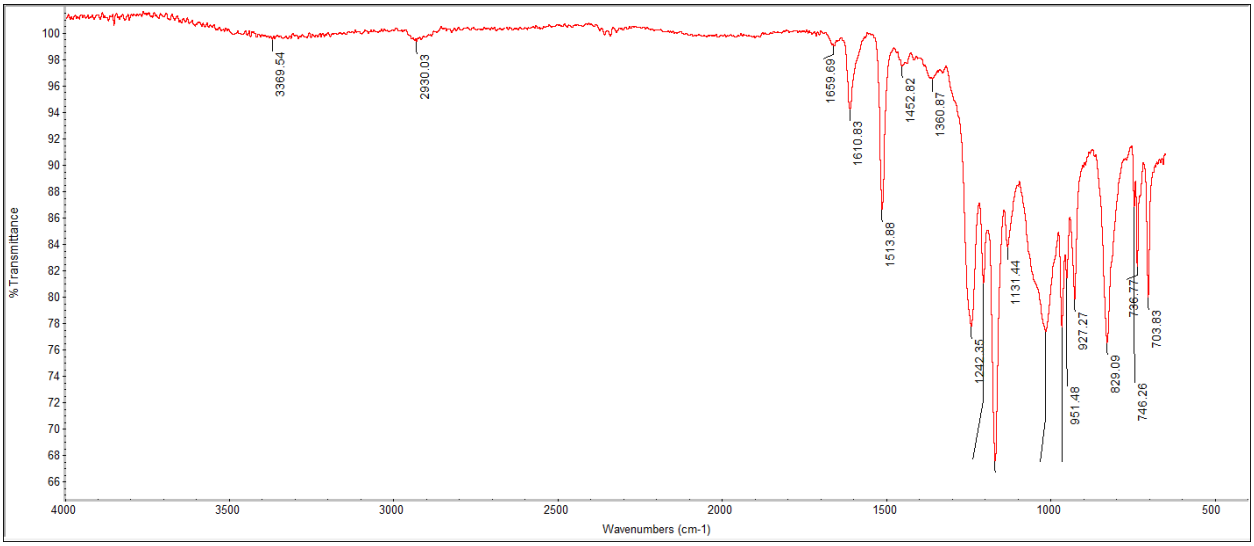

Figure S2.18. FT-IR of **BPAF-CDP**.

3. Low Temperature Mineralization of Perfluorocarboxylic Acids

All figures reused or adapted from Trang and Li et al., *Science*, accepted.

3.1. Abstract

Per- and polyfluoroalkyl substances (PFAS) used in industry and in consumer products pollute water resources at concentrations harmful to human health. Current strategies for PFAS destruction do not utilize perfluorocarbon-specific reactivity, limiting them in efficiency and applicability because of their nonselective destruction mechanisms. Here we report the mineralization of perfluoroalkyl carboxylic acids through a previously unrecognized pathway that proceeds through the sodium hydroxide-mediated defluorination of perfluoroalkyl anions. In this study, decarboxylation of perfluorocarboxylic acids (PFCAs) in a polar aprotic solvent affords access to the reactive perfluoroalkyl ion intermediates and allows mineralization of one of the largest PFAS classes. Analysis of the reaction products from a series of PFCAs after 24 hours shows the degradation produces high amounts of fluoride ion (78–104%), a systematically varied distribution of carbonaceous byproducts, and for PFCAs with carbon chains ≥ 5 carbons, a small amount of trifluoroacetate, which degrades more slowly. Notably, the patterns in the product analysis were inconsistent with the typical one-carbon chain-shortening mechanisms often proposed in PFAS degradation studies. Instead, our computational studies identified a new likely mechanism comprised of fluoride elimination, hydroxide addition, and carbon–carbon bond-scission processes consistent with a broad range of experimental observations. This reactivity might be extended to other PFAS classes as methods to activate their headgroups are developed.

3.2. Introduction

Per- and polyfluoroalkyl substances (PFAS) are anthropogenic substances containing multiple carbon–fluorine bonds. PFAS are used as omniphobic surfactants in many industrial processes and products, including poly(tetrafluoroethylene) production, as water-, oil-, and stain-resistant barriers for fabrics and food service containers, and as components of aqueous film-forming foams for fire suppression (*140*). As a result of their widespread global use, environmental persistence, and bioaccumulation, PFAS contamination is pervasive, having been detected in the blood of 98% of a representative sample of the United States population (*13*), and affects drinking water, surface waters, livestock, and agricultural products around the world (*19*, *141*, *142*). This persistent environmental contamination is alarming because chronic exposure to even low levels of these compounds is associated with negative health effects such as thyroid disease, liver damage, high cholesterol, reduced immune responses, low birth weights, and several cancers (*3*–*8*, *143*). Many of these effects were obscured by PFAS manufacturers for decades (*143*). In recent years, the growing focus on removing parts-per billion (ppb) to parts-per-trillion (ppt) levels of PFAS contamination from drinking water supplies has produced several PFAS removal approaches, including established adsorbents such as activated carbons and ion-exchange resins as well as emerging materials such as cross-linked polymers (*39*, *40*, *50*, *73*, *76*, *144*–*146*). However, the field has advanced to the point where the state-of-the-art is no longer simply PFAS removal but eradicating persistent PFAS compounds through PFAS destruction. Adsorbents or membrane-based separation processes create PFAS-contaminated solid or liquid waste streams but do not address how to degrade these persistent pollutants. PFAS destruction is a daunting task because the strong C–F bonds (*30*) that give PFAS desirable properties such as lipo- and hydrophobicity

and high thermal stability also make these compounds resist end-of-life degradation (*31*, *32*). To address this problem, PFAS degradation methods have been investigated with varying levels of success, such as incineration (*16*), ultrasonication (*147*, *148*), plasma-based oxidation (*103*), electrochemical degradation (*108*, *110*), supercritical water oxidation (*113*), ultraviolet-initiated degradation using additives such as sulfite or iron (*89–91*, *94*, *118*, *119*, *149*) and other combinations of chemical and energy inputs (*84*) (**Table S3.1**). Methods and mechanistic understanding that leverage the unique reactivity of perfluoroalkyl species might offer mild alternatives to address the PFAS contamination problem.

The opportunity to degrade PFAS at high concentrations in non-aqueous solvents has recently been developed through PFAS adsorbents that can be regenerated by a simple solvent wash. This development enables destruction of these compounds after they have been removed from water resources (*73*, *76*), which broadens suitable degradation conditions beyond dilute aqueous environments. Here, we access reactive perfluoroalkyl anions that are mineralized under mild conditions by decarboxylating perfluorocarboxylic acids (PFCAs), one of the largest classes of PFAS compounds, at low temperatures in dipolar aprotic solvents. PFCAs of various chain lengths undergo efficient mineralization in the presence of NaOH in mixtures of water and DMSO at mild temperatures (80–120 °C) and ambient pressure. Under these conditions, perfluorooctanoic acid (PFOA, **1, Figure 3.1**) is completely degraded with greater than 90% defluorination and minimal formation of fluorocarbon byproducts (**Figure 3.4A**). Experimental observations and density functional theory calculations offer strong evidence for degradation pathways distinct from the single-carbon chain-shortening processes proposed in prior PFAS degradation studies (*89*, *96*, *97*, *103*, *109*, *118*). This previously unrecognized reactivity, which is accessible at moderate

temperatures and ambient pressure, is immediately promising for PFCA destruction and may prove generalizable to other PFAS classes as methods to activate their polar groups are identified.

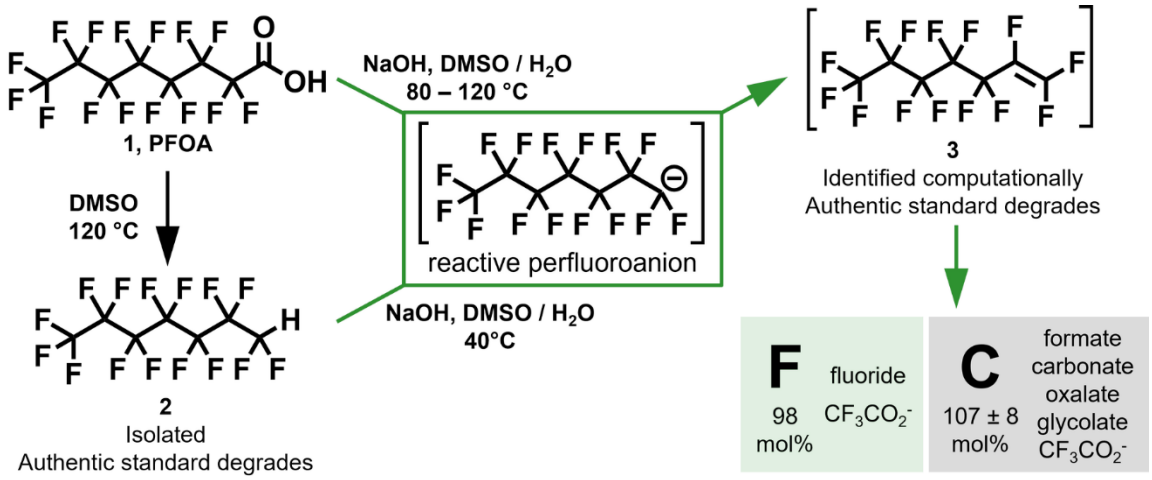

Figure 3.1. Overview of degradation pathways identified in this study. Heating PFCAs in polar aprotic solvents such as DMSO decarboxylates them to 1H-perfluoroalkanes. When this reaction is performed in the presence of NaOH, the PFCA is mineralized the fluoride, carbonate, and formate ions. The 1H-perfluoroalkane undergoes the same degradation process at even lower temperatures. Computational studies identified the corresponding perfluoroalkenes as likely intermediates, and an authentic standard of the seven-carbon perfluoroalkene is competent for the degradation.

3.3. Results and Discussion

Reactive and readily degradable perfluorocarbanions are easily accessed by decarboxylating PFCAs in dipolar aprotic solvents. In a solution of dimethyl sulfoxide (DMSO) and H_2O (8:1 *v*/*v*) at 120 °C, perfluorooctanoic acid (PFOA) decarboxylates to form perfluoro-1H-heptane **2**, which phase-separates from solution as an oil. ^{1}H, ^{13}C, and ^{19}F NMR spectroscopy of the isolated oil confirmed the formation of the decarboxylated product in high purity (**Figure S3.1 to Figure S3.4**). This decarboxylation reaction is consistent with those reported by Lundgren and coworkers, who found that most carboxylic acids decarboxylate reversibly in dimethylformamide (*150*). Lundgren's work was followed up by Gao and coworkers (*151*), who studied the origins of this reversible carboxylation computationally and determined that the lower barrier to decarboxylation was fully induced by solvent effects from the polar aprotic solvent, which we affirmed with our calculations (**Figure 3.2**). Relaxed-scan comparisons of the decarboxylation

energy profiles in both gas and liquid phase show that the solvent effect plays a significant role. The energy profile in the liquid phase has a maximum value, while the energy profile in the gas phase keeps rising, indicating that in the gas phase, the products formed by decarboxylation will return to the reactant with a very low energy barrier.

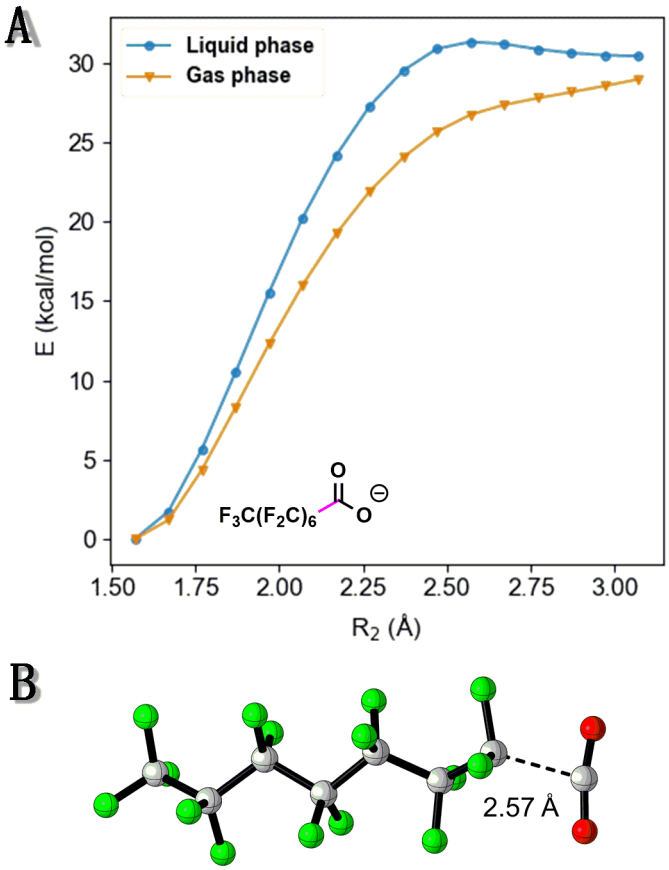

Figure 3.2. A) The scanning coordinates of C–C bond length to show solvent effect in decarboxylation. The bond is colored pink. Hydroxide in the solvent may play a significant role in promoting decarboxylation. B) 3D structure of TS1.

Additionally, McCord and coworkers noted that the decarboxylation of hexafluoropropylene oxide dimer acid (HFPO-DA, also known as GenX) plagued analytical standards when dissolved in dipolar aprotic solvents (*152*). Knappe and coworkers followed up this study by investigating a wider array of PFAS in mixtures of polar aprotic solvents in water (*153*), but this reactivity has not been explored for PFAS degradation until now. We found that

when the same PFOA solution in DMSO/H_2O is subjected to the decarboxylation conditions but in the presence of NaOH (30 equiv), PFOA instead degraded to a mixture of fluoride, trifluoroacetate ions, and carbon-containing byproducts (**Figure 3.4A**). Degradation also occurs in other polar aprotic solvents such as dimethylacetamide and sulfolane, but it does not proceed in pure water (**Figure S 3.12, Table 1.1**). ^{19}F NMR spectroscopy of reaction aliquots collected over 24 hours indicated resonances corresponding to PFOA were no longer detectable within 14 hours. Surprisingly, very few fluorinated intermediates were observed in these spectra. No resonances corresponding to perfluoroalkyl groups containing between four and seven carbons were observed in any of the spectra. Resonances corresponding to sodium perfluoropropionate ($CF_3CF_2CO_2Na$) at -81.5 ppm and -118.2 ppm were observed just above the baseline within spectra of aliquots collected at reaction times shorter than 24 hours, and then are absent in spectra of later aliquots (**Figure 3.3**).

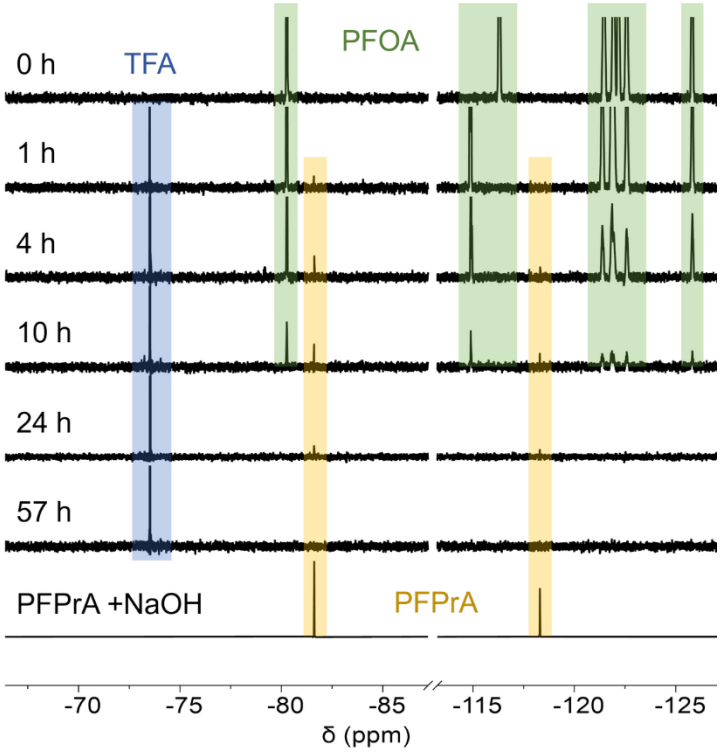

Figure 3.3. Appearance and disappearance of perfluoropropionic acid (PFPrA) during the degradation of PFOA at 120 °C as a function of reaction time. Bottom spectrum: authentic sample of PFPrA and NaOH heated to 120 °C for 1 h. . Blue highlighted peaks correspond to trifluoroacetate (TFA), green highlighted peaks correspond to PFOA, and yellow highlighted peaks correspond to PFPrA. PFPrA is observed as a trace byproduct (in the 10 h spectrum, its concentration is approximately 1–2% of the initial PFOA concentration) that subsequently degrades between reaction times of 24–57 h.

Table 3.1. Defluorination of various PFAS substrates under varying conditions.

Compound	Solvent	Temp (°C)	Time	F IC%[a]
2	DMSO	40	25 min	4%
1	DMSO	40	25 min	n.d.
2	DMSO	120	5 min	11%
1	DMSO	120	5 min	n.d.
2	DMSO	40	48 h	57%
3	DMSO	40	48 h	70%
PFOS	DMSO	120	150 h	0.3%
1	DMAc[b]	120	44 h	31%
1	sulfolane[b]	120	44 h	38%
1	water	120	44 h	0.1%
control[c]	DMSO	120	24 h	0.2%

Defluorination of various PFAS substrates under varying conditions, as measured by fluoride ion concentrations detected by ion chromatography. Perfluoro-1H-heptane (**2**) gives greater fluoride recovery than PFOA at the same times and temperatures, suggesting that decarboxylation is the rate-limiting step in this degradation. Even at low temperatures, PFHp-1H and perfluoro-1-heptene (**3**) both give relatively efficient defluorination (>50%). PFOS does not react under these conditions, and PFOA (**1**) does not defluorinate in pure water, only in polar aprotic solvents such as dimethylacetaminde (DMAc) or sulfolane. Control experiments run without PFOA show that the PTFE reactor does not release fluoride into the reaction. [a] n.d. = not detected. [b] Using standard conditions for DMSO; not optimized for other solvents. 100% degradation of PFOA as all ^{19}F NMR peaks disappeared. [c] Percent calculated relative to a 1 mmol PFOA degradation reaction; average of triplicate reactions.

The only prominent fluorine resonance in the aliquot sampled at 24 hours corresponds to sodium trifluoroacetate (CF_3CO_2Na, -73.6 ppm, **Figure 3.4B**). Integration of this resonance indicated that its intensity plateaus around 4–24 hours, corresponding to only 7% of the F content and 9% of the C content relative to the initial PFOA concentration (**Figure 3.4A, C**). However, resonances corresponding to CF_3CO_2Na ions eventually decrease in intensity and presumably degrade into fluoride, albeit much more slowly than the rate of PFOA disappearance (**Figure 3.4C, inset**). The CF_3CO_2Na ion resonances disappear over 300 hours, which we confirmed by subjecting an authentic sample of sodium trifluoroacetate to the same reaction conditions (**Figure**

3.8). These observations indicate that PFOA degradation is rapid and forms CF_3CO_2Na and trace $CF_3CF_2CO_2Na$ as the only identifiable perfluoroalkyl-containing liquid-phase byproducts, each of which continues to degrade over extended reaction times. Subjecting perfluorooctane sulfonate ions (PFOS) to the basic decarboxylation conditions does not result in decreasing perfluoroalkyl ^{19}F NMR integrations or fluoride formation **(Figure S3.11, Table 1.1**), indicating decarboxylation to the reactive anion intermediate is the key first step of the defluorination process for PFCAs.

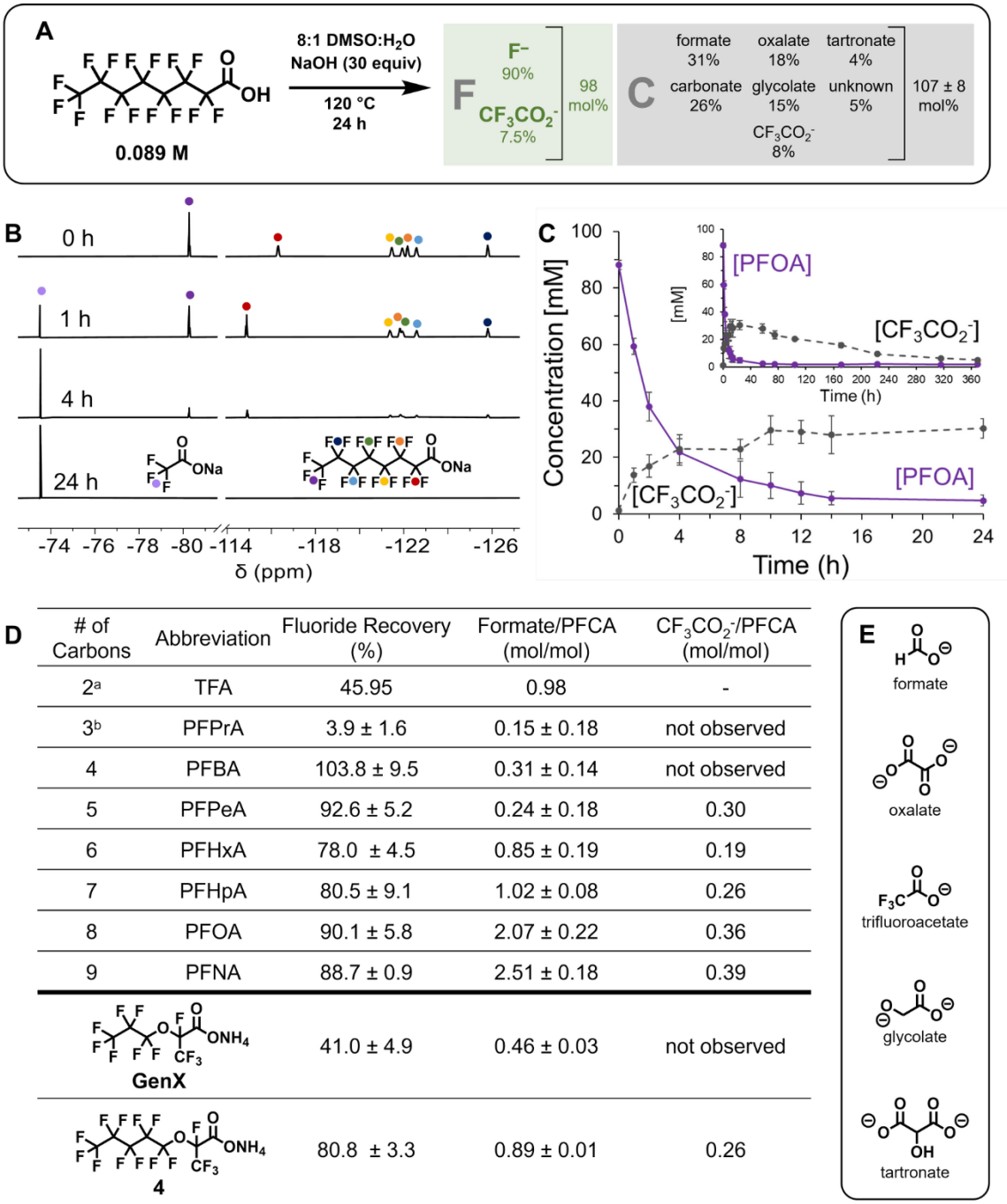

D

# of Carbons	Abbreviation	Fluoride Recovery (%)	Formate/PFCA (mol/mol)	$CF_3CO_2^-$/PFCA (mol/mol)
2[a]	TFA	45.95	0.98	-
3[b]	PFPrA	3.9 ± 1.6	0.15 ± 0.18	not observed
4	PFBA	103.8 ± 9.5	0.31 ± 0.14	not observed
5	PFPeA	92.6 ± 5.2	0.24 ± 0.18	0.30
6	PFHxA	78.0 ± 4.5	0.85 ± 0.19	0.19
7	PFHpA	80.5 ± 9.1	1.02 ± 0.08	0.26
8	PFOA	90.1 ± 5.8	2.07 ± 0.22	0.36
9	PFNA	88.7 ± 0.9	2.51 ± 0.18	0.39
GenX		41.0 ± 4.9	0.46 ± 0.03	not observed
4		80.8 ± 3.3	0.89 ± 0.01	0.26

Figure 3.4. Overall reaction scheme, monitoring PFOA and $CF_3CO_2^-$ concentrations over course of reaction, summary of degradation products from series of PFCAs of different lengths. A) Heating 0.089 M PFOA in 8:1 DMSO:H_2O with 30 equiv NaOH allows 90% of the initial fluorine to be recovered as inorganic fluoride, and residual trifluoroacetate with few other organofluorine byproducts. Formate ions (26 mol%) and several other non-fluorinated byproducts were identified (107 ± 8 mol%). B) ^{19}F NMR spectra from 0–24 h. Peaks corresponding to PFOA perfluoroalkyl fluorines between -115 and -126 ppm as well as at -80 ppm disappear in less than 24 h. Trifluoroacetate (-73.6 ppm) appears and disappears (disappearance shown in inset) more slowly over the course of the reaction. C) Amount of PFOA (purple, solid line) and sodium trifluoroacetate (gray, dashed line) in the reaction over time. Error bars correspond to standard deviation of three experiments. D) Fluoride recovery calculated as mols of fluoride after reaction as detected by ion chromatography / mols of fluorine in PFCA reactant. Formate/PFCA calculated as mols of formate as detected by IC after reaction / mols of PFCA reactant. $CF_3CO_2^-$/PFCA calculated

as mols $CF_3CO_2^-$ as calculated from ^{19}F NMR spectroscopy after 24 h of reaction / mols PFCA reactant. All measurements expressed as average of three trials unless specified and error expressed as a standard deviation. All reaction times 24 hours unless specified. [a] 286 hours, single measurement, [b] 63% ± 12% of PFPrA starting material degraded after 24 h. E) Structures of identified carbon-containing byproducts.

Ion chromatography of the reaction mixtures after PFOA degradation accounts for a high mass balance of fluorine in the PFOA degradation reaction. The heterogenous reaction mixture was diluted with water until all precipitated salts dissolved, then the mixture was analyzed using ion chromatography. 90 ± 6% of the fluorine atoms originating from the PFOA were recovered as fluoride ions after 24 h of reaction at 120 °C. Control experiments showed that the fluorinated PTFE reaction vessels did not contribute a significant amount of fluoride to the fluoride recovery (**Table 3.1**). Fluoride analyses performed at shorter reaction times (**Figure 3.5**) indicated that the fluoride increased proportionally to the decrease in [PFOA], as measured by ^{19}F NMR spectroscopy. This high fluoride recovery indicates that most of the perfluoroalkyl fluorines are defluorinated and mineralized rather than being transformed to smaller-chain PFAS or being lost as volatile fluorocarbons.

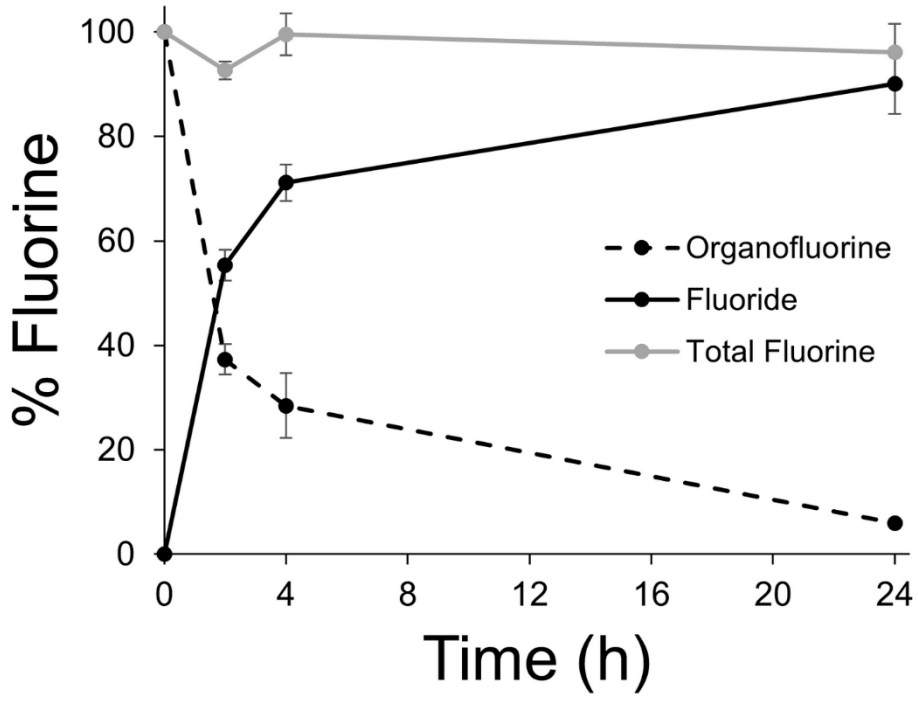

Figure 3.5. Fluorine balance of PFOA degradation performed at 120 °C at different reaction times. Organofluorine content (black dashed line) was measured by integrating all ^{19}F NMR peaks; the fluoride ion (black solid line) were measured by ion chromatography of entire reaction solution. The total fluorine (gray line) is calculated by adding the organofluorine and fluoride ion amounts and remains close to unity throughout the PFOA degradation reaction, indicating little to no loss of volatile organofluorine products.

PFCAs with different chain lengths (2–9 carbons) were degraded, which provided fluoride recoveries between 78% and quantitative at 24 hours for all PFCAs with four or more carbons (**Figure 3.4D**). Although the longer-chain ($C \geq 4$) PFCAs have a similar degradation profile to PFOA in that their perfluoroalkyl peaks disappeared from the ^{19}F NMR spectra (**Figure 3.6**) and $CF_3CO_2^-$ was formed (**Figure 3.4D, Figure 3.7**), the destruction of shorter-chain PFCAs ($C = 2$, 3) is slower and appears to occur by different mechanisms. For trifluoroacetate ($C = 2$), degradation is slow (>6 days, see **Figure 3.8**) likely because the instability of the CF_3^- anion (*154*) hinders decarboxylation, such that destruction occurs either more slowly or by a different mechanism. The carbanion corresponding to PFPrA ($C = 3$) decarboxylation is similarly unstable (*154*), resulting in degradation faster than trifluoroacetate but slower than the longer PFCAs (**Figure 3.6**).

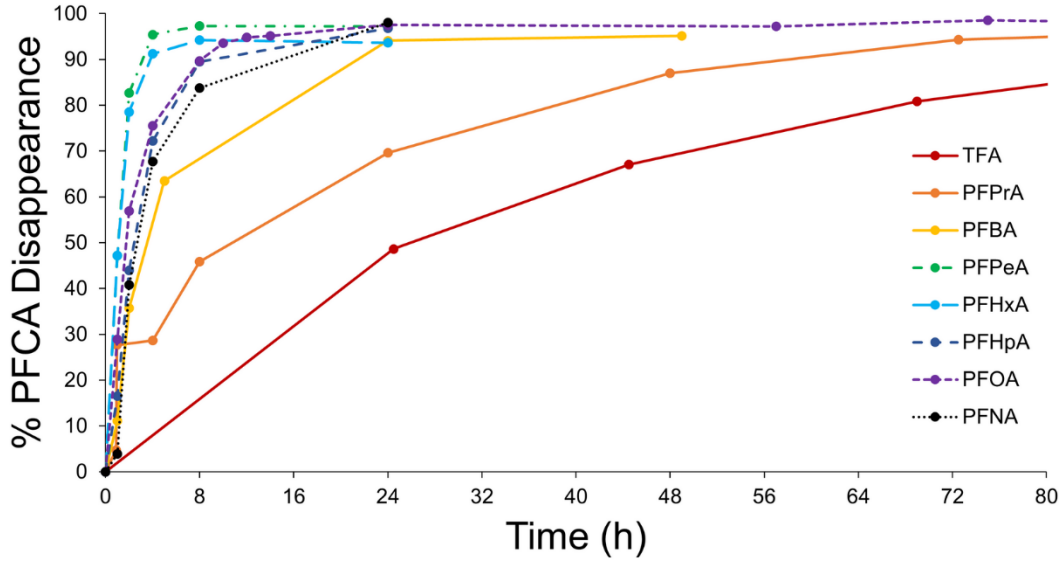

Figure 3.6. Rates of PFCA degradation, as measured by 19F NMR integration of the respective alpha-carbon fluorine resonances of each PFCA.

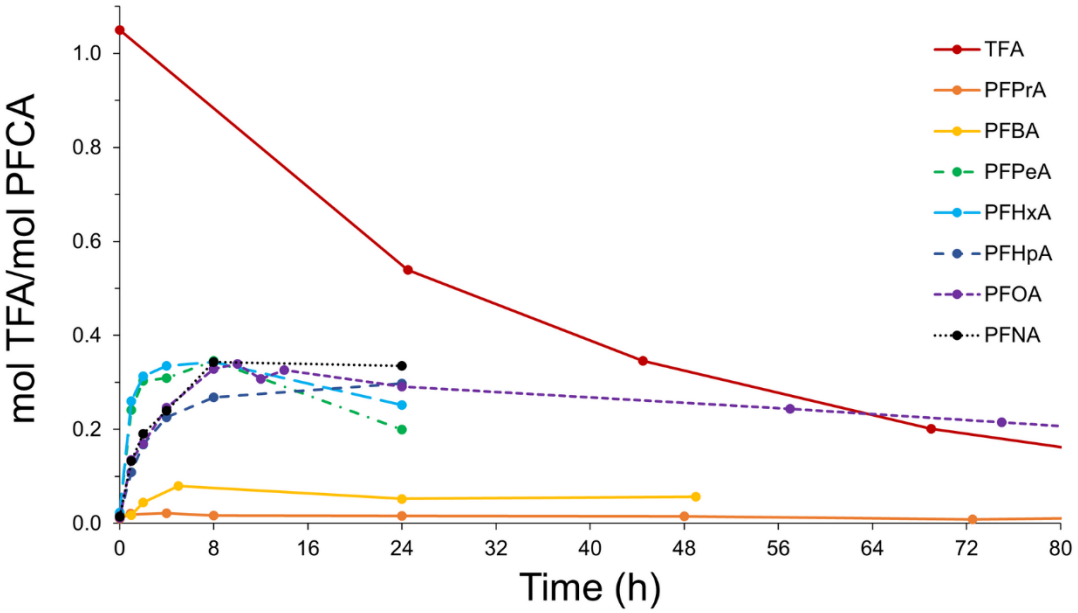

Figure 3.7. Kinetic trace of mols of trifluoroacetate per mol of reactant PFCA, as measured by 19F NMR spectroscopy. For TFA itself, the plot indicates its degradation rate. For PFPrA and PFBA, little or no TFA is formed. For PFCAs with five or more carbons, approximately 0.33 mol TFA/mol PFCA are formed in the early stages of the degradation reaction.

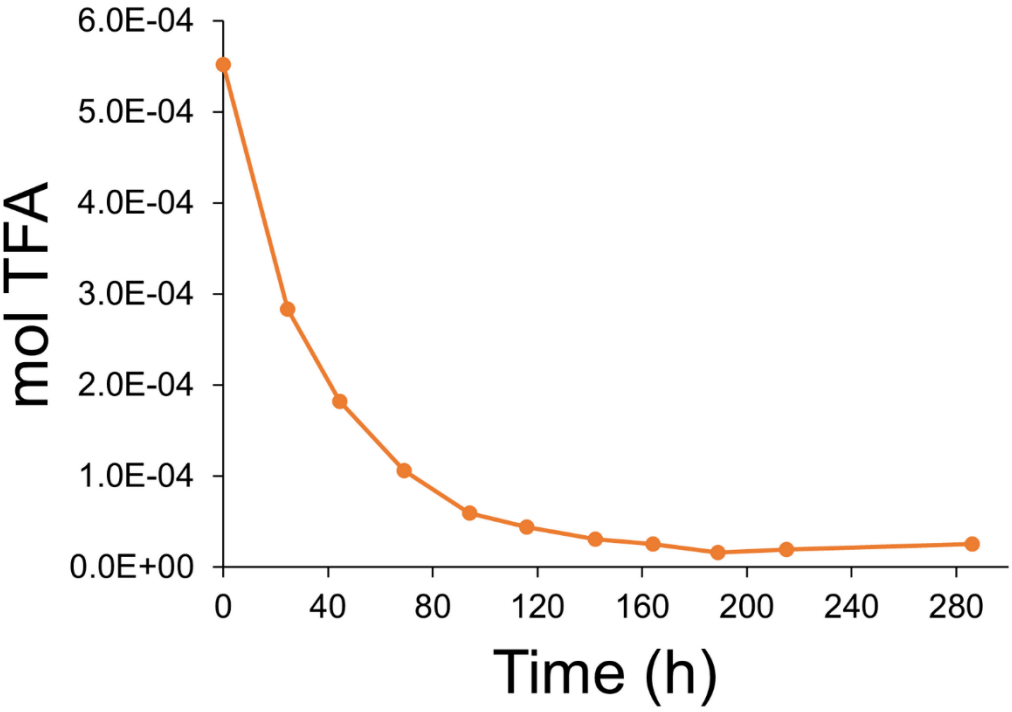

Figure 3.8. Kinetic trace of the degradation of CF_3CO_2Na over time as calculated by NMR concentration. CF_3CO_2Na (0.089 M in DMSO) was degraded at 120 °C with 30 equiv NaOH in 8:1 DMSO:H_2O.

Although the PFPrA ^{19}F NMR peaks disappear completely over three days, fluoride recovery is lower than other PFCAs (3.9 ± 1.6%, **Figure 3.4D**). PFPrA, unlike others in the series, decarboxylates to form a volatile product; in the ^{19}F NMR for PFPrA degradation, peaks corresponding to CF_3CF_2H can be identified (**Figure 3.9–Figure 3.10**). Headspace gas chromatography/electron-impact mass spectrometry also detected the $CF_3CF_2^{+\bullet}$ fragment in the gas phase of the reaction (**Figure 3.11**). This finding was corroborated by atmospheric pressure chemical ionization – mass spectrometry of a liquid aliquot of the reaction that had a prominent peak corresponding to $CF_3CF_2^-$ (**Figure 3.12, compare to Figure 3.11, Figure S 3.20**). It appears to be more favorable to produce volatile CF_3CF_2H than for the C = 3 PFCA to proceed down the destruction pathway; as discussed below, this supports our proposal that a γ-carbon is necessary for the major defluorination pathway to occur.

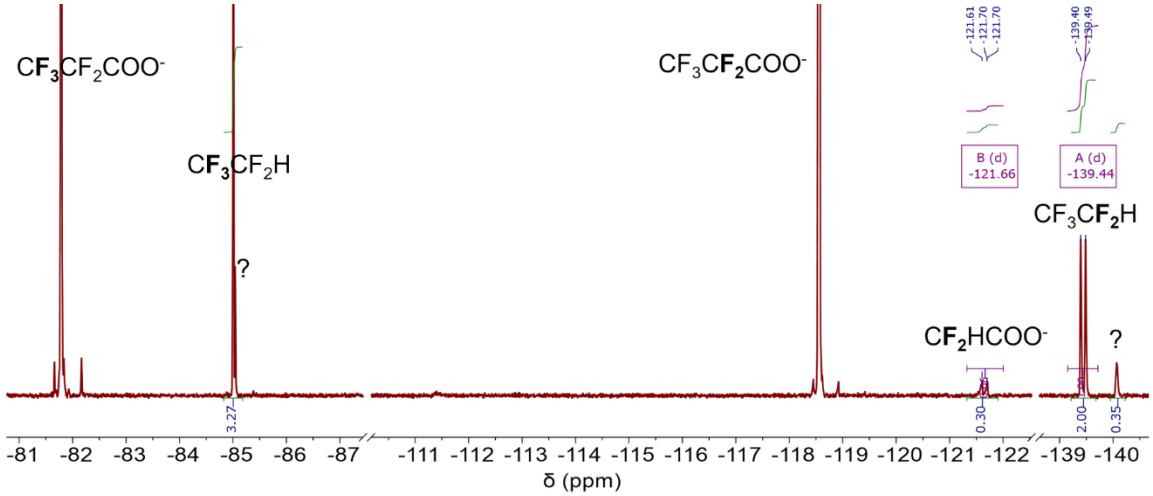

Figure 3.9. ^{19}F NMR (565 MHz, DMSO) spectrum of concentrated aliquot of PFPrA degradation reaction (30 equiv NaOH in 8:1 DMSO:H_2O). The degradation of PFPrA provides evidence for the formation of a volatile protodecarboxylated fluorocarbon CF_3CF_2H, along with difluoroacetate ions. CF_2HCOO^- Actual: -121.66 (d, J = 53.5 Hz) Literature (*155*): (solvent not specified): -123.63 d, J = 56.5 Hz. CF_3CF_2H Actual: δ -85.00 (s, 3F), -139.44 (d, J = 51.4 Hz, 2F). Literature (*156*): $(CD_3)_2SO$: −139.5 (2F, dq, $^2J_{HF}$ = 51.1, $^3J_{FF}$ = 3.0 Hz, HCF_2), −85.1 (3F, dt, $^3J_{HF}$ = $^3J_{FF}$ = 3.0 Hz, CF_3). Unidentified peaks at -85.04 (s), -140.07 (s)

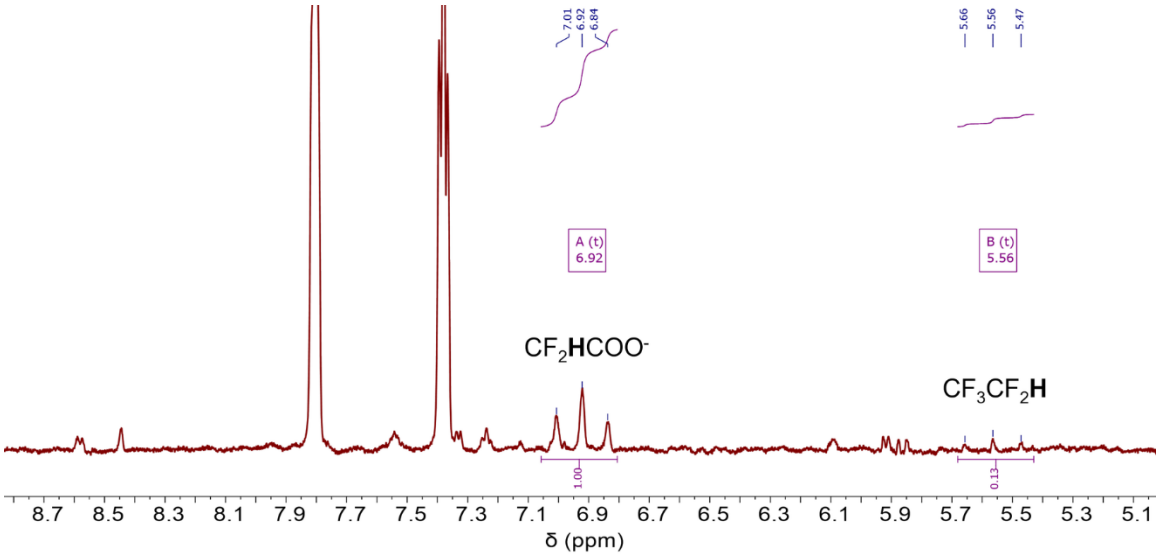

Figure 3.10. ^{1}H NMR (600 MHz, DMSO) spectrum of concentrated aliquot of PFPrA degradation reaction (30 eq. NaOH in 8:1 DMSO:H_2O). The degradation of PFPrA provides evidence for the formation of a volatile protodecarboxylated fluorocarbon CF_3CF_2H, along with difluoroacetate ions. CF_2HCOO^- Actual: δ 6.92 (t, J = 50.8 Hz) Literature (*157*): (CF_2HCOOH, 299.949 MHz, solvent not specified): ^{1}H spectrum: 6.13 ppm, $^2J_{H,F}$ = 53.10 Hz. CF_3CF_2H Actual: δ 5.56 (t, J = 55.8 Hz) Literature (*158*): (neat, referenced to DMSO in D_2O). 5.80 (1H, tq, J = 52.31, 2.55 Hz)

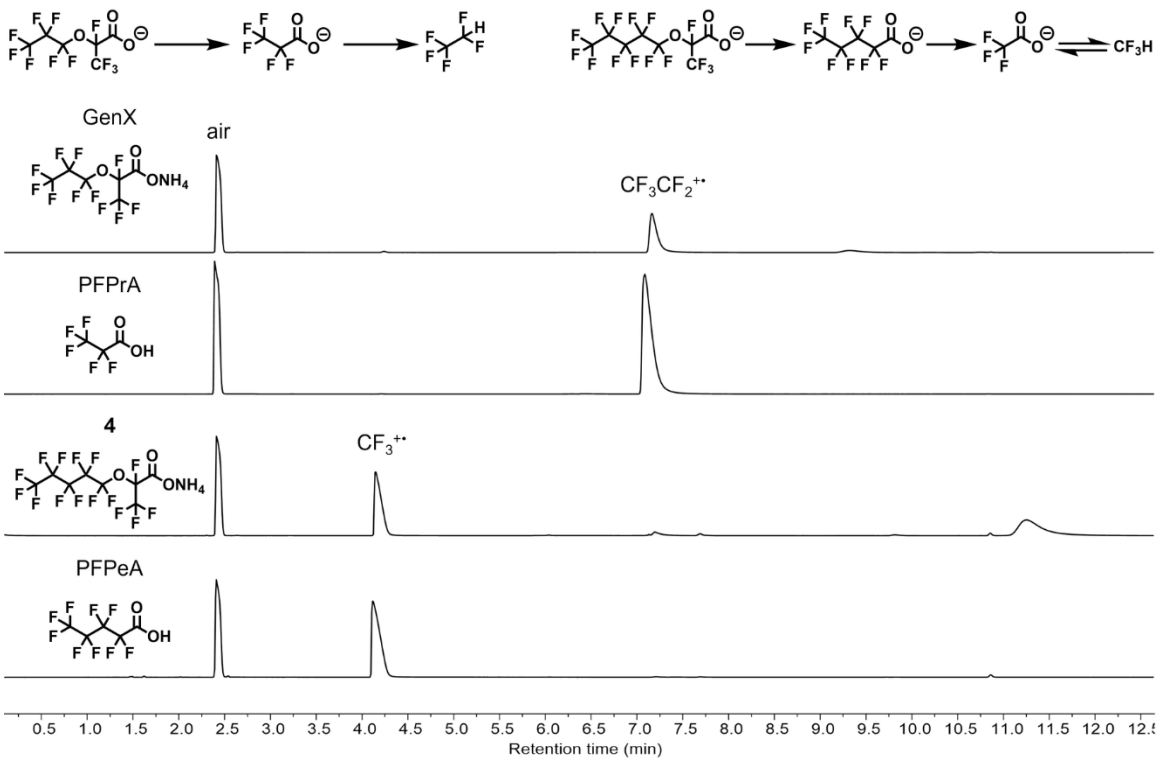

Figure 3.11. GCMS-headspace total ion chromatograms after 4 hours of reaction for GenX (top), perfluoropropionic acid (second from top), **4** (second from bottom), perfluoropentanoic acid (bottom). Both PFPrA and GenX show evidence of $CF_3CF_2^{+\bullet}$ gas fragments, presumably derived from CF_3CF_2H, whereas PFPeA and **4** show only $CF_3^{+\bullet}$ fragments, presumably from an equilibrium between CF_3COOH and CF_3H.

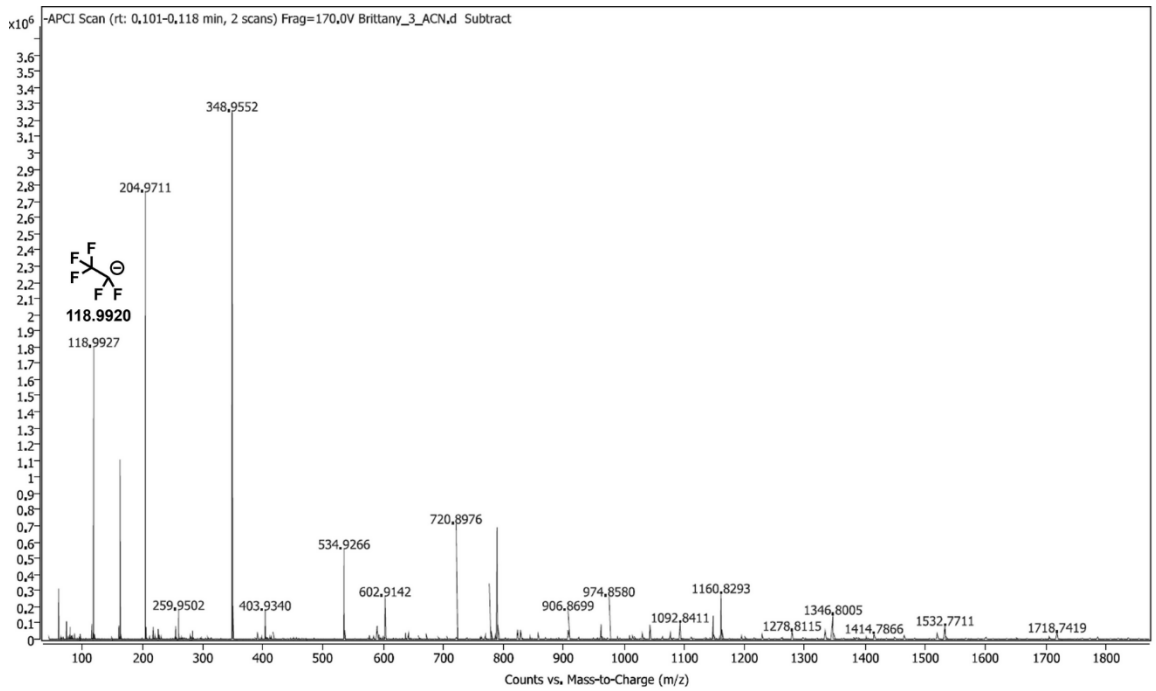

Figure 3.12. APCI-MS spectrum of an aliquot of PFPrA degradation reaction diluted in acetonitrile after 4 hours of heating at 120 °C. The prominent 118.9930 m/z peak identified in this reaction mixture is consistent with the proposed reaction mechanism as it corresponds to $CF_3CF_2^-$, which either comes from the decarboxylation of $CF_3CF_2CO_2^-$ or the deprotonation of CF_3CF_2H.

Previous PFAS degradation studies have suggested that PFCAs (or other PFAS that are PFCA precursors) degrade through a decarboxylation-hydroxylation-elimination-hydrolysis (DHEH) pathway in which each perfluorocarboxylic acid is shortened by one carbon each cycle, producing successively shorter PFCAs (*89*, *96*, *97*, *103*, *109*, *118*). However, the non-conformal degradation of the three-carbon acid and the products observed in the ^{19}F NMR spectra of degradation reactions of PFCAs containing four or more carbons indicate that degradation instead occurs via distinct, non-single-carbon-shortening mechanisms under these conditions.

The hypothesis that degradation does not occur by iterative one-carbon shortening was further supported by quantifying the carbon-containing byproducts formed when PFOA was degraded for 24 h. These byproducts were quantified using a combination of solution ^1H and ^{19}F NMR spectroscopy and quantitative ^{13}C NMR spectroscopy of the precipitate isolated from the reaction and dissolved in D_2O. Furthermore, ion chromatography was performed on the combined

solution and precipitate by adding water to the reaction mixture until the precipitate redissolved. Taken together, these measurements account for the complete carbon balance of the PFOA degradation (107 ± 8 mol% C relative to the $[PFOA]_0$, **Table 1.2, Figure 3.13**). Other than the residual $CF_3CO_2^-$ ions described above, which continue to degrade at longer reaction times, no other organofluorine compounds were detected. Instead, one-, two-, and three-carbon products lacking C–F bonds were identified and quantified.

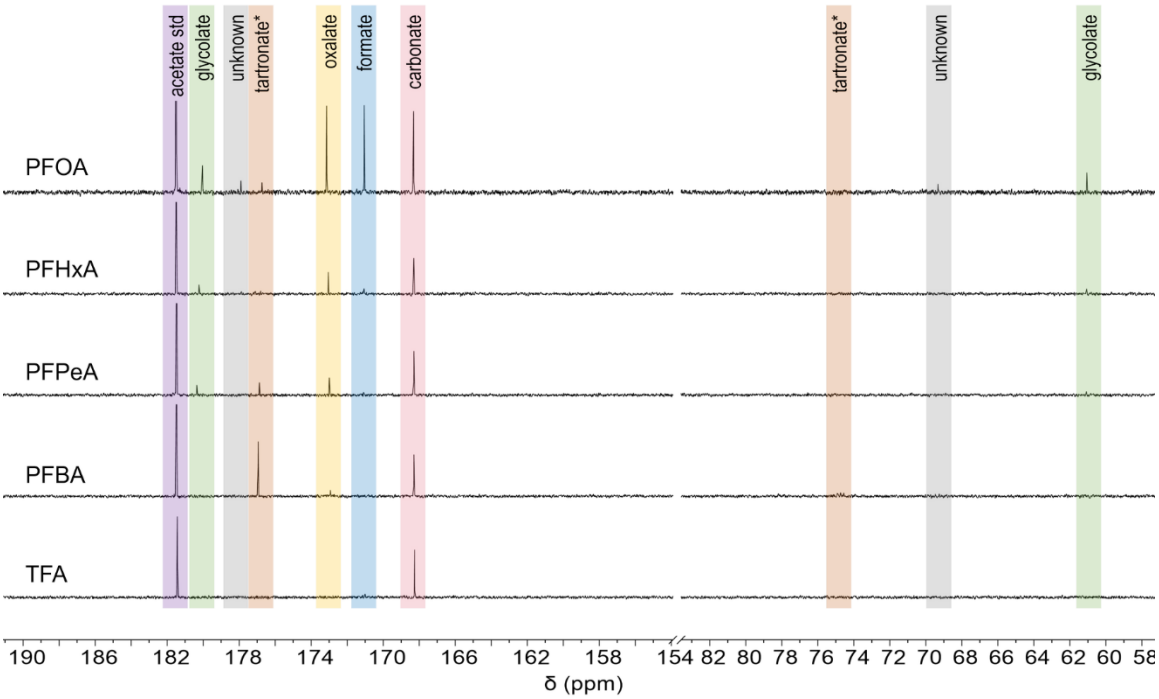

Figure 3.13. Quantitative ^{13}C NMR of isolated reaction precipitate dissolved in D_2O [sodium acetate was used as an internal standard, (50 µL of a 0.68 M solution in D_2O). The PFOA sample was recorded with 900 scans at 40 s delay. Samples other than PFOA were recorded with 300 scans at 40 s delay and have imperfect proton decoupling from the extreme pH sample conditions; Sodium trifluoroacetate (TFA) shows only carbonate (168 ppm) as reaction byproduct. PFBA shows carbonate, trace oxalate ion formation, and enhanced tartronate ion formation compared to other samples. PFPeA shows glycolate (180 ppm, 61 ppm), tartronate, oxalate, and carbonate ion formation. PFHxA shows glycolate, oxalate, formate (present in proton NMR, ion chromatography, hard to see here due to proton coupling), and carbonate. PFOA shows glycolate, tartronate, oxalate, formate, carbonate, and two trace unknown peaks at 178 and 69 ppm. *Tartronate assigned based on literature references (*159*, *160*).

Table 3.2. Distribution of carbonaceous byproducts of the PFOA degradation reaction, as measured by quantitative ^{13}C NMR spectroscopy of the isolated reaction precipitate dissolved in D_2O.

Compound	Mol% C relative to PFOA	Mol/Mol PFOA
Formate[a]	31.1 ± 4.0	2.5 ± 0.3
Carbonate	25.7 ± 3.1	2.1 ± 0.3
Oxalate	17.8 ± 3.0	0.7 ± 0.1
Glycolate	15.0 ± 1.4	0.6 ± 0.1[c]
Trifluoroacetate[b]	8.0 ± 1.0	0.32 ± 0.04
Tartronate[c]	4.3 ± 1.1	0.2 ± 0.1[c]
Unidentified	4.9 ± 2.4	0.4 ± 0.2[c]
Total	106.7 ± 8.3	8.5 ± 0.7[d]

Unless noted, all errors reported as standard deviation of triplicate measurements. [a] Calculated by adding the formate in the reaction solvent, as measured by ^{1}H NMR, to the formate in the reaction precipitate, as measured by ^{13}C NMR. [b] Calculated via ^{19}F NMR spectroscopy. [c] Error estimated as 0.1 based on the signal-to-noise of NMR resonances for low-concentration species. Errors for other products are given as the standard deviation of triplicate measurements. [d] Calculated as mols of carbon per mol of PFOA; *i.e.*, accounting for compounds that have multiple carbons integrated in the analysis.

Quantitative ^{13}C NMR spectroscopy of the precipitate accounted for almost all of the carbon-containing species generated by the PFOA degradation reaction, none of which contain C–F bonds besides trifluoroacetate ions (**Table 3.2**). The byproducts were identified as a distribution of one-carbon (carbonate, formate), two-carbon (oxalate, glycolate, trifluoroacetate), and three-carbon products (tartronate). Quantification by ^{13}C NMR spectroscopy of the precipitate and ^{1}H NMR spectroscopy of the reaction solution indicated 2.5 ± 0.3 equivalents of formate per mol of PFOA starting material (**Table 3.2**). The formate ions were independently quantified by ion chromatography and corresponded to 2.1 ± 0.2 equivalents of formate per mol of PFOA starting material (**Figure 3.4D**). There are several potential pathways for the generation of some of these carbon-containing products that are not further explored in this work. However, the formation of non-fluorinated, relatively oxidized 1–3 carbon products is generally consistent with the proposed mechanism, while accounting for all of the carbon balance of the PFOA degradation reaction.

One Carbon Products: **Carbon and Formate.** The most likely source of carbonate ions is from the initial decarboxylation step, along with other downstream processes that generate carbon dioxide or single-carbon products at the same oxidation state. Under the basic reaction conditions, the carbon dioxide reacts with excess hydroxide ions to provide sodium carbonate within the precipitate. 2.1 ± 0.3 equivalents of carbonate ions per mol of PFOA were detected by quantitative ^{13}C NMR spectroscopy. It should be noted that the carbonate ion concentration could not be independently measured by ion chromatography because available IC capabilities were run in carbonate-based buffers, precluding the detection of this ion. 2.5 ± 0.3 equivalents of formate per mol PFOA were detected, as measured by ^{1}H NMR spectroscopy of the liquid reaction mixture and ^{13}C NMR spectroscopy of the precipitate. This amount is consistent with ion chromatography of the reaction mixture and re-dissolved precipitate, which provided 2.1 ± 0.2 mols of formate per mol of PFOA. Formate formation and the varying amounts of formate produced by PFCAs of other chain lengths inspired a deeper mechanistic study (see below).

Two Carbon Products: **Trifluoroacetate, Glycolate, and Oxalate.** 0.32 ± 0.04 mols of trifluoroacetate per mol of PFOA were detected by ^{19}F NMR spectroscopy of the reaction solution at 24 h reaction time; only trace $CF_3CO_2^-$ was found in the precipitate by ^{19}F NMR spectroscopy. 0.6 ± 0.1 mols of glycolate ions per mol of PFOA were detected, some of which might be formed from the degradation of fluoroacetic acid, which was observed in low-temperature experiments (see main text). Oxalate ions were detected at concentrations corresponding to 0.7 ± 0.1 mols per mol of PFOA. The glycolate and oxalate ions were identified by ^{13}C NMR spectroscopy by comparison to authentic standards.

Three Carbon Products: We assign another carbon-containing product as sodium tartronate (0.2 ± 0.1 equiv per mol PFOA) based on its ^{13}C NMR resonance at 177 ppm, which correlates with a ^{1}H NMR resonance at 4.2 ppm **(Figure S 3.19)**. These chemical shifts match literature reports (*159*, *160*), and the correlation is consistent with an intermediate we propose in the mechanism (**Figure 3.16**). We propose that tartronate is formed in pathway D because it was observed in greater amounts in the degradation of PFBA (C = 4), likely from hydrolysis of INT8 (**Figure 3.16**).

Unidentified Product: A small amount of the PFOA carbon balance is found in an unknown product (4.9 ± 2.4 mol% C) that is likely derived from the reaction of glycolic acid with another intermediate in the pathway, as it was formed in higher concentration when glycolic acid and PFOA were subjected to the degradation conditions together. However, the unknown product did not form when glycolic acid was subjected to the degradation conditions in the absence of PFOA. The unidentified compound has two ^{13}C NMR resonances, one at 177.9 ppm and one at 69.4 ppm (**Figure 3.13**). The two resonances integrate 1:1 with each other, making it likely that it contains either two or four carbons.

Further analysis of the reaction precipitates from degrading the C = 2, 4, 5, and 6 acids (**Figure 3.13**) showed that the presence of oxalate was correlated with the presence of TFA, but it is not a direct degradation product of TFA, whose only carbon-containing degradation products were carbonate ions. The amount of oxalate appeared to increase slightly for PFCA with longer perfluoroalkyl chains, such that we speculate that it is formed, at least in part, within the B/C pathways, as are formate ions. Once the fluorocarbon intermediate is protonated, though, as in INT14 (**Figure 3.13**), it is difficult to get the correct oxidation state for oxalate except through

Cannizzaro reactivity or disproportionation, which could be possible under the extremely basic reaction conditions. We think it is likely that the oxalate either originates from a process in the B pathway preceding INT14 or from further degradation of carbonaceous byproducts.

Identifying and quantifying these carbon products has important implications for PFOA degradation: first, the high recovery of products with no C–F bonds, along with the high fluoride ion recovery, confirm that these conditions efficiently mineralize PFCAs. Furthermore, identifying multiple two- and three-carbon byproducts further implicates mechanisms more complicated than iterative one-carbon shortening processes.

PFCAs of different lengths degrade by different pathways, as indicated by the distinct patterns in their formate and $CF_3CO_2^-$ formation. If the chain-shortening DHEH mechanism were operative, we would expect that resonances belonging to chain-shortened species would appear transiently in the ^{19}F NMR spectra as longer-chain PFCAs speciated into a distribution of shorter-chain PFCAs. Instead, only ^{19}F NMR peaks corresponding to $CF_3CO_2^-$ and trace amounts of $CF_3CF_2CO_2^-$ were detected, and the following byproduct patterns emerged: PFCAs containing four or fewer carbons do not produce any $CF_3CO_2^-$, but all PFCAs containing more than four carbons produce roughly the same sub-stoichiometric amount of $CF_3CO_2^-$: approximately 0.3 equivalents of $CF_3CO_2^-$ per mol of PFCA. PFCAs containing fewer than six carbons do not produce substantial amounts of formate (See **Figure 3.4D**), but PFCAs containing six or more carbons produce increasing amounts of formate, with C = 6 and 7 producing around 1 equivalent of formate per PFCA, C = 8 around 2 equivalents, and C = 9 around 2.5 equivalents. These observations indicate that $CF_3CO_2^-$ and formate production occur by distinct pathways.

Experiments conducted at near-ambient temperatures show that decarboxylation is the rate-limiting step and subsequent defluorination and chain-shortening steps can occur at near-ambient temperature, giving experimental insight into the possible mechanism. Substantial defluorination still occurs when the isolated PFOA degradation product (perfluoro-1H-heptane **2**) is subjected to degradation conditions but heated to only 40 °C (**Table 3.1**). PFCAs have historically been decarboxylated by heating PFCA salts in ethylene glycol at 190–230 °C to give perfluoro-1H-alkanes (*161*, *162*) or by pyrolyzing PFCA salts at 210–300 °C to give perfluoro-1-alkenes (*163–165*), but dipolar aprotic solvent-assisted degradation enables decarboxylation at only 80–120 °C, which can be followed by an even lower-temperature defluorination. When **2** was subjected to the basic degradation conditions, both fluoride and chain-shortened PFCAs are observed by IC and ^{19}F NMR at short reaction times (5 minutes at 120 °C) as well as low temperatures (25 minutes at 40 °C), in contrast to reactions starting from the carboxylated PFOA at the same conditions, where no fluoride or short-chain PFCAs are formed at short reaction times or at low temperatures (**Table 3.1**). Degradation of **2** at 40 °C for 48 hours showed 57% defluorination (**Table 3.1**). Although the insolubility of the polyfluoroalkane standard in the DMSO/water solvent precluded accurate measurements of its concentration by NMR spectroscopy, the presence of the $CF_3CO_2^-$ ^{19}F NMR peak (**Figure 3.14**) indicated that the decarboxylated material likely followed a similar degradation pathway. In this low-temperature experiment, intermediates that were not observed in the higher-temperature experiments became evident; notably, at around -210 ppm, a triplet with J = 48 Hz appeared, which corresponds to the fluoroacetate ion (CH_2FCOO^-; **Figure 3.14**). The fluoroacetate peak does not appear in the higher-temperature degradations because it degrades rapidly at those temperatures, as confirmed by the degradation of a pure standard. Temperature-dependent studies

of the original PFOA degradation reaction showed that the reaction slowed slightly when the reaction was conducted at 100 °C (time to [PFOA] = 0 approximately 100 hours as compared to 16 hours for 120 °C, see **Figure 3.15, Figure S3.14–Figure S3.16**) and slowed dramatically when lowered to 80 °C (>290 hours, **Figure 3.15, Figure S3.17**). Therefore, significant defluorination of PFHp-1H was unexpected at 40 °C and suggests the steps following the decarboxylation are low-barrier or barrierless. These observations further indicate that the degradation does not proceed through successive chain-shortening via iterative decarboxylation steps.

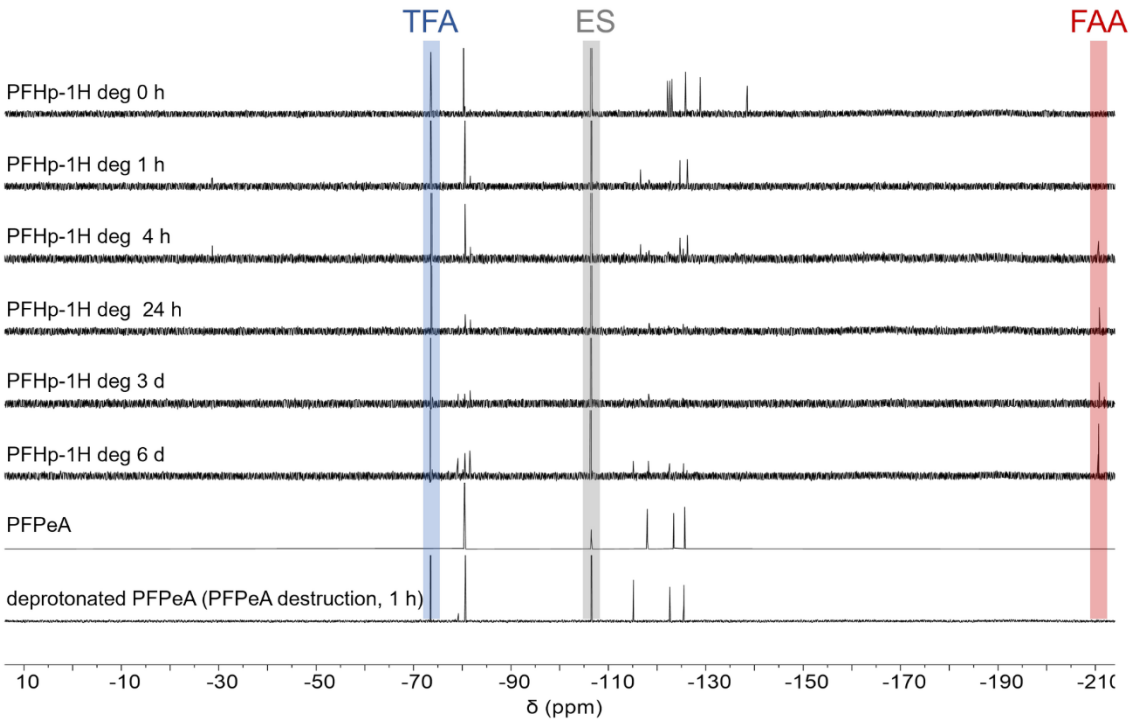

Figure 3.14. ^{19}F NMR spectra (600 MHz) of aliquots from the 40 °C degradation of PFHp-1H. When the degradation is run at this lower temperature, various fluorinated intermediates (fluoroacetic acid, INT8/9, perfluoropentanoic acid) are observed that are not seen in the spectra of degradation reactions run at higher temperatures. These intermediates are shown in greater detail below. TFA = trifluoroacetate, ES = external standard (4,4′-difluorobenzophenone), FAA = fluoroacetic acid.

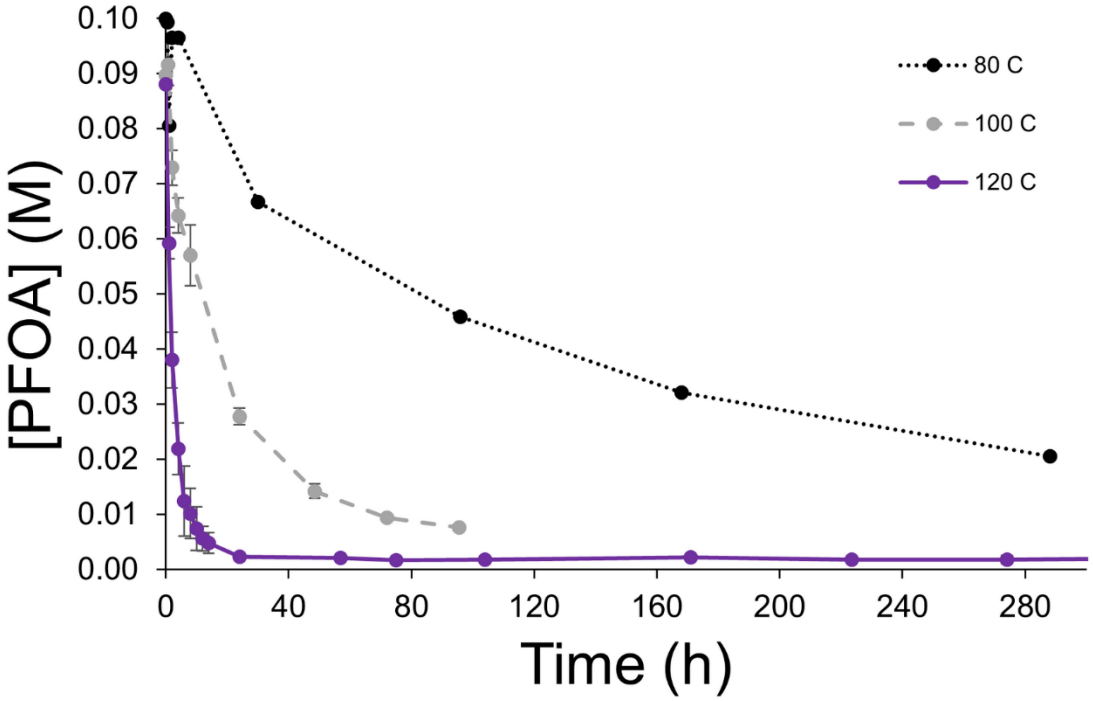

Figure 3.15. Disappearance of PFOA over time at three different reaction temperatures as measured by ^{19}F NMR. [PFOA] = 0 mmol at < 24 h at 120 °C (average of triplicates), 100 h at 100 °C (average of triplicates), and >290 h for 80 °C, showing the high temperature-dependence of the rate-limiting step.

Density functional theory (DFT) was employed to determine the mechanism of this degradation reaction. These studies predict that decarboxylation is the rate-limiting step of the degradation, and that a series of low-barrier or enthalpically barrierless reactions can lead to levels of defluorination in line with experimental observations. DFT calculations were performed at the M06-2X/6-311+G(2d,p)-SMD(DMSO) level (see Supplementary Information for details) and used PFOA as the starting point for the calculations. This mechanism should also be valid for the degradation of straight-chain PFCAs of other lengths. After the initial decarboxylation of PFOA (Compound **1**, **Figure 3.16**) at an activation energy of 27.7 kcal/mol, calculations indicate the resulting anion INT1 would eliminate a fluoride to become a perfluoroalkene INT2 (**Figure 3.16**). Unlike previous PFCA degradation mechanisms in the literature that predict the perfluoroalkyl fragment will hydroxylate after decarboxylation (*89*, *96*, *97*, *103*, *109*, *118*), these computational

results point to the formation of an alkene followed by an enthalpically barrierless hydroxylation of the activated electrophilic alkene. Hydroxylation of the anionic alkyl fragment INT1, as postulated in past literature, is calculated to have an activation energy of 29.7 kcal/mol under our study's conditions (**Figure 3.18**), while formation of the alkene INT2 has a barrier of 19.5 kcal/mol, followed by a hydroxylation with no enthalpic barrier (ΔG = -44.3 kcal/mol). The highly exothermic nature of this alkene hydroxylation step plays a leading role in driving the degradation, in line with observations that the defluorination and chain-shortening steps of the reaction neither have high energy barriers nor lead to the formation of successively shorter PFCAs. Accordingly, when perfluoro-1-heptene **3** is subjected to the degradation conditions (**Table 3.1**), it also degrades to similar products, even at 40 °C, corroborating the computational prediction and indicating that the alkene is likely on the degradation pathway. Further, calculations also suggest that the hydroxylation is specifically favored at the terminal position, as addition on the internal side of the alkene has a barrier of 8.9 kcal/mol (**Figure 3.19**). After this alkene hydroxylation (INT4), calculations suggest that a series of low/no-barrier reactions occur as shown in **Figure 3.16** and **Figure 3.17**. The enol eliminates another fluoride, forming α,β-unsaturated acyl fluoride INT6 through retro 1,4-conjugate addition.

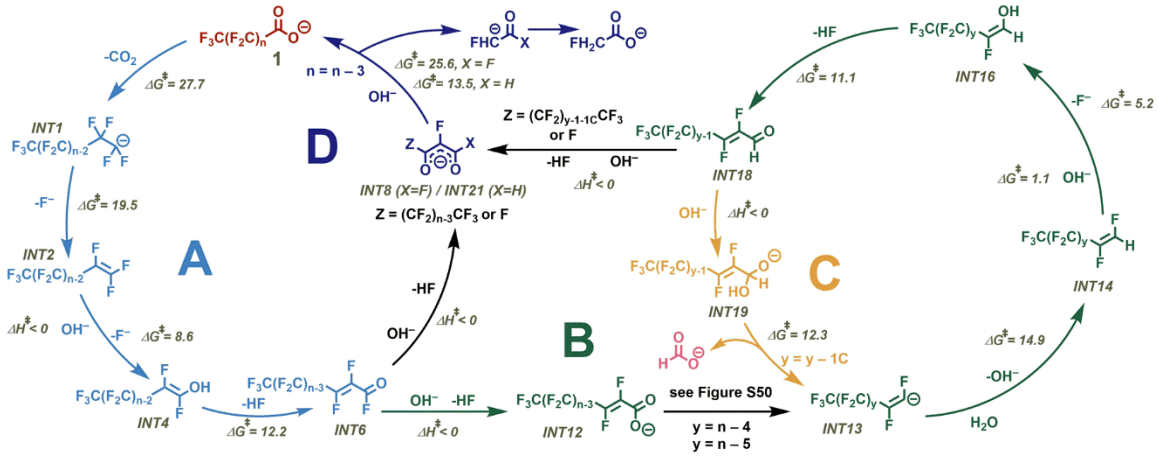

Figure 3.16. Proposed mechanism for PFCA degradation mechanism, with activation energies **energies ($\Delta G^{\ddagger}$, kcal/mol) for each step as calculated at the M06-2X/6-311+G(2d,p)-SMD(DMSO) level.** Cycle AD shows a three-carbon shortening of the original perfluorocarboxylic acid of n carbons ("1," red, top) with one carbon lost as CO_2 (converted to CO_3^{2-} under basic conditions) and two carbons lost to fluoroacetic acid, which readily degrades under these reaction conditions. Pathway B shows the reaction that results from the 1,2 addition of hydroxide to the carboxyl carbon of INT6. Proposed pathways for the conversion of INT12 to INT13, along with pathways for non-fluorinated, carbon-containing byproducts, are described in **Figure 3.22**. The alkene INT13 becomes protonated and proceeds through a similar pathway to Pathway A. At INT18, the aldehyde analogue of acid fluoride INT6, 1,2 addition to the carboxyl carbon leads to the formation of formate via elimination in Pathway C, whereas 1,4 addition to the β carbon leads back to Pathway D. All energies expressed in units of kcal/mol.

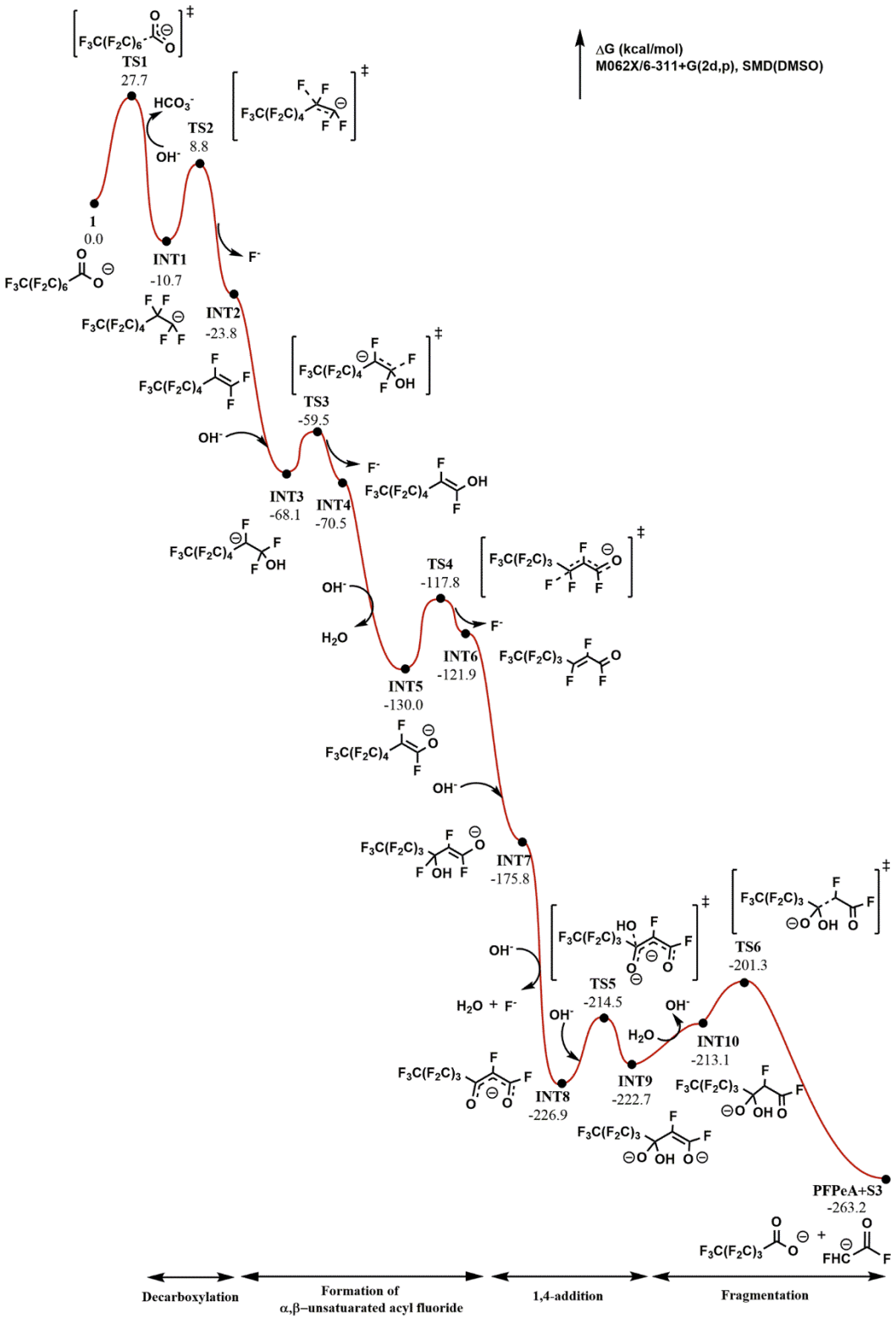

Figure 3.17. Gibbs free energy profile for pathways A and D, X = F. Decarboxylation is the rate-determining step of thermolysis with an energy barrier of 27.7 kcal/mol. This is also consistent with the experimental conditions that decarboxylation requires 120 °C to initiate.

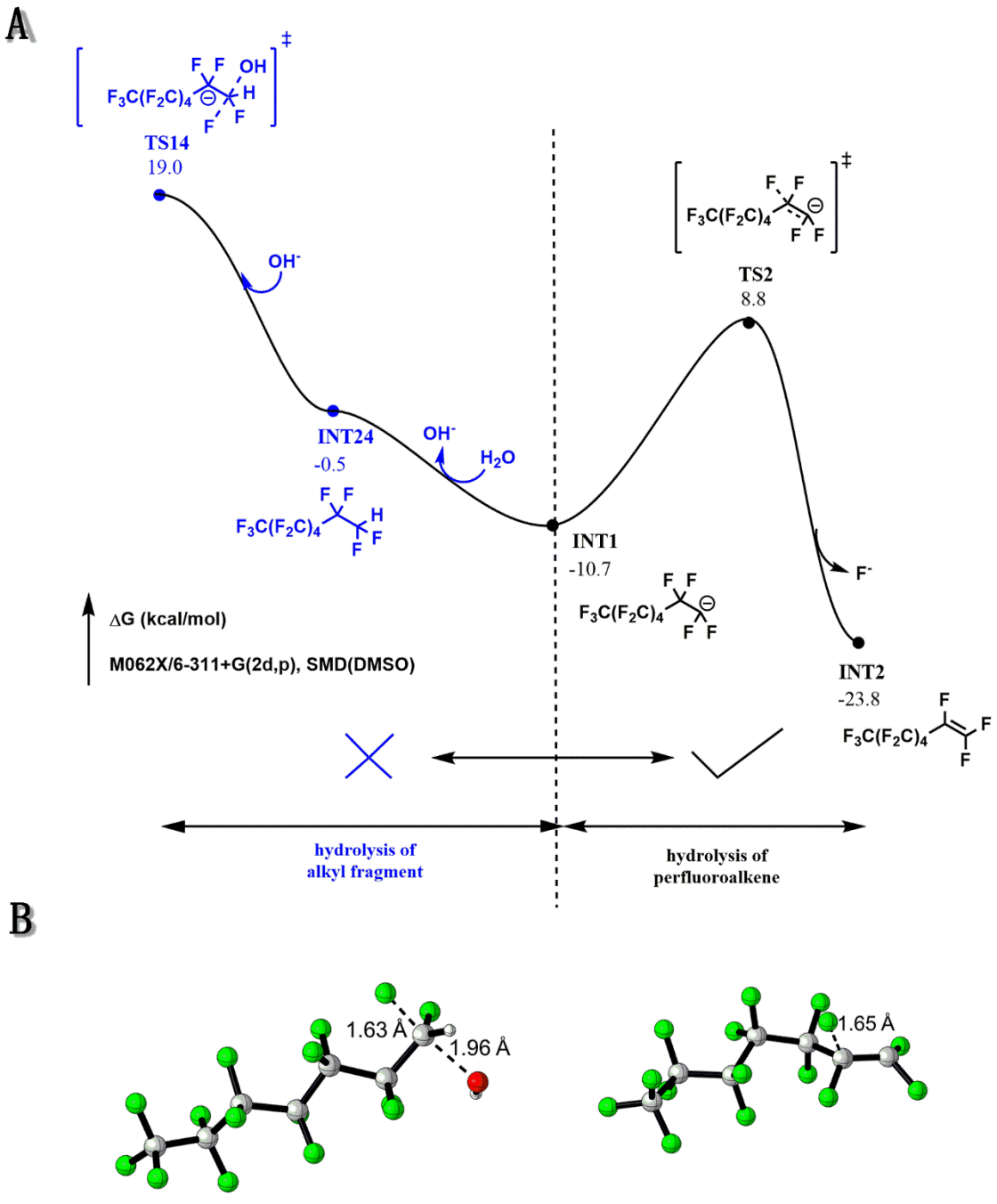

Figure 3.18. Perfluoroanion INT1 can eliminate a fluoride to become a perfluoroalkene INT2 or be protonated by water to become a polyfluoroalkane. Since S_N2 reactions on saturated fluoroalkane carbons require a high energy barrier, INT1 is more likely to generate perfluoroalkene INT2. A) Comparison of β-elimination and protonation of INT1. An S_N2 reaction on a saturated fluoroalkane carbon requires a high energy barrier (29.7 kcal/mol). B) 3D Structures of TS14 and TS2.

The resulting alkene INT2 is easily hydrolyzed; our calculations also suggest that the hydroxylation is specifically favored at the terminal position, As shown in **Figure 3.19**, the relaxed-scan addition energy profiles on the internal side and the terminal side show that the addition on the internal side of the alkene has a barrier of 8.9 kcal/mol, whereas addition on the terminal side does not have an enthalpic barrier.

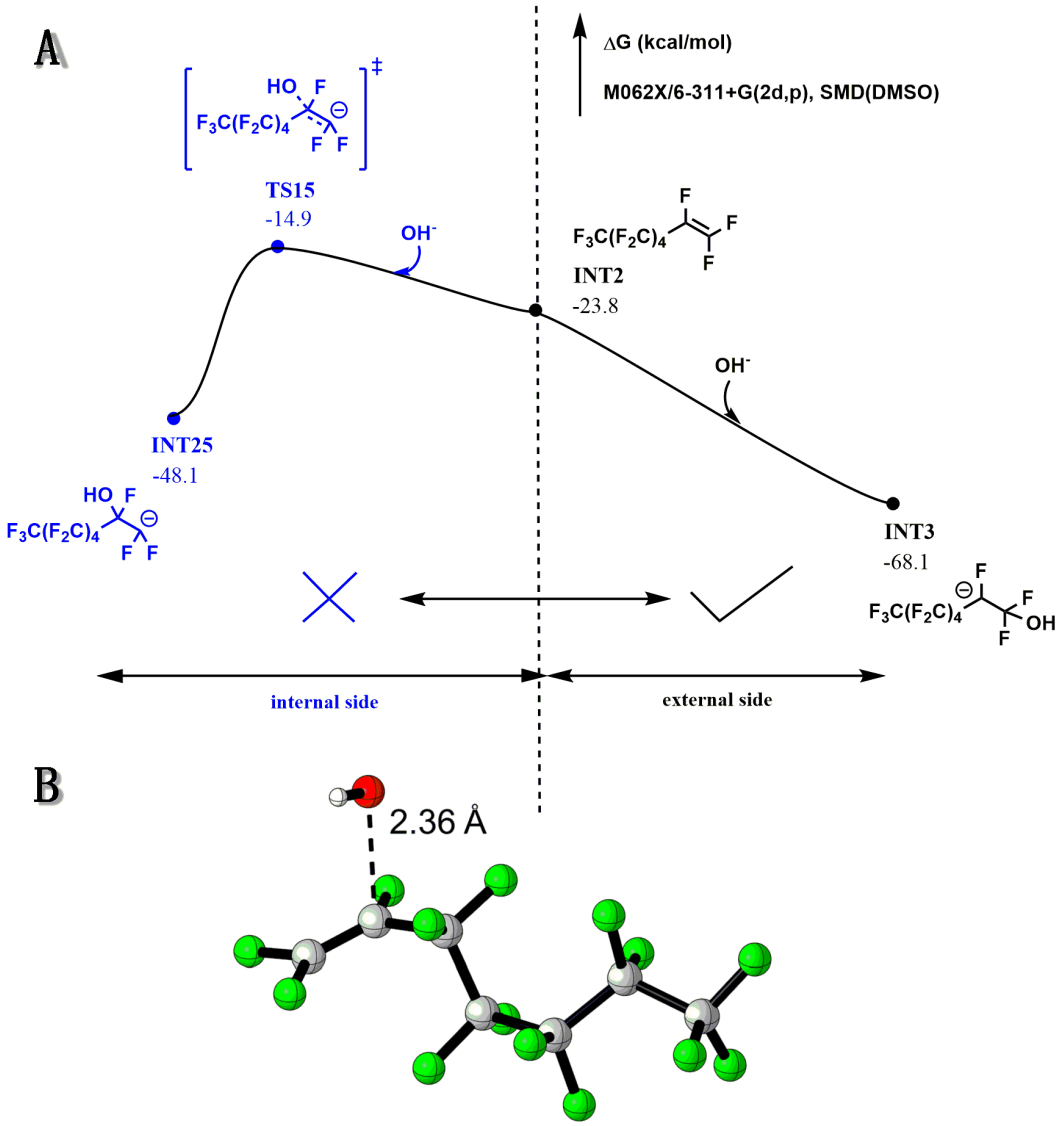

Figure 3.19. Alkene INT2 is easily hydrolyzed; our calculations also suggest that the hydroxylation is specifically favored at the terminal position. The relaxed-scan addition energy profiles on the internal side and the terminal side show that the addition on the internal side of the alkene has a barrier of 8.9 kcal/mol, whereas addition on the terminal side does not have an enthalpic barrier. A) Comparison of hydroxide addition on the internal side and the external side of the alkene. While hydroxide addition on the terminal side has a inflection point, addition on the internal side has no enthalpic barrier. B) 3D structure of TS15.

This resulting α,β-unsaturated acid fluoride INT6 has two plausible reaction pathways that are consistent with the experimental findings: a 1,4-conjugate addition that leads to $CF_3CO_2^-$ formation (**pathway D**) or a 1,2 addition (**pathway B**) that can lead to formate formation (**pathway C**), which together explain the experimentally observed byproduct distribution. Calculations indicate these two options both have no enthalpic barriers and thus very low free energies of activation, indicating that both reactions occur to some extent (**Figure 3.20**). In the enthalpically barrierless 1,4-conjugate addition (**Figure 3.16, pathway D, X = F**) that leads to the formation of shorter PFCAs such as $CF_3CO_2^-$, the hydroxide adds to the β carbon of α,β-unsaturated acyl fluoride INT6, followed by an enthalpically barrierless fluoride elimination to form 1,3-diketone compound INT8. Hydroxide again adds to this intermediate on the ketone carbonyl side to generate INT9, which is more favorable than the addition on the acyl fluoride side (**Figure 3.21**). Finally, fragmentation occurs to generate an equivalent of perfluorocarboxylic acid three carbons shorter than the initial carboxylic acid and an equivalent of fluoroacetic acid, which was observed in the experiments conducted at 40 °C (**Figure 3.14, Figure S 3.10**). As an example, if five-carbon PFCA perfluoropentanoic acid (PFPeA) went through this cycle, it would produce an equivalent of carbon dioxide (1 carbon), an equivalent of trifluoroacetic acid (2 carbons), and an equivalent of fluoroacetic acid (2 carbons) by this pathway. However, from the experimental results, only about 0.3 equiv of $CF_3CO_2^-$ are produced from PFPeA (**Figure 3.4D**), indicating the PFCA degradation does not proceed quantitatively by this process. This pathway also does not account for the substantial amounts of formate produced in reactions from longer PFCAs.

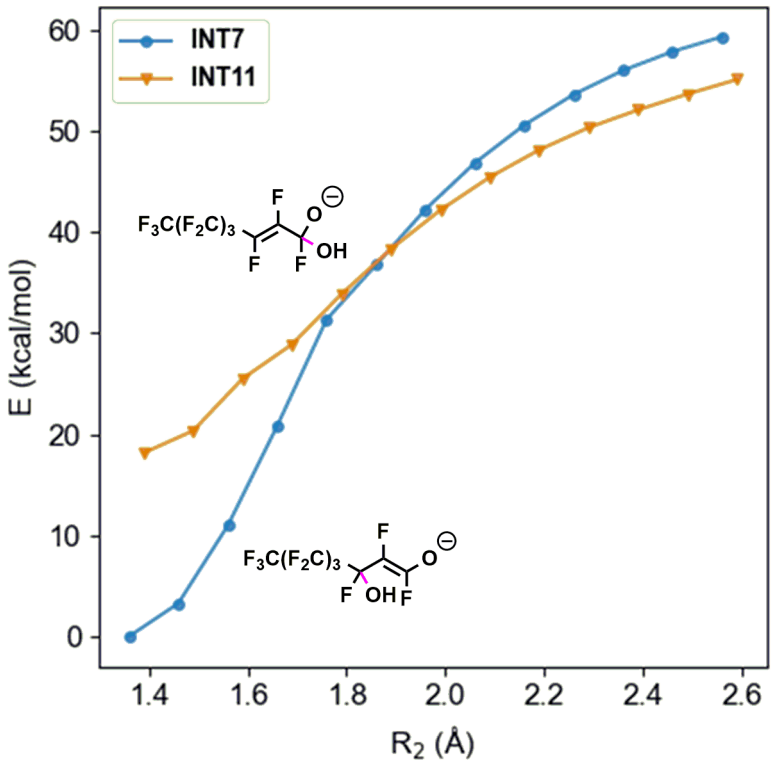

Figure 3.20. The scanning coordinates of the carbon–oxygen bonds of INT7 and INT11. After the formation of hydroxylated perfluoroanion INT3, two consecutive fluoride ion eliminations produce α,β-unsaturated acyl fluoride INT6. When gradually increasing the carbon–oxygen bond length, the energy does not have an inflection point but continuously rises, indicating that 1,2-addition and 1,4-addition both do not have enthalpic barriers.

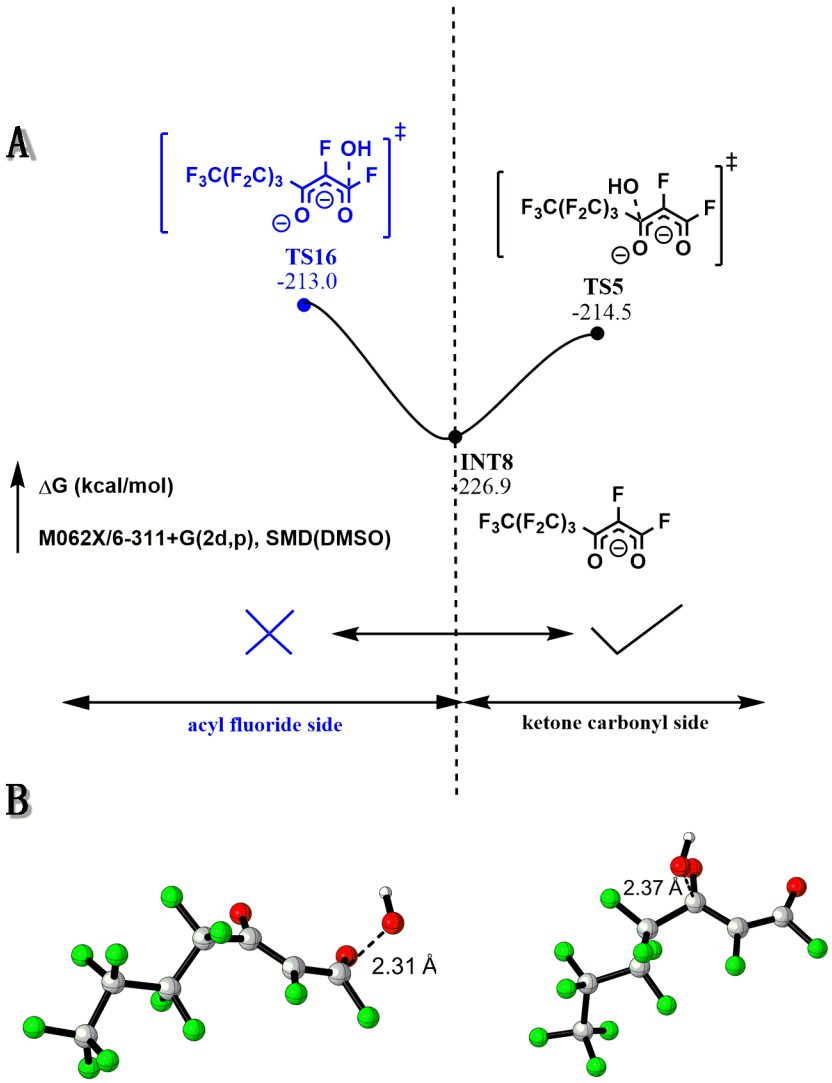

Figure 3.21. 1,4-addition produces 1,3-diketone compound INT8. Subsequent hydroxide addition is favored to occur on the ketone carboxyl side of INT8 rather than the acyl fluoride side. A) Comparison of hydroxide addition on the acyl fluoride side and the ketone carbonyl side of INT8. B) 3D structures of TS16 and TS5.

Formate ion production is explained via a pathway stemming from the favorable 1,2-hydroxylation product, which provides an α,β unsaturated perfluorocarboxylic acid (**pathway B**). As with INT6, there are multiple possible sites for hydroxide addition to INT12, either to the α (13.6 kcal/mol) or β (12.0 kcal/mol) carbons. Possible pathways propagating from both of these processes, along with the formation of oxalate and other carbon byproducts, are described below.

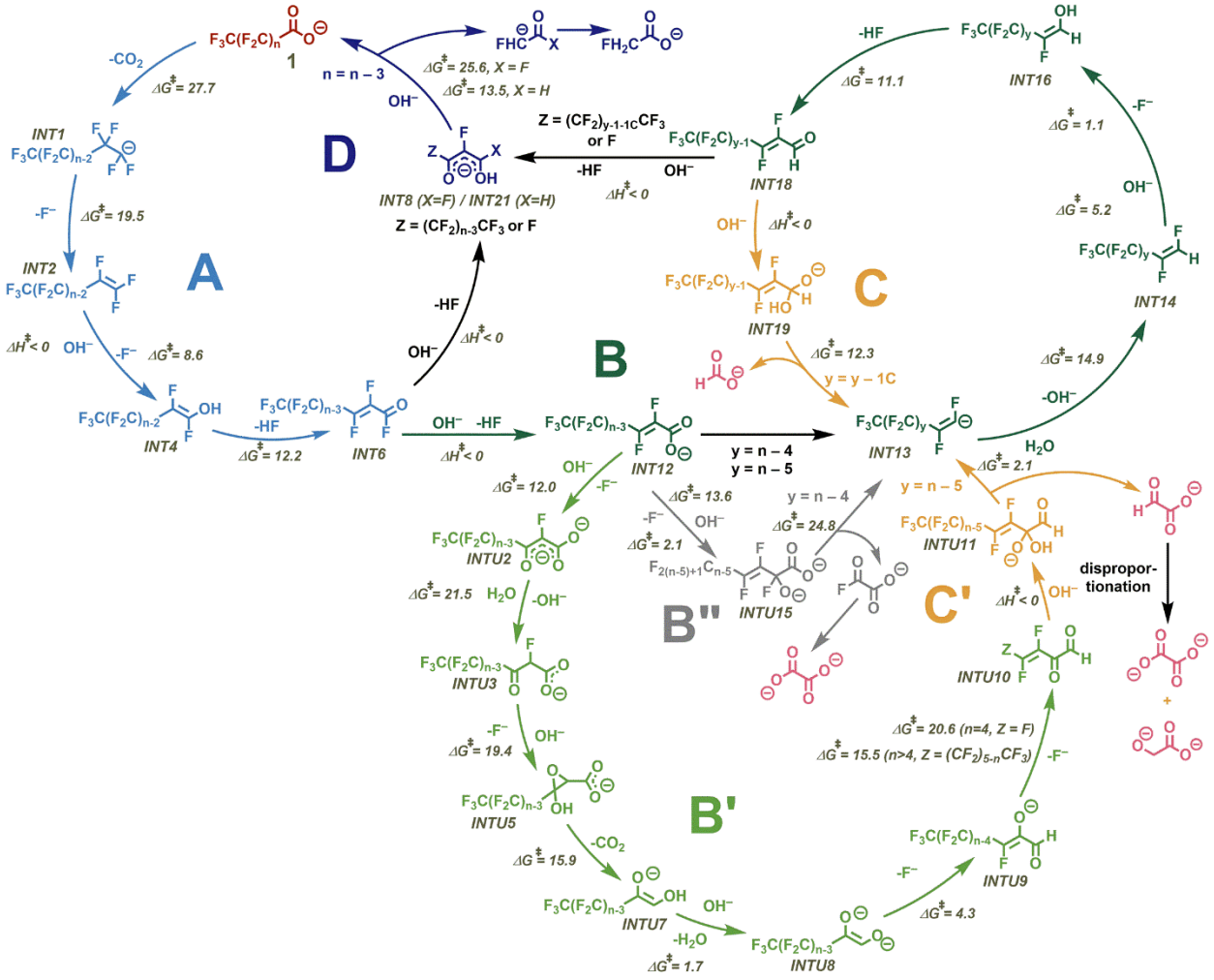

Figure 3.22. Proposed pathways for converting INT12 to INT13 and forming carbon byproducts.

We propose two possible pathways for the transformation of INT12 to INT13 (**Figure 3.22**). In Pathway B″ (**Figure 3.23**), hydroxide addition to the alpha carbon allows an acid fluoride equivalent of oxalate to be generated, eliminating a fluoroalkene anion five carbons in length (for PFOA; generalized to other PFCAs, the alkene is three carbons shorter than the original PFCA length) with a barrier of 24.8 kcal/mol.

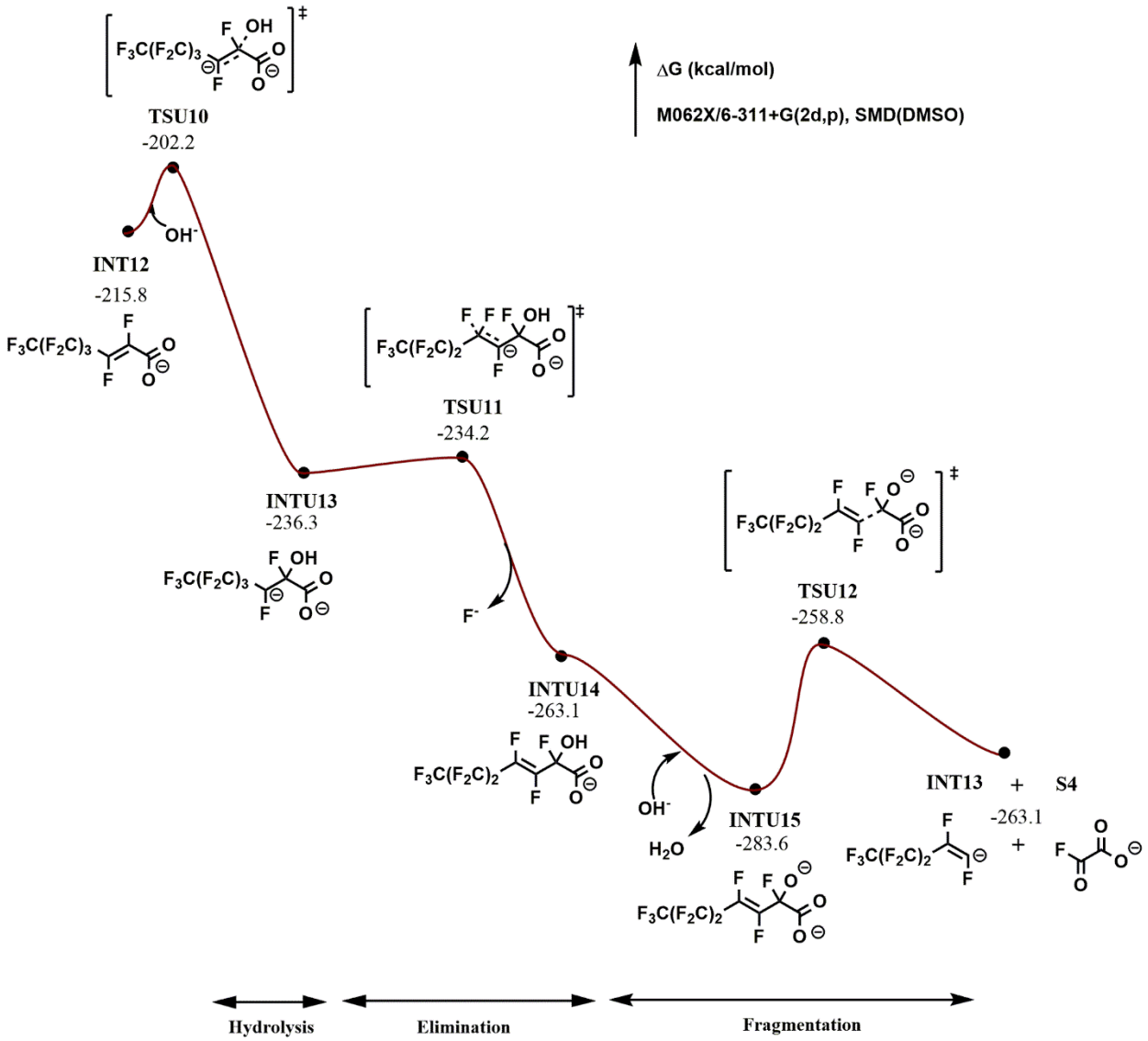

Figure 3.23. Gibbs free energy profile for pathway B″.

In Pathway B′ (**Figure 3.24, Figure 3.25**), 1,4 addition of the hydroxide to INT12 leads to a Darzens-type decarboxylation through an epoxide intermediate INTU5 via TSU2 with a barrier of 19.4 kcal/mol. Interestingly, though carbonate INTU4 has a similar structure to acid fluoride INT9, they have different reactivity (**Figure 3.26**). INT9 tends to fragment, while INTU4 tends to form the epoxide because it cannot form a dianion through fragmentation. For longer PFCAs (original PFCA C > 6), the unsaturated aldehyde intermediate can eliminate a fluoride and pass

through a Pathway C-like process (Pathway C′, **Figure 3.25**) where hydroxide adds to the carbonyl and eliminates off an alkene four carbons shorter than the original PFCA (for PFOA, four carbons in length) and an equivalent of glyoxylate, which can disproportionate into an equivalent of oxalate and an equivalent of glycolate.

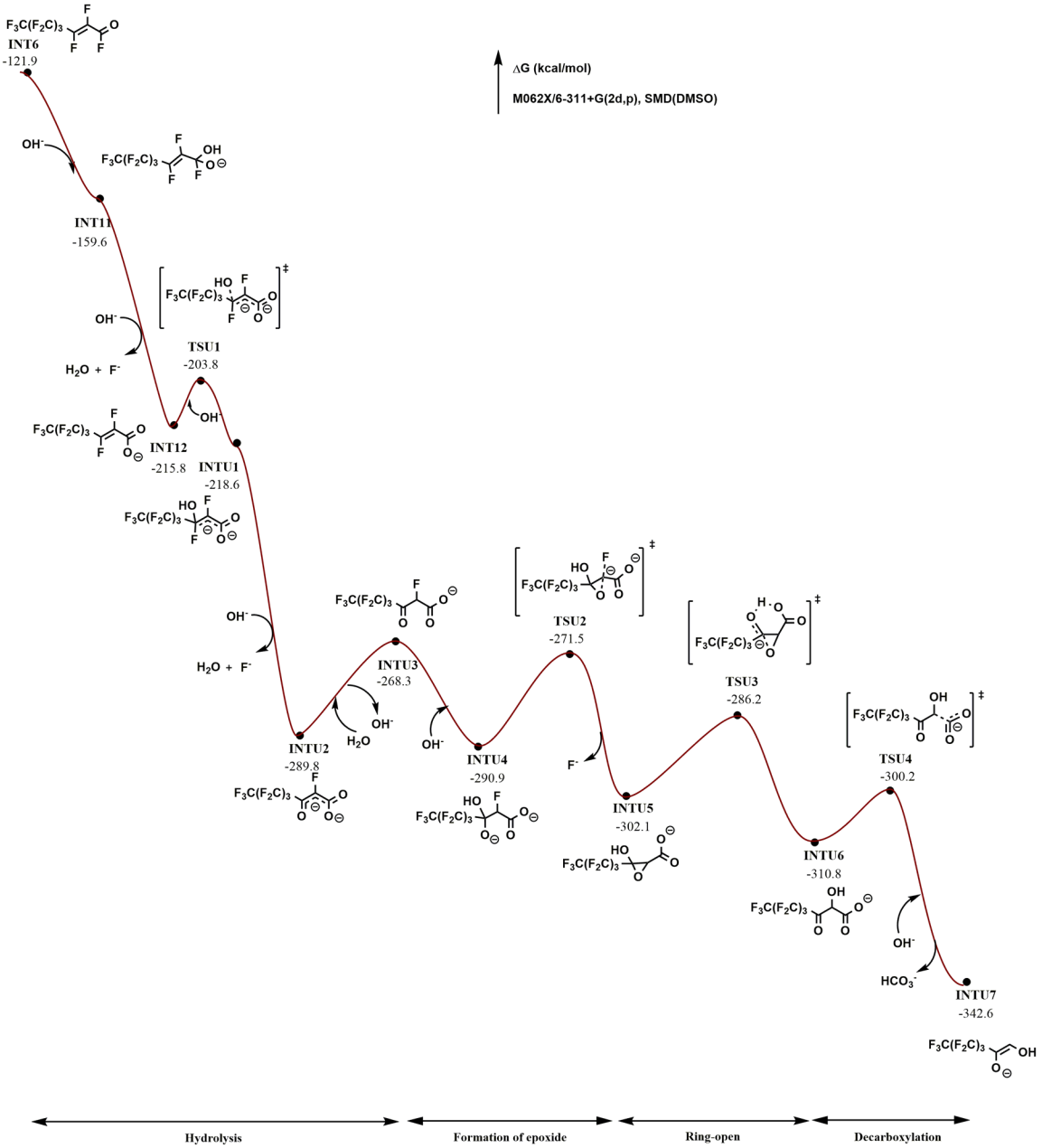

Figure 3.24. Gibbs free energy profile for pathway B′ (I), ending with decarboxylation.

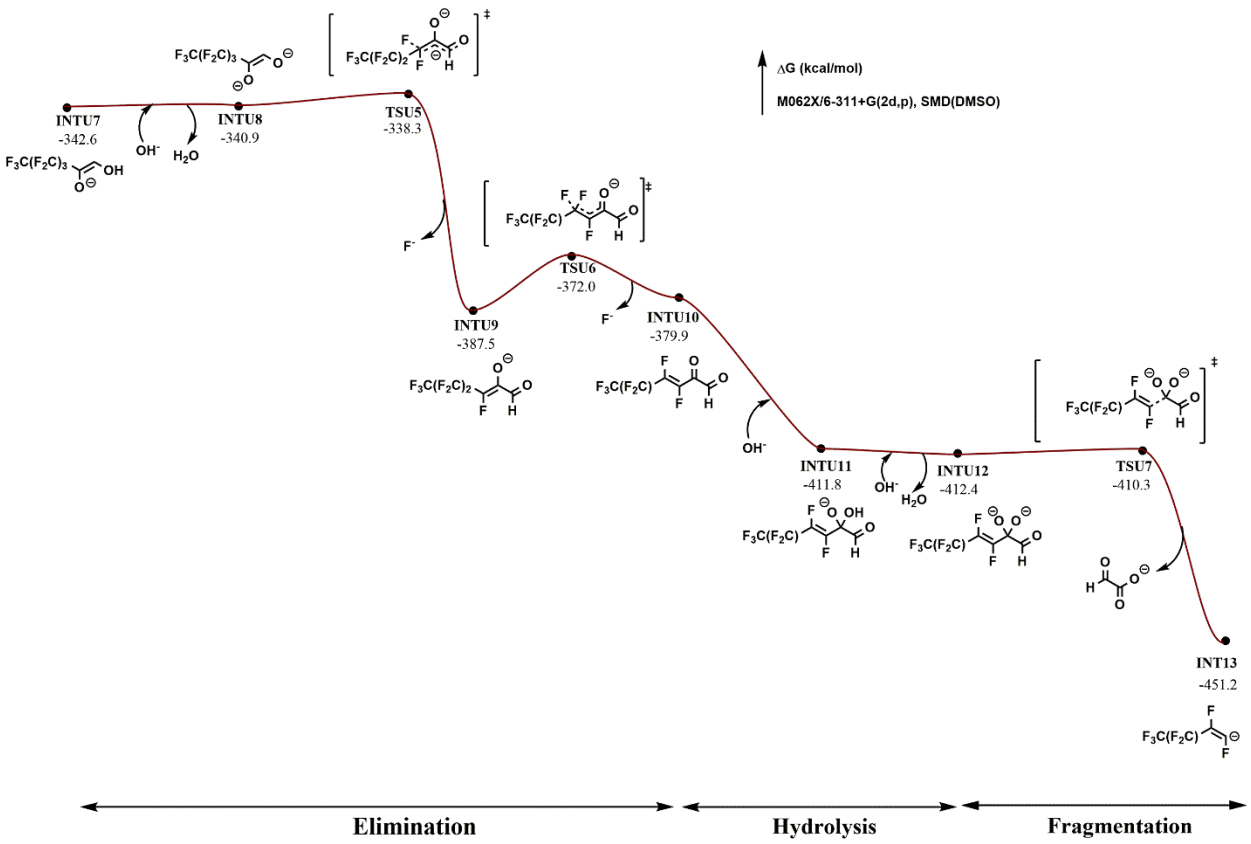

Figure 3.25. Gibbs free energy profile for pathways B′ (II) + pathway C′.

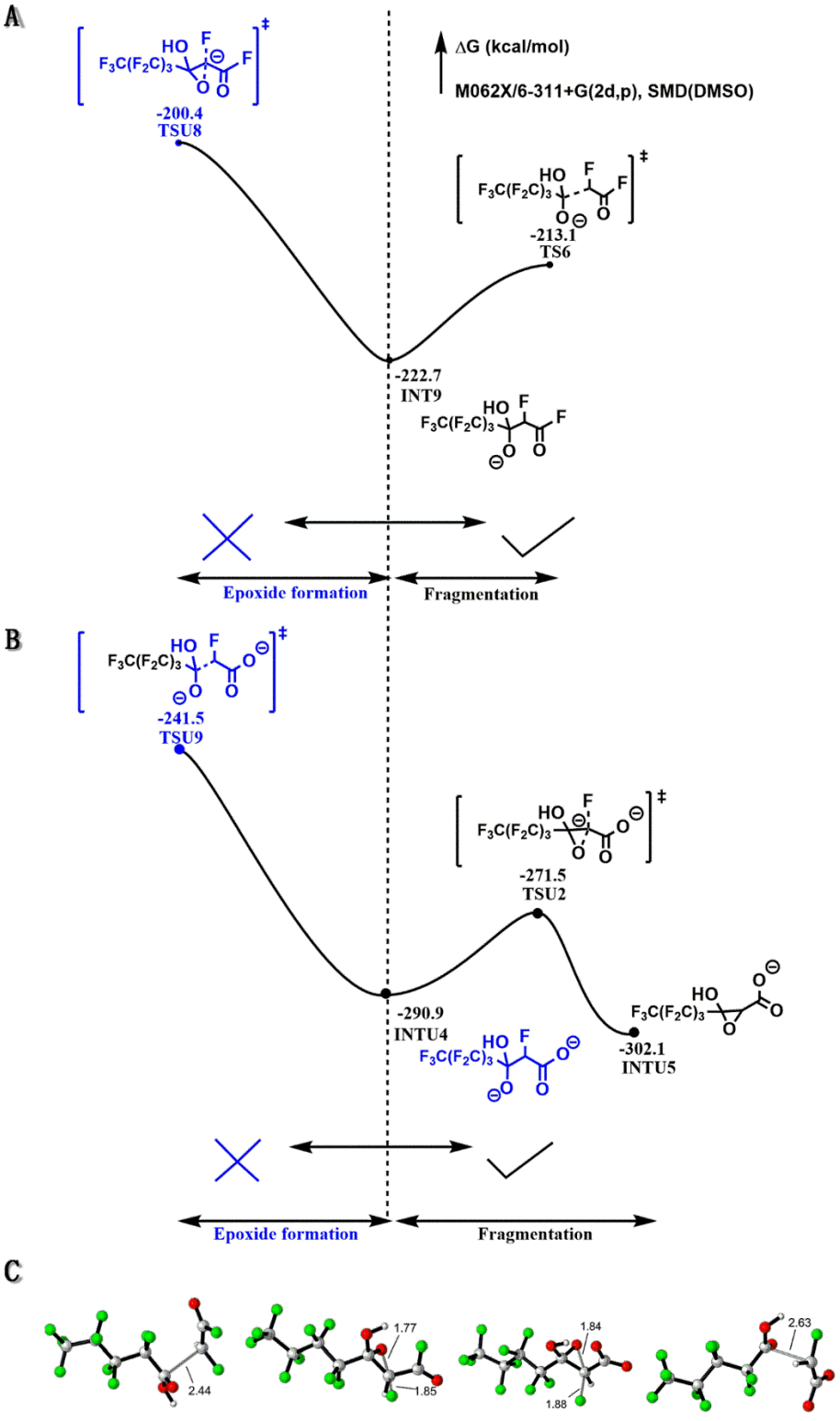

Figure 3.26. A) Comparison of epoxide formation and the fragmentation of INT9 (acid fluoride). B) Comparison of epoxide formation and the fragmentation of INTU4 (carbonate). C) 3D structures of TS6, TSU8, TSU2, TSU9.

While both of these pathways for the conversion of INT12 to INT13 are plausible and supported by computation, the possibility of other active mechanisms cannot be ruled out. The mechanisms explicitly proposed in **Figure 3.22** and its supporting figures show many classes of reactivity at the possible bifurcation points. For example, the C and C′ reactivity modes are the same, even though the resulting byproducts are different; similarly, pathway D-type retro-aldol reactions could occur at other 1,3-dicarbonyl intermediates to create a PFCA + carboxylic acid byproduct equivalent. We expect that the reactivity motifs we have explored through computation may be active at intermediates in the mechanism other than what we have explicitly shown.

However, both of these hydroxylations are more favorable than decarboxylating the α,β unsaturated perfluoroacid (22.3 kcal/mol) and both lead to the formation of perfluoroalkene anion INT13. The chain length of the alkene depends on which hydroxylation pathway the substrate follows, either four carbons shorter than the original chain (1,3-addition, Pathway B″) or five carbons shorter than the original chain (1,4-addition, Pathways B′ and C′). Calculations show that perfluoroalkene anion INT13 is protonated rather than eliminating a fluoride to generate the alkyne and that the hydroxide addition is more likely to happen on the terminal side as it was for the fully fluorinated analogue INT2 (**Figure 3.27, Figure 3.28**). After the protonation, hydroxide adds to the alkene, much like the first post-decarboxylation step in the first proposed pathway. Likewise, α,β-unsaturated aldehyde INT18, an analogue to the α,β-unsaturated acid fluoride INT6, is generated through retro-1,4-addition. The protonation of the alkene likely has a reduced barrier due to solvent effects (**Figure 3.29**).

After generating INT18, the intermediate again faces a bifurcation, with opportunities for both the 1,4-conjugate addition and the 1,2-addition of the hydroxide to the α,β-unsaturated

aldehyde. Similar to the addition to the α,β-unsaturated acyl fluoride, both of these reactions are calculated to have no enthalpic barrier (**Figure 3.30**). However, if INT18 undergoes 1,2-addition of hydroxide to the α,β-unsaturated aldehyde (**Figure 3.16, pathway C; Figure 3.27, Figure 3.32**), the resulting aldehyde (INT19) cannot eliminate a hydride, whereas its acid fluoride counterpart INT10 can eliminate a fluoride. Instead, INT19 can eliminate the entire perfluoroalkyl chain, creating an equivalent of formate and a one-carbon-shorter alkene anion that can either exit the cycle via 1,4-conjugate addition or proceed through the cycle again to form more formate, thus giving rise to the trend of increased formate formation by PFCAs of longer chain length.

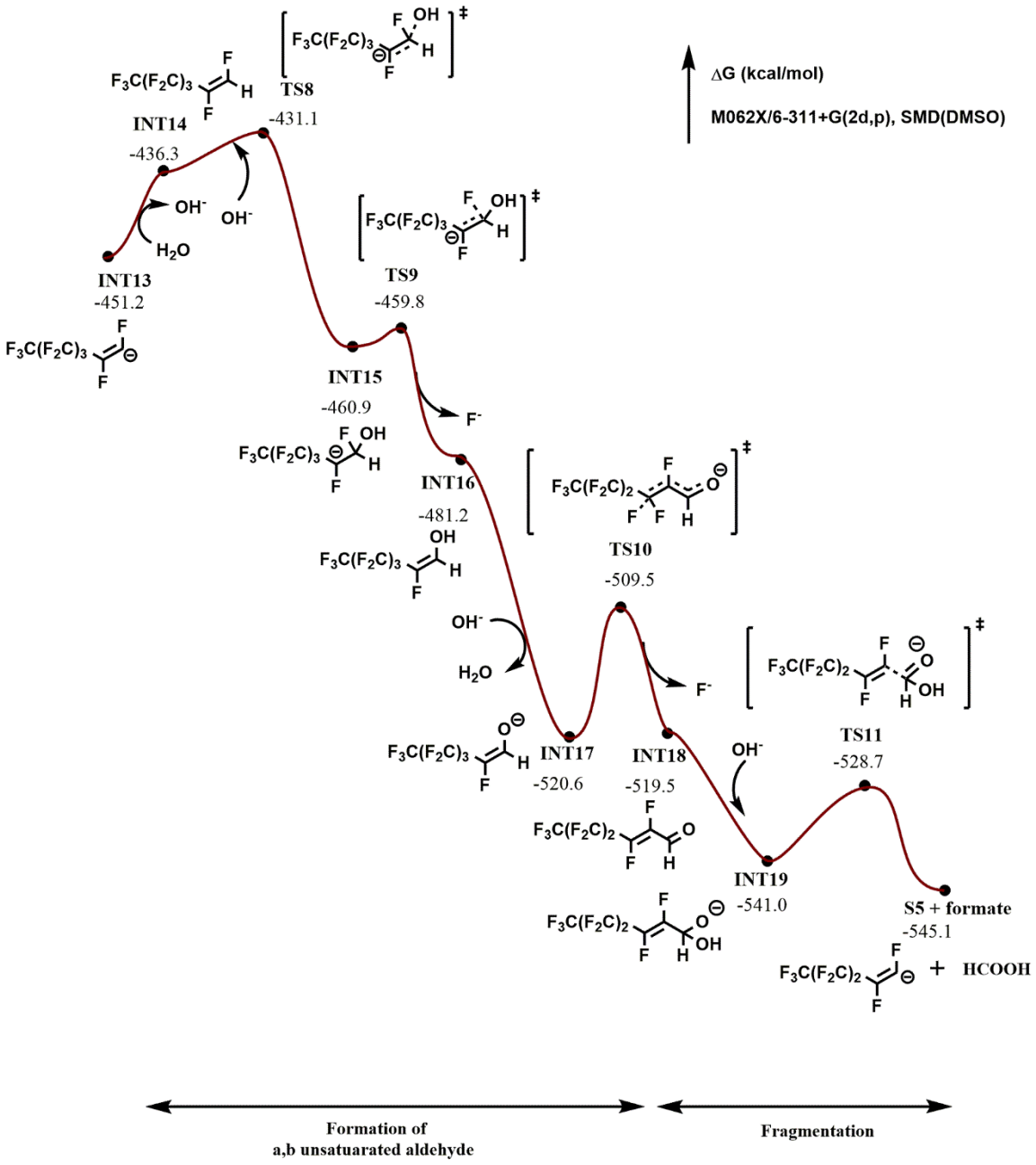

Figure 3.27. Gibbs free energy profile for pathway C.

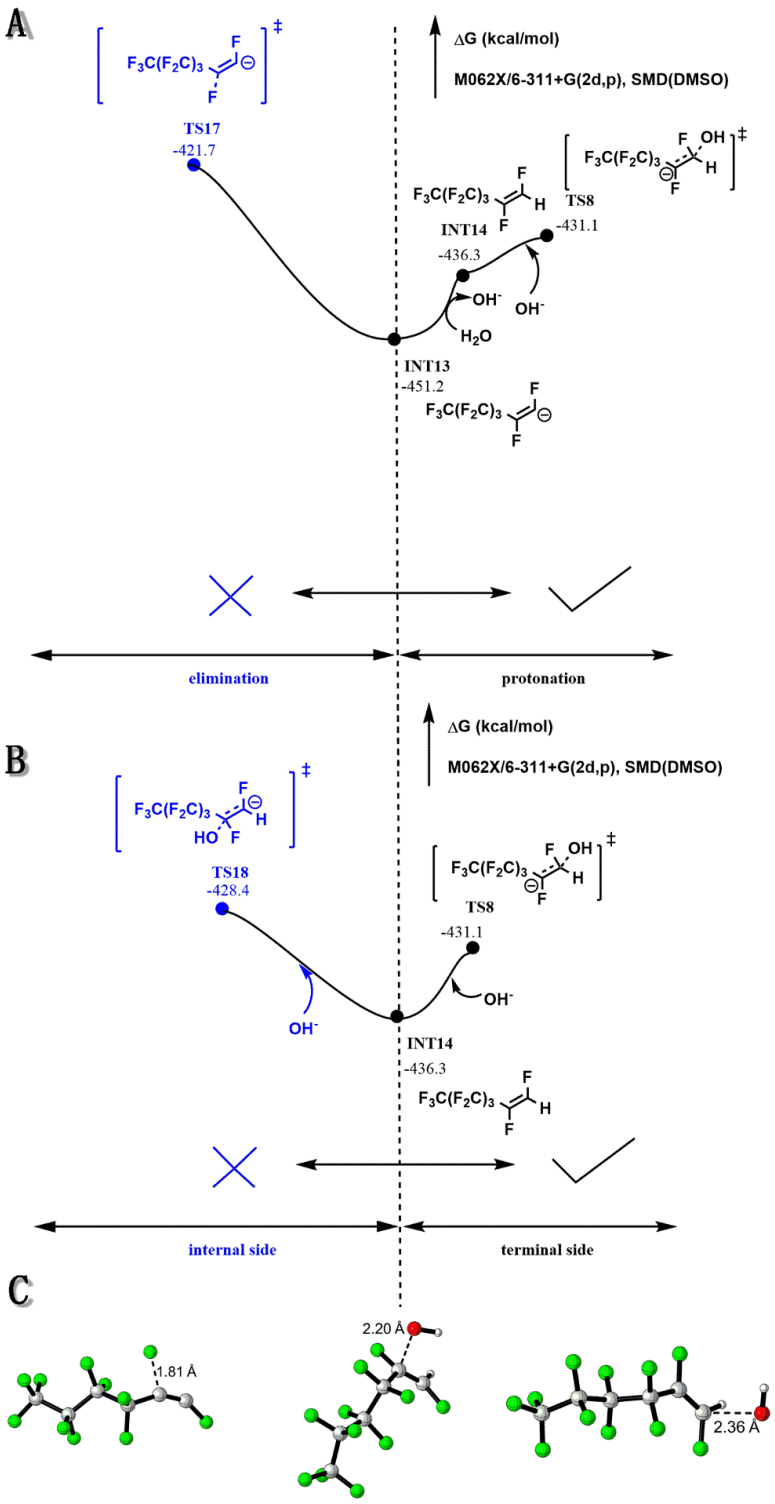

Figure 3.28. A) Comparison of β-elimination and protonation of INT13. B) Comparison of hydroxide addition on the internal side and the terminal side. C) 3D structures of TS17, TS18 and TS8.

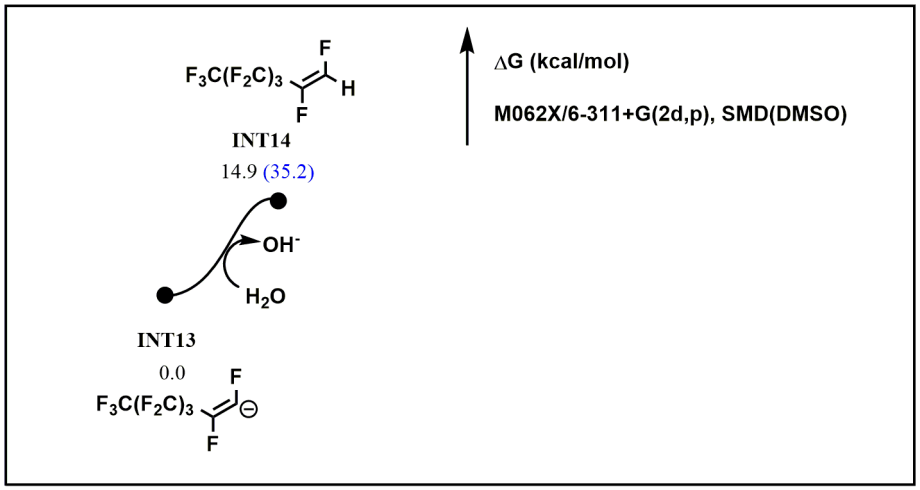

Figure 3.29. Comparison of protonation in solvent and in gas phase (energy in the blue parentheses).

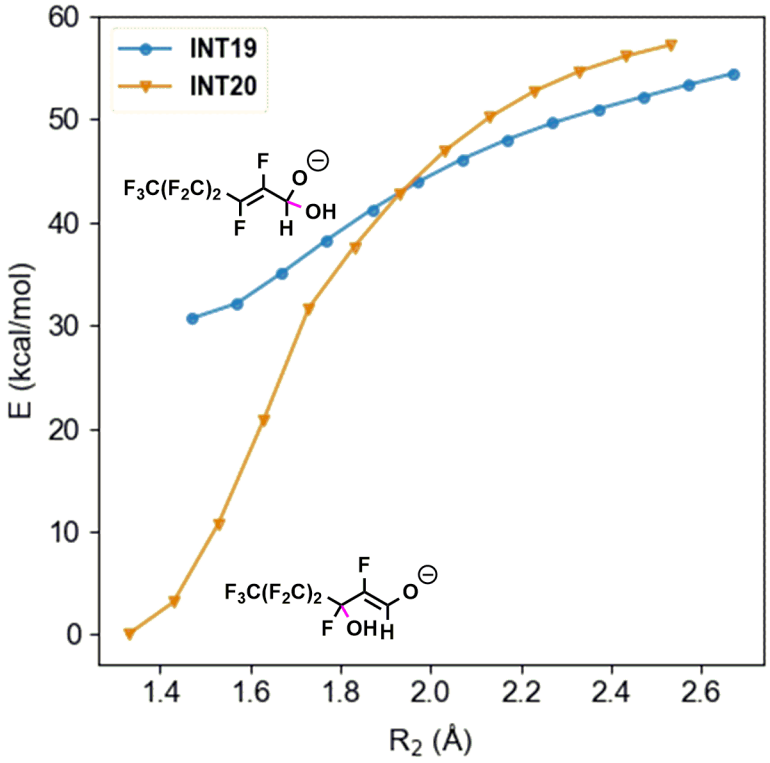

Figure 3.30. Two consecutive eliminations of fluoride ions from INT14 generates α,β-unsaturated aldehyde INT18, an analogue to the α,β-unsaturated acid fluoride INT6. The scanning coordinates of the carbon–oxygen bonds of INT19 and INT20 show that neither 1,2-addition nor 1,4-addition to INT18 has enthalpic barriers.

Through the 1,4-conjugate addition (**Figure 3.16, pathway D, X = H; Figure 3.31, Figure 3.32**), the 1,3-diketone compound generated will be attacked by hydroxide, followed by the same fragmentation as noted before. That is, a perfluorocarboxylic acid and a fluoroacetic aldehyde are formed, the latter of which can be transformed into fluoroacetic acid or be rapidly hydrolyzed.

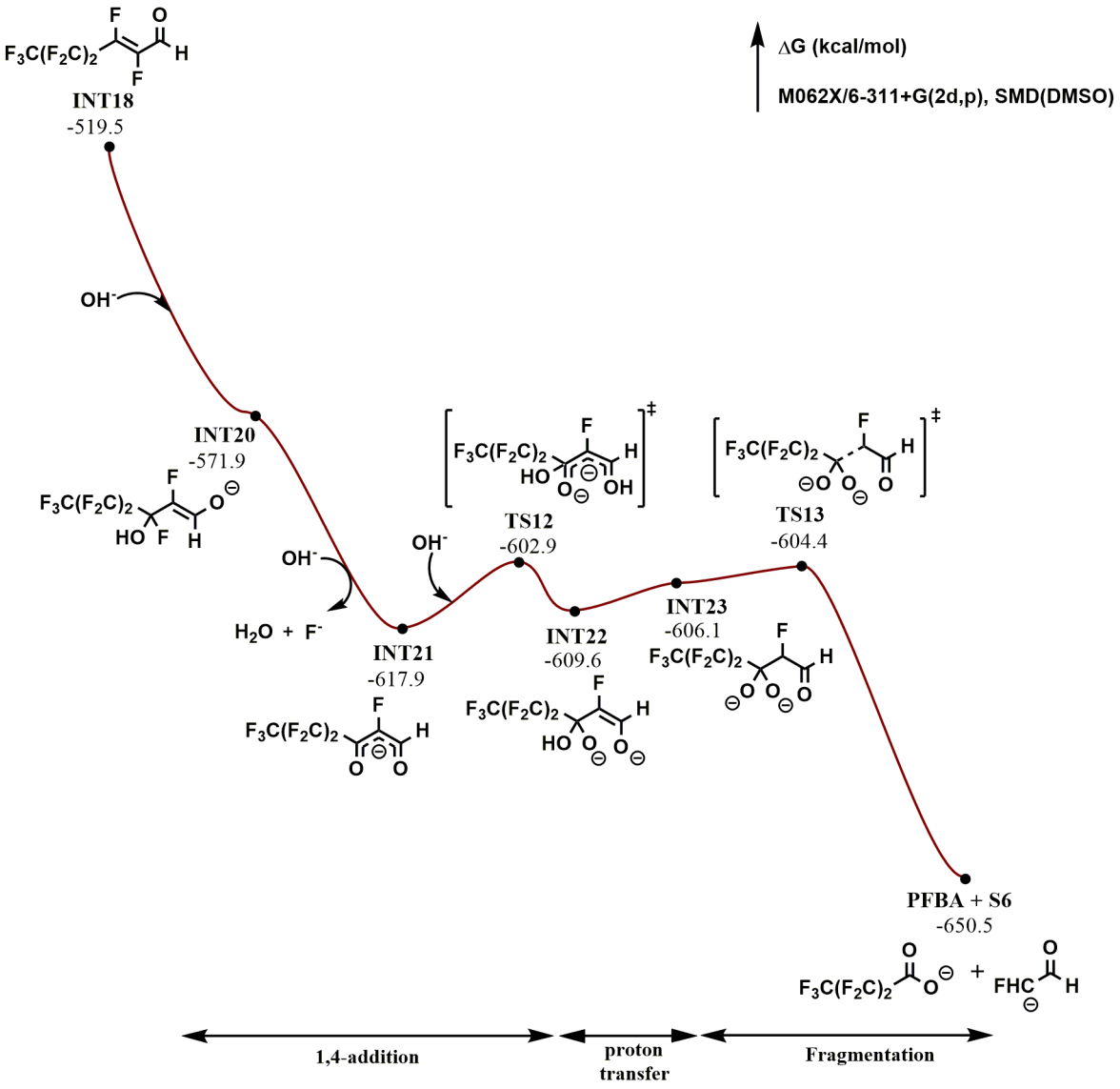

Figure 3.31. Gibbs free energy profile for pathway D, X=H.

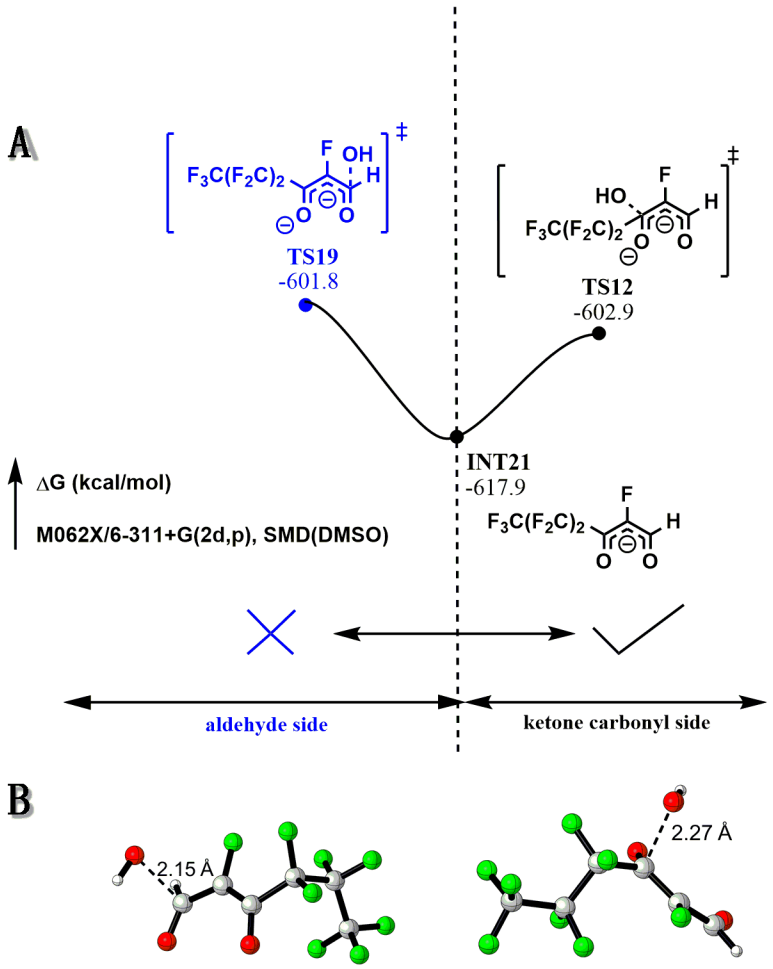

Figure 3.32. As with analogue INT8, hydroxide addition is more favorable on the ketone carboxyl side of 1,3-diketone compound INT21. A) Comparison of hydroxide addition on the aldehyde side and the ketone carbonyl side of INT21. B) 3D structures of TS19 and TS12.

The mechanisms proposed above are consistent with several experimental observations. The calculations affirm that decarboxylation is the rate-determining step of the degradation, and the calculated activation energy of 27.7 kcal/mol is consistent with the experimentally determined value of 30.0 kcal/mol (see chapter appendix). This proposed mechanism is also supported by experimental observations of $CF_3CO_2^-$ and formate distribution from **Figure 3.4D**. By this mechanism, $CF_3CO_2^-$ is produced as a non-stoichiometric byproduct, in accordance with the observation that only approximately 0.3–0.4 equivalents of $CF_3CO_2^-$ are formed per mol of PFCA

for all PFCA with C ≥ 5. This proposed mechanism also explains why four-carbon PFBA does not produce $CF_3CO_2^-$ while the five-carbon PFPeA does, as PFBA that has gone through cycle AD would create $FCOO^-$ that will decompose spontaneously to hydrogen carbonate and fluoride (*166*) or would hydrolyze from INT8 to form tartronate. This two-cycle mechanism also explains why five-carbon PFPeA produces $CF_3CO_2^-$ but no formate, as the carbon chain is not long enough to go through pathway C. The mechanism predicts the amount of formate will increase as the length of the initial PFCA carbon chain increases; this has also been affirmed by experimental results for PFCAs of 6–9 carbons (**Figure 3.4D**). The formation of carbonaceous byproducts such as oxalate, glycolate, and tartronate are also consistent with this mechanism (**Figure 3.22–Figure 3.26**). Furthermore, when conducting reactions with protodecarboxylated perfluoro-1H-heptane **2** or perfluoro-1H-hexane **S1** (**Figure S3.5–Figure S3.8**) at 40 °C, the formation of intermediate products containing five- or four-carbon fluorous chains is observed (**Figure 3.33, Figure 3.35**), respectively, which likely correspond to INT8/INT9 (**Figure 3.34, Figure 3.36**), the intermediate with the highest activation energy (25.6 kcal/mol) in this pathway. The peaks corresponding to this intermediate disappear as peaks corresponding to the five- and four-carbon PFCAs appear. These PFCAs that are shortened by three carbons are logical products of a single pathway AD cycle from their respective starting materials.

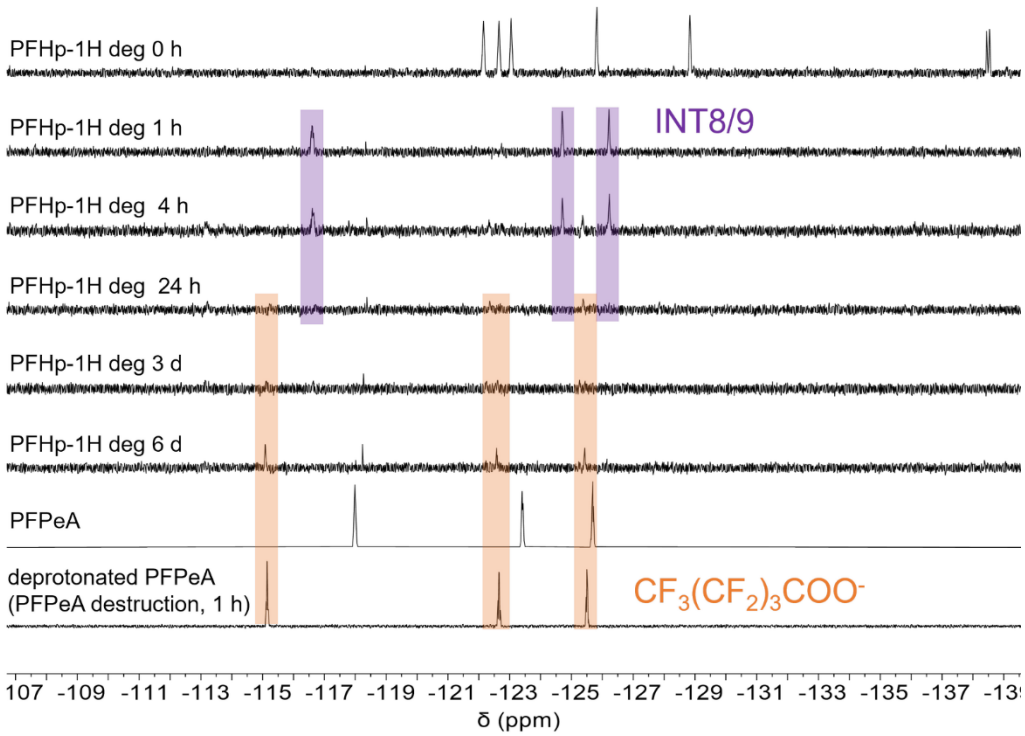

Figure 3.33. Partial ^{19}F NMR spectra (600 MHz) of the 40 °C degradation of **2**. In the first few hours of reaction, an intermediate with 3 CF_2 groups is observed (purple). We hypothesize that this intermediate is INT8/9; see **Figure 3.34** for further assignment of these peaks. In spectra obtained at 24 h, 77 h, and 142 h, resonances corresponding to five-carbon PFPeA are observed (orange), in accordance with the three-carbon shortening process proposed in **Figure 3.16** Pathways A + D.

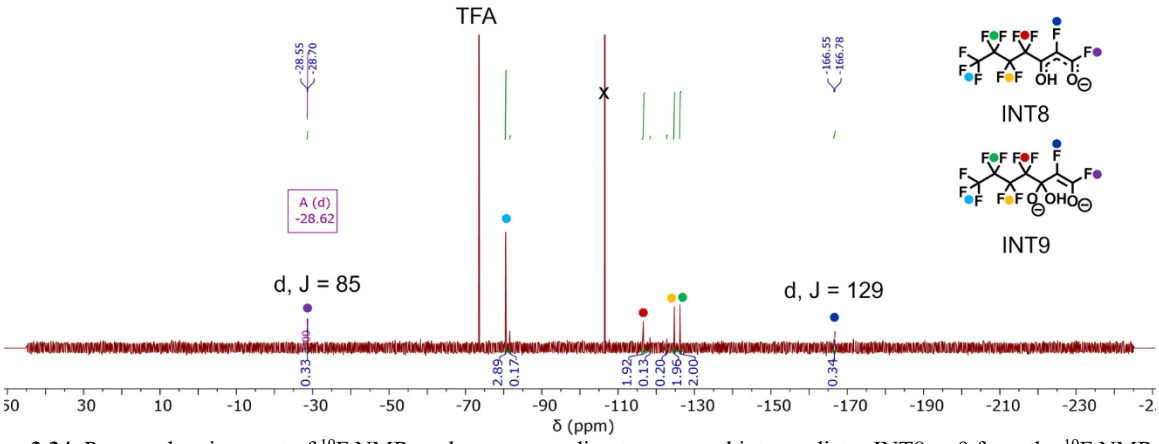

Figure 3.34. Proposed assignment of ^{19}F NMR peaks corresponding to proposed intermediates INT8 or 9 from the ^{19}F NMR spectrum of 1 h aliquot of 40 °C degradation of **2**. TFA = trifluoroacetate, x = 4,4′-difluorobenzophenone standard. Peak assignments marked with colored dots based on the spectrum of PFPeA and the assignment of enol fluorine (*167*). While the relative peak positions are relatively consistent with the proposed structures, the peak integrations and couplings are potentially inconsistent with these structures.

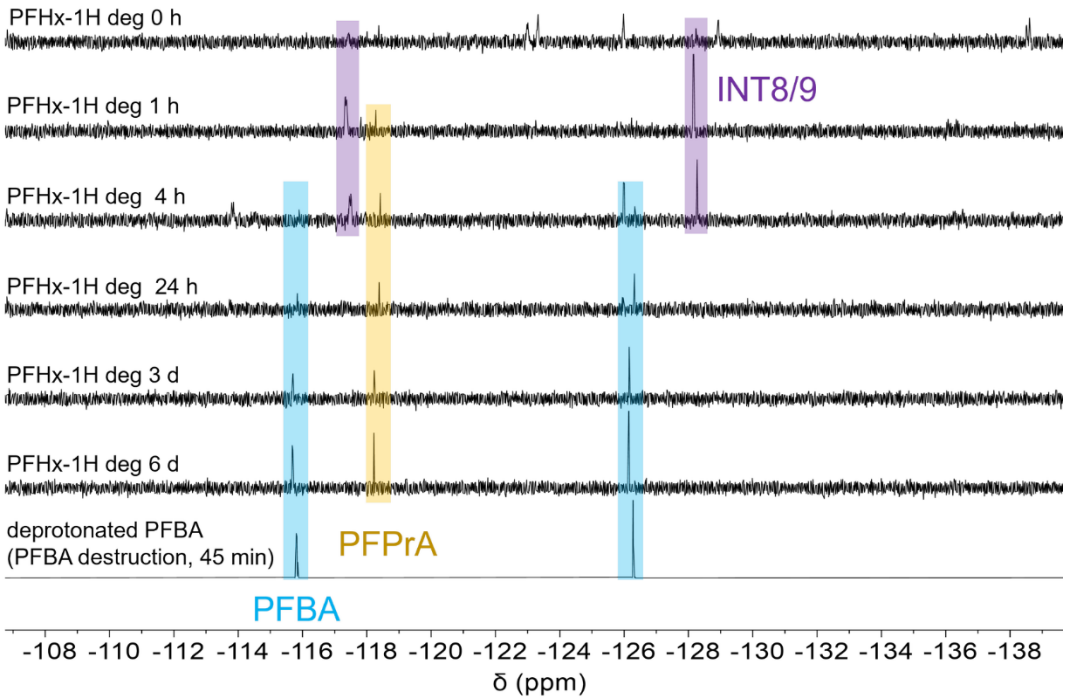

Figure 3.35. Partial ^{19}F NMR spectra (600 MHz) degradation of **S1** performed at 40 °C. In the first few hours of reaction, an intermediate with 3 CF_2 groups is observed (purple). We hypothesize that this intermediate is INT8/9; see **Figure 3.36** for further assignment of these peaks. In spectra obtained at 24 h, 77 h, and 142 h, resonances corresponding to four-carbon PFBA are observed (blue), in accordance with the three-carbon shortening process proposed in **Figure 3.16** Pathways A + D. A peak corresponding to perfluoropropionic acid (PFPrA) is highlighted in yellow.

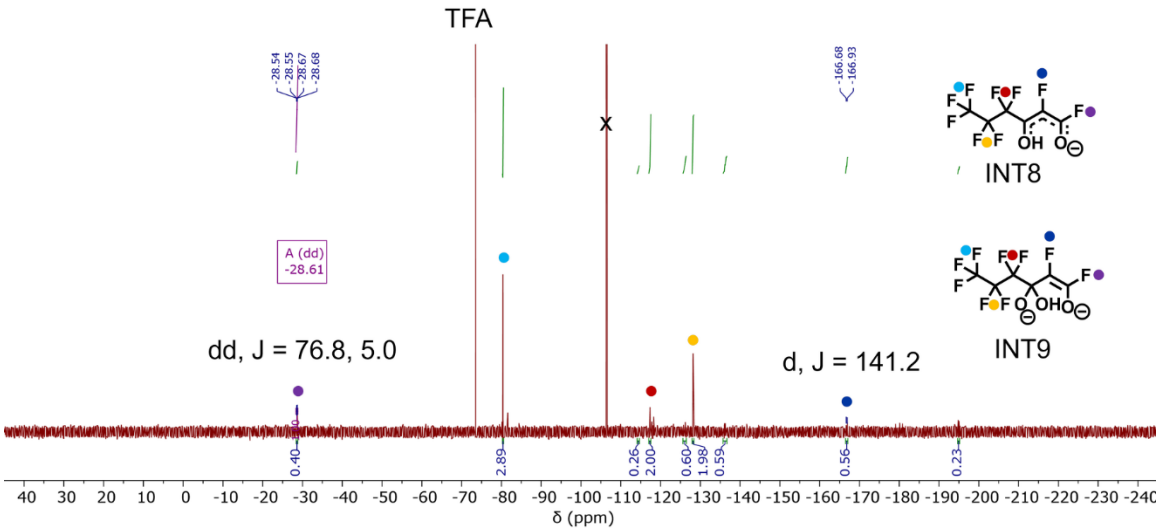

Figure 3.36. Proposed assignment of ^{19}F NMR peaks corresponding to proposed intermediates INT8 or 9 from the ^{19}F NMR spectrum of 1 h aliquot of 40 °C degradation of **S1**. TFA = trifluoroacetate, x = 4,4′-difluorobenzophenone standard. Peak assignments marked with colored dots based on the spectrum of PFBA and the assignment of enol fluorine (*167*). While the relative peak positions are relatively consistent with the proposed structures, the peak integrations and couplings are potentially inconsistent with these structures.

The experimental observations confirm that the computed mechanism provides a complete model to describe the observations made experimentally about this complex degradation. We also performed calculations to test proposed difluorocarbene (**Figure 3.38**), perfluoroalkyl hydroxylation (**Figure 3.18**), and α-lactone mechanisms (*168*, *169*) (**Figure 3.37**) that had been proposed for such degradations, but these were found to have barriers too high to be compatible with the experimental conditions.

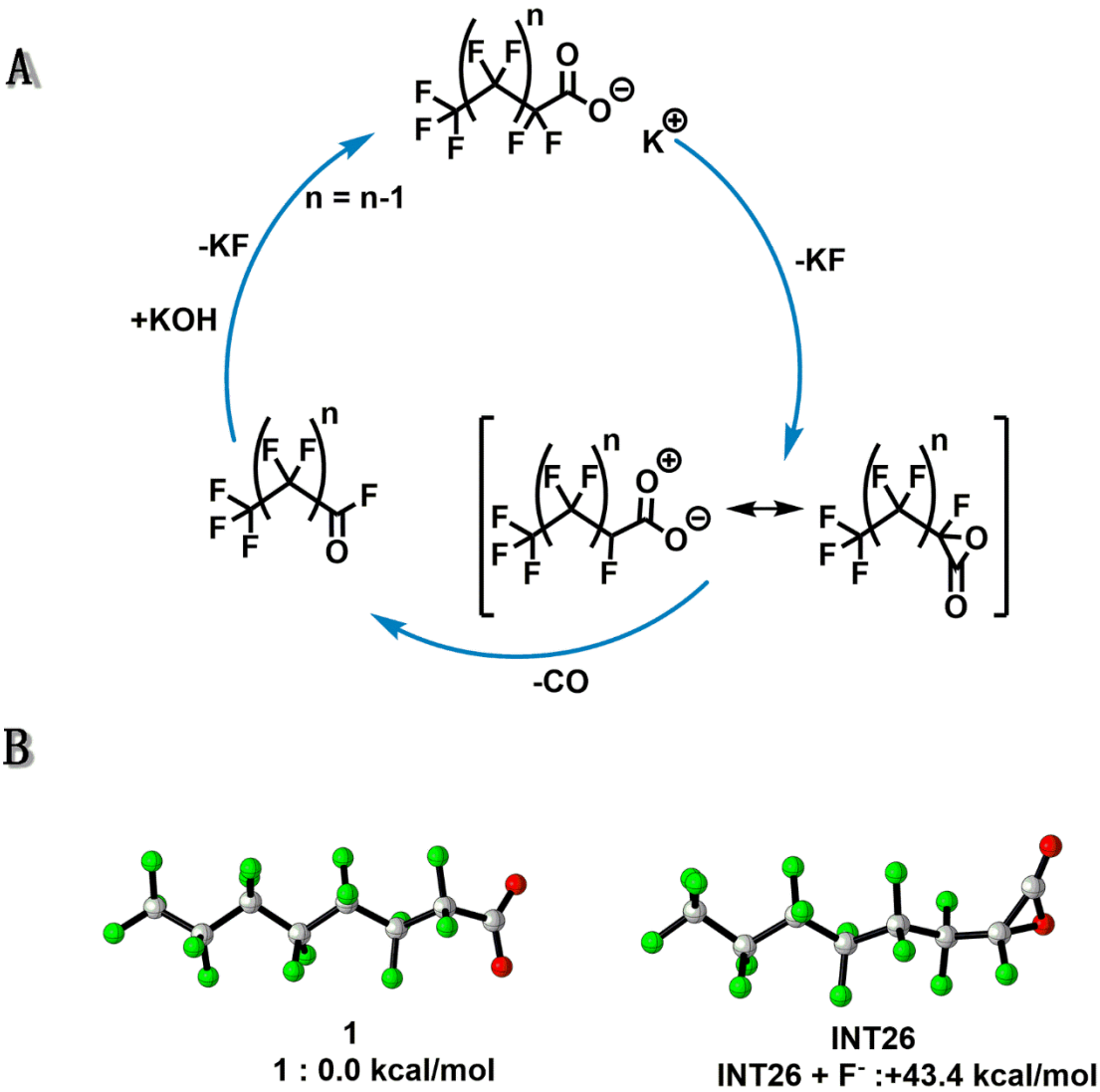

Figure 3.37. A) α-lactone mechanism proposed by Pellerite (*168*) and calculated by Ge et al. (*169*). B) The Gibbs free energy change for selected intermediate indicates that this mechanism is not feasible.

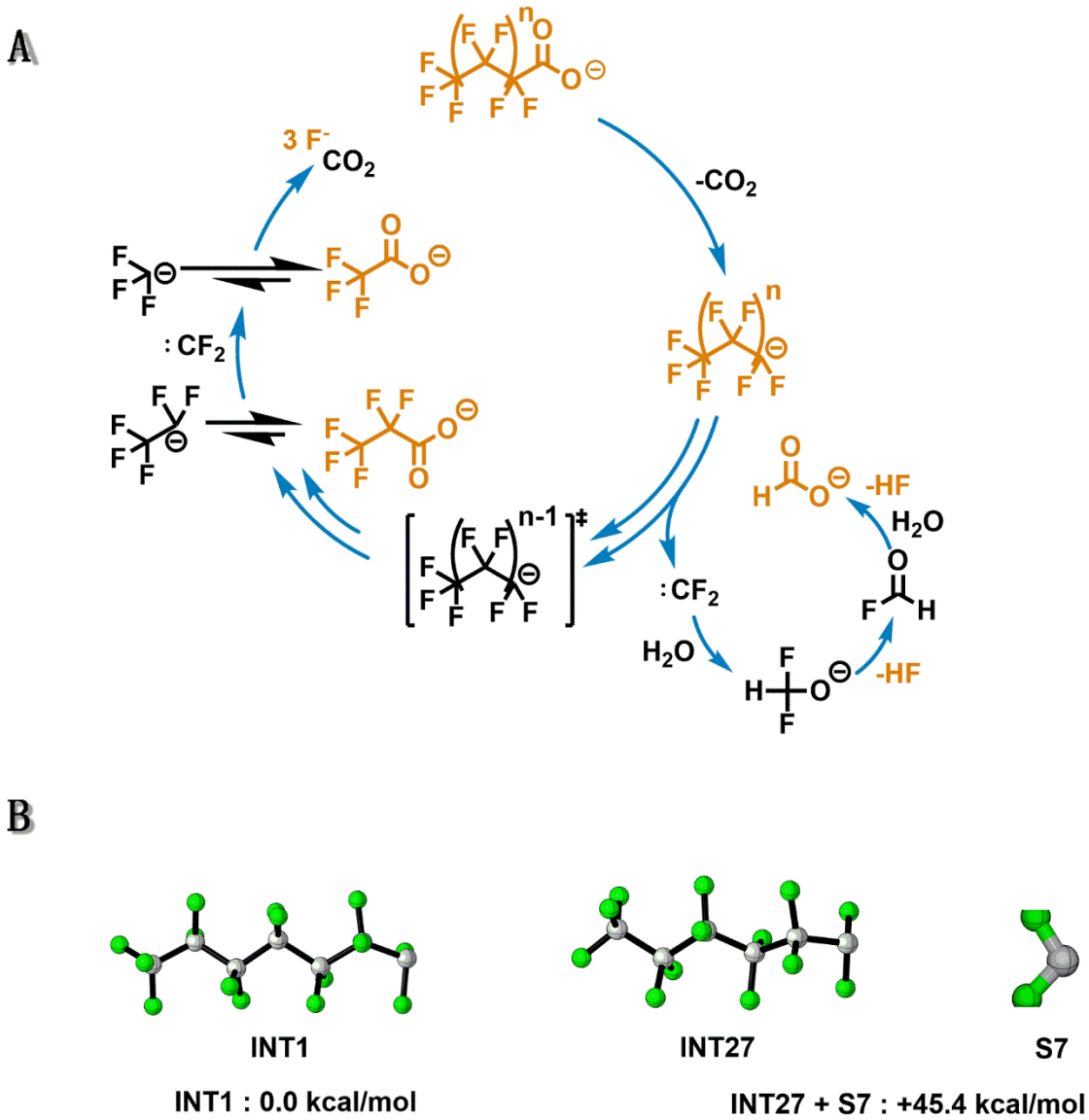

Figure 3.38. A) Mechanism proposed previously assuming that difluorocarbene is the key intermediate. B) The Gibbs free energy change for selected intermediate indicates that this mechanism is not feasible.

3.4. Future Work

Several separate avenues exist for continuing this work. Here, we discuss three possible avenues: efficiency studies and scaleup, extension to perfluorosulfonic acids (PFSAs), and extension to other PFAS compounds.

The ratios of base to solvent, DMSO to water, and solvent to PFOA were not optimized in this work. Preliminary studies on these topics have been conducted and some results are included below. We found that if the amount of base scaled proportionally with the amount of water in the reaction, i.e., the water was kept saturated with base, even as the proportion of water relative to DMSO got larger, the kinetics of the reaction did not suffer. As seen in **Figure 3.39**, the disappearance of PFOA from solution is consistent under each of these conditions. However, when the amount of water is increased relative to the amount of DMSO but the amount of base is held constant, as in **Figure 3.40**, the kinetics of the reaction slow down. While it is tempting to draw simple conclusions about the roles of different reaction components from these two experiments, there are several complicating factors that make optimization from this data difficult: The nearly-saturated aqueous NaOH solution and the DMSO solution are phase-separated, which makes it difficult to rigorously analyze the role of increased [NaOH] or [H_2O]. There could be differences in how various ions partition between the two phases, as well as differences in ion-pairing and the dielectric constant of the medium, in addition to whether hydroxide ions are involved in the decarboxylation process itself. These many factors make it difficult to discern the origin of the overall effect we are observing, which is additionally masked by the fact that the rate-determining step of the degradation is the decarboxylation, making it difficult to study the defluorination portion of the reaction. Further optimization of the water:DMSO, water:base, and PFOA:solvent should be carried out to make the reaction both more efficient and more easily scaled up, but will need extensive parameterization and more advanced analysis techniques to fully understand the factors at play.

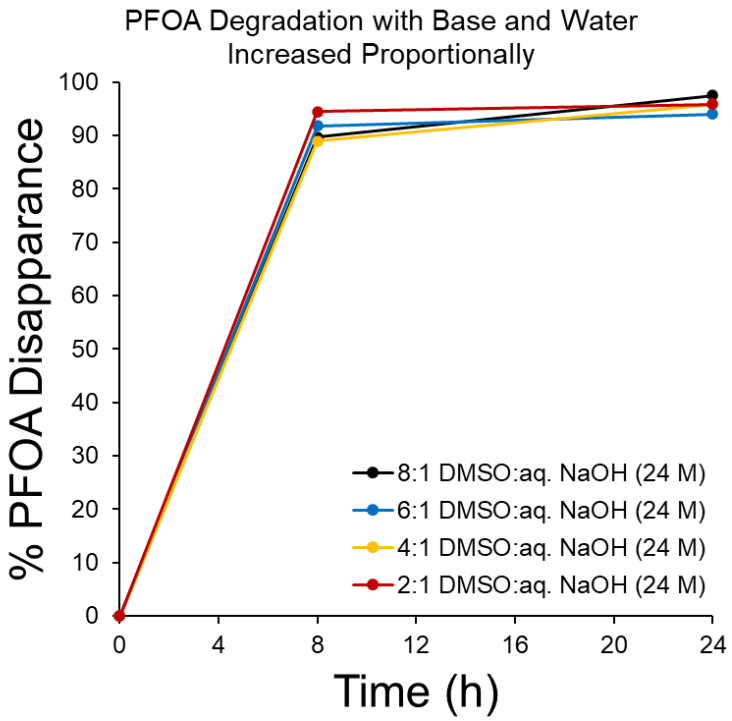

Figure 3.39. Degradation of PFOA with increasing amounts of water and increasing amounts of base (amount of DMSO held constant). PFOA concentration calculated from ^{19}F NMR integration.

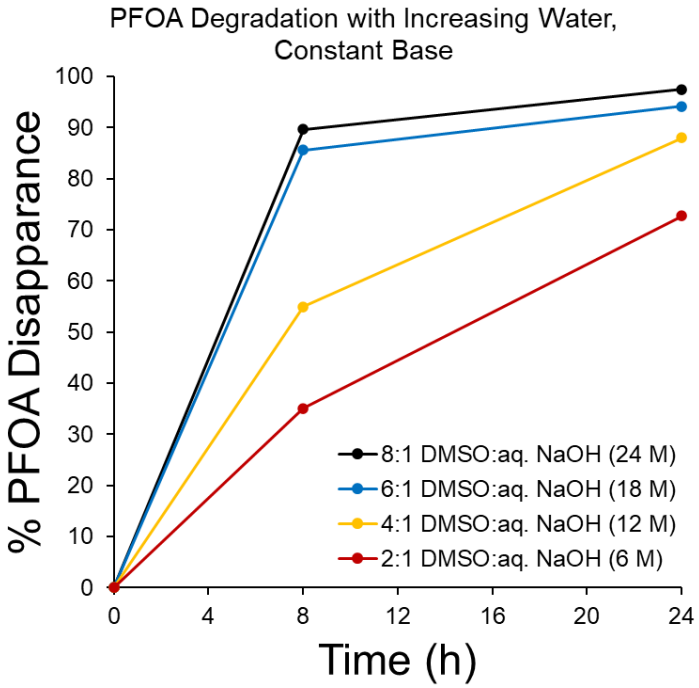

Figure 3.40. Degradation of PFOA with increasing amount of water, amount of DMSO and base held constant. PFOA concentration calculated from ^{19}F NMR integration.

Life-cycle analyses of the PFAS adsorption, adsorbent generation, and PFAS destruction processes should be conducted to determine the total energy and environmental impact of these processes as well as the best way to implement them in an industrial setting. As an alternative, for example, cyclodextrin polymers or other adsorbents made from cheap and benign materials might be destroyed along with the PFAS, removing the need to desorb the pollutant from the polymer. Similarly, an E_{EO} (electric energy per order of magnitude of contaminant removed) analysis would also be helpful to compare the energy efficiency of this method to other similar PFAS destruction methods (*122*). Treatment trains, in which contaminants are filtered out of contaminated water and then are separately treated in concentrated form, are a low-energy-cost alternative to treating large volumes of contaminated water directly. Anderson and coworkers have already demonstrated that the E_{EO} for a pilot-scale PFAS treatment train of a regenerable ion exchange resin coupled with

electrochemical oxidation over Ti_4O_7 electrodes was up to four orders of magnitude lower than for other PFAS treatment technologies targeting PFAS in dilute groundwater (*48*), so it is reasonable to hypothesize that a treatment train based on our destruction method might be similarly efficient if not more so because of the high concentration of the degradation reaction.

Another logical direction to pursue for extending this work is to find a way to bring PFSAs into this reaction manifold. As seen in Chapter 4, both branched PFCAs and ether-containing PFCAs can be degraded by this method; both of those categories encompass many PFAS compounds. However, the headgroup for both of those subclasses is still a carboxylic acid. It has been demonstrated that a variety of perfluoroalkyl acid precursors can be converted into their PFCA and PFSA analogues (*170*); however, PFSAs such as PFOS currently are not able to be degraded by this method. PFSAs, with their sulfonic acid headgroup, need a separate activation method to access the perfluoroalkyl anion / perfluoro-1H-alkane / perfluoro alkene intermediates that can subsequently be degraded by hydroxide. Similar to the decarboxylation reaction used here, the desired desulfonylation reaction will be one that is promoted by or its resulting intermediate is stabilized by electron-withdrawing alkyl substituents (fluorines). However, such reactions appear to be rare in the organic synthesis desulfonylation literature and more research is needed to find the correct desulfonylation approach. Though a reaction compatible with polar aprotic solvent and high base concentrations would be ideal so as to allow a one-pot reaction, desulfonylative transformations that require isolation might also be acceptable.

Similar to the total oxidizable precursor assay employed by Houtz and Sedlak (*170*), attempting to degrade a mixture of PFAS with the mineralization strategy described in this study might be a facile method for determining the classes of PFAS for which this degradation process

is immediately applicable. Some PFCA precursors might be degraded to PFCAs by action of the intensely basic conditions; however, PFAS besides the straight-chain PFCAs, PFECAs, PFSAs, and some fluorotelomer alcohols are often impossible to obtain in gram-scale quantities as required by the current analysis method. If the suitable mass spectrometry methods were available, a screening of the degradation of a sample of AFFF might allow for assessment of which classes of PFAS are susceptible to degradation by the current method. While ^{19}F NMR might be able to determine the decrease in total organic fluorine integration, mass spectrometry would be necessary for deconvoluting which compounds were specifically able to be degraded by this method. We expect that all PFCAs and some PFCA precursors might be degraded, but PFSAs and PFSA precursors will likely prove inert to this method, again pointing to the need for a sulfonic acid headgroup activation method. The fate of telomeric PFAS is also uncertain under this method and would additionally be interesting to investigate.

3.5. Conclusions

This newly discovered perfluorocarbon reactivity leverages low-barrier defluorination mechanisms to mineralize PFAS at mild temperatures with high rates of defluorination and low organofluorine side product formation. In contrast to other proposed PFAS degradation strategies, the conditions described here are specific to fluorocarbons, destroy concentrated PFCAs, give high fluoride ion recovery and low fluorinated byproduct formation, and operate under relatively mild conditions with inexpensive reagents. The proposed mechanism is consistent with both computational and experimental results, provides significant insight into the complexity of PFAS mineralization processes, and may be operative but unrecognized in other PFAS degradation approaches. This understanding will inform the development of engineered PFAS degradation processes and expanding the scope of this mild method to PFAS with other polar head groups. For

these reasons, this newly recognized reactivity of perfluoroalkyl anions, and the ability to access such intermediates efficiently from PFCAs, shows great promise for addressing the global PFAS contamination problem.

3.6. Acknowledgements

We thank Dr. Yongrui Luo at Shanghai Institute of Organic Chemistry for helpful discussions about fluorine NMR, Saman Shafaie at Northwestern University's IMSERC facility for assistance with mass spectrometry, and Rebecca Sponenburg at Northwestern University's QBIC for ion chromatography.

Funding: BBT is supported by the National Science Foundation Graduate Research Fellowship Program (DGE-1842165). KNH is supported by National Science Foundation (CHE-1764328) and the Saul Winstein Chair in Organic Chemistry. Ion chromatography was performed at the Northwestern University Quantitative Bio-element Imaging Center generously supported by NASA Ames Research Center Grant NNA04CC36G. This work made use of the IMSERC at Northwestern University, which has received support from the NIH (1S10OD012016-01 / 1S10RR019071-01A1), Soft and Hybrid Nanotechnology Experimental (SHyNE) Resource (NSF ECCS-1542205), the State of Illinois, and the International Institute for Nanotechnology (IIN). GCMS was performed at the REACT Core Facility at Northwestern University; The REACT Core facility acknowledges funding from the U.S. Department of Energy, Office of Science, Office of Basic Energy Sciences, Catalysis Science program (DE-SC0001329) used for the purchase of the GC/MS analysis system.

3.7. Chapter 3 Appendix

3.7.1. Materials, Instrumentation, and Computational Methods

Materials. Reagents were purchased in reagent grade from commercial suppliers and used without further purification, unless otherwise described. Anhydrous DMSO was obtained by drying with activated 4Å molecular sieves. Reagents were purchased from Fisher or Sigma unless specified.

4,4′-difluorobenzophenone NMR standard (Merck) was prepared by diluting to 0.095 M in DMSO-d_6 and adding 60–80 µL of solution to a coaxial NMR tube insert (Wilmad-Lab Glass, WGS-5BL). Each ^{19}F NMR sample was referenced to 4,4′-difluorobenzophenone (-106.5 ppm) by inserting the coaxial tubes containing the external NMR standard into the NMR sample tube before NMR analysis. ^{13}C NMR samples were quantified using a sodium acetate standard in D_2O (50 µL, 5.33 M). ^{1}H NMR samples were quantified using 4,4′-dihydroxybiphenyl dissolved in DMSO-d_6 (0.68 M). Quantification of samples was conducted by integrating each NMR peak and normalizing with the external standard peak integration, then converting to molar concentration using the known molar amount of the external standard. 25 mL PTFE round bottom flasks were purchased from Ace Glass (United States, 13438-16).

PFCA degradation reactions were conducted on 0.5 mmol or 1 mmol scales.

Instruments

Proton nuclear magnetic resonance (^{1}H NMR) spectra and fluorine nuclear magnetic resonance (^{19}F NMR) spectra were recorded at 25 °C on a 400 MHz Bruker Avance III HD Nanobay equipped with a BBFO Smart probe w/ Z-Gradient (unless stated otherwise). Fluorine-decoupled carbon nuclear magnetic resonance (^{13}C NMR) spectra and two-dimensional C–F spectra were recorded on a Bruker Neo 600 MHz system with a QCI-F cryoprobe w/ Z-Gradient. Quantitative ^{13}C NMR

spectra were recorded on a Bruker Avance III 500 MHz system equipped with a 5mm DCH CryoProbe w/Z-Gradient using a 40 second D1 delay. Other spectra were recorded on a Bruker Avance III 600 MHz with a BBFO Smart Probe w/ Z-Gradient. Experiments used pulse programs adapted from standard Bruker pulses library.

Ion chromatography was performed using a Thermo Scientific Dionex ICS-5000+ equipped with a Dionex AS-DV autosampler and using a Dionex IonPac AS22 column (Product No. 064141, Thermo Scientific, California, USA). The analysis was run using an eluent of 4.5 mM sodium carbonate and 1.4 mM sodium bicarbonate (Product No. 063965 from Thermo Scientific, California, USA) and a Dionex AERS 500 Carbonate 4 mm Electrolytically Regenerated Suppressor (Product No 085029 from Thermo Scientific, California, USA). A flow rate of 1.2 mL/min was used, giving the following retention times: fluoride = 3.3 min; formate = 3.8 min. Elemental standards containing 1000 µg/mL F^-, and 1000 ug/mL $HCOO^-$ (ICF1, ICHCO1, respectively, from Inorganic Ventures, Christiansburg, VA, USA) were mixed to make quantitative standards consisting of 50, 25, 12.5, 6.25, 3.125, 1.56, 0.78 ug/mL of each anion in ultra-pure H_2O (18.2 MΩ·cm). Ultra pure H_2O was used as the calibration blank. Validation experiments indicated an error of approximately 10% for ion chromatography results.

APCI-MS was collected on an Agilent 6545 QTOF Mass Spectrometer equipped with Atmospheric Pressure Chemical Ionization (APCI) source coupled with Agilent 1200 series LC running in direct injection mode. Data acquisition and analysis were done on Agilent Mass Hunter software.

GC/MS analysis was performed in the Reactor Engineering and Catalyst Testing (REACT) core facility at Northwestern University using an Agilent 6850 GC system coupled to an Agilent

5975C MS system. Helium (Airgas, 99.999%) was purified using an Agilent "Big Universal Trap" (Model RMSH-2) and used as a carrier gas. Gas separation was performed using a HP-Plot Q column (19091P-Q04E, 30m x 0.320 mm x 20 um) starting at 50 °C for 4 minutes. The temperature was then ramped to 220 °C at 30 °C/min and held for 3 minutes. The flow rate of He was maintained at 1.2 mL/min (inlet split ratio of 10:1). The MS was operated in scan mode (Gain factor = 1, EM voltage = 2518, MS Source = 250 °C, MS Quad = 150 °C) from m/z = 5 to m/z = 300. A solvent delay was not used.

Geometry optimizations, frequency analyses, and single-point energies were calculated at the theoretical M06-2X/6-311+G(2d,p)-SMD-(DMSO) level (*171*, *172*) using the Gaussian 16 package (*173*) with default convergence criteria. M06-2X functional gives refined energies for organic systems (*174*). Frequency outcomes were examined to confirm stationary points as minima (no imaginary frequencies) or transition states (only one imaginary frequency). Paton's GoodVibes (*175*) was used to correct entropy and enthalpy by Grimme's quasi-harmonic approximation (*176*) and Head-Gordon's method (*177*). 3D structures of molecules were generated by CYL view (*178*). All energies are in kcal/mol if not labeled otherwise. All bond lengths are in Angstroms (Å).

3.7.2. Synthetic Procedures and NMR Characterization of Synthesized Compounds

General PFCA Destruction Procedure: Perfluorooctanoic acid (207 mg, 0.500 mmol) and sodium hydroxide (0.600 g, 15.0 mmol) were added to a 25 mL PTFE round bottom flask along with a PTFE-coated magnetic stirbar. 5 mL DMSO was added to the reaction vessel, followed by 0.625 mL distilled or de-ionized water. The vessel was sonicated for approximately 15 seconds, then the t = 0 aliquot was taken by diluting a 50 µL aliquot into 500 µL of deuterated solvent. The vessels were sealed with a rubber septum and pierced with a needle that was left in the septum to prevent overpressure. The vented vessels were then added to an oil bath preheated to 120 °C and stirred at 500 RPM for the specified time, usually 24 hours. Liquid aliquots for reactions monitored over time were taken using a syringe inserted through the rubber septum and diluted as above with solids removed by centrifugation if necessary. The reactions were removed from the heat and cooled for at least 40 minutes before workup. The entire contents of the reaction were diluted with distilled or deionized water until the solids at the bottom were completely dissolved (typically 20–40 mL water added) and were transferred to a polypropylene centrifuge tube. The resulting fluoride- and formate- containing solution was further diluted in water 100x–500x for ion chromatography analysis. For carbonaceous products quantification, the contents of the reaction were added to a 15 mL polypropylene centrifuge tube, centrifuged, and the DMSO solvent was decanted. The remaining solids were rinsed and centrifuged 2x with dichloromethane, then dried overnight at 120 °C on high vac. A portion of the solids (~30 mg) was dissolved (750 µL D_2O + 50 µL NaOAc standard in D_2O) for quantitative ^{13}C NMR analysis.

Scheme S1

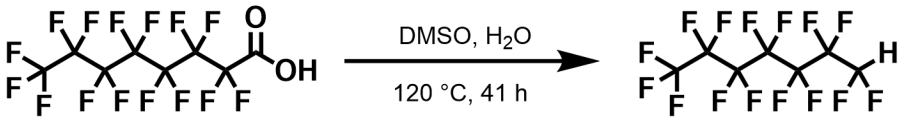

Scheme S3.1. General procedure to decarboxylate perfluorocarboxylic acids and synthesis of perfluoro-1H-heptane (2). PFOA (1.035 g, 2.500 mmol) was added to a glass pressure vessel with PTFE screw-top and PTFE-coated magnetic stirbar and dissolved in a mixture of DMSO (5.00 mL) and deionized H_2O (0.625 mL). The solution was heated to 120 °C for 41 h, then was removed from heat and allowed to cool to room temperature for 2 h. The product phase-separated as a clear liquid on the bottom of the vessel and was decanted via micropipette to provide **2** as a colorless oil (0.703 g, 76% yield). ^{19}F NMR (564 MHz, DMSO) δ -83.614, -123.990, -124.648, -125.218, -128.289, -131.643, -140.332. ^{13}C NMR (151 MHz, DMSO) δ 116.223, 109.800, 109.315, 109.196, 109.152 (d, J^2_{CH} = 7.5 Hz), 107.548, 107.498, 106.194 (d, J^1_{CH} = 197.7 Hz). ^{1}H NMR (400 MHz, DMSO) δ 5.94 (tt, J = 51.4, 5.1 Hz, 1H).

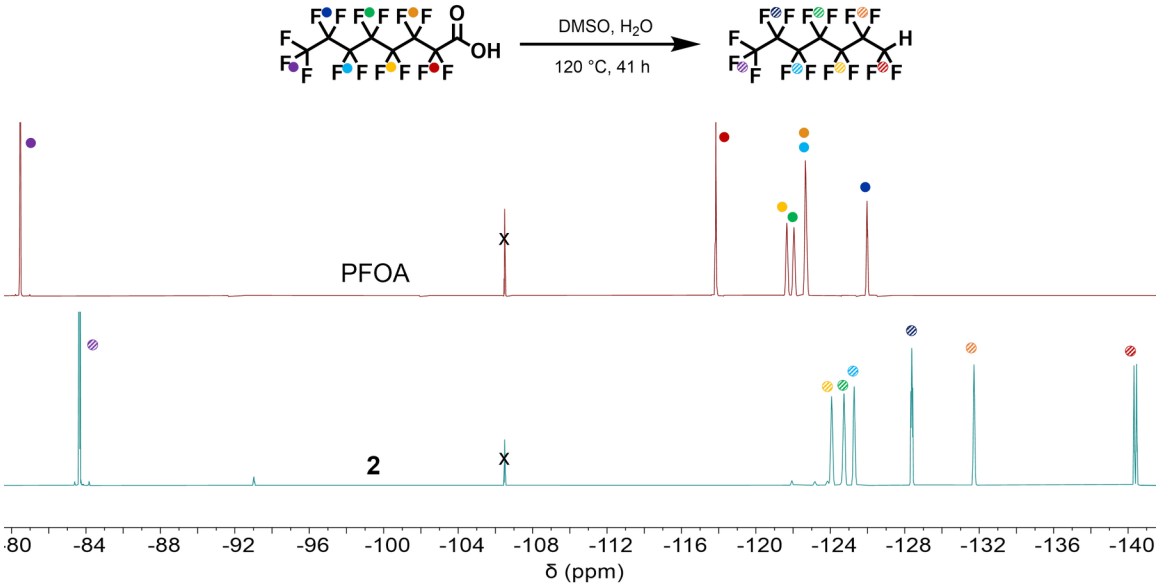

Figure S3.1. ^{19}F NMR spectra of PFOA (top, DMSO-*d*$_6$, 400 MHz) and **2** (bottom, DMSO-*d*$_6$, 600 MHz). PFHp-1H is insoluble in DMSO, and so it was analyzed as a neat oil in an inner coaxial insert tube with a solution of a 4,4′-difluorobenzophenone standard (-106.5 ppm) dissolved in DMSO-*d*$_6$ in an outer tube.

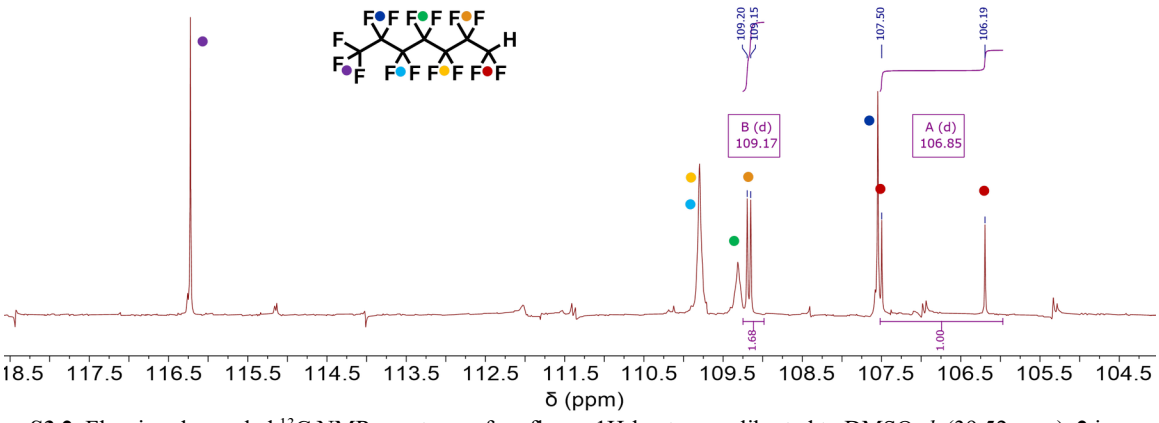

Figure S3.2. Fluorine-decoupled ^{13}C NMR spectrum of perfluoro-1H-heptane, calibrated to DMSO-*d*$_6$ (39.52 ppm). **2** is insoluble in DMSO, and so it was analyzed as a neat oil in an inner coaxial insert tube with a solution of a 4,4′-difluorobenzophenone standard (-106.5 ppm) dissolved in DMSO-*d*$_6$ in an outer tube.

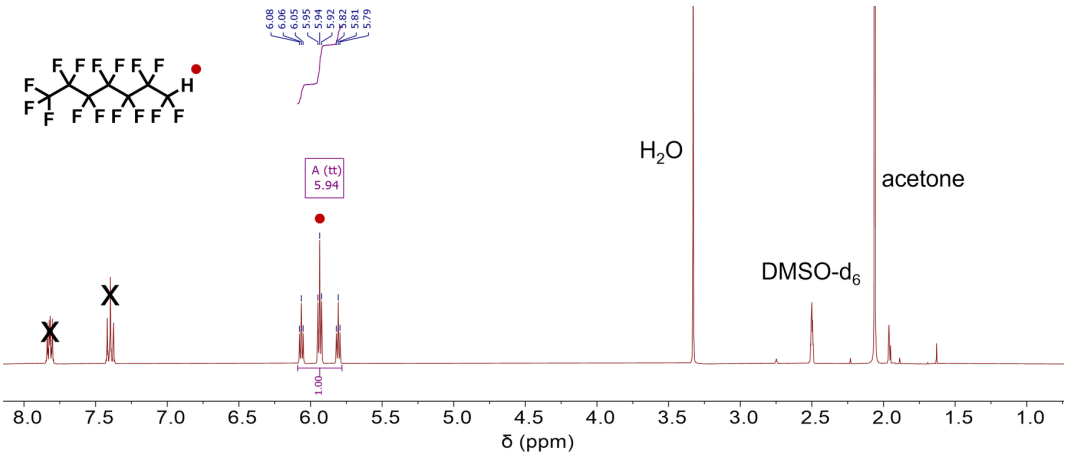

Figure S3.3. ^{1}H NMR spectrum of perfluoro-1H-heptane (DMSO-*d*$_6$, 600 MHz). **2** is insoluble in DMSO, and so it was analyzed as a neat oil in an inner coaxial insert tube with a solution of a 4,4′-difluorobenzophenone standard (7.3–7.8 ppm, marked with X) dissolved in DMSO-*d*$_6$ in an outer tube.

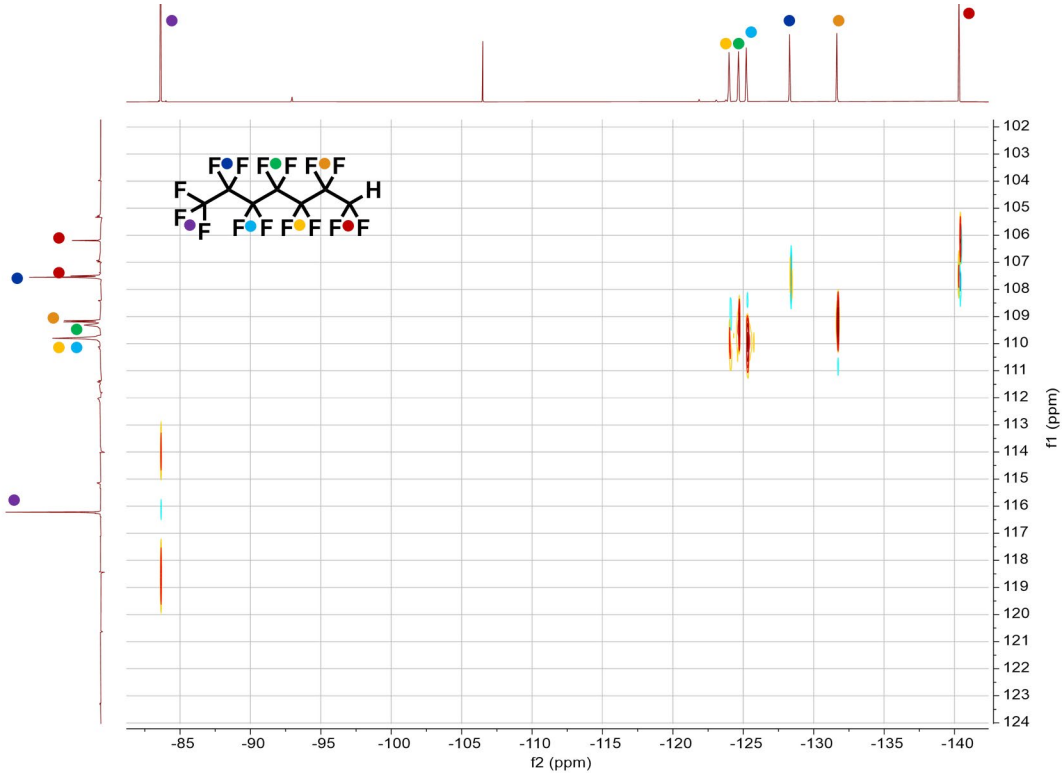

Figure S3.4. ^{19}F–^{13}C HSQC spectrum of perfluoro-1H-heptane used to assign the ^{13}C resonances. The ^{19}F resonances were assigned by comparison to PFOA.

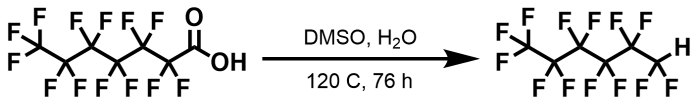

Scheme S3.2. Perfluoro-1H-hexane (S1). S1 was obtained using the above procedure as a colorless oil (0.654 g, 84% yield). ^{19}F NMR (564 MHz, DMSO) δ -83.73 (tt, *J* = 10.4, 2.4 Hz), -124.955, -125.559, -128.487, -131.875, -140.31 (d, *J* = 51.7 Hz). ^{13}C NMR (151 MHz, DMSO) δ 116.282, 109.757, 109.340, 109.13 (d, *J* = 6.6 Hz), 107.560, 106.81 (d, *J* = 195.8 Hz). ^{1}H NMR (600 MHz, DMSO) δ 5.85 (tt, *J* = 51.7, 5.1 Hz, 1H).

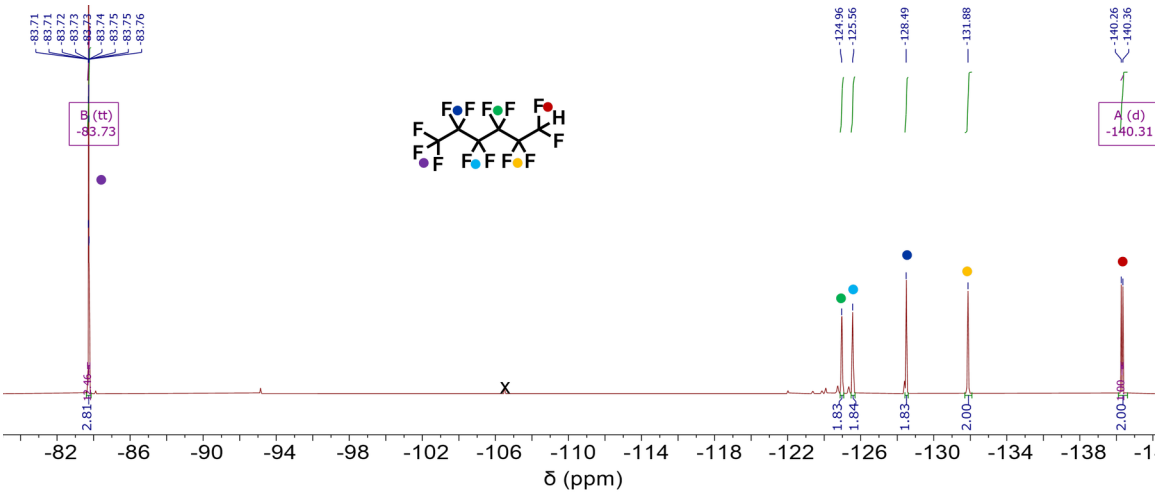

Figure S3.5. ^{19}F NMR spectra of perfluoro-1H-hexane (DMSO-*d*$_6$, 600 MHz). **S1** is insoluble in DMSO, and so it was analyzed as a neat oil in an inner coaxial insert tube with a solution of a 4,4′-difluorobenzophenone standard (-106.5 ppm) dissolved in DMSO-*d*$_6$ in an outer tube.

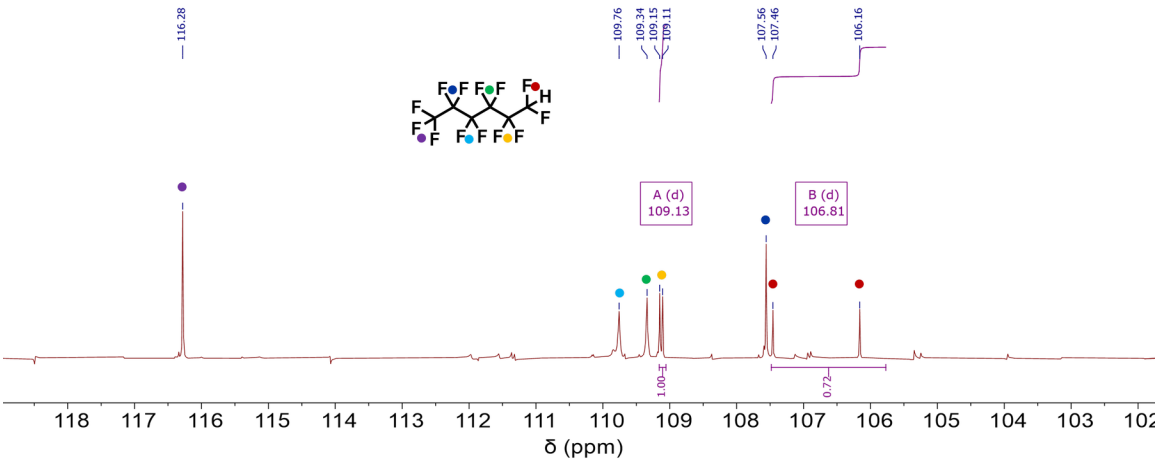

Figure S3.6. Fluorine-decoupled ^{13}C NMR spectrum of perfluoro-1H-hexane, calibrated to DMSO-d$_6$ (39.52 ppm). **S1** neat in coaxial insert tube with 4,4′-difluorobenzophenone standard dissolved in DMSO-d$_6$ in outer tube.

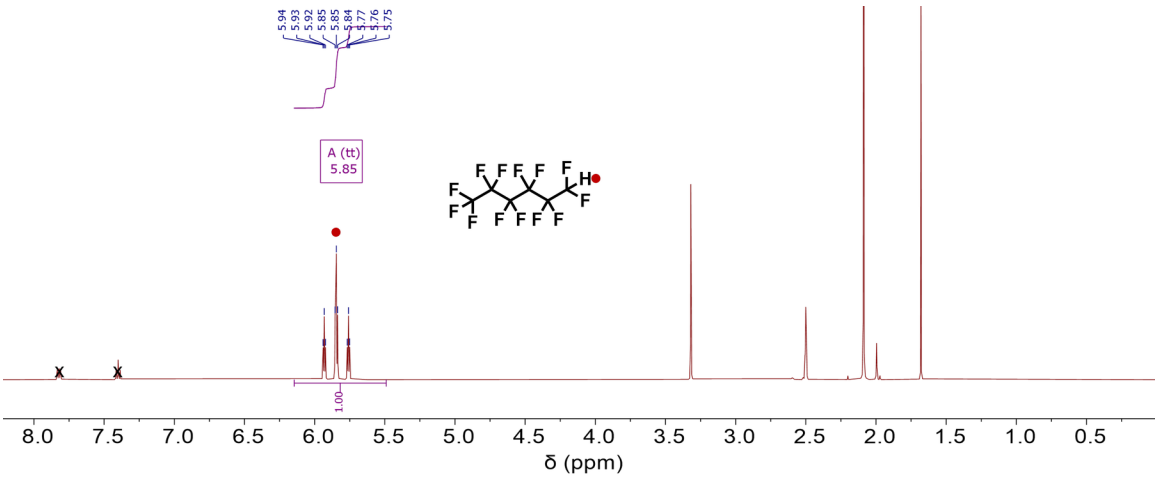

Figure S3.7. ^{1}H NMR spectrum of perfluoro-1H-hexane (DMSO-d_6, 600 MHz). **S1** is insoluble in DMSO, and so it was analyzed as a neat oil in an inner coaxial insert tube with a solution of a 4,4′-difluorobenzophenone standard (7.3–7.8 ppm, marked with X) dissolved in DMSO-d_6 in an outer tube.

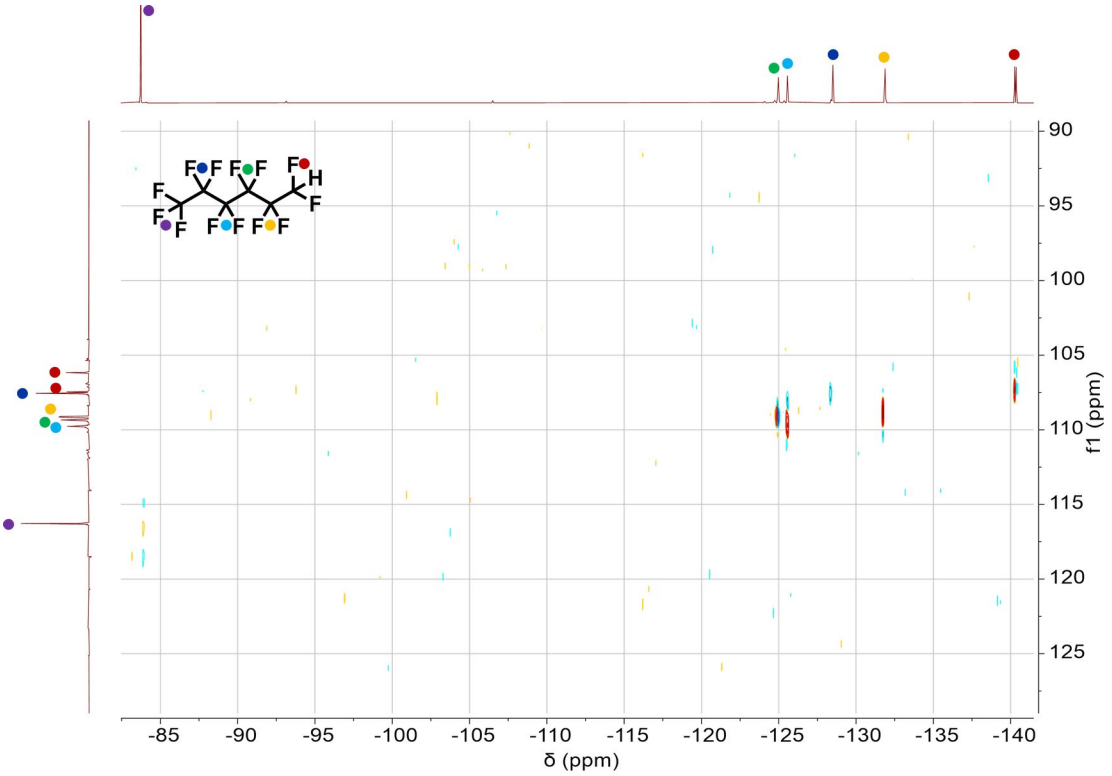

Figure S3.8. ^{19}F–^{13}C HSQC of perfluoro-1H-hexane used to assign carbon peaks. Fluorine peaks assigned based on PFOA and literature.

Table S3.1. Emerging PFAS Destruction Methods.

Ref. No.	Technique	Matrix/ Reagents	Substrates	Time, (Temp, Press.)	Conc	Result	Specific Drawbacks	Proposed Mechanism	Evidence for Mechanism	See	Related publications	Overall Drawbacks
(*147*)	Sonication	MQ	PFOA, PFOS	120–180 min	5 ppm PFOS, 5 ppm PFOA	> 90% F^-	-	Desulfonylation > alkene > CF_3 radical, difluorocarbene, CF > CO, CO_2, F^-	GC-MS headspace	Figure 3	(*148*)	"Designing an effective ultrasound reactor has proven to be one of the most challenging aspects for the application of sonolysis in water treatment due to challenges in the optimization of operating conditions and parameters such as frequency and power"; matrix components may also reduce efficiency (*84*)
(*103*)	Plasma	NaCl, aqueous	PFOA, PFOS	120 min	8.3 ppm	5 mg/L F^- per 8.3 mg/L orig PFOA (60%); 4.4 mg/L F^- for PFOS (53%)	PFAS adsorbed to the reactor (~20–40%), many short-chain PFAS byproducts formed	DHEH	None	Figure 7	-	-
(*108*)	Electrochemical, Ti/RuO_2	100 mg.L NaCl, 1500 mg/L Na_2SO_4	PFOA, PFOS	6 h	5 ppm	98% F^- for PFOS, 58% F^- for PFOA	Quantifying the removal of PFOA due to electrochemical treatment versus sorption difficult to determine; PFOA sorption in zero-current control = 67%	None	N/A	Section 3.3	-	Energy consumption, the formation of toxic by-products, electrode issues such as mass transfer and fouling, and the lack of cost-effective and scalable electrode materials. (*111*, *112*)
(*109*)	Electrochemical, Ti/SnO_2-Sb-Bi	1.4 g/L $NaClO_4$	PFOA	3 h	50 ppm	63.8% F^-, observation of distribution of smaller PFCAs	High energy consumption; oxidation of other matrix components	DHEH, O_2 generation from two perfluoroalcohol radicals	Mostly proposed, water as O source [$C_4F_9(^{18}O)$]- supported by ^{18}O tests, one MS peak.	-	-	
(*110*)	Electrochemical, BDD	DI water, 0.1 M Na_2SO_4	PFBS, PFHxS, PFOS	43 h	2.9 ppm PFBS, 11 ppm PFHxS, 15 ppm PFOS	45% PFBS, 91% PFHxS, 98% PFOS decrease, overall 66% F^-	Complete oxidation of bromide and chloride at 120 h groundwater treatment and production of toxic byproducts, elevated short-chain concentrations after treatment, inefficient defluorination, optimization needed	PFSA > shorter-chain PFCAs	Literature	-	-	
(*110*)	Electrochemical, BDD	Concentrated groundwater	PFBA, PFPeA, PFHxA, PFHpA, PFOA, PFBS, PFHxS, PFOS and 6:2 FTSA	18 h	0.02-20 ppm	Decrease of PFBS (83%), PFHxS (92%), PFOS (96%) and 6:2 FTSA (60%). PFBA, PFPeA, PFHxA and PFHpA increased. 42% F^-						

(*89*)	UV-sulfite / hydrated electrons	10 mM Na_2SO_3, and 5 mM $NaHCO_3$ (pH 9.5, adjusted by 1 M NaOH)	PFCAs, PFSAs, diPFCAs, FTCAs	48 h	10 ppm (relative to PFOA)	F^- ratios of 98.2–49.1% for PFCAs, 81.4-63.2% for diPFCAs, 0.71–33.4% for telomeric PFCAs, 0.94-57.0% for PFSAs, smaller-chain PFAS generated during degradation	Generation of shorter-chain PFAS, generation of H-substituted PFAS	DHEH, H/F exchange	MS of intermediates, monitored degradation of alternate/proposed intermediates, DFT calculations of BDE of intermediates	-	(*90*, *91*)	Hydrated electron processes can require extreme operating conditions, such as high temperature, high reductant dosage, and high solution pH. Needs testing in complex matrices. (*84*)
(*92*)	Oxidation-reduction-oxidation (basic persulfate oxidation, UV-sulfite reduction)	Aqueous. Ox: $K_2S_2O_8$ at pH ≥ 12, Red: 10 mM of Na_2SO_3 and 5 mM of $NaHCO_3$ at pH 12.	PFCAs, PFSAs, FTCAs, FTSAs	40 min–24 h per step	207-10 ppm (relative to PFOA)	97–103% F^- except for n = 7, 8 fluorotelomers (85–89%), n = 4 PFSA (94%), and n = 4 FTSA (93%)	Complicated treatment train	Detailed mechanism proposal, see paper	Literature, study of SO_4^- radical vs OH radical, characterization of intermediate distribution, stoichiometry of reactants consumed, DFT calculations of BDE of intermediates	-	-	
(*118*)	Persulfate-UV	pH 3.0-3.1, $K_2S_2O_8$ (6.4-50.0 mM), aqueous solution	PFOA	12 h	559 ppm	disappearance of PFOA after 4 h, production of F^- after PFOA disappeared; 73.8% F^- plus shorter-chain PFCAs	Formation of shorter-chains PFCAs	DHEH	Observations and literature	Figure 2	-	"Generally, higher doses of persulfate, high temperature, or creating extreme pH conditions are necessary to achieve an effective degradation of PFOA"; not effective for PFOS (*84*)
(*96*)	UV photolysis	aqueous	PFOA	72 h	559 ppm	34% F^-, shorter PFCAs formed	Low defluorination	DHEH	^{18}O experiments	Table 1 Entry 2	-	PFOA does not absorb at wavelengths >220 nm (*84*)
(*96*)	UV, tungstic heteropolyacid	aqueous, 6.68 mM tungstic polyacid	PFOA	24 h	559 ppm	88% F^-, suppressed shorter-chain PFCA generation compared to direct photolysis	Catalyst needs to be separated from reaction mixture	Proposed catalyst coordination and reoxidation steps, proposed photo-Kolbe decarboxylation cleavage, hydrolysis downstream	UV studies of catalyst under anaerobic conditions, ^{18}O experiments	-	-	-
(*149*)	VUV-Fe	aqueous, $FeCl_3{\cdot}6H_2O$ (20 μM), various additives tested	PFOA	72 h	15 ppm	100% F^-, shorter PFCAs formed	Interference from matrix constituents	Direct photolysis leading to perfluoroalkyl radical, hydrolysis to shorter-chain PFCA; Fe^{3+} complex with PFOA leading to PFOA radical, hydrolysis to shorter-chain PFCA	Literature, none	Figure 1	-	-
(*87*)	Thermal treatment of AC in N_2 gas stream	Activated carbon	PFOA, PFHxA, PFOS	10 min	10 mg PFAS/g	~27–76% F^- at 700 °C, ~80% F^- at 1000 °C. Volatile organic fluorine found at 800–900 °C.	PFAS destroyed on surface of GAC at 700 °C and destroyed in gas phase at 1000 °C but in equilibrium with volatilizing at temperatures between 700–1000 °C, which gives incomplete destruction. Fluorine mass balance difficult to quantify; error is 20–30%.	None	N/A	Figures 2, 3, 4	(*86*)	-

(*179*)	Thermal treatment of GAC	PFAS adsorbed to granulated activated carbon with surface water	7 PFCAs, 3 PFSAs, HFPO-DA	10 °C/min ramp, 30 min hold	not specified	Thermal degradation of PFAS from 150–600 °C for PFOA, 450–600 °C for PFOS; 80–90% F^- for PFOA and PFOS at temperatures ≥700 °C	High temperature	Radical and alkene-based mechanism	Organofluorine species identified by TD−Pyr− GC−MS	Figure 4	-	-
(*97*)	Hydrothermal Alkaline	1-5 M NaOH, aqueous	PFOS	8 h, 350 °C, 2–16.5 MPa	50 ppm	Low concentrations of PFHpA, PFHxA and PFPeA, 80–90% F^-	High temperature, pressure	Nucleophilic hydroxide substitution of sulfonic acid head group, subsequent DHEH	Observation of shorter-chain intermediates, literature	Figure 2	(*180*)	-
This Study	Basic polar aprotic solvent-assisted	8:1 DMSO:H_2O, 2.67 M NaOH	PFCAs	24 h, 120 °C	36,800 ppm	80–100 F^-, TFA, formate formed	Organic solvent	Detailed mechanism proposal, see paper	DFT calculations of activation energies, explanation of byproducts, NMR of intermediates, explanation of chain-length patterns, monitored degradation of intermediates	-	-	-

Summary of emerging PFAS degradation methods and their major drawbacks. DHEH = decarboxylation–hydroxylation–elimination–hydrolysis (*89*).

3.7.3. NMR Spectroscopy Monitoring of PFCA Degradation

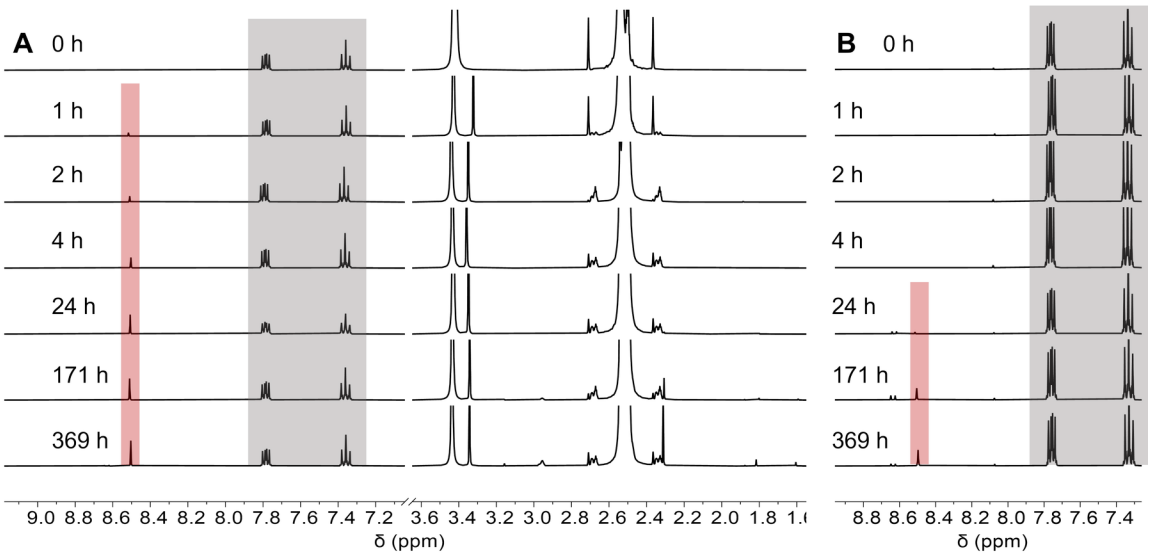

Figure S3.9. ^{1}H NMR spectra to monitor formate ion formation at 120 °C as a function of reaction time. Peaks highlighted in gray correspond to the 4,4′-difluorobenzophenone external standard, and peaks highlighted red correspond to formate ions. A) PFOA degradation reaction: the formate ion concentration increases steadily over the course of the reaction, even after all PFOA has been degraded (24 h) and only TFA remains. B) Control reaction of water, DMSO, and NaOH in the absence of PFOA demonstrates a slower background reaction that also produces a small amount of formate, presumably from the degradation of the DMSO solvent. In both cases, formate production was confirmed by ion chromatography. However, ^{1}H NMR spectroscopy is not sufficient for formate quantification, as much of the formate precipitates out of the reaction and cannot be detected in solution.

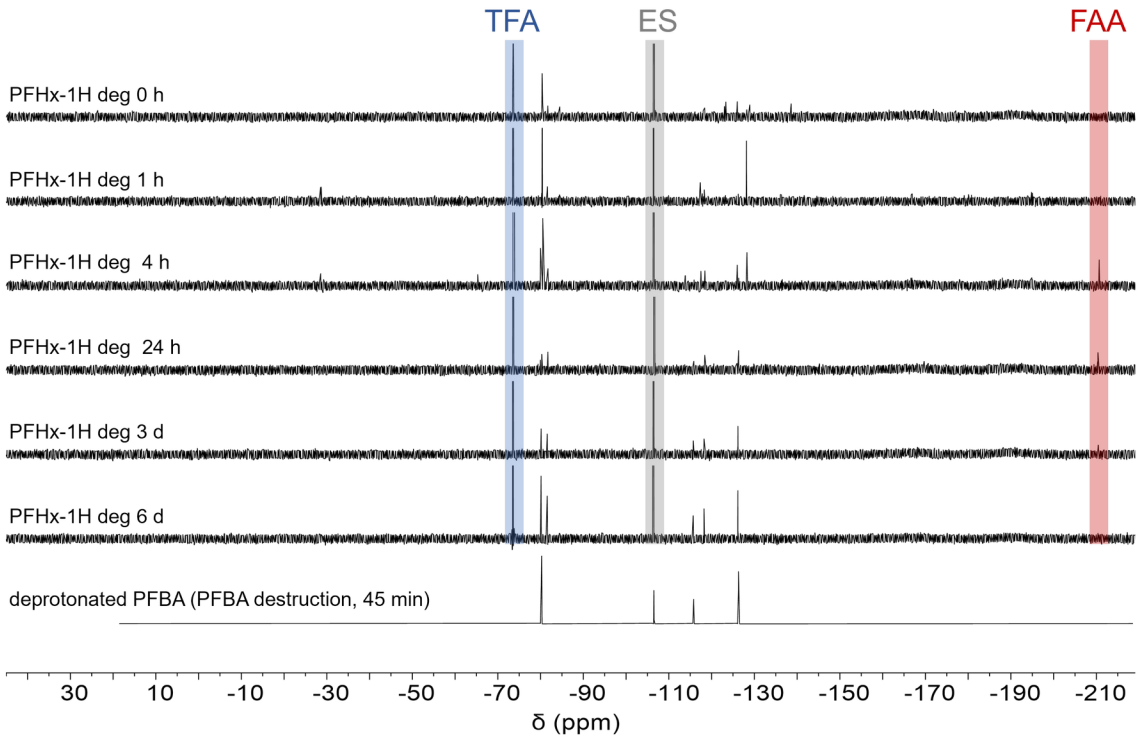

Figure S3.10. ^{19}F NMR spectra (600 MHz) of aliquots from the 40 °C degradation of **S1**. When the degradation is run at this lower temperature, various fluorinated intermediates (fluoroacetic acid, INT8/9, perfluorobutanoic acid) are observed that are not seen in the spectra of degradation reactions run at higher temperatures. These intermediates are shown in greater detail below. TFA = trifluoroacetate, ES = external standard (4,4′-difluorobenzophenone), FAA = fluoroacetic acid.

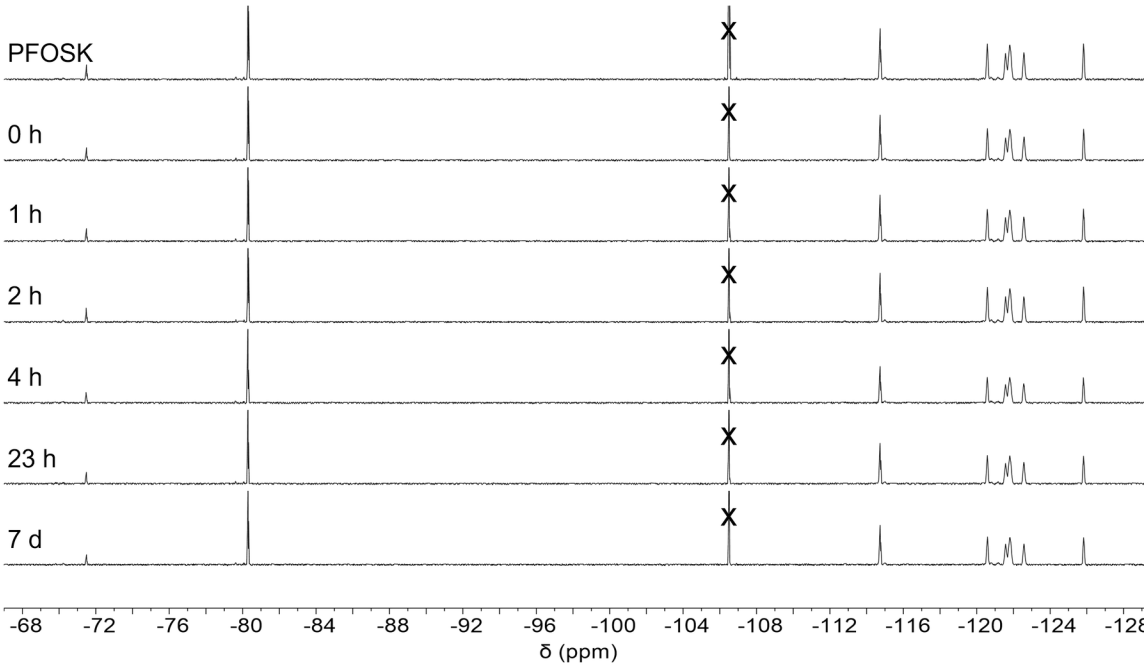

Figure S3.11. ^{19}F NMR spectra of aliquots of perfluorooctanesulfonic acid potassium salt (PFOSK, 0.089 M) in DMSO:H_2O (8:1) in the presence of NaOH (30 equiv) and heated to 120 °C. 4,4′-difluorobenzophenone was used as an external standard (X). No degradation of PFOSK is observed, implicating decarboxylation as the first step of PFCA degradation under these conditions.

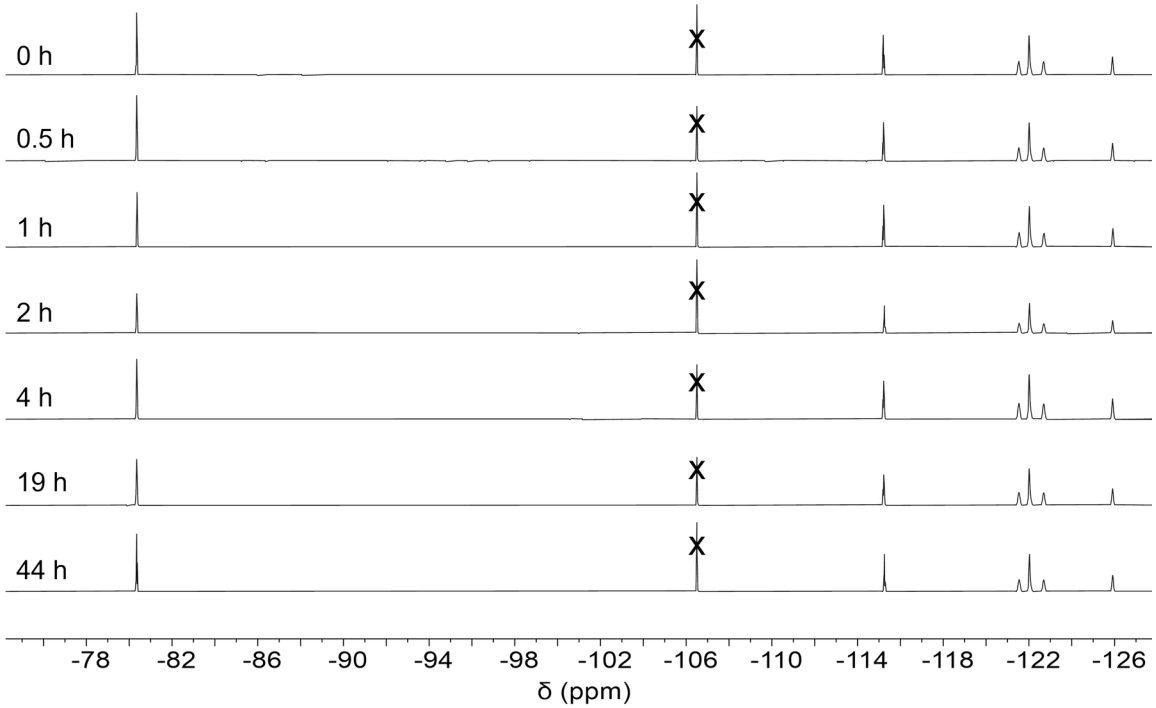

Figure S3.12. ^{19}F NMR spectra of 0.089 M perfluorooctanoic acid (PFOA) in water with 30 equiv NaOH heated to 120 °C. No change in the spectra over time shows that this decarboxylation needs polar aprotic solvent to occur. 4,4'-difluorobenzophenone standard is crossed out.

3.7.4. PFCA Kinetic Degradation Traces and Fittings

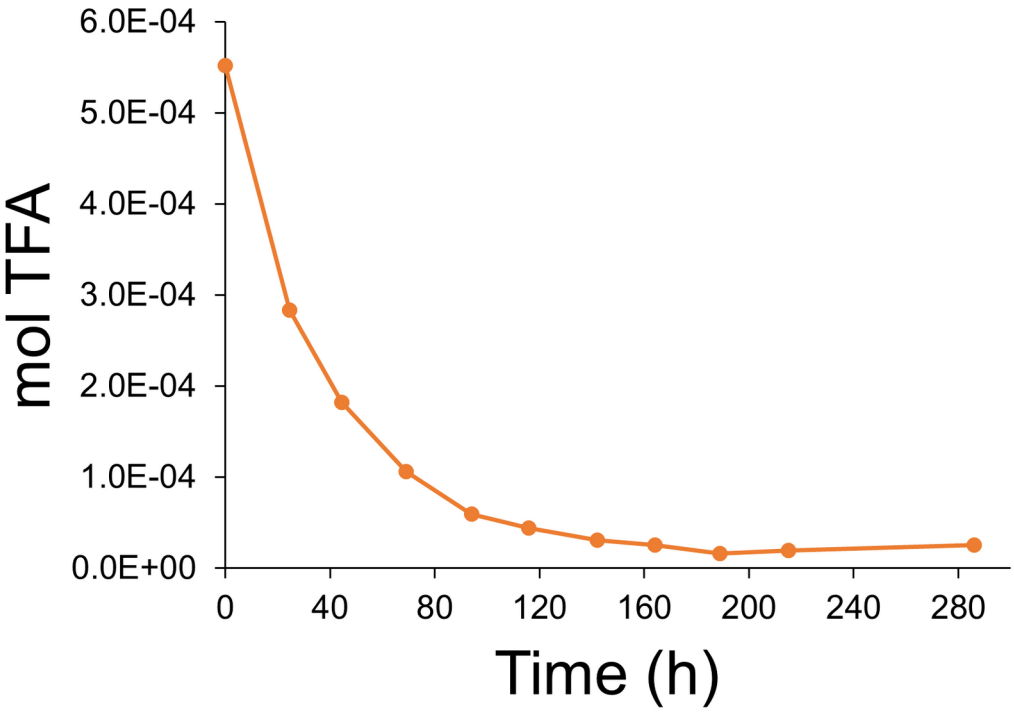

Figure S3.13. Kinetic trace of the degradation of CF_3CO_2Na over time as calculated by NMR concentration. CF_3CO_2Na (0.089 M in DMSO) was degraded at 120 °C with 30 equiv NaOH in 8:1 DMSO:H_2O.

Decay Curve Fittings: Kinetic traces for PFOA degradation at different temperatures were fitted to the equation $y = ae^{-x/b} + c$ in MATLAB using the Curve Fitting application.

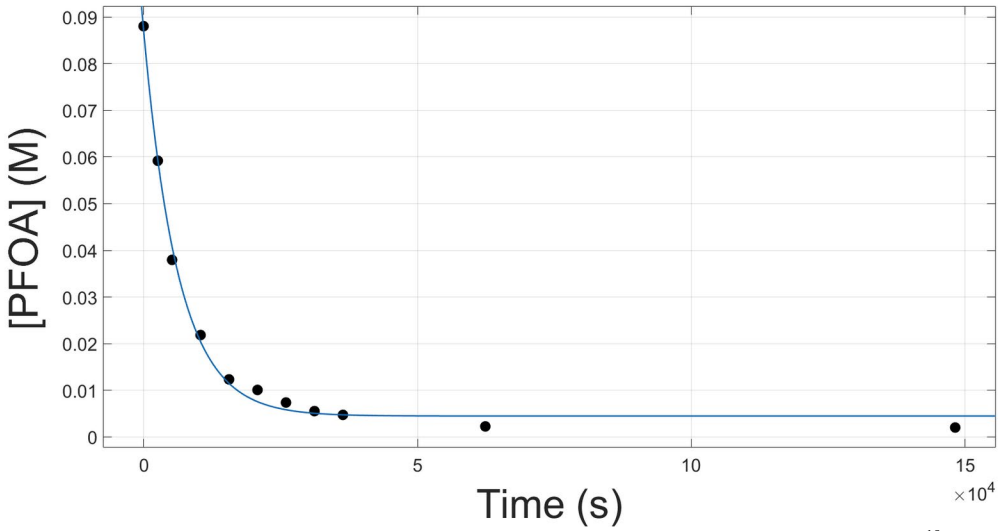

Figure S3.14. Fitted curve for degradation of PFOA at 120 °C as calculated from the integral of F2 in the ^{19}F NMR over time. Data is average of triplicate runs (see **Figure S21**).

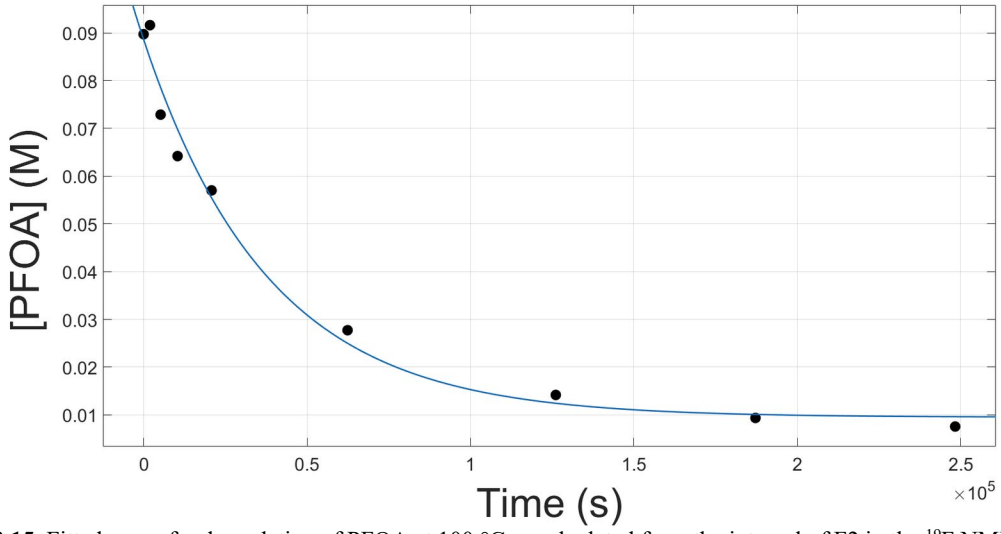

Figure S3.15. Fitted curve for degradation of PFOA at 100 °C as calculated from the integral of F2 in the ^{19}F NMR over time. Data is average of triplicate runs (see **Figure S21**).

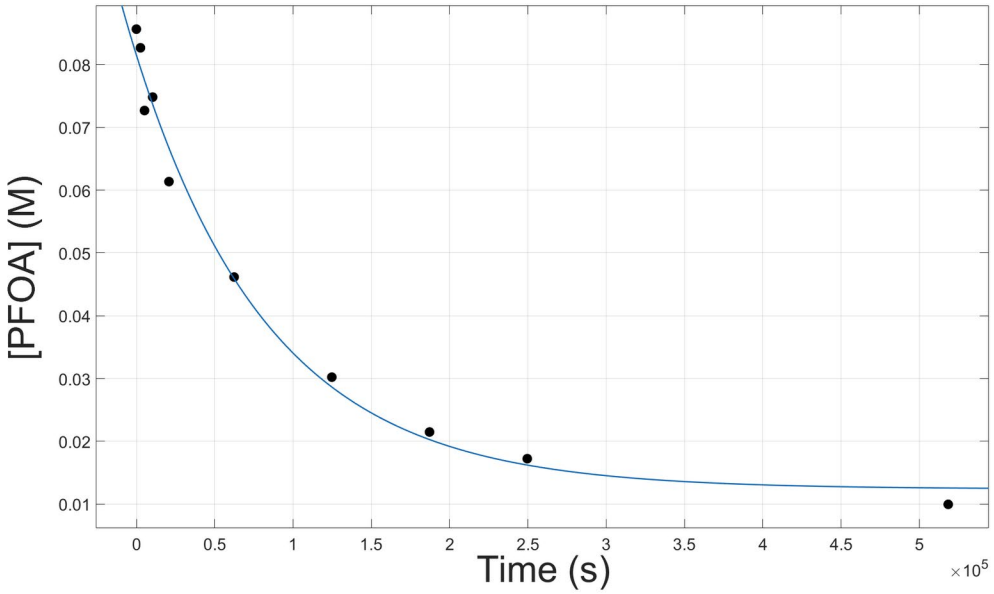

Figure S3.16. Fitted curve for degradation of PFOA at 90 °C as calculated from the integral of F2 in the ^{19}F NMR over time. Data is average of duplicate runs.

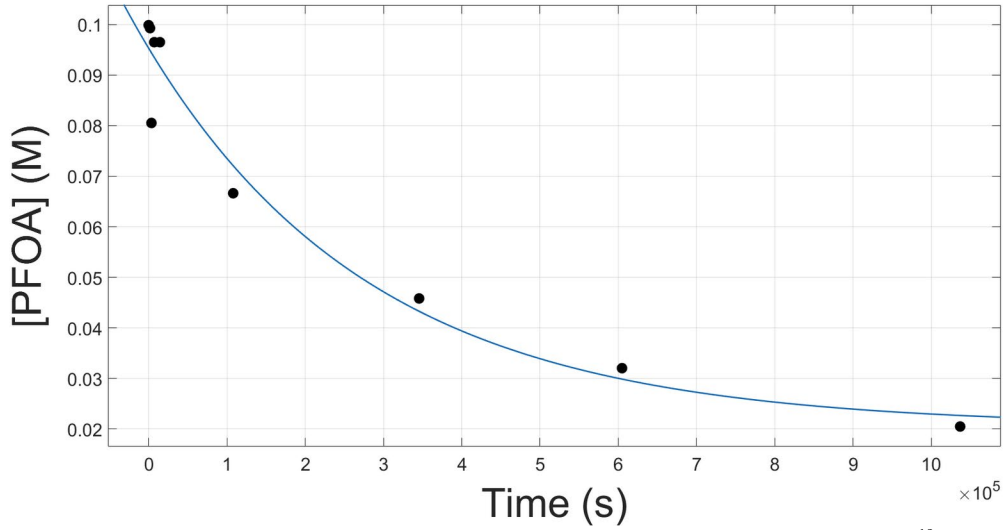

Figure S3.17. Fitted curve for degradation of PFOA at 80 °C as calculated from the integral of F2 in the ^{19}F NMR over time. Data from single trial.

Table S3.2. Summary of kinetic fitting parameters for degradation of PFOA at various temperatures.

°C	a	b	c	k	adjusted R^2	trial replicates
80	0.07476	2.90 x 10^5	0.02057	3.45 x 10^{-6}	0.9466	single run
90	0.06934	8.62 x 10^4	0.01227	1.16 x 10^{-5}	0.9842	duplicate
100	0.07908	3.82 x 10^4	0.00953	2.62x 10^{-5}	0.9813	triplicate
120	0.08268	6.32 x 10^3	0.00449	1.58 x 10^{-4}	0.9949	triplicate

Kinetic fitting parameters for PFOA degradation at different temperatures (**Figures S25–S28**) as fitted to the equation $y = ae^{-x/b} + c$ in MATLAB using the Curve Fitting application.

Experimental Determination of $\Delta G^{\ddagger}$

Using the Eyring equation:

$$k = \frac{\kappa k_B T}{h} e^{-\frac{\Delta G^{\ddagger}}{RT}}$$

where
κ is the transmission coefficient, assumed to be 1 in this case
k_B is the Boltzmann constant (1.38 x 10^{-23} J/K)
T is the temperature in Kelvin
h is Planck's constant (6.626 x 10^{-34} J•s)
$\Delta G^{\ddagger}$ is the Gibbs energy of activation
R is the gas constant (8.3145 J/mol•K, or 1.987 cal/mol•K)

$\Delta G^{\ddagger}_{393}$ = 30.0 kcal/mol

3.7.5. Quantification of Carbon-Containing Byproducts

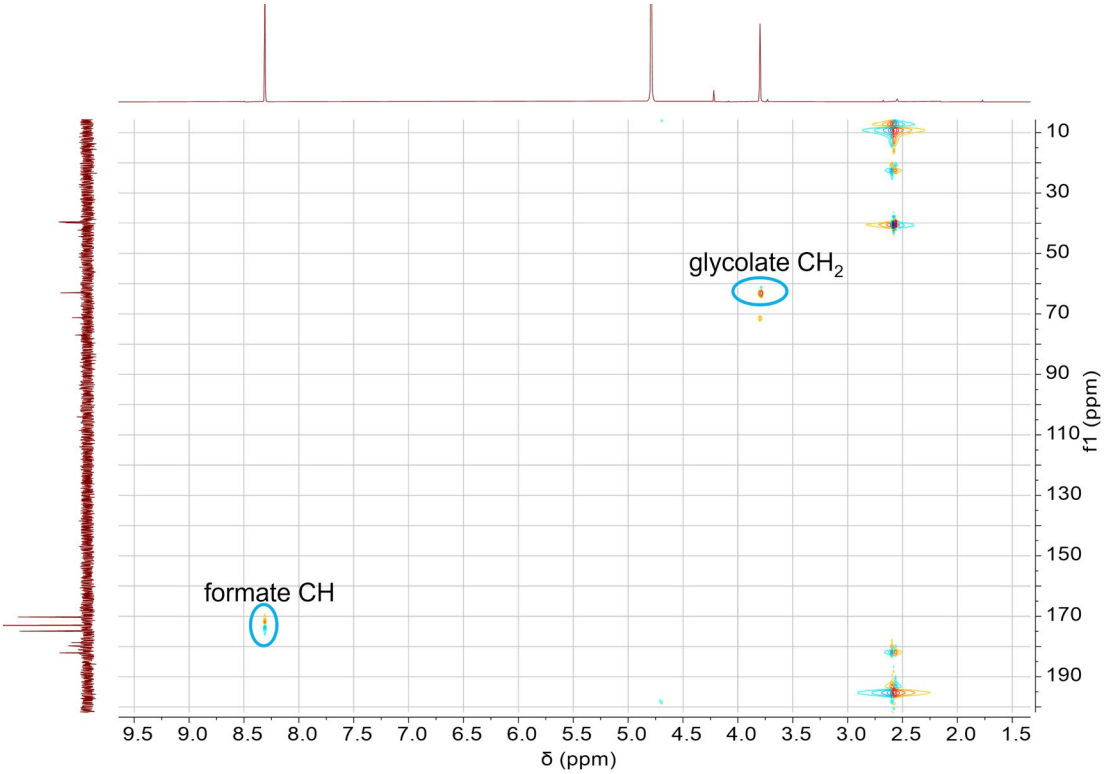

Figure S3.18. HSQC of isolated PFOA reaction precipitate dissolved in D_2O with 30 µL DMSO standard allows for identification of some carbonaceous byproducts

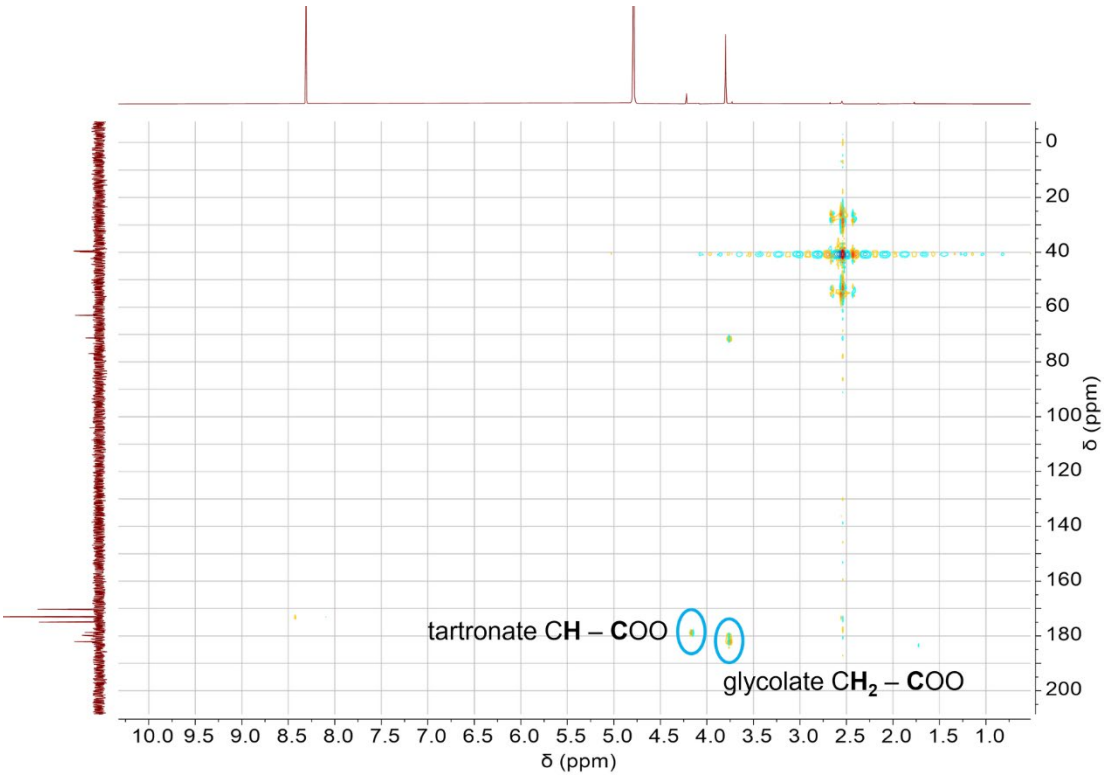

Figure S3.19. HMBC of isolated PFOA reaction precipitate dissolved in D_2O with 30 µL DMSO standard allows for identification of some carbonaceous byproducts

3.7.6. Mass Spectrometry of PFAS Degradation Reactions

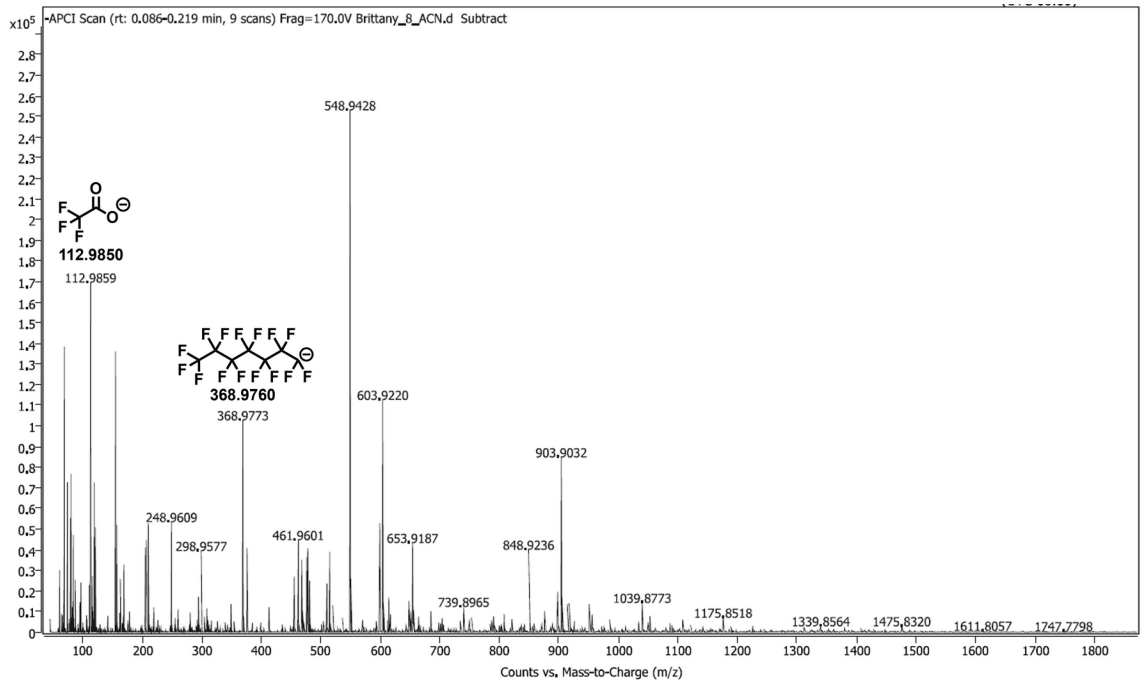

Figure S3.20. APCI-MS spectrum of an aliquot of PFOA degradation reaction diluted in acetonitrile after 4 hours of heating at 120 °C.

3.7.7. XYZ Coordinates of Optimized DFT Structures and Corresponding Energies

1
E(DMSO)[M06-2X/6-311++G(2d,p), SMD (DMSO)] = -1953.114266 a.u.
Gcorr(DMSO)[M06-2X/6-311++G(2d,p)] = 0.04928 a.u.
Hcorr(DMSO)[M06-2X/6-311++G(2d,p)] = 0.121697 a.u.
G = E(DMSO) + Gcorr= -1953.064986 a.u.
H = E(DMSO) + Hcorr= -1952.992569 a.u.

C	4.77319800	-0.14754100	-0.41572100
O	4.99396900	-1.35866900	-0.28532200
O	5.35808600	0.74082100	-1.03988300
C	3.49173700	0.31425800	0.36442500
C	2.21099300	-0.33527800	-0.19594800
C	0.90948200	0.41123100	0.19183200
C	-0.35828100	-0.46657000	0.02986500
C	-1.65660300	0.37668700	-0.05226800
C	-2.92111200	-0.45864700	0.26857600
F	3.57861600	-0.01994200	1.67645900
F	3.30982400	1.65580900	0.31415800
F	2.10506900	-1.59966000	0.24397000
F	2.28513100	-0.35233000	-1.53930200
F	0.98404700	0.80155100	1.47151100
F	0.77205400	1.49476600	-0.58732000
F	-0.45306600	-1.29427300	1.07907300
F	-0.25547400	-1.19109700	-1.09131100
F	-1.58565800	1.38571700	0.82494300
F	-1.76838200	0.88147700	-1.28727300
F	-3.02614600	-0.59122200	1.59351900
F	-2.81202300	-1.67120500	-0.28803000
C	-4.22286600	0.18965800	-0.25218100
F	-5.26027900	-0.42597300	0.29344300
F	-4.25502700	1.47277400	0.08319900
F	-4.30487900	0.08027400	-1.56813100

TS1
E(DMSO)[M06-2X/6-311++G(2d,p), SMD (DMSO)] = -1953.064359 a.u.
Gcorr(DMSO)[M06-2X/6-311++G(2d,p)] = 0.043547 a.u.
Hcorr(DMSO)[M06-2X/6-311++G(2d,p)] = 0.117816 a.u.
G = E(DMSO) + Gcorr= -1953.020812 a.u.
H = E(DMSO) + Hcorr= -1952.946543 a.u.

C	5.26639900	-1.02744200	-0.44095600
O	5.24462100	-1.69568800	0.51083500
O	5.47305900	-0.55548200	-1.48326400
C	3.49279300	0.71512700	0.22183100
C	2.21531900	-0.11407300	0.23781200
C	0.86447100	0.57927700	-0.07360200
C	-0.37831900	-0.21760500	0.39840000
C	-1.68647200	0.22667800	-0.30408500
C	-2.95322900	-0.20579400	0.47556500
F	3.35660700	1.58800400	1.32213500
F	3.31170500	1.58012400	-0.87998900
F	2.08789900	-0.70222100	1.45469700
F	2.33866300	-1.10585800	-0.68603500
F	0.81918400	1.78220100	0.52123700
F	0.75319000	0.75985000	-1.40370200
F	-0.53213200	-0.04607800	1.72069800
F	-0.19852500	-1.52194000	0.14852100
F	-1.70290100	1.56112000	-0.41781800
F	-1.72831000	-0.31176400	-1.53029000
F	-3.14819700	0.64246100	1.48955400
F	-2.78593400	-1.44186100	0.96239200
C	-4.23005200	-0.20709100	-0.39301100
F	-5.28830000	-0.31602000	0.39604200
F	-4.31495300	0.92642900	-1.07727600
F	-4.22209700	-1.22612600	-1.23708800

INT1
E(DMSO)[M06-2X/6-311++G(2d,p), SMD (DMSO)] = -1764.479498 a.u.
Gcorr(DMSO)[M06-2X/6-311++G(2d,p)] = 0.036801 a.u.
Hcorr(DMSO)[M06-2X/6-311++G(2d,p)] = 0.103691 a.u.
G = E(DMSO) + Gcorr= -1764.442697 a.u.
H = E(DMSO) + Hcorr= -1764.375807 a.u.

C	4.20136300	-0.07233900	-0.00445300
C	2.83164800	0.42295900	0.43959700
C	1.56266200	-0.32894200	-0.04082800
C	0.25904600	0.50309200	0.07037800
C	-1.02088600	-0.37158200	0.04869000
C	-2.28678900	0.43862600	-0.32651600
F	4.20180200	0.13803900	-1.40261700
F	4.07114800	-1.48454600	0.08504900

F	2.69167500	1.71959800	0.05781800
F	2.78032500	0.38938100	1.79756900
F	1.69632200	-0.69296300	-1.32586500
F	1.39962300	-1.44348600	0.69838500
F	0.19948000	1.36368300	-0.95798200
F	0.26304700	1.19806300	1.21636300
F	-0.87710200	-1.35619300	-0.84813800
F	-1.19805000	-0.91422100	1.26125500
F	-2.31609200	0.60691200	-1.65184500
F	-2.25123800	1.63740100	0.26884200
C	-3.59905800	-0.26008800	0.09090600
F	-4.61837600	0.34692900	-0.49767100
F	-3.57533800	-1.53125400	-0.28840900
F	-3.76588300	-0.19849100	1.40206200

TS2
E(DMSO)[M06-2X/6-311++G(2d,p), SMD (DMSO)] = -1764.447022 a.u.
Gcorr(DMSO)[M06-2X/6-311++G(2d,p)] = 0.035404 a.u.
Hcorr(DMSO)[M06-2X/6-311++G(2d,p)] = 0.102308 a.u.
G = E(DMSO) + Gcorr= -1764.411618 a.u.
H = E(DMSO) + Hcorr= -1764.344714 a.u.

C	-0.82274300	-0.11163400	-0.09904300
C	0.20325900	0.97896100	0.28582200
C	-2.27461700	0.43749000	-0.14228400
C	1.69236100	0.74541200	-0.11555000
F	0.10397200	1.22314900	1.59278700
F	-0.16788100	2.10641300	-0.36532800
F	-0.53776700	-0.58812700	-1.31830600
F	-0.78239700	-1.10891800	0.79064400
C	-3.33731400	-0.68073500	-0.04264500
F	-2.46707000	1.08065600	-1.29783900
F	-2.47917500	1.28649000	0.87256100
C	2.36530000	-0.57268300	0.22257600
F	1.74282900	0.91116900	-1.45961000
F	2.35679200	1.77581600	0.44318900
F	-4.51684600	-0.19033300	-0.39407000
F	-3.02580300	-1.67998200	-0.85816000
F	-3.42051600	-1.13914500	1.19597300
C	3.72300800	-0.64996500	0.05187500
F	1.63311100	-1.64256100	-0.19744300
F	1.86944200	-0.67662000	1.79144300

F	4.25417600	-1.83329100	-0.36778200
F	4.40429500	0.37738400	-0.53522500

INT2
E(DMSO)[M06-2X/6-311++G(2d,p), SMD (DMSO)] = -1664.501639 a.u.
Gcorr(DMSO)[M06-2X/6-311++G(2d,p)] = 0.036315 a.u.
Hcorr(DMSO)[M06-2X/6-311++G(2d,p)] = 0.101983 a.u.
G = E(DMSO) + Gcorr= -1664.465324 a.u.
H = E(DMSO) + Hcorr= -1664.399656 a.u.

C	2.79182500	-1.38547500	-0.15575400
C	2.45240100	-0.25186600	0.43257700
C	1.88800700	0.96251700	-0.22925700
C	0.40364500	1.23924400	0.12607100
F	2.56932700	-0.13964300	1.75793600
F	0.33995200	1.62953200	1.40445800
F	-0.03546800	2.23586700	-0.65506900
F	3.25921700	-2.40255900	0.50943700
C	-0.51469100	0.00787700	-0.05549400
F	-0.33791600	-0.80537500	0.99625400
F	-0.16178700	-0.64954300	-1.16842500
C	-2.01171900	0.38408000	-0.16098700
F	-2.29093800	1.35645800	0.71527300
F	-2.25885700	0.82167300	-1.39836100
C	-2.95589200	-0.80551200	0.12330600
F	-2.97440500	-1.08755300	1.41557700
F	-4.18115500	-0.48744800	-0.26365300
F	-2.55174200	-1.87340600	-0.55231200
F	1.98624300	0.87591500	-1.56196100
F	2.69864900	-1.62796800	-1.42990800
F	2.56983000	2.05347400	0.17711400

INT3
E(DMSO)[M06-2X/6-311++G(2d,p), SMD (DMSO)] = -1740.492919 a.u.
Gcorr(DMSO)[M06-2X/6-311++G(2d,p)] = 0.048745 a.u.
Hcorr(DMSO)[M06-2X/6-311++G(2d,p)] = 0.116177 a.u.
G = E(DMSO) + Gcorr= -1740.444174 a.u.
H = E(DMSO) + Hcorr= -1740.376742 a.u.

C	3.52727300	-0.71427400	-0.20976100

C	2.06967600	-0.60524100	0.00297300
C	1.54219700	0.75507400	-0.16253100
C	0.09162000	0.94877700	0.34132700
F	1.85754300	-0.97539300	1.36316300
F	0.05691800	0.95333000	1.68204300
F	-0.33769600	2.15998900	-0.08081100
F	4.30247000	-0.06675200	0.75994100
C	-0.92825700	-0.09503000	-0.16654900
F	-0.79411900	-1.23216900	0.52993200
F	-0.71603300	-0.34865700	-1.46469300
C	-2.39656900	0.38613500	-0.02637800
F	-2.56591400	1.03095800	1.13565700
F	-2.68346300	1.22032900	-1.03198500
C	-3.41809800	-0.77279600	-0.07349600
F	-3.40348400	-1.45887800	1.05836300
F	-4.63308300	-0.27254500	-0.24950200
F	-3.13951100	-1.58930800	-1.08160600
F	1.55702200	1.14383100	-1.46383700
F	3.93091700	-2.02442400	-0.02957000
O	3.91283500	-0.27123000	-1.42531500
H	4.88238600	-0.26461800	-1.45210500
F	2.22264400	1.79508700	0.49747400

TS3
E(DMSO)[M06-2X/6-311++G(2d,p), SMD (DMSO)] = -1740.477606 a.u.
Gcorr(DMSO)[M06-2X/6-311++G(2d,p)] = 0.047194 a.u.
Hcorr(DMSO)[M06-2X/6-311++G(2d,p)] = 0.115023 a.u.
G = E(DMSO) + Gcorr= -1740.430412 a.u.
H = E(DMSO) + Hcorr= -1740.362583 a.u.

C	2.95074000	1.04895900	0.04882200
C	2.40012100	-0.08645300	-0.49282000
C	1.68908300	-1.16609300	0.18537100
C	0.17858400	-1.32834400	-0.13748800
F	2.15632900	-0.07631700	-1.84936300
F	0.03468300	-1.71038700	-1.41554300
F	-0.33170700	-2.30059800	0.64817800
F	1.84046500	2.35805900	0.36846600
C	-0.66310000	-0.05466200	0.08586500
F	-0.43511700	0.80034700	-0.92069400
F	-0.30968800	0.52018600	1.24150900
C	-2.18500300	-0.34239600	0.15370500

F	-2.52449100	-1.26042500	-0.76085600
F	-2.48651500	-0.80931100	1.37007000
C	-3.04822400	0.91411800	-0.09645000
F	-3.03801500	1.24126200	-1.37889600
F	-4.29741500	0.66144600	0.26732400
F	-2.58990200	1.93395300	0.61766200
F	1.79836700	-1.08890100	1.52698300
F	3.35215100	0.95382800	1.33264500
O	3.77924500	1.76012300	-0.73070800
H	3.57955800	2.69379000	-0.56408500
F	2.19233100	-2.41042700	-0.16662800

INT4E(DMSO)[M06-2X/6-311++G(2d,p), SMD (DMSO)] = -1640.497449 a.u.
G_{corr}(DMSO)[M06-2X/6-311++G(2d,p)] = 0.047743 a.u.
H_{corr}(DMSO)[M06-2X/6-311++G(2d,p)] = 0.114179 a.u.
G = E(DMSO) + G_{corr} = -1640.449706 a.u.
H = E(DMSO) + H_{corr} = -1640.38327 a.u.

C	2.85944600	-1.34885300	-0.15502800
C	2.44201300	-0.23105600	0.42926800
C	1.87396400	0.97858800	-0.22393300
C	0.38627500	1.24064500	0.12945200
F	2.47974300	-0.13723100	1.76898500
F	0.31163100	1.61993900	1.41129500
F	-0.06193500	2.24174400	-0.64344100
F	3.25806300	-2.35025900	0.61297600
C	-0.52391900	0.00597900	-0.06704000
F	-0.34021800	-0.82302000	0.97151800
F	-0.17427900	-0.63238200	-1.19168900
C	-2.02445300	0.37311700	-0.16083300
F	-2.31043800	1.32715800	0.73340200
F	-2.28020700	0.83162800	-1.38931600
C	-2.95925300	-0.82838400	0.10415800
F	-2.97465900	-1.13273500	1.39150600
F	-4.18761300	-0.51281000	-0.27576200
F	-2.54915400	-1.88238200	-0.58964100
F	1.97355700	0.91194700	-1.55764500
O	2.96269000	-1.56782300	-1.45017900
H	2.84212300	-2.51618500	-1.63477500
F	2.53683300	2.08490700	0.19113900

INT5

E(DMSO)[M06-2X/6-311++G(2d,p), SMD (DMSO)] = -1640.061417 a.u.
G_{corr}(DMSO)[M06-2X/6-311++G(2d,p)] = 0.035336 a.u.
H_{corr}(DMSO)[M06-2X/6-311++G(2d,p)] = 0.100773 a.u.
G = E(DMSO) + G_{corr} = -1640.026081 a.u.
H = E(DMSO) + H_{corr} = -1639.960644 a.u.

C	2.86156400	-1.39937900	-0.32407400
C	2.51872700	-0.25233000	0.35189000
C	1.91802900	0.94832900	-0.21894500
C	0.43741200	1.20964100	0.16452900
F	2.45242400	-0.25473500	1.72901700
F	0.36361500	1.53120700	1.46573500
F	-0.03308700	2.25363400	-0.54970400
F	3.20911300	-2.40409200	0.59355000
C	-0.49104300	-0.00232300	-0.07900800
F	-0.32299800	-0.88490700	0.91847800
F	-0.17325800	-0.59672000	-1.23580400
C	-1.98807500	0.38873300	-0.14047700
F	-2.26011300	1.30454000	0.79849400
F	-2.25505800	0.90602100	-1.34439000
C	-2.93823100	-0.80952600	0.08020600
F	-2.95393500	-1.16606400	1.35468300
F	-4.16521800	-0.46100000	-0.27894300
F	-2.55115900	-1.84256600	-0.65686700
F	1.98220600	0.95701400	-1.56346300
O	2.93798500	-1.68812300	-1.49814500
F	2.55033700	2.10279100	0.21148400

TS4
E(DMSO)[M06-2X/6-311++G(2d,p), SMD (DMSO)] = -1640.040513 a.u.
G_{corr}(DMSO)[M06-2X/6-311++G(2d,p)] = 0.033828 a.u.
H_{corr}(DMSO)[M06-2X/6-311++G(2d,p)] = 0.099765 a.u.
G = E(DMSO) + G_{corr} = -1640.006685 a.u.
H = E(DMSO) + H_{corr} = -1639.940748 a.u.

C	3.64600700	-0.98767500	-0.32728100
C	2.43813000	-0.46540400	0.27784500
C	1.74322400	0.57128200	-0.21546300
C	0.36278000	0.95668300	0.28505400
F	2.06730800	-1.00740800	1.45156200
F	0.31331600	1.01500100	1.61903500

F	-0.01761800	2.13333800	-0.23435600
F	4.13970200	-2.00954700	0.40452000
C	-0.68408900	-0.08625100	-0.18618200
F	-0.51700400	-1.21656500	0.51590300
F	-0.46603800	-0.35292300	-1.48351800
C	-2.15070700	0.38731200	-0.03979900
F	-2.31006200	1.04701400	1.11412400
F	-2.44564400	1.20711200	-1.05411800
C	-3.16577300	-0.77781000	-0.06478500
F	-3.12910200	-1.45550200	1.07137000
F	-4.38542500	-0.28732100	-0.22847300
F	-2.89206400	-1.59846600	-1.07107100
F	1.99936000	1.02716100	-1.42132800
O	4.19361500	-0.64306600	-1.31978800
F	2.45589800	2.33763100	0.66990100

INT6

E(DMSO)[M06-2X/6-311++G(2d,p), SMD (DMSO)] = -1540.049441 a.u.

G_{corr}(DMSO)[M06-2X/6-311++G(2d,p)] = 0.034397 a.u.

H_{corr}(DMSO)[M06-2X/6-311++G(2d,p)] = 0.098281 a.u.

$G = E(DMSO) + G_{corr}$ = -1540.015044 a.u.

$H = E(DMSO) + H_{corr}$ = -1539.95116 a.u.

C	4.00480900	-0.38827400	-0.39493400
C	2.66942000	-0.31640900	0.23667900
C	1.80938000	0.67256200	0.02369800
C	0.43217600	0.76996300	0.64636300
F	2.35681600	-1.31945300	1.04395800
F	0.43465400	0.25407000	1.88055900
F	0.07358700	2.06185400	0.71307600
O	4.48470800	0.38359600	-1.14442700
F	4.64764600	-1.48819500	-0.00208300
C	-0.62170800	0.02405000	-0.20443800
F	-0.42409400	-1.29220600	-0.05025200
F	-0.42197200	0.34393200	-1.49026400
C	-2.08275400	0.37803600	0.16290200
F	-2.20745700	0.47562600	1.49153800
F	-2.39035700	1.55392000	-0.39183300
C	-3.10126600	-0.66905500	-0.33975100
F	-3.03953400	-1.76741900	0.39504700
F	-4.32182900	-0.16392900	-0.25397200
F	-2.84747000	-0.97512200	-1.60559300

F	2.08023300	1.66203100	-0.79992700

INT7
E(DMSO)[M06-2X/6-311++G(2d,p), SMD (DMSO)] = -1616.058051 a.u.
G_{corr}(DMSO)[M06-2X/6-311++G(2d,p)] = 0.048909 a.u.
H_{corr}(DMSO)[M06-2X/6-311++G(2d,p)] = 0.113731 a.u.
G = E(DMSO) + G_{corr} = -1616.009142 a.u.
H = E(DMSO) + H_{corr} = -1615.94432 a.u.

C	3.64735000	-0.76575300	0.33815800
C	2.43300500	-0.55062700	-0.23628300
C	1.83826900	0.78746900	-0.37380200
C	0.41263400	0.94973400	0.22607100
F	1.76861200	-1.56303700	-0.87608100
F	0.50958400	0.88539900	1.56751200
F	-0.05331800	2.17918000	-0.09195400
O	4.41458300	0.03812800	0.88481000
F	4.05143900	-2.07921800	0.29957000
C	-0.67056900	-0.07243300	-0.19122900
F	-0.48787800	-1.21029900	0.49981800
F	-0.59608600	-0.34402800	-1.50002700
C	-2.10954400	0.43160000	0.09249300
F	-2.15635000	1.06735500	1.27048400
F	-2.47634800	1.27898800	-0.87577900
C	-3.15313500	-0.70778300	0.13726900
F	-3.04344300	-1.40256100	1.25876200
F	-4.36930900	-0.18286100	0.08233200
F	-2.99049300	-1.52236000	-0.89734500
F	1.63437400	1.08945700	-1.74006200
O	2.59354100	1.76810100	0.18396500
H	3.42988300	1.35278100	0.51864300

INT8
E(DMSO)[M06-2X/6-311++G(2d,p), SMD (DMSO)] = -1515.607827 a.u.
G_{corr}(DMSO)[M06-2X/6-311++G(2d,p)] = 0.033937 a.u.
H_{corr}(DMSO)[M06-2X/6-311++G(2d,p)] = 0.097523 a.u.
G = E(DMSO) + G_{corr} = -1515.57389 a.u.
H = E(DMSO) + H_{corr} = -1515.510304 a.u.

C	3.95805700	-0.46657700	-0.32059100

C	2.65602400	-0.25512500	0.18137600
C	1.87832600	0.87068800	-0.09976600
C	0.45616400	0.90512600	0.54274300
F	2.14775700	-1.23574100	0.99186300
F	0.45882500	0.52088200	1.83728600
F	-0.00824200	2.17102400	0.50454400
O	4.64975200	0.19516300	-1.03768500
F	4.46636700	-1.67092600	0.13406500
C	-0.57073000	0.04207400	-0.21899600
F	-0.37154700	-1.25396700	0.06601900
F	-0.38928000	0.21895700	-1.53802100
C	-2.04479100	0.39409700	0.10126600
F	-2.18480800	0.65026000	1.40859100
F	-2.39779200	1.48059100	-0.59509000
C	-3.03142600	-0.73643800	-0.26365600
F	-2.94235500	-1.73577600	0.60005800
F	-4.26920000	-0.26202400	-0.23597500
F	-2.77249300	-1.18971900	-1.48388600
O	2.16964300	1.83419700	-0.80473200

TS5

E(DMSO)[M06-2X/6-311++G(2d,p), SMD (DMSO)] = -1591.504072 a.u.

G_{corr}(DMSO)[M06-2X/6-311++G(2d,p)] = 0.041853 a.u.

H_{corr}(DMSO)[M06-2X/6-311++G(2d,p)] = 0.10965 a.u.

G = E(DMSO) + G_{corr} = -1591.462219 a.u.

H = E(DMSO) + H_{corr} = -1591.394422 a.u.

C	-3.55065200	-1.10358500	0.30517800
C	-2.48993100	-0.38360700	-0.22727100
C	-1.77385500	0.63902700	0.45404900
C	-0.38817600	1.01800200	-0.13633400
F	-2.16891200	-0.62442700	-1.54439400
F	-0.31388900	1.17719500	-1.46901600
F	0.08197200	2.14154100	0.44759000
O	-4.08911600	-1.12153900	1.38551100
O	-1.97033700	0.99501200	1.61300700
O	-2.52225300	2.52336000	-0.77685800
H	-2.96972700	2.70695200	0.05448800
F	-4.05851600	-2.00612900	-0.65370200
C	0.64681000	-0.08927500	0.20360200
F	0.46704700	-1.13365900	-0.62919100
F	0.47111000	-0.53151000	1.46036700

C	2.12270700	0.36782600	0.09398500
F	2.29796400	1.16771800	-0.96662800
F	2.45577900	1.04277500	1.20273000
C	3.11929400	-0.80271800	-0.04785500
F	3.05178300	-1.33692700	-1.25823800
F	4.35268300	-0.35107300	0.14357300
F	2.86366800	-1.74057500	0.85581000

INT9

E(DMSO)[M06-2X/6-311++G(2d,p), SMD (DMSO)] = -1591.521889 a.u.

G_{corr}(DMSO)[M06-2X/6-311++G(2d,p)] = 0.046575 a.u.

H_{corr}(DMSO)[M06-2X/6-311++G(2d,p)] = 0.112254 a.u.

G = E(DMSO) + G_{corr} = -1591.475314 a.u.

H = E(DMSO) + H_{corr} = -1591.409635 a.u.

C	-3.49910600	-0.98126500	-0.08961200
C	-3.05978200	0.30120300	-0.07538800
C	-1.70528300	0.90032900	0.28256400
C	-0.56218700	-0.14080600	0.03239500
F	-0.70825000	-0.86140200	-1.11139100
O	-2.97545200	-2.08975900	-0.00571300
O	-1.60777100	1.42784000	1.47489800
O	-1.43219100	1.90002700	-0.77486900
H	-1.15792200	2.65593800	-0.24174300
F	-4.93818200	-1.02175400	-0.26501000
F	-0.49783200	-1.03411200	1.05402000
F	-4.02234100	1.30357600	-0.12479600
C	0.85926400	0.48586500	-0.09306900
C	1.98805700	-0.49665800	0.31067000
C	3.38840400	-0.07823000	-0.19295000
F	1.10247500	0.83244800	-1.37513100
F	1.01958700	1.58087800	0.66196500
F	1.75183500	-1.71966800	-0.18989300
F	2.05848500	-0.57629600	1.64683700
F	3.50746100	-0.28956800	-1.49576000
F	3.62252700	1.20324600	0.05958400
F	4.30701600	-0.80661900	0.43286000

INT10

E(DMSO)[M06-2X/6-311++G(2d,p), SMD (DMSO)] = -1592.038358 a.u.

G_{corr}(DMSO)[M06-2X/6-311++G(2d,p)] = 0.059893 a.u.

H_{corr}(DMSO)[M06-2X/6-311++G(2d,p)] = 0.126051 a.u.
G = E(DMSO) + G_{corr} = -1591.978465 a.u.
H = E(DMSO) + H_{corr} = -1591.912307 a.u.

C	3.48130100	0.99458200	-0.13578200
C	3.00824300	-0.35075600	-0.59820500
C	1.72444400	-0.80230100	0.21959300
C	0.52915900	0.12952300	-0.19205800
F	0.58400000	0.49874700	-1.50129400
O	3.09937700	2.04999800	-0.50420200
O	1.91682200	-0.84283300	1.49071700
O	1.38583200	-2.07010200	-0.39720900
H	1.40928000	-2.67833600	0.35233300
F	4.43040300	0.91400100	0.81209700
F	0.56567700	1.27261200	0.53350000
F	3.98507900	-1.28644500	-0.34073500
H	2.83683000	-0.31502200	-1.67296300
C	-0.87200600	-0.49706100	0.01613700
C	-1.98761700	0.56519800	0.18583100
C	-3.41139300	0.00955200	-0.04160800
F	-1.20317200	-1.24676800	-1.05129200
F	-0.89973000	-1.27543500	1.10606500
F	-1.81155000	1.56523500	-0.69099600
F	-1.94669100	1.06053200	1.42923200
F	-3.63712600	-0.20149200	-1.32963800
F	-3.58036900	-1.12824400	0.62018900
F	-4.29709300	0.89441600	0.39984300

TS6
E(DMSO)[M06-2X/6-311++G(2d,p), SMD (DMSO)] = -1592.015604 a.u.
G_{corr}(DMSO)[M06-2X/6-311++G(2d,p)] = 0.055916 a.u.
H_{corr}(DMSO)[M06-2X/6-311++G(2d,p)] = 0.123535 a.u.
G = E(DMSO) + G_{corr} = -1591.959688 a.u.
H = E(DMSO) + H_{corr} = -1591.892069 a.u.

C	3.40535100	1.23498700	-0.23538400
C	3.40730700	-0.05592400	-0.72468400
C	1.50356000	-1.24088100	0.24159400
C	0.51788900	-0.11697800	-0.11523600
F	0.63707000	0.30533400	-1.38221800
O	2.94376000	2.26581800	-0.68160000

O	1.86683700	-1.42423000	1.37334200
O	1.51394400	-2.17159800	-0.72726600
H	2.02788600	-2.92717500	-0.39756300
F	3.97520400	1.30734800	1.04542900
F	0.70580000	0.91668600	0.71883100
F	4.22524400	-0.98939600	-0.11283100
H	3.24336500	-0.25501900	-1.77184000
C	-0.94784800	-0.59266700	0.06105800
C	-1.95711300	0.57327500	0.19856400
C	-3.41449900	0.15476200	-0.09286100
F	-1.29513800	-1.34155000	-0.99785800
F	-1.04515000	-1.35072300	1.16342100
F	-1.63937000	1.55900800	-0.65053100
F	-1.91169600	1.04324500	1.45001200
F	-3.59597000	-0.04130400	-1.38956900
F	-3.70808400	-0.96106000	0.56284100
F	-4.23185100	1.11717300	0.30972600

PFPeA
E(DMSO)[M06-2X/6-311++G(2d,p), SMD (DMSO)] = -1239.739617 a.u.
G_{corr}(DMSO)[M06-2X/6-311++G(2d,p)] = 0.022082 a.u.
H_{corr}(DMSO)[M06-2X/6-311++G(2d,p)] = 0.07736 a.u.
G = E(DMSO) + G_{corr} = -1239.717535 a.u.
H = E(DMSO) + H_{corr} = -1239.662257 a.u.

C	-2.84528300	-0.33932800	-0.18533300
C	-1.55377900	0.39824300	0.31645700
F	-1.54328100	0.49209200	1.66984500
O	-3.49607300	0.26394200	-1.04186500
O	-3.00368900	-1.43908200	0.36043000
F	-1.45781900	1.66187500	-0.16328500
C	-0.26921600	-0.34000300	-0.10458000
C	1.00501600	0.53627100	-0.05233700
C	2.31519100	-0.28067500	-0.03356500
F	-0.07098200	-1.40637200	0.68731600
F	-0.40887000	-0.77302200	-1.37142200
F	0.99094100	1.29891200	1.05060000
F	1.04349500	1.33001600	-1.12981000
F	2.50194900	-0.84839800	1.14819900
F	2.28377300	-1.22281200	-0.96805300
F	3.33707600	0.52927400	-0.27809800

S3
E(DMSO)[M06-2X/6-311++G(2d,p), SMD (DMSO)] = -351.821033 a.u.
G_{corr}(DMSO)[M06-2X/6-311++G(2d,p)] = 0.000198 a.u.
H_{corr}(DMSO)[M06-2X/6-311++G(2d,p)] = 0.033629 a.u.
G = E(DMSO) + G_{corr} = -351.820835 a.u.
H = E(DMSO) + H_{corr} = -351.787404 a.u.

C	-0.55908200	-0.15439300	0.00010700
C	0.66984400	-0.72503400	0.00079700
O	-1.69780600	-0.61418500	-0.00045400
F	-0.47296400	1.26951500	0.00024900
F	1.81257500	0.06099200	-0.00052400
H	0.86137900	-1.78451700	0.00068200

INT11
E(DMSO)[M06-2X/6-311++G(2d,p), SMD (DMSO)] = -1616.029125 a.u.
G_{corr}(DMSO)[M06-2X/6-311++G(2d,p)] = 0.045918 a.u.
H_{corr}(DMSO)[M06-2X/6-311++G(2d,p)] = 0.112973 a.u.
G = E(DMSO) + G_{corr} = -1615.983207 a.u.
H = E(DMSO) + H_{corr} = -1615.916152 a.u.

C	-2.45073400	-0.12081400	0.31984700
C	-1.58218700	0.77231300	-0.13154800
C	-0.19357100	0.98584300	0.41141000
C	0.84214900	0.02097000	-0.20800200
C	2.23404800	0.05799600	0.46848600
F	-1.83767800	1.57504300	-1.17010700
F	-0.14231100	0.81898400	1.74754800
F	0.19931100	2.24290800	0.13022900
F	0.37814900	-1.23203100	-0.10764700
F	0.97187600	0.32778900	-1.50914400
F	2.17772300	-0.64991500	1.60207600
F	2.58121600	1.31721300	0.76081500
F	-2.05810300	-0.89316200	1.33682100
C	-3.90122700	-0.38898400	-0.06953500
O	-4.72977700	-0.34775100	0.85789400
C	3.35164600	-0.54309500	-0.41158600
F	3.65443000	0.27902900	-1.40413900
F	4.43343900	-0.73208300	0.33003100
F	2.96327600	-1.70798800	-0.91332800

F	-3.69294800	-1.86259000	-0.57469400
O	-4.18535700	0.28386500	-1.24903600
H	-5.13509800	0.45694700	-1.20144100

INT12
E(DMSO)[M06-2X/6-311++G(2d,p), SMD (DMSO)] = -1515.589855 a.u.
G_{corr}(DMSO)[M06-2X/6-311++G(2d,p)] = 0.033678 a.u.
H_{corr}(DMSO)[M06-2X/6-311++G(2d,p)] = 0.097949 a.u.
G = E(DMSO) + G_{corr} = -1515.556177 a.u.
H = E(DMSO) + H_{corr} = -1515.491906 a.u.

C	2.70501900	0.32680800	0.21894000
C	1.86495000	-0.67348700	-0.02175500
C	0.49724100	-0.83722700	0.59441800
C	-0.58218500	-0.05553300	-0.19099800
C	-2.00636300	-0.10933300	0.40479000
F	2.12763200	-1.64702200	-0.89470900
F	0.46933400	-0.41743900	1.87202500
F	0.15925800	-2.14117900	0.57481200
F	-0.21067900	1.23180600	-0.24390900
F	-0.61321700	-0.55246100	-1.43829600
F	-2.01421700	0.55781800	1.56551600
F	-2.36353700	-1.38068500	0.62357300
F	2.28474100	1.25984900	1.08355700
C	4.10381500	0.56548800	-0.37622600
O	4.62862800	1.62794900	-0.01492100
O	4.51261200	-0.32880100	-1.13079700
C	-3.09752800	0.52065400	-0.48954100
F	-3.24903700	-0.17003400	-1.60864300
F	-4.24414700	0.50401200	0.17792800
F	-2.79497800	1.77562600	-0.78652300

TS7
E(DMSO)[M06-2X/6-311++G(2d,p), SMD (DMSO)] = -1515.550264 a.u.
G_{corr}(DMSO)[M06-2X/6-311++G(2d,p)] = 0.02953 a.u.
H_{corr}(DMSO)[M06-2X/6-311++G(2d,p)] = 0.094666 a.u.
G = E(DMSO) + G_{corr} = -1515.520734 a.u.
H = E(DMSO) + H_{corr} = -1515.455598 a.u.

C	-3.76516100	1.81778500	0.08597400

C	-2.84602400	-0.45921800	-0.18914100
C	-1.75231500	-1.20060800	-0.00278000
C	-0.53238600	-0.70707900	0.68684800
C	0.60362000	-0.29031500	-0.27799600
C	1.99062500	-0.13895100	0.39231200
F	-1.57022600	-2.48451600	-0.45189600
F	-0.00268600	-1.67985200	1.48661600
F	-0.80022500	0.35913700	1.45961900
F	0.72346800	-1.21237900	-1.24755500
F	0.27162200	0.87904300	-0.85071700
F	2.53952500	-1.35146700	0.53671300
F	1.86661100	0.42669300	1.60060000
O	-4.80452400	1.54525100	-0.36504200
O	-2.86736600	2.38938100	0.55824600
F	-3.80149400	-1.18756900	-0.88871700
C	2.97396100	0.72435700	-0.42718200
F	2.65309100	2.00638000	-0.34422700
F	2.95790000	0.35332900	-1.70140800
F	4.20032500	0.56310100	0.05054500

INT13
E(DMSO)[M06-2X/6-311++G(2d,p), SMD (DMSO)] = -1326.96338 a.u.
G_{corr}(DMSO)[M06-2X/6-311++G(2d,p)] = 0.022378 a.u.
H_{corr}(DMSO)[M06-2X/6-311++G(2d,p)] = 0.080251 a.u.
G = E(DMSO) + G_{corr} = -1326.941002 a.u.
H = E(DMSO) + H_{corr} = -1326.883129 a.u.

C	-3.47176500	0.74020000	-0.51052300
C	-2.60354900	-0.25360200	-0.31438500
C	-1.34945800	-0.34381400	0.48991800
C	-0.08346500	0.01459200	-0.32123200
C	1.25065800	-0.39262300	0.34775400
F	-2.80126700	-1.42900600	-0.99688700
F	-1.15679600	-1.60941400	0.95531700
F	-1.38210000	0.47618500	1.55954400
F	-0.14146100	-0.60195000	-1.51316700
F	-0.07602400	1.34202600	-0.53190000
F	1.45289200	-1.70182000	0.15415300
F	1.20335000	-0.15196600	1.66476000
F	-3.09910200	1.87979000	0.21170900
C	2.47490500	0.35763100	-0.21929600
F	3.58377000	-0.23441400	0.20247800

F	2.45315800	0.33270200	-1.54592600
F	2.48536200	1.61627800	0.19176200

INT14
E(DMSO)[M06-2X/6-311++G(2d,p), SMD (DMSO)] = -1327.4713 a.u.
G_{corr}(DMSO)[M06-2X/6-311++G(2d,p)] = 0.035704 a.u.
H_{corr}(DMSO)[M06-2X/6-311++G(2d,p)] = 0.094259 a.u.
G = E(DMSO) + G_{corr} = -1327.435596 a.u.
H = E(DMSO) + H_{corr} = -1327.377041 a.u.

C	-3.30856900	0.76929600	-0.47225000
C	-2.55846500	-0.30643600	-0.33208800
C	-1.32015600	-0.43751500	0.51244400
C	-0.05651000	-0.01923700	-0.27519600
C	1.27927700	-0.14274100	0.48879400
F	-2.85260300	-1.41748400	-1.01471800
F	-1.17934700	-1.71790300	0.89734700
F	-1.40856000	0.33566800	1.60721200
F	0.00376500	-0.78600500	-1.37504200
F	-0.21391700	1.26235500	-0.63862100
F	1.44367600	-1.40620900	0.89846300
F	1.25029400	0.66997500	1.55188900
F	-3.01521300	1.89668500	0.16959800
H	-4.18737200	0.81050400	-1.10273400
C	2.53117700	0.23125800	-0.33760900
F	3.59544700	0.10352600	0.44395900
F	2.66837900	-0.57681500	-1.37751900
F	2.46217200	1.48306700	-0.76277200

TS8
E(DMSO)[M06-2X/6-311++G(2d,p), SMD (DMSO)] = -1403.378123 a.u.
G_{corr}(DMSO)[M06-2X/6-311++G(2d,p)] = 0.042692 a.u.
H_{corr}(DMSO)[M06-2X/6-311++G(2d,p)] = 0.105958 a.u.
G = E(DMSO) + G_{corr} = -1403.335431 a.u.
H = E(DMSO) + H_{corr} = -1403.272165 a.u.

C	3.13720700	-0.50396000	-0.67834000
C	2.17523700	0.39481000	-0.49616700
C	0.98949100	0.30998700	0.39261000
C	-0.32811800	0.05375300	-0.37590700

C	-1.61301700	0.29979600	0.44898800
F	2.29175800	1.60482400	-1.09853700
F	0.81766000	1.47700100	1.06894700
F	1.13065000	-0.67868100	1.29362200
F	-0.36796800	0.86385500	-1.44543200
F	-0.32208100	-1.21881000	-0.80580300
F	-1.84569500	1.61624800	0.50776500
F	-1.45915000	-0.17048200	1.69358500
F	2.99862800	-1.74400600	-0.22231700
H	3.95752400	-0.34313000	-1.35621800
O	5.04261000	-0.26550200	0.69727400
H	5.06462000	0.68489500	0.85028300
C	-2.86734500	-0.36896700	-0.15354900
F	-3.94628300	0.10658900	0.45211000
F	-2.82856800	-1.68095100	0.01806100
F	-2.94936700	-0.10117200	-1.45067400

INT15

E(DMSO)[M06-2X/6-311++G(2d,p), SMD (DMSO)] = -1403.431621 a.u.

G_{corr}(DMSO)[M06-2X/6-311++G(2d,p)] = 0.048638 a.u.

H_{corr}(DMSO)[M06-2X/6-311++G(2d,p)] = 0.109148 a.u.

$G = E(DMSO) + G_{corr}$ = -1403.382983 a.u.

$H = E(DMSO) + H_{corr}$ = -1403.322473 a.u.

C	3.23094800	-0.17918300	-0.45600100
C	2.36769500	0.80003500	0.21252300
C	1.08532500	0.33852100	0.76426400
C	-0.17469600	0.41359200	-0.15051300
C	-1.35320600	-0.47392700	0.32100700
F	2.05683900	1.83180100	-0.73397300
F	0.69048000	1.08448900	1.87364700
F	1.17120600	-0.94237300	1.21531300
F	-0.61928600	1.68607300	-0.21488700
F	0.12311000	0.01803000	-1.39738200
F	-1.50715200	-0.40616800	1.65096200
F	-1.10543400	-1.74710500	-0.01928600
F	2.55796800	-1.06136900	-1.41280400
H	3.93494100	0.35039400	-1.10209100
O	3.85449200	-1.02984300	0.43306900
H	4.42331700	-1.62160400	-0.07584600
C	-2.70980500	-0.08687200	-0.30799100
F	-3.58857900	-1.05441300	-0.07310600

F	-2.59201800	0.07040400	-1.62026900
F	-3.17288600	1.03584900	0.22218900

TS9
E(DMSO)[M06-2X/6-311++G(2d,p), SMD (DMSO)] = -1403.428673 a.u.
G_{corr}(DMSO)[M06-2X/6-311++G(2d,p)] = 0.047464 a.u.
H_{corr}(DMSO)[M06-2X/6-311++G(2d,p)] = 0.107915 a.u.
G = E(DMSO) + G_{corr} = -1403.381209 a.u.
H = E(DMSO) + H_{corr} = -1403.320758 a.u.

C	3.31962800	-0.11971700	-0.29628100
C	2.30369300	0.77647100	0.04043600
C	1.05235400	0.42805100	0.70457800
C	-0.20399100	0.37431200	-0.21566600
C	-1.38657300	-0.42690700	0.38130100
F	2.05688900	1.74325500	-0.94844600
F	0.68441900	1.34230000	1.68589200
F	1.13354300	-0.76739200	1.33810000
F	-0.63627400	1.62395700	-0.47610200
F	0.10970000	-0.20763500	-1.38349200
F	-1.53714000	-0.15534900	1.68522400
F	-1.14319500	-1.73705200	0.23731700
F	2.89383200	-1.32401100	-1.40455900
H	4.06286200	0.31643100	-0.96084400
O	3.79950200	-0.90325400	0.71024000
H	4.32637200	-1.60021000	0.29863400
C	-2.73973900	-0.13377400	-0.30214000
F	-3.62695400	-1.04136600	0.08657400
F	-2.61712300	-0.19517300	-1.62207500
F	-3.19075200	1.06504200	0.03567000

INT16
E(DMSO)[M06-2X/6-311++G(2d,p), SMD (DMSO)] = -1303.465409 a.u.
G_{corr}(DMSO)[M06-2X/6-311++G(2d,p)] = 0.048309 a.u.
H_{corr}(DMSO)[M06-2X/6-311++G(2d,p)] = 0.10697 a.u.
G = E(DMSO) + G_{corr} = -1303.4171 a.u.
H = E(DMSO) + H_{corr} = -1303.358439 a.u.

C	-3.40871400	-0.65293200	-0.39597500
C	-2.53699300	0.34132200	-0.29137500

C	-1.27936100	0.38674600	0.51217200
C	-0.03129400	0.00458900	-0.31659300
C	1.31392300	0.37320800	0.35221800
F	-2.72723200	1.46647400	-1.01184800
F	-1.34931900	-0.45193400	1.55847400
F	-1.07282600	1.63952200	0.98270100
F	-0.06547800	-1.31898300	-0.53751100
F	-0.09106200	0.63557900	-1.49913900
F	1.25931200	0.11659100	1.66538500
F	1.54238200	1.67902000	0.17334400
H	-4.26866700	-0.51585900	-1.04424100
O	-3.27544900	-1.81968500	0.25437800
H	-4.02904200	-2.38668700	0.04402400
C	2.51652400	-0.40021000	-0.23048400
F	2.48428200	-0.35876100	-1.55640400
F	2.49676900	-1.66299400	0.16613400
F	3.64059200	0.16034100	0.19057800

INT17

E(DMSO)[M06-2X/6-311++G(2d,p), SMD (DMSO)] = -1302.996352 a.u.

G_{corr}(DMSO)[M06-2X/6-311++G(2d,p)] = 0.034948 a.u.

H_{corr}(DMSO)[M06-2X/6-311++G(2d,p)] = 0.092916 a.u.

G = E(DMSO) + G_{corr} = -1302.961404 a.u.

H = E(DMSO) + H_{corr} = -1302.903436 a.u.

C	-3.48302800	-0.73685300	-0.35404800
C	-2.58296400	0.29816900	-0.22843400
C	-1.32557300	0.34561300	0.51433100
C	-0.05677500	0.00747700	-0.31178700
C	1.29139800	0.36593000	0.35740600
F	-2.72913600	1.39515600	-1.06605100
F	-1.33915900	-0.51386400	1.55660700
F	-1.07728000	1.60540700	1.01884000
F	-0.06276500	-1.31290300	-0.57655400
F	-0.10526000	0.66658500	-1.48327700
F	1.25202600	0.09272500	1.66930200
F	1.52657200	1.67528200	0.19719300
H	-4.28016000	-0.48121700	-1.08416300
O	-3.51576300	-1.84468500	0.22785400
C	2.49632700	-0.39489300	-0.23559600
F	2.46592500	-0.34148800	-1.56175300
F	3.62187700	0.16552400	0.18817100

F	2.48830500	-1.66286300	0.14753300

TS10
E(DMSO)[M06-2X/6-311++G(2d,p), SMD (DMSO)] = -1302.977232 a.u.
G_{corr}(DMSO)[M06-2X/6-311++G(2d,p)] = 0.033502 a.u.
H_{corr}(DMSO)[M06-2X/6-311++G(2d,p)] = 0.091771 a.u.
G = E(DMSO) + G_{corr} = -1302.94373 a.u.
H = E(DMSO) + H_{corr} = -1302.885461 a.u.

C	3.82554900	-0.01249400	-0.40244400
C	2.51451900	0.50175700	-0.06904800
C	1.35412300	-0.18481100	-0.05147800
C	-0.00198900	0.48932200	0.00402500
C	-1.24718300	-0.37416300	0.38995600
F	2.51724800	1.79699600	0.34179500
F	0.96405700	-0.89317800	1.77842200
F	1.33141400	-1.37791500	-0.61942500
F	0.00922200	1.54711700	0.82358300
F	-0.23967000	0.97246400	-1.25299200
F	-1.55644800	-0.18937200	1.67678900
F	-1.07236900	-1.67794500	0.15534800
H	4.61497300	0.75596500	-0.31531700
O	4.08443200	-1.14614600	-0.74937300
C	-2.51546200	0.03708500	-0.39788900
F	-2.71213600	1.34837600	-0.31685300
F	-2.43906900	-0.31837000	-1.67210100
F	-3.56533200	-0.57783800	0.13783100

INT18
E(DMSO)[M06-2X/6-311++G(2d,p), SMD (DMSO)] = -1202.995254 a.u.
G_{corr}(DMSO)[M06-2X/6-311++G(2d,p)] = 0.033674 a.u.
H_{corr}(DMSO)[M06-2X/6-311++G(2d,p)] = 0.090349 a.u.
G = E(DMSO) + G_{corr} = -1202.96158 a.u.
H = E(DMSO) + H_{corr} = -1202.904905 a.u.

C	-3.71295900	-0.41482400	0.38207300
C	-2.30535500	-0.56888300	-0.07131200
C	-1.42550000	0.40661800	-0.26240500
C	0.00661000	0.22778200	-0.71423000
C	0.94886200	-0.01483100	0.48337200

F	-1.94384800	-1.83419500	-0.28379700
F	-1.73769300	1.66942800	-0.02882200
F	0.11790300	-0.81062500	-1.55465500
F	0.40535100	1.34295400	-1.34708100
F	0.60694100	-1.17816700	1.05209400
F	0.76838600	0.97797800	1.36587400
H	-4.24939400	-1.37257100	0.47379900
O	-4.21719700	0.64701400	0.62494500
C	2.45312900	-0.07738100	0.15261900
F	2.69582600	-1.02202800	-0.74323200
F	2.87796000	1.08718000	-0.31250400
F	3.12009000	-0.36079600	1.26389400

INT19

E(DMSO)[M06-2X/6-311++G(2d,p), SMD (DMSO)] = -1278.950611 a.u.

G_{corr}(DMSO)[M06-2X/6-311++G(2d,p)] = 0.04664 a.u.

H_{corr}(DMSO)[M06-2X/6-311++G(2d,p)] = 0.105728 a.u.

G = E(DMSO) + G_{corr} = -1278.903971 a.u.

H = E(DMSO) + H_{corr} = -1278.844883 a.u.

C	-3.48659200	-0.14403000	0.58515000
C	-2.05037400	-0.37155300	0.09002000
C	-1.11431800	0.50067000	-0.26249800
C	0.28168000	0.16408600	-0.71242200
C	1.26133900	0.04565000	0.47353300
F	-1.70526100	-1.67286500	0.04225200
F	-1.29964600	1.82637500	-0.20949700
F	0.32720300	-0.99374000	-1.39619900
F	0.74012600	1.14354600	-1.52253300
F	0.89210500	-1.00361700	1.22192200
F	1.16872400	1.16317200	1.21240000
H	-3.56529800	-0.82406700	1.46723500
O	-3.82564600	1.09449100	0.76500500
O	-4.30121300	-0.85080900	-0.42027300
H	-4.61435600	-0.11845700	-0.96665800
C	2.74907200	-0.14479300	0.12045200
F	2.92167900	-1.22040400	-0.63476500
F	3.22306200	0.91506500	-0.51762500
F	3.43753000	-0.30276600	1.24584000

TS11

E(DMSO)[M06-2X/6-311++G(2d,p), SMD (DMSO)] = -1278.926456 a.u.
G_{corr}(DMSO)[M06-2X/6-311++G(2d,p)] = 0.042154 a.u.
H_{corr}(DMSO)[M06-2X/6-311++G(2d,p)] = 0.103303 a.u.
G = E(DMSO) + G_{corr} = -1278.884302 a.u.
H = E(DMSO) + H_{corr} = -1278.823153 a.u.

C	-4.21059700	0.08318200	0.25786800
C	-2.02834100	0.01529200	0.08377900
C	-0.94069500	0.78017700	0.10932400
C	0.41471800	0.57884400	-0.48496700
C	1.37992900	-0.15999500	0.46399900
F	-1.85104900	-1.15368800	-0.62661400
F	-0.97892600	1.94611800	0.83061600
F	0.35236900	-0.14222400	-1.62492300
F	0.99112200	1.77079500	-0.78662600
F	0.87657000	-1.37810500	0.71793300
F	1.45594900	0.52770600	1.61628600
H	-4.19005300	0.88000200	1.00318600
O	-4.57701800	0.23989200	-0.89967000
O	-4.36364800	-1.12330100	0.88158900
H	-4.48725000	-1.77602400	0.17666200
C	2.82279100	-0.36560400	-0.03391800
F	2.84119100	-1.06092900	-1.16253000
F	3.42996900	0.79621200	-0.23095700
F	3.50233700	-1.04234100	0.88773500

S5
E(DMSO)[M06-2X/6-311++G(2d,p), SMD (DMSO)] = -1089.171999 a.u.
G_{corr}(DMSO)[M06-2X/6-311++G(2d,p)] = 0.013571 a.u.
H_{corr}(DMSO)[M06-2X/6-311++G(2d,p)] = 0.065611 a.u.
G = E(DMSO) + G_{corr} = -1089.158428 a.u.
H = E(DMSO) + H_{corr} = -1089.106388 a.u.

C	2.92762700	-0.46464300	-0.38160200
C	1.98371200	0.42757200	-0.07844400
C	0.63302400	0.27225600	0.54277300
C	-0.47067800	-0.02507400	-0.49249000
F	2.52670000	-1.75334400	-0.00581600
F	2.19322300	1.73853600	-0.42822900
F	0.60875900	-0.73154600	1.44639500
F	0.26541700	1.40853900	1.19052700

F	-0.19277200	-1.19371000	-1.09056600
F	-0.46167100	0.94947000	-1.41858500
C	-1.91233100	-0.12442300	0.04025700
F	-2.01182900	-1.06635900	0.96819100
F	-2.31352300	1.03096700	0.55148700
F	-2.72187100	-0.43967800	-0.96706600

Formate
E(DMSO)[M06-2X/6-311++G(2d,p), SMD (DMSO)] = -189.762029 a.u.
G_{corr}(DMSO)[M06-2X/6-311++G(2d,p)] = 0.01005 a.u.
H_{corr}(DMSO)[M06-2X/6-311++G(2d,p)] = 0.038226 a.u.
G = E(DMSO) + G_{corr} = -189.751979 a.u.
H = E(DMSO) + H_{corr} = -189.723803 a.u.

C	0.13093100	0.40154300	0.00004400
H	0.11314100	1.49760800	0.00042000
O	1.12633900	-0.26600400	-0.00005000
O	-1.10704000	-0.08963400	-0.00014700
H	-1.05312400	-1.06176500	0.00089000

INT20
E(DMSO)[M06-2X/6-311++G(2d,p), SMD (DMSO)] = -1278.999481 a.u.
G_{corr}(DMSO)[M06-2X/6-311++G(2d,p)] = 0.046262 a.u.
H_{corr}(DMSO)[M06-2X/6-311++G(2d,p)] = 0.103647 a.u.
G = E(DMSO) + G_{corr} = -1278.953219 a.u.
H = E(DMSO) + H_{corr} = -1278.895834 a.u.

C	3.38311700	0.90695200	-0.38062200
C	2.11874800	0.83336200	0.08547800
C	1.43628100	-0.45980800	0.31714800
C	0.00936900	-0.57368500	-0.31216900
C	-1.18327600	-0.03874800	0.51943400
F	1.40650600	1.97619900	0.33493400
F	1.13988700	-0.61794200	1.71997200
F	0.00157600	0.06360800	-1.50711100
F	-0.27212400	-1.86810400	-0.55658400
F	-0.88022300	1.09633100	1.15962500
F	-1.53750800	-0.96149200	1.42696400
H	3.80567200	1.90518500	-0.53919600
O	4.11099300	-0.13595900	-0.64946300

O	2.18858900	-1.47879400	-0.10352700
H	3.15837500	-1.05137600	-0.37695200
C	-2.43622000	0.25632500	-0.33493400
F	-3.47948600	0.43628900	0.46771000
F	-2.27044200	1.35736900	-1.05434000
F	-2.70027600	-0.75805500	-1.14960800

INT21
E(DMSO)[M06-2X/6-311++G(2d,p), SMD (DMSO)] = -1178.543293 a.u.
G_{corr}(DMSO)[M06-2X/6-311++G(2d,p)] = 0.033347 a.u.
H_{corr}(DMSO)[M06-2X/6-311++G(2d,p)] = 0.089702 a.u.
G = E(DMSO) + G_{corr} = -1178.509946 a.u.
H = E(DMSO) + H_{corr} = -1178.453591 a.u.

C	-3.66129800	-0.57836500	0.26114100
C	-2.30493500	-0.48179700	-0.13625900
C	-1.48688900	0.64841900	-0.14286100
C	-0.01537500	0.46064100	-0.62982400
C	0.90728600	-0.09181400	0.47122700
F	-1.76778500	-1.68361500	-0.55937300
F	0.08888400	-0.34511100	-1.71129000
F	0.48249900	1.66221500	-0.98769100
F	0.53117500	-1.33903700	0.79023600
F	0.78785000	0.68611100	1.56055900
H	-4.05257600	-1.61104900	0.15905500
O	-4.39266300	0.31528200	0.67977900
O	-1.78242900	1.79328500	0.20687600
C	2.40942900	-0.15415200	0.13047800
F	2.62037700	-0.89463500	-0.94934100
F	2.90755900	1.05722900	-0.07086500
F	3.05655300	-0.70705400	1.15268700

TS12
E(DMSO)[M06-2X/6-311++G(2d,p), SMD (DMSO)] = -1254.436548 a.u.
G_{corr}(DMSO)[M06-2X/6-311++G(2d,p)] = 0.042355 a.u.
H_{corr}(DMSO)[M06-2X/6-311++G(2d,p)] = 0.102135 a.u.
G = E(DMSO) + G_{corr} = -1254.394193 a.u.
H = E(DMSO) + H_{corr} = -1254.334413 a.u.

C	3.29765300	-1.15580600	0.18540900

C	2.15803000	-0.40054400	0.42682200
C	1.36933400	0.39248600	-0.46138800
C	-0.07502900	0.73057000	0.00828000
C	-0.97489200	-0.53040600	-0.07186400
F	1.78385400	-0.36085600	1.76819100
F	-0.22532300	1.18930700	1.26605600
F	-0.64128400	1.63257500	-0.82521900
F	-0.69666000	-1.34430700	0.96264300
F	-0.74923800	-1.20959600	-1.21068800
H	3.66685500	-1.62541500	1.12442500
O	3.91643700	-1.37675800	-0.87619000
O	1.55826400	0.48341300	-1.67588900
O	1.88757400	2.47288300	0.29470300
H	2.35113400	2.54184100	-0.54503700
C	-2.49374400	-0.26222400	-0.03070500
F	-2.82018900	0.53263100	0.98090900
F	-2.91404700	0.29038100	-1.16156400
F	-3.13759200	-1.41871000	0.12414800

INT22

E(DMSO)[M06-2X/6-311++G(2d,p), SMD (DMSO)] = -1254.450677 a.u.

G_{corr}(DMSO)[M06-2X/6-311++G(2d,p)] = 0.046842 a.u.

H_{corr}(DMSO)[M06-2X/6-311++G(2d,p)] = 0.104407 a.u.

G = E(DMSO) + G_{corr} = -1254.403835 a.u.

H = E(DMSO) + H_{corr} = -1254.34627 a.u.

C	-3.60472400	0.20469600	-0.31570100
C	-2.26286100	0.11700700	-0.55118000
C	-1.13388700	-0.71751300	-0.00605600
C	-0.09929200	0.26748100	0.76418600
C	1.20180500	0.70014200	0.05867100
F	-1.77125100	1.12676800	-1.41133900
F	-0.69434200	1.44366600	1.13009100
F	0.31340300	-0.29004200	1.93284000
F	0.93484400	1.35813800	-1.07630100
F	1.82633700	1.58993400	0.87528100
H	-4.03316800	1.03943000	-0.92086000
O	-4.40896600	-0.45899100	0.41411900
O	-1.44925200	-1.72750000	0.73321000
O	-0.29903800	-1.12504500	-1.17772100
H	-0.24291000	-2.07464400	-1.01635300
C	2.24590600	-0.42700200	-0.24917300

F	3.44517800	-0.06928500	0.22493600
F	1.93979700	-1.58574400	0.31962900
F	2.38963800	-0.61136400	-1.55337500

INT23

E(DMSO)[M06-2X/6-311++G(2d,p), SMD (DMSO)] = -1254.44469 a.u.

G_{corr}(DMSO)[M06-2X/6-311++G(2d,p)] = 0.045437 a.u.

H_{corr}(DMSO)[M06-2X/6-311++G(2d,p)] = 0.10404 a.u.

G = E(DMSO) + G_{corr} = -1254.399253 a.u.

H = E(DMSO) + H_{corr} = -1254.34065 a.u.

C	-3.47237900	-0.76819300	0.18740600
C	-2.15173700	-0.55488300	-0.47439400
C	-1.47766400	0.72081500	0.21940100
C	0.06222600	0.69941300	-0.29405000
C	1.12831800	-0.03062400	0.55787600
F	-1.43279200	-1.75887200	-0.26905300
F	0.20256300	0.20119000	-1.57655600
F	0.54060600	1.97584300	-0.36784900
F	0.72886100	-1.22041900	1.03209900
F	1.48899600	0.73952400	1.60524900
H	-3.41041500	-1.33381400	1.13432700
O	-4.53788000	-0.38306500	-0.22984500
O	-1.44382700	0.57386600	1.54789600
O	-2.06421500	1.77510000	-0.33605900
H	-2.24518300	-0.42283300	-1.55058200
C	2.44210500	-0.33513000	-0.19958300
F	2.28489500	-1.32838700	-1.06945800
F	2.89831600	0.73043100	-0.85117200
F	3.38164100	-0.71252600	0.67233900

TS13

E(DMSO)[M06-2X/6-311++G(2d,p), SMD (DMSO)] = -1254.442007 a.u.

G_{corr}(DMSO)[M06-2X/6-311++G(2d,p)] = 0.045413 a.u.

H_{corr}(DMSO)[M06-2X/6-311++G(2d,p)] = 0.10266 a.u.

G = E(DMSO) + G_{corr} = -1254.396594 a.u.

H = E(DMSO) + H_{corr} = -1254.339347 a.u.

C	-3.36582900	-0.56023400	-0.63110900
C	-2.36581700	0.44288700	-0.40274000

C	-1.06906600	-0.42029400	0.65363900
C	0.05800300	0.72949300	0.65974300
C	1.24331000	0.53654600	-0.30923000
F	-1.79425000	0.83455900	-1.63179700
F	-0.38199800	2.00577900	0.41856900
F	0.64914500	0.80637000	1.89194900
F	0.86058600	0.62890200	-1.58962600
F	2.09311300	1.58532400	-0.09908500
H	-3.19146600	-1.16541100	-1.54431500
O	-4.29398600	-0.84757400	0.11460200
O	-0.59359200	-1.41112300	-0.04140000
O	-1.61589000	-0.52279600	1.81127900
H	-2.67457700	1.32806100	0.14495000
C	2.10890700	-0.75514300	-0.16133200
F	1.86205700	-1.64151400	-1.11038800
F	3.40657700	-0.41933000	-0.30018100
F	1.99774200	-1.32789500	1.02830200

6

E(DMSO)[M06-2X/6-311++G(2d,p), SMD (DMSO)] = -1001.947909 a.u.

G_{corr}(DMSO)[M06-2X/6-311++G(2d,p)] = 0.012778 a.u.

H_{corr}(DMSO)[M06-2X/6-311++G(2d,p)] = 0.062475 a.u.

G = E(DMSO) + G_{corr} = -1001.935131 a.u.

H = E(DMSO) + H_{corr} = -1001.885434 a.u.

C	2.24000800	0.06429800	-0.17808200
C	0.83658100	-0.40555800	0.34174700
F	0.79646600	-0.41137000	1.69851400
O	2.79163100	-0.70284100	-0.97085400
O	2.57408400	1.16054900	0.29012700
F	0.52841500	-1.66309200	-0.05805000
C	-0.29768000	0.51570100	-0.14278700
C	-1.70529400	-0.11073000	-0.07743900
F	-0.33175000	1.63232300	0.59753900
F	-0.08060200	0.85792800	-1.42693200
F	-1.90693700	-0.67229000	1.10971900
F	-1.86822600	-1.02774200	-1.02093000
F	-2.62263500	0.83491600	-0.25706100

S6

E(DMSO)[M06-2X/6-311++G(2d,p), SMD (DMSO)] = -252.545844 a.u.

Gcorr(DMSO)[M06-2X/6-311++G(2d,p)] = 0.009188 a.u.
Hcorr(DMSO)[M06-2X/6-311++G(2d,p)] = 0.040346 a.u.
G = E(DMSO) + Gcorr= -252.536656 a.u.
H = E(DMSO) + Hcorr= -252.505498 a.u.

C	0.63748200	-0.30665700	-0.00002100
C	-0.48555700	0.45585800	0.00000000
O	1.85350600	0.07602900	0.00001000
F	-1.73141200	-0.18215500	0.00000500
H	-0.57475300	1.53297300	-0.00001300
H	0.41785800	-1.39701900	0.00001200

INT24
E(DMSO)[M06-2X/6-311++G(2d,p), SMD (DMSO)] = -1764.996384 a.u.
G_{corr}(DMSO)[M06-2X/6-311++G(2d,p)] = 0.051569 a.u.
H_{corr}(DMSO)[M06-2X/6-311++G(2d,p)] = 0.118723 a.u.
G = E(DMSO) + G_{corr} = -1764.944815 a.u.
H = E(DMSO) + H_{corr} = -1764.877661 a.u.

C	-1.51673500	-0.33739500	-0.03875400
C	-2.76990500	0.43779100	0.43655200
C	-4.09524700	-0.14403600	-0.06858200
F	-1.68237200	-0.70893500	-1.31414400
F	-1.37555900	-1.43508900	0.71784500
F	-4.05171300	-1.48556600	0.08003200
F	-2.67637700	1.71291400	0.02285000
F	-2.78741500	0.41926700	1.77824700
H	-4.93293500	0.27114000	0.49236000
F	-4.23113900	0.13081400	-1.37909000
C	-0.22048400	0.50544200	0.06410700
C	1.05809800	-0.37147700	0.05357600
C	2.32261200	0.43777500	-0.32761100
C	3.63520100	-0.25866200	0.09280800
F	3.61025100	-1.53044400	-0.28394200
F	3.79956100	-0.19390000	1.40378800
F	2.34826500	0.59868500	-1.65318900
F	2.28159500	1.63868900	0.26229500
F	0.90624300	-1.36088100	-0.83571100
F	1.22794300	-0.90333600	1.27012900
F	-0.17172200	1.35260300	-0.97176300
F	-0.24533100	1.20790600	1.20333900

F	4.65351500	0.34751900	-0.49678800

TS14
E(DMSO)[M06-2X/6-311++G(2d,p), SMD (DMSO)] = -1840.883225 a.u.
G_{corr}(DMSO)[M06-2X/6-311++G(2d,p)] = 0.061362 a.u.
H_{corr}(DMSO)[M06-2X/6-311++G(2d,p)] = 0.130947 a.u.
G = E(DMSO) + G_{corr} = -1840.821863 a.u.
H = E(DMSO) + H_{corr} = -1840.752278 a.u.

C	1.28199700	0.48196900	0.01129600
C	2.58136500	-0.32209600	0.31363700
C	3.92466500	0.38297900	0.07219300
F	1.37138600	1.08705300	-1.18172000
F	1.03810300	1.38793000	0.97003800
F	3.37062800	1.91229700	0.13843500
F	2.44304900	-1.41330100	-0.47543700
F	2.50322500	-0.68946200	1.60445100
H	4.62225200	0.56517200	0.86682400
O	4.84357300	-1.33028200	0.33403700
H	4.68477200	-1.93440600	-0.39793200
F	4.29097300	0.43970500	-1.21383900
C	0.02369200	-0.43697200	-0.06251000
C	-1.29589700	0.35697000	0.12927300
C	-2.52948800	-0.41018900	-0.41034900
C	-3.86593700	0.10977300	0.16414000
F	-3.90870900	1.43348400	0.08591500
F	-4.00904900	-0.25787900	1.42701700
F	-2.57711600	-0.27632900	-1.73915200
F	-2.42687000	-1.70887200	-0.10140500
F	-1.21823900	1.52480700	-0.52191500
F	-1.47797400	0.59831700	1.43440400
F	-0.02872300	-1.03289600	-1.26365000
F	0.07464800	-1.38167200	0.88545800
F	-4.86510900	-0.39686000	-0.54273900

TS15
E(DMSO)[M06-2X/6-311++G(2d,p), SMD (DMSO)] = -1740.404938 a.u.
G_{corr}(DMSO)[M06-2X/6-311++G(2d,p)] = 0.045724 a.u.
H_{corr}(DMSO)[M06-2X/6-311++G(2d,p)] = 0.114398 a.u.
G = E(DMSO) + G_{corr} = -1740.359214 a.u.
H = E(DMSO) + H_{corr} = -1740.29054 a.u.

C	3.49146300	0.57346600	0.02872900
C	2.67941700	-0.44709100	-0.24436400
C	1.25319800	-0.45129200	0.24428400
C	0.39226200	0.66576700	-0.39373900
F	2.85291500	-1.07150100	-1.42627100
F	0.93431000	1.86369500	-0.11975300
F	0.38861400	0.49526800	-1.72558700
F	4.72536500	0.66661400	-0.47134800
C	-1.08179600	0.78630800	0.08049800
F	-1.63455600	1.75944000	-0.66771500
F	-1.08722200	1.18572100	1.35820900
C	-1.98020400	-0.46608800	-0.03437700
F	-1.75526100	-1.09942500	-1.19092900
F	-1.71326000	-1.28585200	0.98765100
C	-3.48995200	-0.12948600	0.02256100
F	-3.89108000	0.42406500	-1.11058000
F	-4.16995900	-1.25121600	0.21103800
F	-3.74210400	0.69994800	1.02622000
F	1.17270100	-0.28721700	1.57521100
F	3.34209600	1.37941600	1.08198900
F	0.64857200	-1.60304400	-0.10419200
O	3.12033800	-2.14494300	0.82837000
H	2.81079600	-2.91318000	0.33600500

INT25

E(DMSO)[M06-2X/6-311++G(2d,p), SMD (DMSO)] = -1740.461376 a.u.

G_{corr}(DMSO)[M06-2X/6-311++G(2d,p)] = 0.049246 a.u.

H_{corr}(DMSO)[M06-2X/6-311++G(2d,p)] = 0.116617 a.u.

G = E(DMSO) + G_{corr} = -1740.41213 a.u.

H = E(DMSO) + H_{corr} = -1740.344759 a.u.

C	-2.45051000	-1.49293600	0.64239600
C	-2.69791000	-0.17170500	-0.08817000
C	-1.74766200	0.98527000	0.29494300
C	-0.29624200	1.07772500	-0.26549600
F	-2.54816700	-0.28397500	-1.48191300
F	-0.33851700	1.25944700	-1.58948700
F	0.20697000	2.20428300	0.28848600
F	-3.59937000	-2.25089600	0.21048400
C	0.70922000	-0.06462600	0.03385800

F	0.65926400	-0.97040300	-0.94953700
F	0.41114100	-0.63988900	1.20338100
C	2.17112700	0.44500600	0.10819600
F	2.39711300	1.30416900	-0.89532400
F	2.37194100	1.05995300	1.27689400
C	3.21459200	-0.69146500	-0.00943100
F	3.30229800	-1.12158700	-1.25788600
F	4.39886700	-0.22688700	0.36255300
F	2.88385900	-1.70569300	0.77848500
F	-1.66308700	1.08847100	1.63229500
F	-1.43232400	-2.11947400	-0.09756000
F	-2.30406200	2.13518400	-0.15929600
O	-3.95181500	0.29467500	0.18184100
H	-4.51451300	-0.47533000	0.35333000

TS16
E(DMSO)[M06-2X/6-311++G(2d,p), SMD (DMSO)] = -1591.501492 a.u.
G_{corr}(DMSO)[M06-2X/6-311++G(2d,p)] = 0.04165 a.u.
H_{corr}(DMSO)[M06-2X/6-311++G(2d,p)] = 0.109539 a.u.
G = E(DMSO) + G_{corr} = -1591.459842 a.u.
H = E(DMSO) + H_{corr} = -1591.391953 a.u.

C	3.70177600	-0.49399300	-0.55162500
C	2.39737500	-0.22024900	-0.00750200
C	1.60707800	0.85679900	-0.33651100
C	0.22807100	0.93509200	0.38576300
F	1.96079600	-1.11274800	0.93918500
F	0.28613200	0.65151100	1.70927400
F	-0.25460900	2.19624000	0.28705200
O	4.31137700	0.11591000	-1.38224200
O	1.81649800	1.77142500	-1.15994700
O	4.80120100	0.00853400	1.41509400
H	4.95931700	0.90302900	1.09772300
F	4.04061300	-1.82603000	-0.34987800
C	-0.84250000	0.01998100	-0.24436600
F	-0.63109400	-1.25215200	0.13285000
F	-0.74385200	0.08295500	-1.58316400
C	-2.29749300	0.39948100	0.12594600
F	-2.37495600	0.73792500	1.42035700
F	-2.68405200	1.44289100	-0.61888600
C	-3.31059900	-0.74052200	-0.11491800
F	-3.18101300	-1.68954600	0.79956700

F	-4.54161800	-0.25088700	-0.04225800
F	-3.13125600	-1.27010700	-1.31873200

TS17

E(DMSO)[M06-2X/6-311++G(2d,p), SMD (DMSO)] = -1326.914735 a.u.

G_{corr}(DMSO)[M06-2X/6-311++G(2d,p)] = 0.020814 a.u.

H_{corr}(DMSO)[M06-2X/6-311++G(2d,p)] = 0.078772 a.u.

G = E(DMSO) + G_{corr} = -1326.893921 a.u.

H = E(DMSO) + H_{corr} = -1326.835963 a.u.

C	3.60592000	-0.12298600	-0.55430600
C	2.54871600	0.23672500	-0.05364100
C	1.28207700	-0.06174600	0.62605800
C	-0.01009700	0.38254700	-0.12303400
C	-1.21070200	-0.56166300	0.12994600
F	2.18789900	2.00901900	-0.08717400
F	1.20415900	0.44738600	1.87821700
F	1.20349000	-1.41822500	0.77099200
F	-0.39685400	1.60428700	0.27100700
F	0.21502300	0.40137400	-1.44483600
F	-1.29283200	-0.85387700	1.43685000
F	-1.05154700	-1.69233700	-0.56806300
F	4.43662900	-1.08917600	-0.87211100
C	-2.57102200	0.04702600	-0.28267400
F	-3.48371100	-0.91617900	-0.30679400
F	-2.95871900	0.97011100	0.58388200
F	-2.49346500	0.59101500	-1.49020300

TS18

E(DMSO)[M06-2X/6-311++G(2d,p), SMD (DMSO)] = -1403.376233 a.u.

G_{corr}(DMSO)[M06-2X/6-311++G(2d,p)] = 0.045144 a.u.

H_{corr}(DMSO)[M06-2X/6-311++G(2d,p)] = 0.106635 a.u.

G = E(DMSO) + G_{corr} = -1403.331089 a.u.

H = E(DMSO) + H_{corr} = -1403.269598 a.u.

C	2.76935500	1.39111200	0.35338600
C	2.36289300	0.12813900	0.45499000
C	1.15858200	-0.42684700	-0.26239100
C	-0.15018800	0.19009200	0.29856700
C	-1.43575900	-0.56646600	-0.12078800

F	2.63820900	-0.52627500	1.59342300
F	1.02764200	-1.75246200	-0.07534900
F	1.17975500	-0.15354600	-1.57655800
F	-0.10158200	0.17739000	1.64200500
F	-0.24915200	1.46732200	-0.10604300
F	-1.59459200	-1.63260000	0.67335100
F	-1.34566500	-0.98354400	-1.39039600
F	2.38097300	2.14727600	-0.70739500
H	3.51611600	1.84590000	0.98642000
C	-2.71123600	0.29488700	-0.00269400
F	-3.77717000	-0.48681700	-0.10681400
F	-2.74061400	0.90633200	1.17518500
F	-2.75779000	1.20283700	-0.96517200
O	3.56663200	-1.31986300	-0.69224900
H	4.04882700	-0.64570300	-1.18097400

TS19

E(DMSO)[M06-2X/6-311++G(2d,p), SMD (DMSO)] = -1254.434562 a.u.

G_{corr}(DMSO)[M06-2X/6-311++G(2d,p)] = 0.042018 a.u.

H_{corr}(DMSO)[M06-2X/6-311++G(2d,p)] = 0.10211 a.u.

G = E(DMSO) + G_{corr} = -1254.392544 a.u.

H = E(DMSO) + H_{corr} = -1254.332452 a.u.

C	-2.94947900	-0.83186100	-0.50895000
C	-1.79047700	0.00799900	-0.23720500
C	-0.82230800	-0.10847600	0.72505300
C	0.35932300	0.89796200	0.64962200
C	1.46716500	0.52158800	-0.35002800
F	-1.66427500	1.02111400	-1.17423700
F	0.00777000	2.17295100	0.33295800
F	0.96670700	0.97848000	1.85752200
F	2.50533300	1.37105300	-0.19589800
F	1.01442200	0.65100400	-1.60738600
H	-3.30167100	-0.71166200	-1.54613900
O	-3.26409700	-1.82909600	0.14974900
O	-0.70171500	-0.95439100	1.65018100
C	2.03829900	-0.90181600	-0.22358300
F	2.46299600	-1.14456400	1.00779900
F	1.13978600	-1.81069200	-0.56732700
F	3.07759100	-1.01571500	-1.05205100
O	-4.44585200	0.66875800	-0.14247100
H	-4.81311800	0.10443800	0.54460400

INT26
E(DMSO)[M06-2X/6-311++G(2d,p), SMD (DMSO)] = -1853.044898 a.u.
G_{corr}(DMSO)[M06-2X/6-311++G(2d,p)] = 0.047232 a.u.
H_{corr}(DMSO)[M06-2X/6-311++G(2d,p)] = 0.11804 a.u.
G = E(DMSO) + G_{corr} =$_{corr}$ = -1852.997666 a.u.
H = E(DMSO) + H_{corr} = -1852.926858 a.u.

C	-2.94947900	-0.83186100	-0.50895000
C	-1.79047700	0.00799900	-0.23720500
C	-0.82230800	-0.10847600	0.72505300
C	0.35932300	0.89796200	0.64962200
C	1.46716500	0.52158800	-0.35002800
F	-1.66427500	1.02111400	-1.17423700
F	0.00777000	2.17295100	0.33295800
F	0.96670700	0.97848000	1.85752200
F	2.50533300	1.37105300	-0.19589800
F	1.01442200	0.65100400	-1.60738600
H	-3.30167100	-0.71166200	-1.54613900
O	-3.26409700	-1.82909600	0.14974900
O	-0.70171500	-0.95439100	1.65018100
C	2.03829900	-0.90181600	-0.22358300
F	2.46299600	-1.14456400	1.00779900
F	1.13978600	-1.81069200	-0.56732700
F	3.07759100	-1.01571500	-1.05205100
O	-4.44585200	0.66875800	-0.14247100
H	-4.81311800	0.10443800	0.54460400

INT27
E(DMSO)[M06-2X/6-311++G(2d,p), SMD (DMSO)] = -1526.687926 a.u.
G_{corr}(DMSO)[M06-2X/6-311++G(2d,p)] = 0.027651 a.u.
H_{corr}(DMSO)[M06-2X/6-311++G(2d,p)] = 0.088876 a.u.
G = E(DMSO) + G_{corr} = -1526.660275 a.u.
H = E(DMSO) + H_{corr} = -1526.59905 a.u.

C	3.56550300	0.08156600	-0.06897200
C	2.17429400	0.54491800	0.34152400
C	0.94646600	-0.33857400	0.00044300
C	-0.40734500	0.41502100	0.05472000
C	-1.62280900	-0.53525000	0.18643200

F	3.53535500	-1.30917900	0.22082900
F	3.52585900	0.09111800	-1.48204400
F	2.15199400	0.69005200	1.69311000
F	1.94276600	1.76744200	-0.20477200
F	0.87842900	-1.36174400	0.87403900
F	1.06922300	-0.84837800	-1.23548900
F	-0.42293000	1.24713200	1.10579600
F	-0.55250900	1.13766200	-1.06700400
F	-1.72959300	-0.93413300	1.45838600
F	-1.44995100	-1.60860100	-0.59626700
C	-2.96155500	0.12419500	-0.21193500
F	-3.96057000	-0.64743200	0.19208200
F	-3.07633700	1.31352400	0.36507800
F	-3.04143800	0.26795200	-1.52521800

S7

E(DMSO)[M06-2X/6-311++G(2d,p), SMD (DMSO)] = -237.693767 a.u.

G_{corr}(DMSO)[M06-2X/6-311++G(2d,p)] = -0.016377 a.u.

H_{corr}(DMSO)[M06-2X/6-311++G(2d,p)] = 0.010922 a.u.

G = E(DMSO) + G_{corr} = -237.710144 a.u.

H = E(DMSO) + H_{corr} = -237.682845 a.u.

C	0.00000000	0.00000000	0.59047700
F	0.00000000	-1.02383600	-0.19682600
F	0.00000000	1.02383600	-0.19682600

TSU1

E(DMSO)[M06-2X/6-311++G(2d,p), SMD (DMSO)] = -1591.488496 a.u.

Gcorr(DMSO)[M06-2X/6-311++G(2d,p)] = 0.043511 a.u.

Hcorr(DMSO)[M06-2X/6-311++G(2d,p)] = 0.11051 a.u.

G = E(DMSO) + Gcorr= -1591.444985 a.u.

H = E(DMSO) + Hcorr= -1591.377986 a.u.

C	-3.71864800	-1.15747200	0.25941900
C	-2.46871100	-0.50653000	-0.26961400
C	-1.80838600	0.57653400	0.17981500
C	-0.41834100	0.93219300	-0.30653100
F	-2.03089000	-0.98910600	-1.48034100
F	-0.31819300	1.00167100	-1.64184600
F	-0.00149200	2.10760000	0.22107800
O	-4.20161500	-2.05446000	-0.46682400

C	0.63823500	-0.10050000	0.17087600
F	0.51296500	-1.23767700	-0.53258800
F	0.42672100	-0.38239000	1.46848600
C	2.10379700	0.38759000	0.04487300
F	2.27993600	1.06045700	-1.10042200
F	2.38985200	1.19933300	1.07082100
C	3.13312100	-0.76411200	0.06884400
F	3.11540300	-1.43858300	-1.07048300
F	4.34782300	-0.25871900	0.23975200
F	2.87044700	-1.59441800	1.07043600
F	-1.98164900	0.99929700	1.44155200
O	-2.53581400	2.36858000	-0.64389300
H	-2.23149100	3.09603400	-0.09010500
O	-4.14172300	-0.75280100	1.36396700

INTU1
E(DMSO)[M06-2X/6-311++G(2d,p), SMD (DMSO)] = -1591.516658 a.u.
Gcorr(DMSO)[M06-2X/6-311++G(2d,p)] = 0.04802 a.u.
Hcorr(DMSO)[M06-2X/6-311++G(2d,p)] = 0.11318 a.u.
G = E(DMSO) + Gcorr= -1591.468638 a.u.
H = E(DMSO) + Hcorr= -1591.403478 a.u.

C	3.83428900	-0.87650500	-0.34675100
C	2.37243400	-0.74130000	-0.07462200
C	1.86724300	0.66121100	-0.07691400
C	0.40616100	0.80054100	0.44620700
F	2.06121400	-1.22400600	1.25499200
F	0.33695700	0.64685800	1.77997300
F	-0.00386400	2.08003100	0.19179900
O	4.50635500	-1.67151400	0.36734900
C	-0.66280600	-0.12503700	-0.17894500
F	-0.59898600	-1.34222000	0.38242900
F	-0.48107800	-0.24818300	-1.50100200
C	-2.10807400	0.40754600	0.02168900
F	-2.25937100	0.91868500	1.25138300
F	-2.35540500	1.36678000	-0.87937000
C	-3.18962500	-0.68033000	-0.15892900
F	-3.20859500	-1.50792400	0.87450400
F	-4.37775500	-0.09590400	-0.25090400
F	-2.96822500	-1.37395700	-1.26804500
F	1.77606200	1.16297600	-1.37565000
O	2.62492100	1.57608700	0.65434400

H	2.24285500	2.46222500	0.56061900
O	4.28757700	-0.22797500	-1.33319400

INTU2
E(DMSO)[M06-2X/6-311++G(2d,p), SMD (DMSO)] = -1491.099371 a.u.
Gcorr(DMSO)[M06-2X/6-311++G(2d,p)] = 0.033874 a.u.
Hcorr(DMSO)[M06-2X/6-311++G(2d,p)] = 0.097175 a.u.
G = E(DMSO) + Gcorr= -1491.065497 a.u.
H = E(DMSO) + Hcorr= -1491.002196 a.u.

C	4.07695500	-0.62105900	-0.28988800
C	2.70061500	-0.25745800	0.16763400
C	1.93467000	0.85074100	-0.10257100
C	0.51044600	0.87069600	0.54916600
F	2.12065100	-1.21294100	0.99838000
F	0.47568300	0.50195200	1.85605700
F	0.02231200	2.13759800	0.51425700
O	4.53608100	-1.70783500	0.14945400
C	-0.53099500	0.01450600	-0.20283200
F	-0.38077800	-1.28446400	0.10718100
F	-0.34303300	0.15205600	-1.52764700
C	-2.00353700	0.40204700	0.08673300
F	-2.16715700	0.68936300	1.38599400
F	-2.33176900	1.47875500	-0.63930100
C	-3.00944300	-0.71519600	-0.26643500
F	-2.95893200	-1.69609000	0.62227900
F	-4.23831900	-0.21351500	-0.26811800
F	-2.74778700	-1.20598500	-1.47172600
O	2.16714600	1.86021100	-0.81321900
O	4.65551000	0.17434500	-1.06711500

INTU3
E(DMSO)[M06-2X/6-311++G(2d,p), SMD (DMSO)] = -1491.597622 a.u.
Gcorr(DMSO)[M06-2X/6-311++G(2d,p)] = 0.047996 a.u.
Hcorr(DMSO)[M06-2X/6-311++G(2d,p)] = 0.111136 a.u.
G = E(DMSO) + Gcorr= -1491.549626 a.u.
H = E(DMSO) + Hcorr= -1491.486486 a.u.

C	3.11728700	-1.24329800	0.08415600
C	3.17682300	0.31914000	0.12049000

C	1.86249500	0.84142400	-0.38478800
C	0.64345900	0.82330600	0.57506500
F	4.18035100	0.82985100	-0.66832700
F	0.99691500	0.61377700	1.84892200
F	0.11533500	2.07268400	0.52115700
O	4.11174100	-1.82808200	-0.34342200
C	-0.47758900	-0.20000300	0.17674800
F	-0.60014100	-1.13317200	1.12431900
F	-0.17720900	-0.78482900	-0.99101800
C	-1.86811900	0.45574300	0.00538000
F	-2.20076300	1.10402300	1.13117700
F	-1.83199900	1.31717000	-1.01961400
C	-3.01727300	-0.53726200	-0.28479800
F	-3.21792200	-1.34695500	0.74360200
F	-4.12630000	0.16436600	-0.49067800
F	-2.76762000	-1.25933500	-1.36663300
O	1.69389900	1.30412100	-1.47601000
O	2.03128500	-1.67479800	0.51931700
H	3.34627600	0.63755900	1.15122900

INTU4
E(DMSO)[M06-2X/6-311++G(2d,p), SMD (DMSO)] = -1567.555407 a.u.
Gcorr(DMSO)[M06-2X/6-311++G(2d,p)] = 0.061602 a.u.
Hcorr(DMSO)[M06-2X/6-311++G(2d,p)] = 0.126622 a.u.
G = E(DMSO) + Gcorr= -1567.493805 a.u.
H = E(DMSO) + Hcorr= -1567.428785 a.u.

C	3.81439100	-0.94764600	-0.15240000
C	2.31482300	-0.69690100	0.13811500
C	1.84972100	0.68699800	-0.37006200
C	0.38532700	0.97656300	0.13412300
F	0.29152400	1.17627700	1.47721200
F	-0.06329000	2.12621300	-0.44212400
O	4.10325600	-2.00787400	-0.73241000
C	-0.67336400	-0.10495100	-0.18127700
F	-0.55741700	-1.10934900	0.71592400
F	-0.51324300	-0.63213600	-1.40258600
C	-2.13366600	0.41441500	-0.11357800
F	-2.29829200	1.26628900	0.90829400
F	-2.42550900	1.05109500	-1.25644900
C	-3.17790200	-0.70901800	0.06641700
F	-3.15375500	-1.18184500	1.30403300

F	-4.38926200	-0.21906500	-0.17045000
F	-2.94874000	-1.70320700	-0.78215100
O	1.91384500	0.74600400	-1.67192100
O	4.60865300	-0.06783900	0.27264600
O	2.59068000	1.69746100	0.35261000
H	3.48880600	1.31107100	0.41157700
F	2.14543400	-0.82823100	1.53835500
H	1.71669400	-1.48421700	-0.31751200

TSU2
E(DMSO)[M06-2X/6-311++G(2d,p), SMD (DMSO)] = -1567.522204 a.u.
Gcorr(DMSO)[M06-2X/6-311++G(2d,p)] = 0.059366 a.u.
Hcorr(DMSO)[M06-2X/6-311++G(2d,p)] = 0.124625 a.u.
G = E(DMSO) + Gcorr= -1567.462838 a.u.
H = E(DMSO) + Hcorr= -1567.397579 a.u.

C	4.22569300	0.32017900	-0.22307700
C	2.90580200	-0.44245700	-0.34021500
C	1.67955800	0.31765300	-0.08100400
C	0.38758800	-0.48845800	0.08236800
F	0.36367100	-1.17490000	1.24826700
O	5.17483100	-0.10445400	-0.89485300
O	1.90833200	0.73853600	-1.34635500
O	1.68865500	1.25978700	0.93843100
H	2.65994100	1.49712800	0.97975300
F	0.28122500	-1.40425800	-0.91264700
F	3.32917800	-1.59581000	1.07887700
H	2.84500800	-1.29116400	-0.99821000
C	-0.90094100	0.36892200	0.05862400
C	-2.16879900	-0.44413600	-0.30333200
C	-3.48632000	0.25730900	0.09199200
F	-1.10256300	0.91414300	1.27199100
F	-0.79623000	1.36100600	-0.83600200
F	-2.15158000	-1.63333900	0.31629900
F	-2.20398400	-0.64284400	-1.62726100
F	-3.66505300	0.22533000	1.40392500
F	-3.47949100	1.52018900	-0.31556200
F	-4.50242200	-0.37154200	-0.48547900
O	4.22628100	1.31590600	0.55585800

INTU5

E(DMSO)[M06-2X/6-311++G(2d,p), SMD (DMSO)] = -1467.574059 a.u.
Gcorr(DMSO)[M06-2X/6-311++G(2d,p)] = 0.060697 a.u.
Hcorr(DMSO)[M06-2X/6-311++G(2d,p)] = 0.122871 a.u.
G = E(DMSO) + Gcorr= -1467.513362 a.u.
H = E(DMSO) + Hcorr= -1467.451188 a.u.

C	-4.39158000	-0.01878300	-0.02004200
C	-3.03645800	0.64647400	-0.26192000
C	-1.83745500	-0.18326200	-0.04718200
C	-0.54325300	0.47127700	0.38401800
F	-0.50852300	0.58127800	1.72790500
O	-5.36051100	0.73143200	0.10984000
O	-2.23872400	0.12412500	-1.34987700
O	-1.91660400	-1.46256200	0.37357700
H	-2.92601900	-1.64612600	0.28527700
F	-0.44744100	1.71315900	-0.13369000
H	-2.99997700	1.72462200	-0.15929000
C	0.71061900	-0.31905000	-0.05651800
C	2.00095200	0.53592500	-0.05911600
C	3.29372100	-0.30888100	-0.04534600
F	0.89725600	-1.36054300	0.76769900
F	0.52051100	-0.78361500	-1.30033800
F	2.02213400	1.33005900	1.02040100
F	2.02346900	1.29479900	-1.16032500
F	3.49696900	-0.83849600	1.15065300
F	3.21440400	-1.28185600	-0.94452900
F	4.32414000	0.46922100	-0.34504900
O	-4.37660600	-1.28508800	0.04972300

TSU3
E(DMSO)[M06-2X/6-311++G(2d,p), SMD (DMSO)] = -1467.546213 a.u.
Gcorr(DMSO)[M06-2X/6-311++G(2d,p)] = 0.058277 a.u.
Hcorr(DMSO)[M06-2X/6-311++G(2d,p)] = 0.121759 a.u.
G = E(DMSO) + Gcorr= -1467.487936 a.u.
H = E(DMSO) + Hcorr= -1467.424454 a.u.

C	4.03422600	0.67851000	0.29366600
C	2.88094900	-0.27492900	0.57177900
C	1.84012600	-0.19532900	-0.48619500
C	0.50093600	-0.86060800	-0.13570600
F	0.44689300	-1.33115300	1.12824200

O	5.13709500	0.36494500	-0.05062600
O	3.03266900	-1.58118300	0.22710800
O	1.96514800	0.23512600	-1.62027700
H	2.80627100	2.07789300	0.73591000
F	0.22386300	-1.87849300	-0.97642400
H	2.53219000	-0.06946200	1.60004300
C	-0.64727000	0.16789200	-0.26470900
C	-1.95276200	-0.26712400	0.44464100
C	-3.20085300	0.49825400	-0.04611500
F	-0.25078800	1.32866400	0.29005800
F	-0.92217300	0.38661100	-1.55887500
F	-1.83673000	-0.04459900	1.75921700
F	-2.17177700	-1.57326200	0.24079800
F	-2.95472900	1.80218100	-0.07350900
F	-3.55640700	0.09745400	-1.25667000
F	-4.20671000	0.26903500	0.78686500
O	3.73839400	1.98156300	0.48661500

INTU6
E(DMSO)[M06-2X/6-311++G(2d,p), SMD (DMSO)] = -1467.587186 a.u.
Gcorr(DMSO)[M06-2X/6-311++G(2d,p)] = 0.059994 a.u.
Hcorr(DMSO)[M06-2X/6-311++G(2d,p)] = 0.12368 a.u.
G = E(DMSO) + Gcorr= -1467.527192 a.u.
H = E(DMSO) + Hcorr= -1467.463506 a.u.

C	3.07308400	1.31353300	0.06015200
C	3.13751600	-0.23789700	0.38194200
C	1.93955000	-0.86213600	-0.27754300
C	0.58833600	-0.86428400	0.48459700
F	0.64590600	-0.22955200	1.66580000
O	4.06225000	1.71560200	-0.57940100
O	4.31710100	-0.78627000	-0.10788700
O	1.93734400	-1.38904700	-1.35557300
F	0.26903400	-2.15476000	0.74008100
H	3.05658500	-0.35238300	1.46627700
C	-0.56365500	-0.26529700	-0.35870400
C	-1.77721600	0.16220200	0.49862400
C	-3.07280900	0.35083100	-0.32163600
F	-0.13003700	0.80231800	-1.03617900
F	-0.98109200	-1.18766700	-1.24278300
F	-1.50482900	1.32280700	1.10223600
F	-2.02045000	-0.77253200	1.42917900

F	-2.82990700	1.07342300	-1.40726500
F	-3.57452300	-0.81983000	-0.68301000
F	-3.96864600	0.98347200	0.42342400
O	2.07227200	1.91441500	0.46328200
H	4.73373000	-0.02605300	-0.55759000

TSU4
E(DMSO)[M06-2X/6-311++G(2d,p), SMD (DMSO)] = -1467.56727 a.u.
Gcorr(DMSO)[M06-2X/6-311++G(2d,p)] = 0.056975 a.u.
Hcorr(DMSO)[M06-2X/6-311++G(2d,p)] = 0.121283 a.u.
G = E(DMSO) + Gcorr= -1467.510295 a.u.
H = E(DMSO) + Hcorr= -1467.445987 a.u.

C	2.52598700	1.67582300	0.05899500
C	3.12114900	-0.37397700	0.47441900
C	2.04689400	-0.88614100	-0.23441700
C	0.69269800	-0.96990500	0.45158700
F	0.69959800	-0.44745100	1.69924300
O	3.00646300	1.86922200	-1.00447500
O	4.35334000	-0.49059700	-0.11907100
O	2.10209300	-1.27810900	-1.42520300
F	0.32736300	-2.27406500	0.57680600
H	3.13968200	-0.25382000	1.54633500
C	-0.43784000	-0.27701200	-0.34831600
C	-1.68481400	0.04886600	0.50795100
C	-2.95125000	0.32760000	-0.33140900
F	0.01131800	0.87722600	-0.86432600
F	-0.82660000	-1.07043700	-1.36030400
F	-1.44287800	1.13764600	1.24644500
F	-1.96190100	-0.98038800	1.32234000
F	-2.67474500	1.17480100	-1.31474300
F	-3.43203400	-0.79357900	-0.84673300
F	-3.88064200	0.86586900	0.44722700
O	1.96818800	2.06240400	1.03234300
H	4.16740300	-0.72764600	-1.04155900

INTU7
E(DMSO)[M06-2X/6-311++G(2d,p), SMD (DMSO)] = -1278.987059 a.u.
Gcorr(DMSO)[M06-2X/6-311++G(2d,p)] = 0.048508 a.u.
Hcorr(DMSO)[M06-2X/6-311++G(2d,p)] = 0.10651 a.u.
G = E(DMSO) + Gcorr= -1278.938551 a.u.

H = E(DMSO) + Hcorr= -1278.880549 a.u.

C	3.29679600	-0.61603300	0.63189400
C	2.54643000	0.12407900	-0.21727900
C	1.21746200	0.62619000	0.29362800
F	1.14903600	0.64286400	1.65272400
F	0.97665900	1.90197500	-0.12474200
C	0.00739800	-0.21442900	-0.17304500
F	-0.01757600	-1.36086700	0.53669800
F	0.12849300	-0.53408600	-1.46916000
C	-1.36244100	0.48873000	-0.00513300
F	-1.40690500	1.17209900	1.14732400
F	-1.53942700	1.34437400	-1.02100600
C	-2.56100600	-0.48346300	-0.00638500
F	-2.61500900	-1.16605400	1.12761200
F	-3.68529900	0.21004900	-0.13414500
F	-2.46602600	-1.33349400	-1.02117500
O	2.86604200	0.39116600	-1.43682600
H	3.06887100	-0.86177000	1.65684800
O	4.48885200	-1.11380300	0.15207000
H	4.50863800	-0.79932400	-0.76804100

INTU8
E(DMSO)[M06-2X/6-311++G(2d,p), SMD (DMSO)] = -1278.452041 a.u.
Gcorr(DMSO)[M06-2X/6-311++G(2d,p)] = 0.034676 a.u.
Hcorr(DMSO)[M06-2X/6-311++G(2d,p)] = 0.09191 a.u.
G = E(DMSO) + Gcorr= -1278.417365 a.u.
H = E(DMSO) + Hcorr= -1278.360131 a.u.

C	-3.47200100	0.71588600	-0.34947000
C	-2.63850400	-0.39147100	-0.33749100
C	-1.37728800	-0.35013200	0.45943800
F	-1.37019800	0.52615500	1.50664900
F	-1.08699100	-1.58351900	1.03234100
C	-0.09353300	-0.00449800	-0.34368100
F	-0.06833500	1.32950100	-0.57047800
F	-0.08748400	-0.61244600	-1.54201200
C	1.24562500	-0.38150700	0.33944700
F	1.20179600	-0.13898300	1.65894000
F	1.48448100	-1.68938900	0.15305900
C	2.46807800	0.38286100	-0.21132900

F	2.46431800	1.64346700	0.19918100
F	3.58322000	-0.19316100	0.22733600
F	2.47692800	0.36065000	-1.53885200
O	-2.79462400	-1.51054000	-1.04549700
H	-4.34094200	0.51627500	-1.02267500
O	-3.43449000	1.87009200	0.23871200

TSU5
E(DMSO)[M06-2X/6-311++G(2d,p), SMD (DMSO)] = -1278.445993 a.u.
Gcorr(DMSO)[M06-2X/6-311++G(2d,p)] = 0.032731 a.u.
Hcorr(DMSO)[M06-2X/6-311++G(2d,p)] = 0.090135 a.u.
G = E(DMSO) + Gcorr= -1278.413262 a.u.
H = E(DMSO) + Hcorr= -1278.355858 a.u.

C	3.71878500	-0.08205700	-0.51281900
C	2.57336400	0.60433100	-0.03788500
C	1.39548700	-0.14900800	0.22252500
F	1.35403600	-1.41953700	-0.23782400
F	1.11082700	-0.44193300	1.80348200
C	0.02453800	0.47915300	-0.05722200
F	-0.11075800	0.58381600	-1.41329800
F	-0.11700900	1.71216600	0.44698000
C	-1.22904000	-0.30479300	0.44477500
F	-1.06340200	-1.63428400	0.44207000
F	-1.53204000	0.08001800	1.69450500
C	-2.48963500	-0.02777200	-0.40605200
F	-2.42149800	-0.63602300	-1.58246600
F	-3.55887900	-0.49349200	0.23489900
F	-2.65419200	1.27585400	-0.60002100
O	2.58236800	1.92136100	0.18431200
H	4.52233000	0.66020700	-0.73355600
O	3.97424700	-1.29868800	-0.71947500

INTU9
E(DMSO)[M06-2X/6-311++G(2d,p), SMD (DMSO)] = -1178.525239 a.u.
Gcorr(DMSO)[M06-2X/6-311++G(2d,p)] = 0.031733 a.u.
Hcorr(DMSO)[M06-2X/6-311++G(2d,p)] = 0.089049 a.u.
G = E(DMSO) + Gcorr= -1178.493506 a.u.
H = E(DMSO) + Hcorr= -1178.43619 a.u.

C	-3.79077200	-0.02941600	0.25801200
C	-2.42290900	-0.65695500	0.02963400
C	-1.42795700	0.14533100	-0.46716400
F	-1.65365700	1.48253600	-0.70183000
C	-0.02043600	-0.20822400	-0.70884400
F	0.46123100	0.43659400	-1.81883800
F	0.14054400	-1.53342100	-0.90840900
C	0.93910800	0.18200000	0.44128300
F	0.74406000	1.47612400	0.75345000
F	0.63997900	-0.56757600	1.51522800
C	2.44809700	0.01362300	0.18292800
F	2.87402800	0.86949900	-0.73622800
F	3.11382800	0.25173500	1.31107800
F	2.72953000	-1.22086500	-0.21444500
O	-2.38547100	-1.87871100	0.33370400
H	-4.61336300	-0.72870500	0.01362500
O	-4.01244600	1.04107700	0.76269900

TSU6
E(DMSO)[M06-2X/6-311++G(2d,p), SMD (DMSO)] = -1178.498823 a.u.
Gcorr(DMSO)[M06-2X/6-311++G(2d,p)] = 0.030046 a.u.
Hcorr(DMSO)[M06-2X/6-311++G(2d,p)] = 0.0876 a.u.
G = E(DMSO) + Gcorr= -1178.468777 a.u.
H = E(DMSO) + Hcorr= -1178.411223 a.u.

C	-3.94585700	-0.07634500	-0.26423500
C	-2.58783700	0.63111900	-0.31667500
C	-1.37580800	-0.15049200	-0.15712700
F	-1.50369800	-1.49451100	-0.09745100
C	-0.13500400	0.34221400	-0.02020300
F	0.24435800	0.64739600	2.03172400
F	0.11945100	1.61504300	-0.24334900
C	1.07302600	-0.57274300	-0.09889600
F	1.09602500	-1.50733200	0.85441900
F	1.02088400	-1.23828700	-1.28700900
C	2.44330000	0.14220900	-0.12647900
F	3.38862700	-0.79351100	-0.21469100
F	2.52405200	0.91306600	-1.20884500
F	2.68726500	0.87713300	0.93857400
O	-2.61392500	1.83623200	-0.45712100
H	-4.72306600	0.43765500	-0.85517300
O	-4.17364100	-1.02428100	0.43168500

INTU10
E(DMSO)[M06-2X/6-311++G(2d,p), SMD (DMSO)] = -1078.514592 a.u.
Gcorr(DMSO)[M06-2X/6-311++G(2d,p)] = 0.031303 a.u.
Hcorr(DMSO)[M06-2X/6-311++G(2d,p)] = 0.086442 a.u.
G = E(DMSO) + Gcorr= -1078.483289 a.u.
H = E(DMSO) + Hcorr= -1078.42815 a.u.

C	-3.60886800	0.59723200	-0.15617100
C	-2.55426600	-0.50593700	-0.02749800
C	-1.17792000	-0.10845400	0.38064000
F	-1.08161500	1.03217000	1.05837500
C	-0.07952100	-0.80558400	0.11532900
F	-0.12082900	-1.92242000	-0.58703500
C	1.32241600	-0.40559100	0.51655200
F	1.32840100	0.19606600	1.71474700
F	2.09292800	-1.50193400	0.57822200
C	1.98091500	0.56153800	-0.48373600
F	1.28756100	1.69060100	-0.54322500
F	3.21862300	0.83579000	-0.09968700
F	2.01499200	0.00854000	-1.68925600
O	-2.85214700	-1.63480600	-0.30889000
H	-4.64614600	0.23953900	-0.06005900
O	-3.31172100	1.72379600	-0.42859600

INTU11
E(DMSO)[M06-2X/6-311++G(2d,p), SMD (DMSO)] = -1154.485333 a.u.
Gcorr(DMSO)[M06-2X/6-311++G(2d,p)] = 0.043074 a.u.
Hcorr(DMSO)[M06-2X/6-311++G(2d,p)] = 0.101363 a.u.
G = E(DMSO) + Gcorr= -1154.442259 a.u.
H = E(DMSO) + Hcorr= -1154.38397 a.u.

C	-3.16714100	0.84937700	-0.01711700
C	-2.40427600	-0.44176800	0.31226200
C	-0.98563300	-0.39667500	-0.28877200
F	-0.65545300	-1.35176900	-1.16505600
C	-0.04925400	0.47975700	0.03988400
F	-0.29276800	1.43552300	0.94831000
C	1.36505000	0.50825400	-0.45628600
F	1.45830100	0.10829200	-1.73872000

F	1.85514400	1.76247300	-0.37122400
C	2.31541700	-0.38771400	0.35369700
F	1.94693900	-1.65883200	0.24730100
F	3.56241100	-0.26980700	-0.08909000
F	2.28566600	-0.03749300	1.63538900
O	-2.40556000	-0.62804300	1.60849500
H	-4.16960000	0.84167600	0.45559300
O	-2.76804200	1.80261500	-0.63553500
O	-3.11999100	-1.46513500	-0.42290000
H	-3.36880300	-2.08002400	0.27971900

INTU12
E(DMSO)[M06-2X/6-311++G(2d,p), SMD (DMSO)] = -1153.957796 a.u.
Gcorr(DMSO)[M06-2X/6-311++G(2d,p)] = 0.033008 a.u.
Hcorr(DMSO)[M06-2X/6-311++G(2d,p)] = 0.087809 a.u.
G = E(DMSO) + Gcorr= -1153.924788 a.u.
H = E(DMSO) + Hcorr= -1153.869987 a.u.

C	-3.14643200	0.81602800	0.22506300
C	-2.46337900	-0.54939300	0.27118500
C	-1.02492500	-0.43718100	-0.31853800
F	-0.64428700	-1.48333600	-1.07481700
C	-0.08362300	0.47442300	-0.09113300
F	-0.31766700	1.51042300	0.74779000
C	1.33949400	0.44780900	-0.53588500
F	1.49321200	-0.12891900	-1.74645400
F	1.83271500	1.70824400	-0.61567900
C	2.27350800	-0.30922000	0.42123900
F	1.93310300	-1.59218000	0.47735400
F	3.54001100	-0.22994600	0.01839300
F	2.19062000	0.20836300	1.64405000
O	-2.30819100	-0.98047600	1.54036300
H	-4.06690200	0.79156200	0.85296500
O	-2.88557800	1.80644300	-0.42971600
O	-3.25002100	-1.24849100	-0.57818100

TSU7
E(DMSO)[M06-2X/6-311++G(2d,p), SMD (DMSO)] = -1153.949929 a.u.
Gcorr(DMSO)[M06-2X/6-311++G(2d,p)] = 0.028563 a.u.
Hcorr(DMSO)[M06-2X/6-311++G(2d,p)] = 0.085895 a.u.
G = E(DMSO) + Gcorr= -1153.921366 a.u.

H = E(DMSO) + Hcorr= -1153.869987 a.u.

C	-3.66984200	0.41110800	-0.07539200
C	-2.65505100	-0.73185400	-0.15294500
C	-1.01222400	0.32267500	0.00742600
F	-0.79581500	1.08969000	-1.11368800
C	0.10262100	0.13949200	0.71679700
F	0.07331900	-0.62380700	1.85300500
C	1.50282700	0.56857700	0.42739700
F	1.56033400	1.75987300	-0.21061200
F	2.22560200	0.69186000	1.57201800
C	2.28685700	-0.41674600	-0.45168900
F	1.71418700	-0.53142300	-1.64538800
F	3.54300600	-0.00813000	-0.63171700
F	2.31977100	-1.61788500	0.12117300
O	-2.75490800	-1.48928500	0.88369200
H	-4.69187000	0.04478600	-0.33162800
O	-3.52417900	1.57457600	0.22808600
O	-2.52127500	-1.16602900	-1.36191000

TSU8
E(DMSO)[M06-2X/6-311++G(2d,p), SMD (DMSO)] = -1591.9986 a.u.
Gcorr(DMSO)[M06-2X/6-311++G(2d,p)] = 0.058518 a.u.
Hcorr(DMSO)[M06-2X/6-311++G(2d,p)] = 0.12484 a.u.
G = E(DMSO) + Gcorr= -1591.940082 a.u.
H = E(DMSO) + Hcorr= -1591.87376 a.u.

C	-4.15546600	-0.13610900	-0.38700500
C	-2.82725300	0.49947000	-0.27002000
C	-1.63881000	-0.31453200	-0.01755300
C	-0.34544500	0.49493900	0.15124500
F	-0.33687800	1.13878900	1.33604600
O	-5.08051500	0.23364800	-1.01706100
O	-1.93895100	-0.64097900	-1.29695700
O	-1.56999400	-1.30901700	0.94162700
H	-2.36137600	-1.85751100	0.86913800
F	-4.25627300	-1.27861400	0.33667100
F	-0.26848100	1.43005600	-0.81944800
F	-3.49297300	1.32660600	1.24805500
H	-2.70492800	1.43508400	-0.78954500
C	0.94052000	-0.36377700	0.08074200

C	2.19487000	0.45964200	-0.30160000
C	3.52313300	-0.25016100	0.04191000
F	1.16930400	-0.93130600	1.27579100
F	0.79261900	-1.33245400	-0.83284400
F	2.18434000	1.63216300	0.34818600
F	2.18797100	0.68832500	-1.61967200
F	3.74286700	-0.23173300	1.34728700
F	3.49385400	-1.50876700	-0.37761100
F	4.52061500	0.37986800	-0.56321300

TSU9
E(DMSO)[M06-2X/6-311++G(2d,p), SMD (DMSO)] = -1567.471645 a.u.
Gcorr(DMSO)[M06-2X/6-311++G(2d,p)] = 0.056442 a.u.
Hcorr(DMSO)[M06-2X/6-311++G(2d,p)] = 0.12331 a.u.
G = E(DMSO) + Gcorr= -1567.415203 a.u.
H = E(DMSO) + Hcorr= -1567.348335 a.u.

C	-3.86474600	-1.04640000	-0.09984100
C	-3.61878500	0.10148600	-0.93497800
C	-1.51987200	0.91241500	0.43175000
C	-0.45982900	-0.07746700	-0.07828200
F	-0.56361100	-0.34721600	-1.39058500
O	-3.32280900	-2.14411400	-0.47468700
O	-1.92788900	0.85627700	1.55963200
O	-1.55238200	1.99749600	-0.36133200
H	-2.40683400	2.43323700	-0.19146700
F	-0.53482400	-1.22240300	0.61475100
F	-4.08418900	1.37738800	-0.48216900
H	-2.80794400	0.21677900	-1.63421700
C	0.96653500	0.49356100	0.14262200
C	2.07257600	-0.58981300	0.12417200
C	3.48282400	-0.01683500	-0.13633400
F	1.23582200	1.39747000	-0.81355300
F	1.02198000	1.11112300	1.33334800
F	1.81936400	-1.49213600	-0.83284400
F	2.09859800	-1.20800800	1.31035700
F	3.62034900	0.33352000	-1.40569100
F	3.69570400	1.04328600	0.63344900
F	4.38889800	-0.94175500	0.14814600
O	-4.62445000	-0.93129900	0.91315600

TSU10
E(DMSO)[M06-2X/6-311++G(2d,p), SMD (DMSO)] = -1591.486114 a.u.
Gcorr(DMSO)[M06-2X/6-311++G(2d,p)] = 0.043743 a.u.
Hcorr(DMSO)[M06-2X/6-311++G(2d,p)] = 0.110753 a.u.
G = E(DMSO) + Gcorr= -1591.442371 a.u.
H = E(DMSO) + Hcorr= -1591.375361 a.u.

C	3.83242000	-0.88441800	-0.39115700
C	2.61306900	-0.23798000	0.27359900
C	1.63649900	0.40306200	-0.38716100
C	0.32321900	0.83935600	0.14865900
F	2.27698200	-0.73066400	1.47312000
F	0.32366600	0.95088200	1.49077800
F	-0.02558000	2.05509600	-0.36483700
O	4.11209000	-2.01162300	0.05723700
C	-0.83174600	-0.12212600	-0.22372500
F	-0.70200900	-1.24000500	0.51220300
F	-0.72138200	-0.45641000	-1.52008000
C	-2.25311500	0.45157600	-0.01427000
F	-2.30799400	1.16543500	1.11814700
F	-2.55452000	1.25162600	-1.04498300
C	-3.34645700	-0.63528600	0.06684400
F	-3.28196600	-1.28315800	1.21972700
F	-4.53907200	-0.06363700	-0.03054600
F	-3.20383400	-1.50181300	-0.92837700
F	1.77905100	0.78294300	-1.68350700
O	4.06272700	1.19444400	1.33250700
H	4.53097900	1.33053800	0.50362400
O	4.35463500	-0.25635800	-1.32914100

INTU13
E(DMSO)[M06-2X/6-311++G(2d,p), SMD (DMSO)] = -1591.544297 a.u.
Gcorr(DMSO)[M06-2X/6-311++G(2d,p)] = 0.047579 a.u.
Hcorr(DMSO)[M06-2X/6-311++G(2d,p)] = 0.11277 a.u.
G = E(DMSO) + Gcorr= -1591.496718 a.u.
H = E(DMSO) + Hcorr= -1591.431527 a.u.

C	-4.16901800	0.53002200	0.00554600
C	-2.86342700	-0.30610500	0.28145800
C	-1.59549500	0.49333300	0.11952000
C	-0.39749600	-0.35389400	-0.01816200

F	-2.95170600	-0.69546600	1.64800800
F	-0.36135500	-1.28976800	0.96902500
F	-0.24789000	-1.07129000	-1.21391800
O	-4.32144600	1.59191000	0.61788900
C	0.93509900	0.42862700	0.08749100
F	1.12303300	0.80990200	1.36856800
F	0.89113400	1.53945600	-0.66903900
C	2.19552400	-0.35891800	-0.34998200
F	2.12627000	-1.63625500	0.05399300
F	2.29706400	-0.33386300	-1.68652600
C	3.51180100	0.21962300	0.21362000
F	3.63611000	-0.04937600	1.50509800
F	4.53857900	-0.32775900	-0.42704900
F	3.55523400	1.53488500	0.03840100
F	-1.72969000	1.15929600	-1.15198400
O	-2.94009400	-1.47061200	-0.45707500
H	-3.83934800	-1.40697600	-0.84557600
O	-4.95766300	-0.02967300	-0.79863600

TSU11
E(DMSO)[M06-2X/6-311++G(2d,p), SMD (DMSO)] = -1591.539641 a.u.
Gcorr(DMSO)[M06-2X/6-311++G(2d,p)] = 0.046228 a.u.
Hcorr(DMSO)[M06-2X/6-311++G(2d,p)] = 0.111416 a.u.
G = E(DMSO) + Gcorr= -1591.493413 a.u.
H = E(DMSO) + Hcorr= -1591.428225 a.u.

C	4.12862000	-0.67177500	0.07167400
C	2.92697400	0.33786600	0.22099400
C	1.60156400	-0.28342800	-0.07055200
C	0.40095800	0.40888100	0.05321700
F	2.94127100	0.72900000	1.58440500
F	0.32827800	1.16720000	1.17052200
F	0.04981100	1.54012500	-1.04542500
O	4.04817600	-1.75148400	0.66527900
C	-0.90614000	-0.38299500	-0.08364100
F	-1.06050300	-1.13580500	1.03709400
F	-0.86288700	-1.22734500	-1.12820200
C	-2.21714800	0.43702500	-0.23885800
F	-2.18987200	1.56895200	0.47674400
F	-2.42197500	0.73745200	-1.52790600
C	-3.46849300	-0.34456300	0.22740100
F	-3.53112900	-0.41140200	1.54953600

F	-4.55754900	0.28217000	-0.20645100
F	-3.46559600	-1.57602500	-0.27018800
F	1.70100100	-1.03489000	-1.25104900
O	3.21211800	1.46148400	-0.52152000
H	4.13989800	1.29683800	-0.79720200
O	5.07526200	-0.21722200	-0.61700200

INTU14
E(DMSO)[M06-2X/6-311++G(2d,p), SMD (DMSO)] = -1491.588193 a.u.
Gcorr(DMSO)[M06-2X/6-311++G(2d,p)] = 0.046879 a.u.
Hcorr(DMSO)[M06-2X/6-311++G(2d,p)] = 0.110902 a.u.
G = E(DMSO) + Gcorr= -1491.541314 a.u.
H = E(DMSO) + Hcorr= -1491.477291 a.u.

C	3.88036100	-0.31423500	0.58217600
C	2.82325000	0.03112100	-0.53684500
C	1.42146000	-0.13014900	-0.02556300
C	0.43294000	0.74589800	0.05331100
F	3.00408100	1.36660800	-0.87697300
F	0.54173100	1.99342600	-0.40502100
O	3.70075800	0.21608900	1.67993900
C	-0.93721200	0.46267100	0.61577500
F	-1.46673600	1.61056900	1.07820100
F	-0.88158900	-0.41828100	1.62786600
C	-1.89159900	-0.10239300	-0.45561600
F	-1.93229500	0.76440100	-1.47853100
F	-1.39571400	-1.26976600	-0.88839000
C	-3.34249000	-0.35936000	-0.00546200
F	-3.92266500	0.76506100	0.38586000
F	-4.02288100	-0.85271100	-1.03345800
F	-3.37691500	-1.23676700	0.98643800
F	1.20997600	-1.37444300	0.40959100
O	3.02004500	-0.75737600	-1.62546800
H	3.88055200	-1.18855700	-1.42163200
O	4.77747800	-1.07691800	0.17112100

INTU15
E(DMSO)[M06-2X/6-311++G(2d,p), SMD (DMSO)] = -1491.08802 a.u.
Gcorr(DMSO)[M06-2X/6-311++G(2d,p)] = 0.032457 a.u.
Hcorr(DMSO)[M06-2X/6-311++G(2d,p)] = 0.096837 a.u.
G = E(DMSO) + Gcorr= -1491.055563 a.u.

H = E(DMSO) + Hcorr= -1490.991183 a.u.

C	3.95028000	-0.51309400	0.31135500
C	2.87091000	0.11907300	-0.63611500
C	1.47203700	-0.17315500	-0.06912700
C	0.48130800	0.59247100	0.37229800
F	3.04232200	1.63124500	-0.23526000
F	0.58037600	1.92844700	0.49670500
O	3.51875400	-0.88419500	1.42912400
C	-0.89381300	0.12017900	0.75007300
F	-1.41662600	0.95419900	1.67730700
F	-0.88248100	-1.12029800	1.27384500
C	-1.86191900	0.10851600	-0.45043600
F	-1.87004500	1.33467900	-0.99838000
F	-1.40760900	-0.77074600	-1.35519400
C	-3.32581600	-0.26507700	-0.15064100
F	-3.87978100	0.60667800	0.67931400
F	-4.01002500	-0.25465900	-1.29018300
F	-3.40547200	-1.47867100	0.37647200
F	1.18668300	-1.48052600	-0.19865500
O	2.91866300	-0.04177800	-1.88160600
O	5.11333300	-0.58485200	-0.12228900

TSU12
E(DMSO)[M06-2X/6-311++G(2d,p), SMD (DMSO)] = -1591.539641 a.u.
Gcorr(DMSO)[M06-2X/6-311++G(2d,p)] = 0.046228 a.u.
Hcorr(DMSO)[M06-2X/6-311++G(2d,p)] = 0.111416 a.u.
G = E(DMSO) + Gcorr= -1591.493413 a.u.
H = E(DMSO) + Hcorr= -1591.428225 a.u.

C	4.07605900	0.59013100	0.36860000
C	3.64548700	-0.74330400	-0.31489600
C	1.37119400	-0.33971500	0.05851400
C	0.37087400	0.52730300	-0.09467200
F	3.56674300	-0.61815300	-1.69831300
F	0.54121600	1.58402800	-0.95427800
O	4.09141300	0.54546500	1.60861300
C	-1.01373900	0.54244400	0.46510700
F	-1.47554700	1.81519500	0.58254900
F	-1.06453300	-0.01863200	1.69266000
C	-2.02277700	-0.21832900	-0.41923300

F	-1.95696800	0.27494700	-1.66795300
F	-1.67260200	-1.51390500	-0.44598300
C	-3.50101300	-0.16020400	0.00778500
F	-3.96782900	1.07881600	-0.05586200
F	-4.21805000	-0.91958900	-0.81626900
F	-3.65630700	-0.61895500	1.24221700
F	1.03374300	-1.38360500	0.89722500
O	3.79662000	-1.84797100	0.11384600
O	4.39630200	1.51359800	-0.39885600

S4
E(DMSO)[M06-2X/6-311++G(2d,p), SMD (DMSO)] = -401.887993 a.u.
Gcorr(DMSO)[M06-2X/6-311++G(2d,p)] = -0.004819 a.u.
Hcorr(DMSO)[M06-2X/6-311++G(2d,p)] = 0.028553 a.u.
G = E(DMSO) + Gcorr= -401.892812 a.u.
H = E(DMSO) + Hcorr= -401.85944 a.u.

C	0.18741500	-0.84810300	0.00000000
O	1.37337200	-1.19037000	0.00000000
O	-0.86421500	-1.49564100	0.00000000
C	0.00000000	0.71577900	0.00000000
O	0.82212800	1.56185900	0.00000000
F	-1.30830700	1.08746100	0.00000000

4. Low Temperature Mineralization of Perfluorocarboxylic Acids

All figures reused or adapted from Trang and Li et al., *Science*, accepted.

4.1. Abstract

Perfluoroether carboxylic acids (PFECAs), used as replacement compounds for legacy per- and polyfluoroalkyl substances (PFAS) such as perfluorooctanoic acid, are a major source of PFAS contamination. As these compounds are used as surfactants in industrial processes, they pervasively contaminate areas around fluoropolymer manufacturers. While PFECAs are similar to their straight-chain legacy PFAS predecessors, the presence of an ether bond induces certain differences in properties and reactivity. Here, we degrade PFECAs via a polar-aprotic-solvent-assisted alkaline mineralization method that is known to degrade PFCAs. Consistent with literature on the decarboxylation of PFECAs, we observed decarboxylation and defluorination at near-ambient temperatures. In contrast to the previous study on PFCA degradation, we were able to observe the formation of a proto-de-trifluoromethylated intermediate, which was identified by both ^{19}F NMR spectroscopy as well as mass spectrometry. Computational studies show that the ether is eliminated through a S_N2 reaction as an alkoxide at higher reaction temperatures, then subsequently eliminates to form a carboxylic acid. This carboxylic acid degrades in a manner consistent with previously studied PFCA degradation and the overall mechanism demonstrates the applicability of this degradation method to a variety of PFAS structure classes.

4.2. Introduction

Perfluoroether carboxylic acids (PFECAs) are a major class of emerging PFAS contaminants. These compounds, carboxylic PFAS structures containing at least one ether bond and supposedly easier to metabolize than alkyl PFAS, were introduced as industrial replacements for PFOA in an effort to reduce the potential for such perfluorinated processing aids to bioaccumulate in organisms and the environment. In 2015, a branched PFECA called ammonium hexafluoropropylene dimer acid (also known as FRD-902, the trade name GenX, or HFPO-DA in its acid form) was identified in water sampled from the Cape Fear River in North Carolina, along with several other perfluoro(poly)ether carboxylates and sulfonates (*181*). In 2016, it was discovered that GenX pervasively contaminates the Cape Fear River, which serves as the primary drinking water source for over 350,000 residents of North Carolina (*182*), and that the source was a PFAS manufacturer located along the river basin (*183*). Though manufacturer had a 2009 consent order with the US EPA to "recover and capture (destroy) or recycle" GenX "at an overall efficiency of 99% from all the effluent process streams and the air emissions," these contaminants were not disposed of properly (*184*). In 2020, a report showed that miscommunication between the EPA and the local office in charge of enforcing the consent order resulted in the agency not checking for manufacturer compliance with the consent order for eight years (*185*) and the manufacturer violating the Toxic Substances Control Act multiple times (*186*).

The urgency to find ways to remediate these compounds becomes more apparent as more per- and polyfluoroether compounds are discovered. Multiple manufacturers are using polyfluorinated ether carboxylate structures as PFAS replacements, yet these structures remain unknown, unstudied, and unavailable as analytical standards because they are considered confidential business information. For example, new chloroperfluoropolyether carboxylates in

were discovered through non-targeted mass spectroscopy of soil downwind of another PFAS manufacturer in New Jersey in 2020 (*187*). However, further study of the predicted breakdown compounds from this class of polyfluoroether pollutants and comparison to the other soil components where the chloroperfluoropolyether carboxylates were found showed no evidence of ether bond cleavage (*188*). As more PFECA contamination is discovered in the environment, understanding the toxicology, reactivity, and physical properties of per- and polyfluoroether carboxylates remains of utmost importance, especially as the US EPA recently named a 10 ppt health advisory limit for GenX (*23*).

Here, we demonstrate that the polar-aprotic-solvent-assisted alkaline mineralization method described in Chapter 3 is able to degrade PFECAs in addition to straight-chain PFCAs. While the mechanism is similar to that for straight-chain PFCAs, the presence of an ether introduces barriers to degradation that result in observable intermediates that further clarify the mechanism. Our experimental observations were corroborated by computational studies that further elucidated the reactivity of these substrates, particularly the occurrence of a S_N2 reaction to eliminate the ether linkage and form a carboxylic acid. This extension of the mineralization method from Chapter 3 demonstrates that degradation via polar-aprotic-solvent-assisted alkaline mineralization is not limited to straight-chain PFCAs but can be generalized to other PFAS degradation classes.

4.3. Results and Discussion

Decarboxylation of PFECA GenX occurs at lower temperatures than for straight-chain perfluoroalkane PFCAs. McCord and co-workers noted that quantitative protodecarboxylation of branched perfluoroether carboxylic acid HFPO-DA (parent acid of GenX) occurred at 30 °C in polar aprotic solvents such as acetone, DMSO, and acetonitrile, whereas decarboxylation of PFOA

did not occur under the same conditions (*152*). They further hypothesized that the "stability of the intermediate carbanion would be crucial to this pathway" and that the stability of the branched perfluoroanion that would be produced from the decarboxylation of GenX was more stable than the primary perfluoroanion produced from PFOA, thus their difference in reactivities. In accordance with this hypothesis, we observed decarboxylation and branched CF_3 chain defluorination occuring at 40 °C (**Figure 4.2**). This finding is consistent with computational results indicating the barrier for GenX decarboxylation is only 20.4 kcal/mol (**Figure 4.4**). However, because of the presence of the ether oxygen in place of the γ-carbon, the structure is unable to eliminate a γ-fluorine and instead forms perfluoroether carboxylic acid intermediate **5** through hydrolysis (**Figure 4.1**), which builds up in solution. This intermediate was observed by both ^{19}F NMR and ESI-MS of the reaction solution (**Figure 4.2, Figure 4.3, Figure 4.5**).

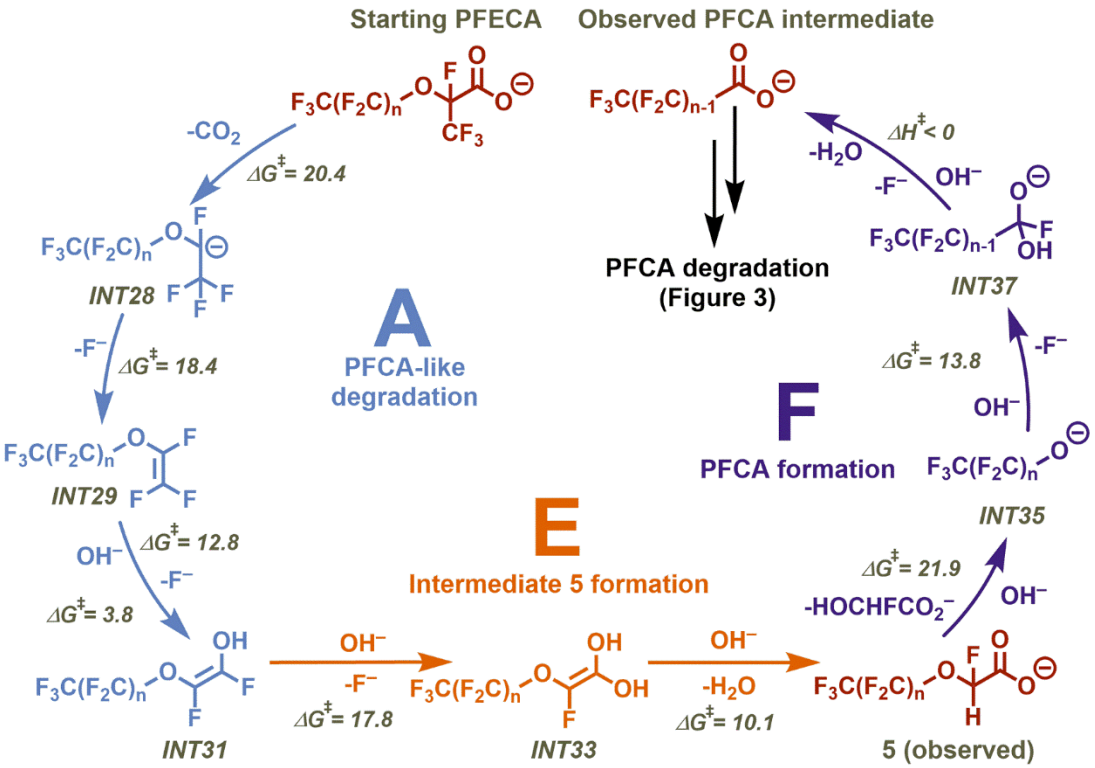

Figure 4.1. Proposed mechanism for branched perfluoroether carboxylic acid degradation. Pathway A (blue) shows the branched CF_3 defluorinating in the same manner as PFCAs in Figure 3. The lack of γ-fluorines forces formation of **5** via Pathway E (orange), observed by NMR and MS. Calculations show the hydroxide-mediated S_N2 that eliminates the perfloroalkoxide tail in Pathway F (purple), leading to the formation of a perfluorocarboxylic acid that is degraded according to the mechanism set out in Figure 3. All energies expressed in units of kcal/mol.

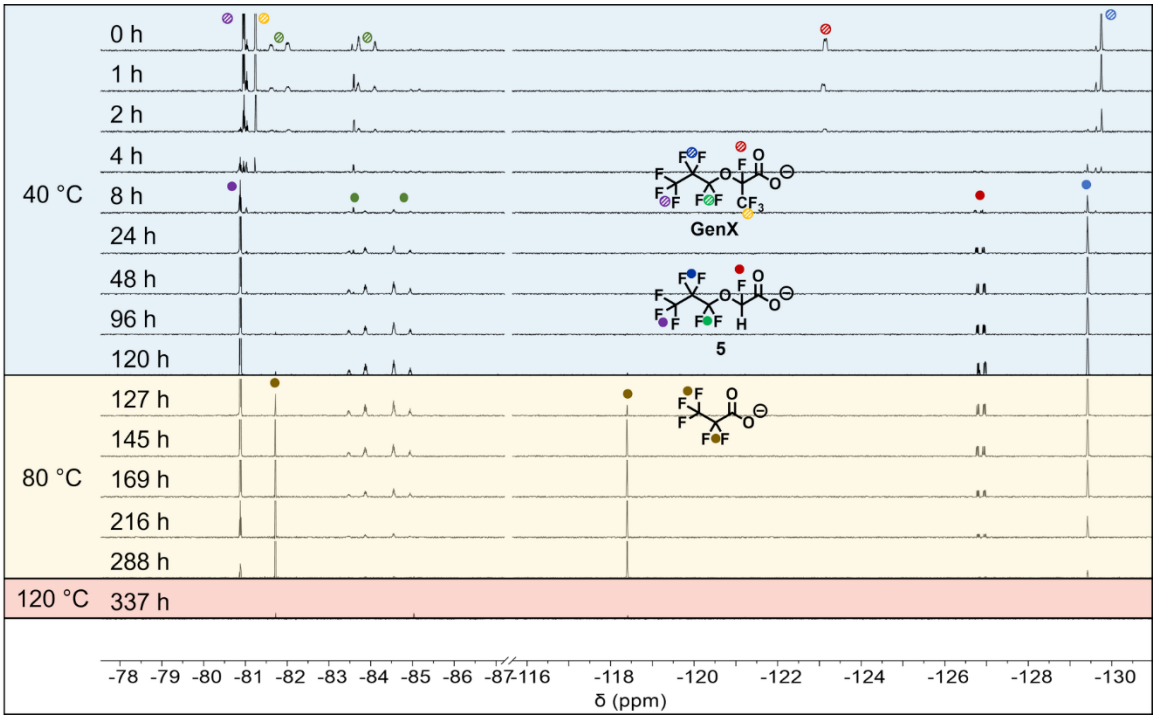

Figure 4.2. ^{19}F NMR spectra of degradation of GenX over time at increasing temperature stages. Starting material for GenX (top, shaded dots) disappear as GenX is converted to compound **5** and falls out of solution, presumably because of an insoluble intermediate that is converted to intermediate **5** over time, causing **5** to slowly increase in concentration (brightly colored dots, until 120 h). When the temperature is increased to 80 °C (121 h), peaks corresponding to PFPrA (brown dots) appear from **5** degradation as predicted, then disappear more quickly after the temperature is increased to 120 °C (289 h).

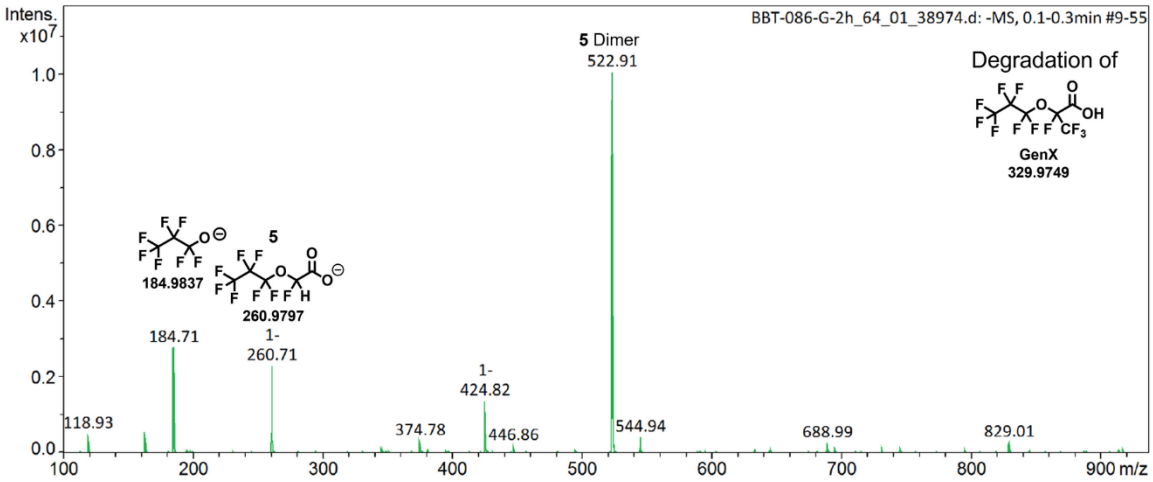

Figure 4.3. ESI-MS of spectrum of an aliquot of GenX degradation reaction diluted in acetonitrile after 2 hours of heating at 120 °C. Molecular species identified from this reaction mixture are consistent with the proposed reaction mechanism, especially the **5** and **5** dimer at 260.71 m/z and 522.91 m/z.

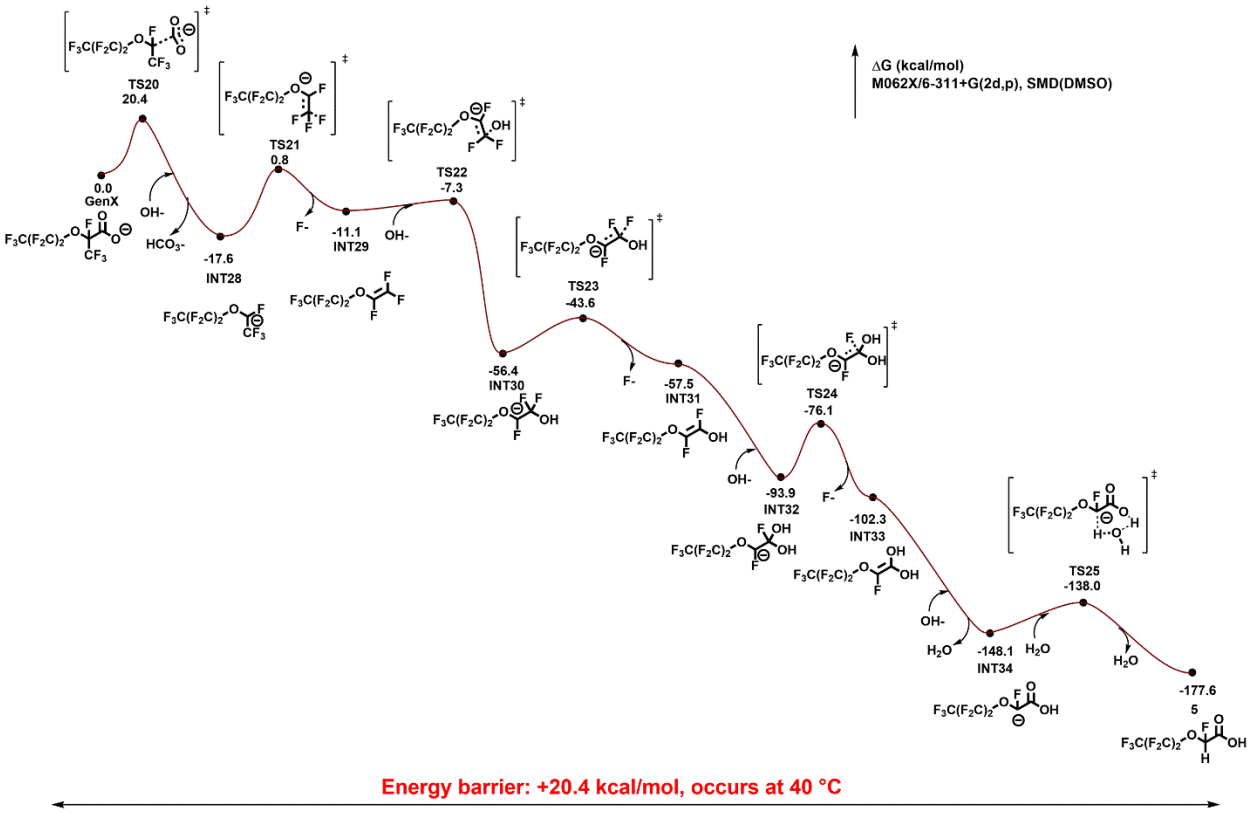

Figure 4.4. Gibbs free energy profile for pathways A and E for GenX.

Calculations show that the decarboxylation of intermediate **5** is unfavorable (**Figure 4.7, Figure 4.8**); rather, a hydroxide-mediated S_N2 with a barrier of 21.9 kcal/mol occurs in which the perfluoroalkoxide tail is eliminated (**Figure 4.6**). This process only occurs when the temperature is increased (80 °C, **Figure 4.2, Figure 4.5**). The perfluoroalkoxide tail eliminates two fluorines to form a carboxylic acid ($\Delta G^{\ddagger}$ = 21.9 kcal/mol) with the same number of carbons as the original perfluoroether tail. Because GenX contains a three-carbon tail, it produces the C3 PFCA (PFPrA), the degradation of which leads to incomplete defluorination (41%, **Figure 3.4D**) and formation of CF_3CF_2H (**Figure 4.9, Figure 4.10, Figure 4.14**). These observations are consistent with those of the direct degradation of PFPrA, which also did not produce fluoride and showed evidence of CF_3CF_2H (**Figures 3.4D**, **3.9, 3.10, 3.12, 4.14**). The experimental observations show that temperatures of 40 °C, 80 °C, and 120 °C are necessary to form INT1, to form the PFCA analogue,

and to initiate PFCA degradation, respectively. These temperature steps correspond with the calculated energy barriers of 20.4 kcal/mol, 21.9 kcal/mol, and 27.7 kcal/mol, respectively (**Figure 4.2, Figure 4.4, Figure 4.6**).

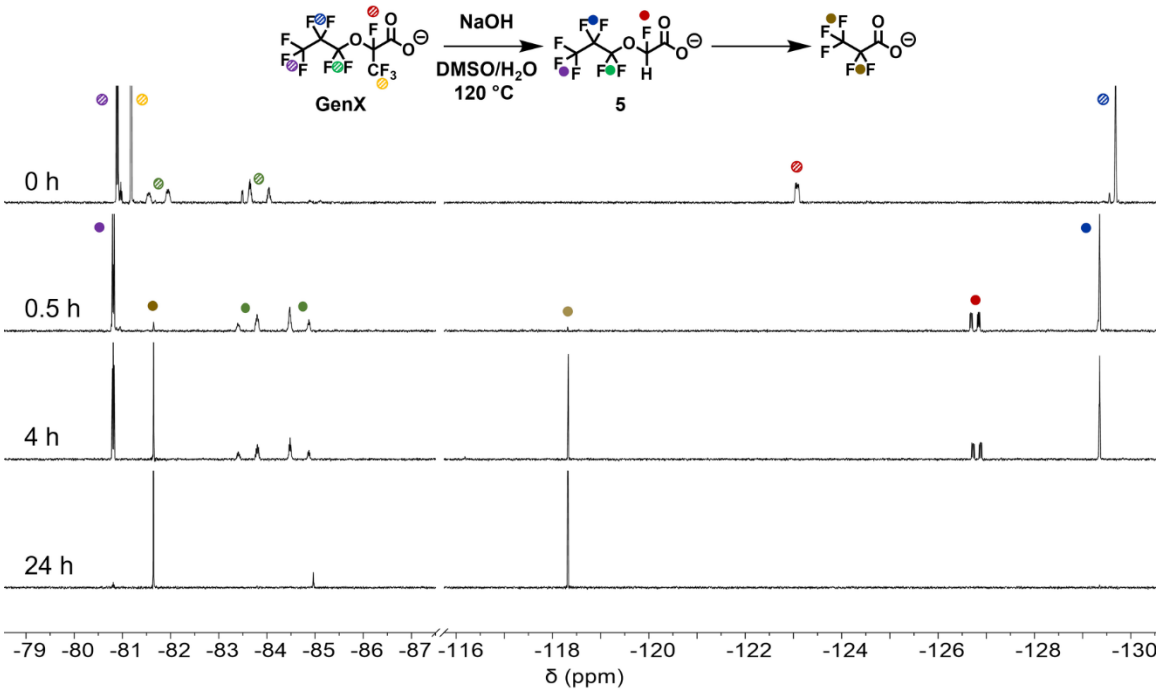

Figure 4.5. ^{19}F NMR spectra of GenX degradation reaction at 120 °C. The starting material (added as GenX ammonium salt) quickly decarboxylates and proto-de-trifluoromethylates to intermediate **5**, which was also detected by ESI-MS (**Figure 4.3**). Over the course of several hours, **5** degrades to PFPrA, which subsequently degrades further, mainly to CF_3CF_2H, as described for the degradation of PFPrA (**Figure 3.4, Figure 4.9**).

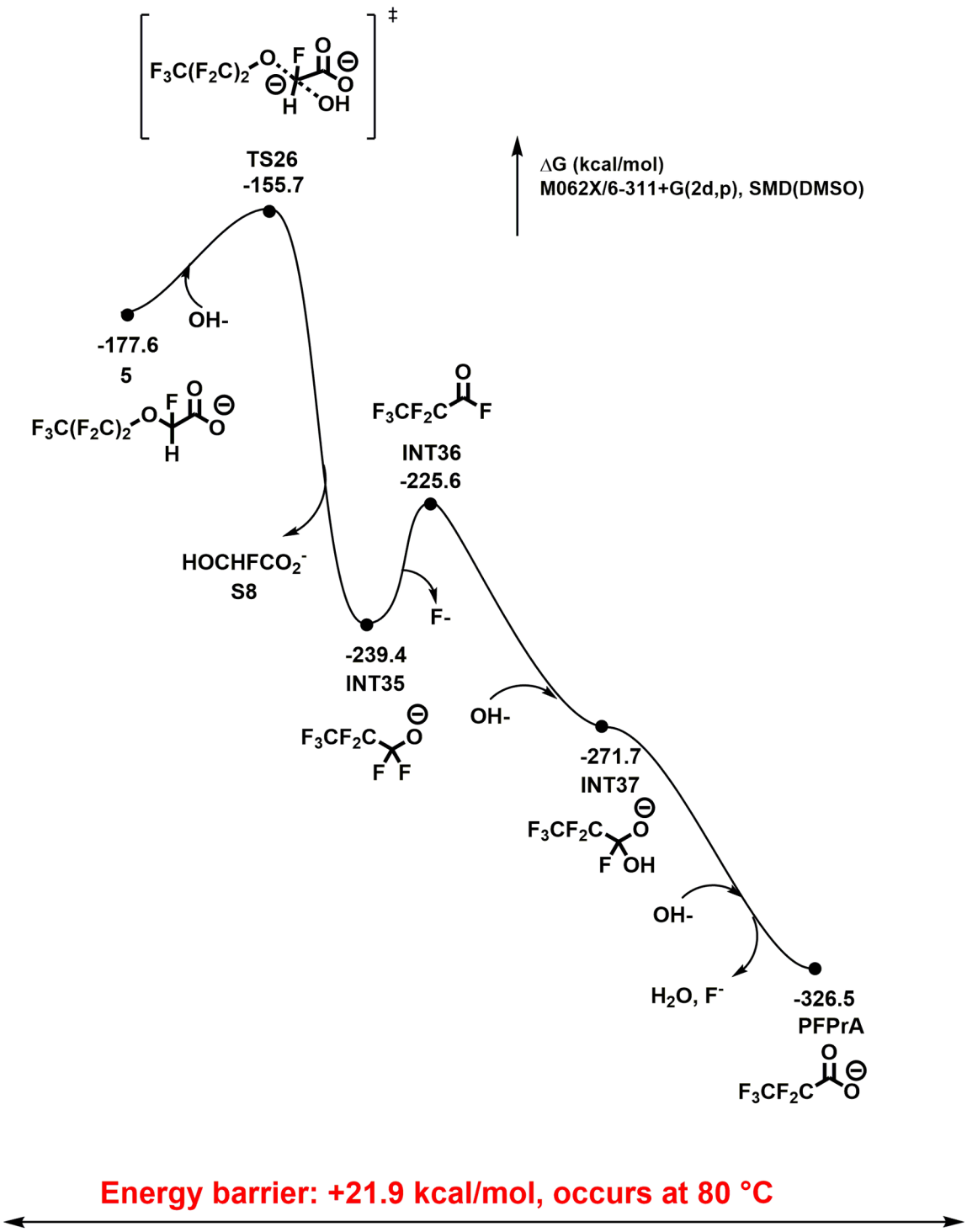

Figure 4.6. Gibbs free energy profile for pathway F for GenX.

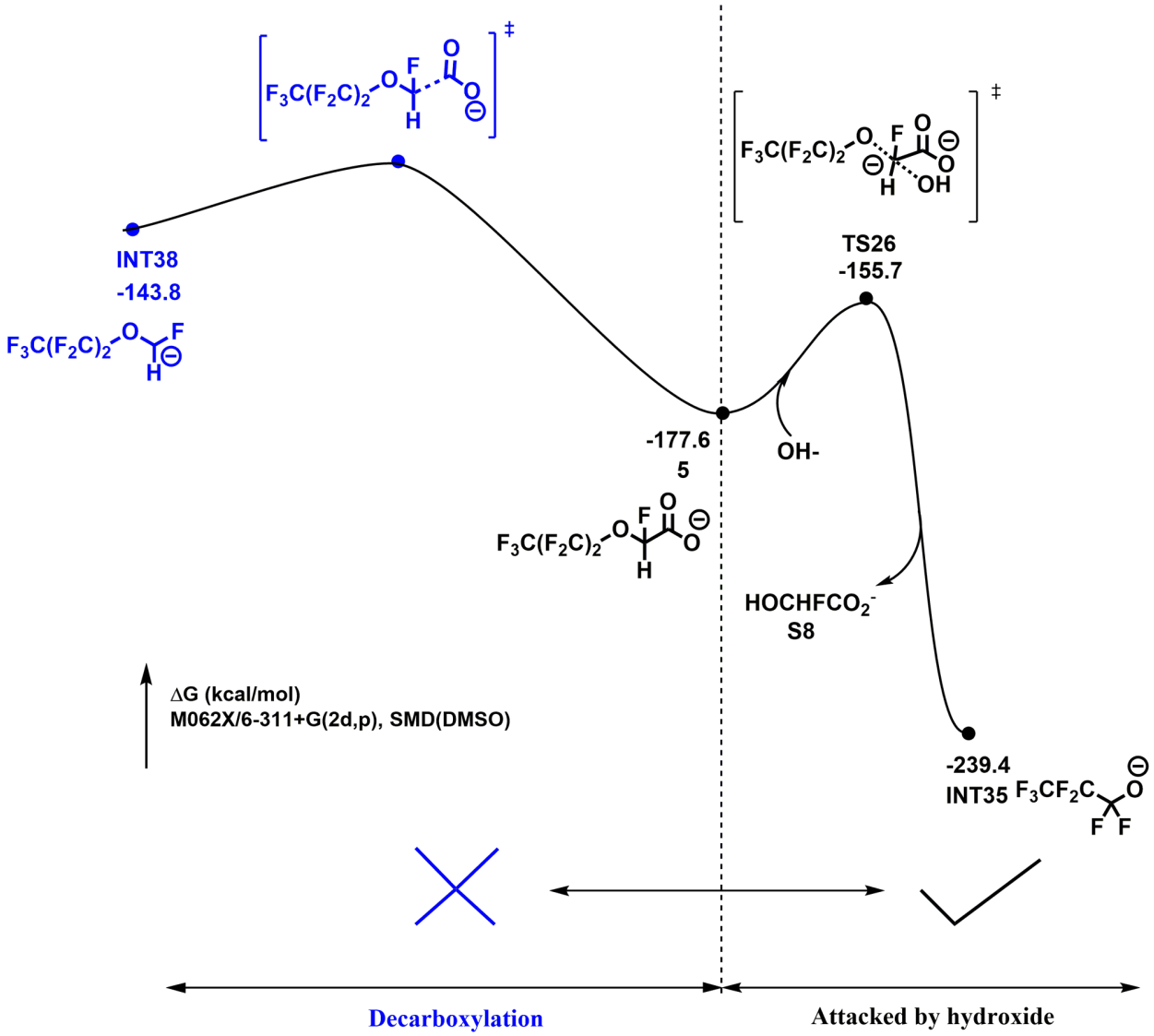

Figure 4.7. Comparison of hydroxide attack vs. decarboxylation of **5**. The transition state for the transformation of **5** to INT38 will be higher than the energy of INT38, which is already 33.8 higher than **5**, disfavoring the reaction compared to TS26 (21.9 kcal/mol relative to **5**) and INT35 (-61.8 kcal/mol relative to **5**).

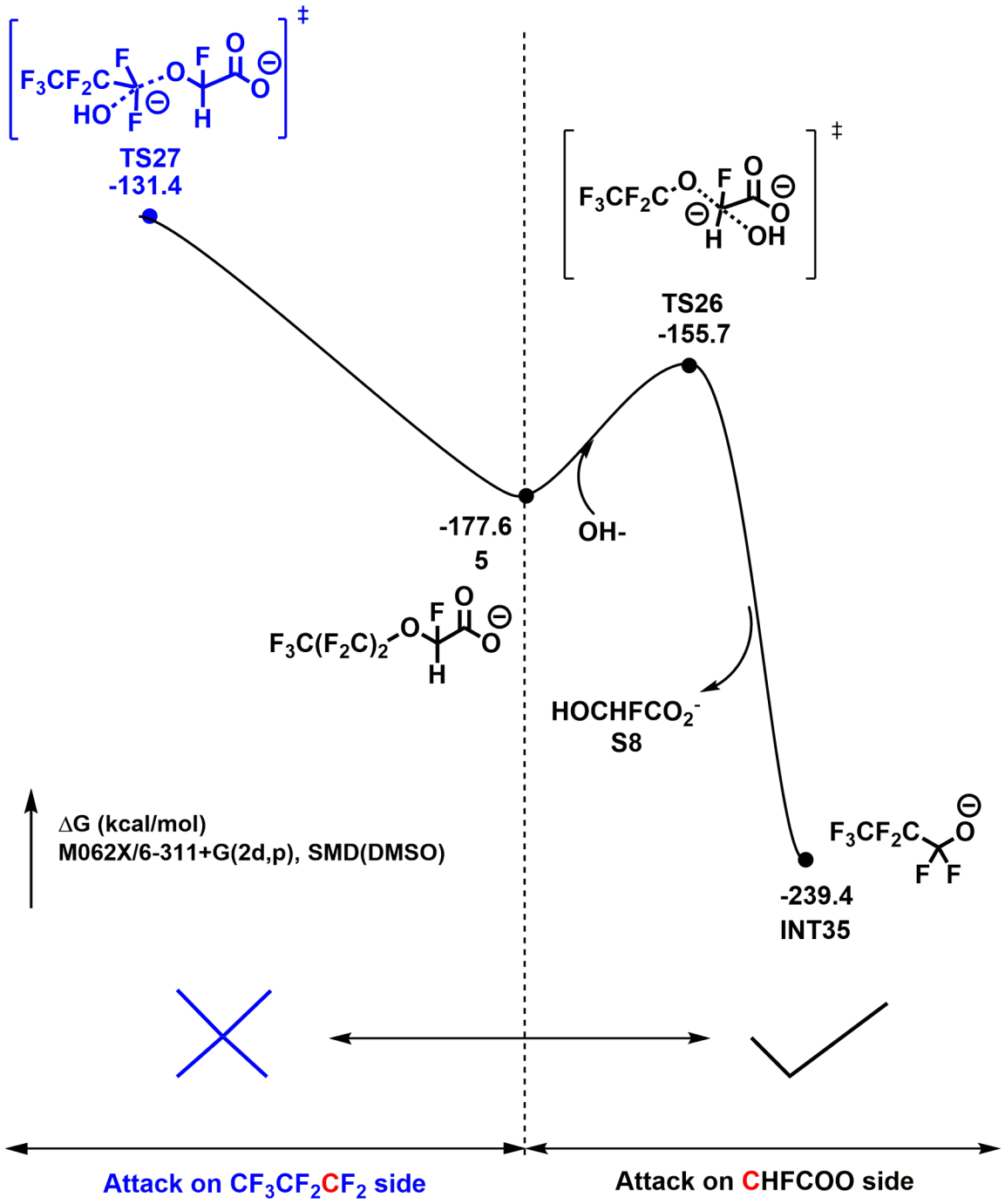

Figure 4.8. Comparison of hydroxide attack on different sides of compound **5**.

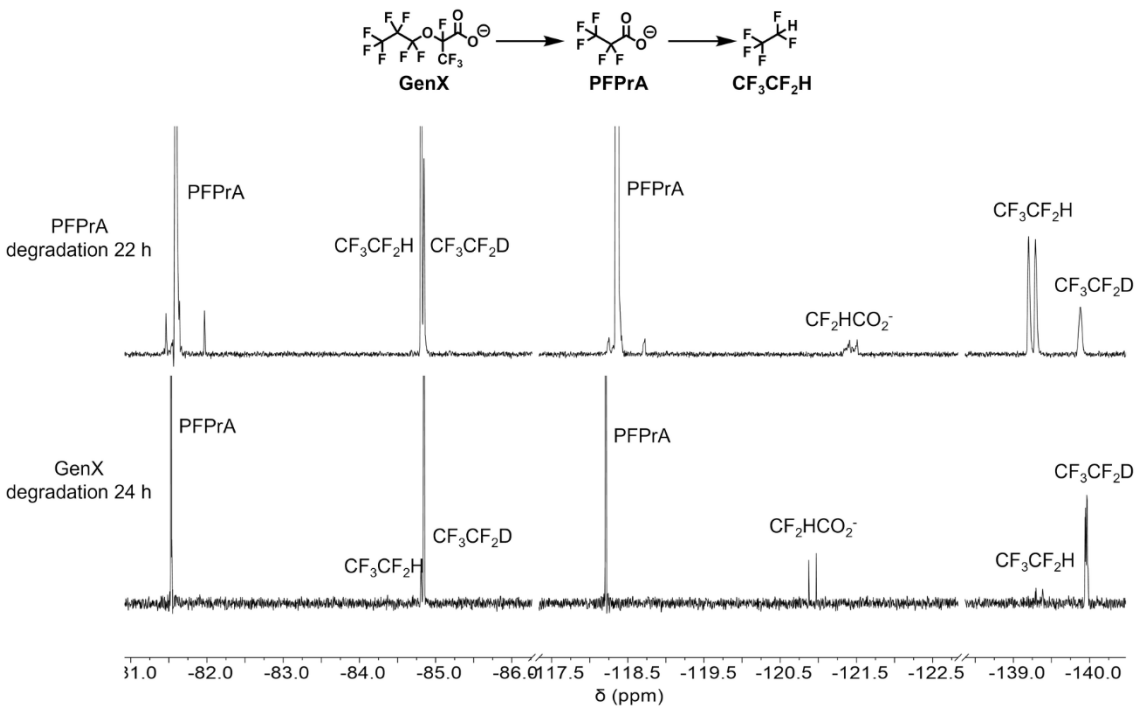

Figure 4.9. ^{19}F NMR spectra of the degradation of perfluoropropionic acid (top) after 22 hours and GenX (bottom) after 24 hours at 120 °C. Peaks corresponding to the same compounds appear in the degradation of each, indicating that GenX degrades to PFPrA and then follows the PFPrA degradation pathway, including producing CF_3CF_2H, which volatilizes and does not defluorinate, resulting in a lower fluoride recovery than for longer-chain analogues. Identity of CF_3CF_2D hypothesized.

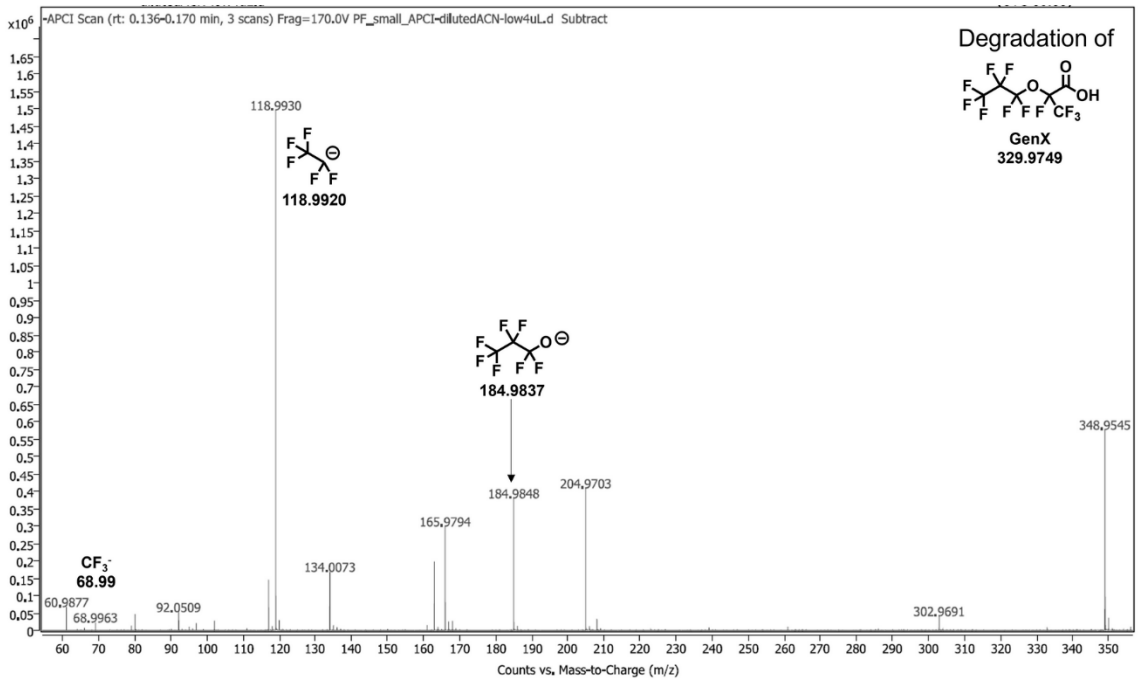

Figure 4.10. APCI-MS spectrum of an aliquot of GenX degradation reaction diluted in acetonitrile after 7 hours of heating at 120 °C. Molecular species identified from this reaction mixture are consistent with the proposed reaction mechanism, especially the prominent 118.9930 m/z peak corresponding to $CF_3CF_2^-$, which either comes from the decarboxylation of $CF_3CF_2CO_2^-$ or the deprotonation of CF_3CF_2H.

These observations indicate that fluoride recovery from the destruction of GenX is low (**Figure 3.4D**) not because perfluoroethers inherently escape defluorination, but because GenX degrades to PFPrA, which degrades to mainly CF_3CF_2H. To show that this low fluoride recovery is related to the degradation of PFPrA and is not inherent to molecules with the ether linkage, we degraded a longer perfluoroalkyl ether acid, Compound **4**, with a five-carbon perfluoroalkyl tail. According to our proposed mechanism, this longer molecule should degrade to PFPeA, which has a higher fluoride recovery because it can go through the degradation cycle mechanism proposed in **Figure 3.16**. Degradation of **4** (**Figure 4.11–Figure 4.14**) proceeded by a similar mechanism as that of GenX and gave fluoride recoveries (81%) consistent with those obtained from the five-carbon PFCA, PFPeA (**Figure 3.4D**). These findings indicate that perfluoroalkyl ether carboxylates also degrade via perfluoroalkyl anion-based processes and the low fluoride recovery from GenX is because of its short perfluoroalkyl tail, not because of the ether linkage. Intermediates in the degradation of **4**, as observed by APCI-MS (**Figure 4.13**), also corroborate the proposed mechanism (**Figure 4.1**).

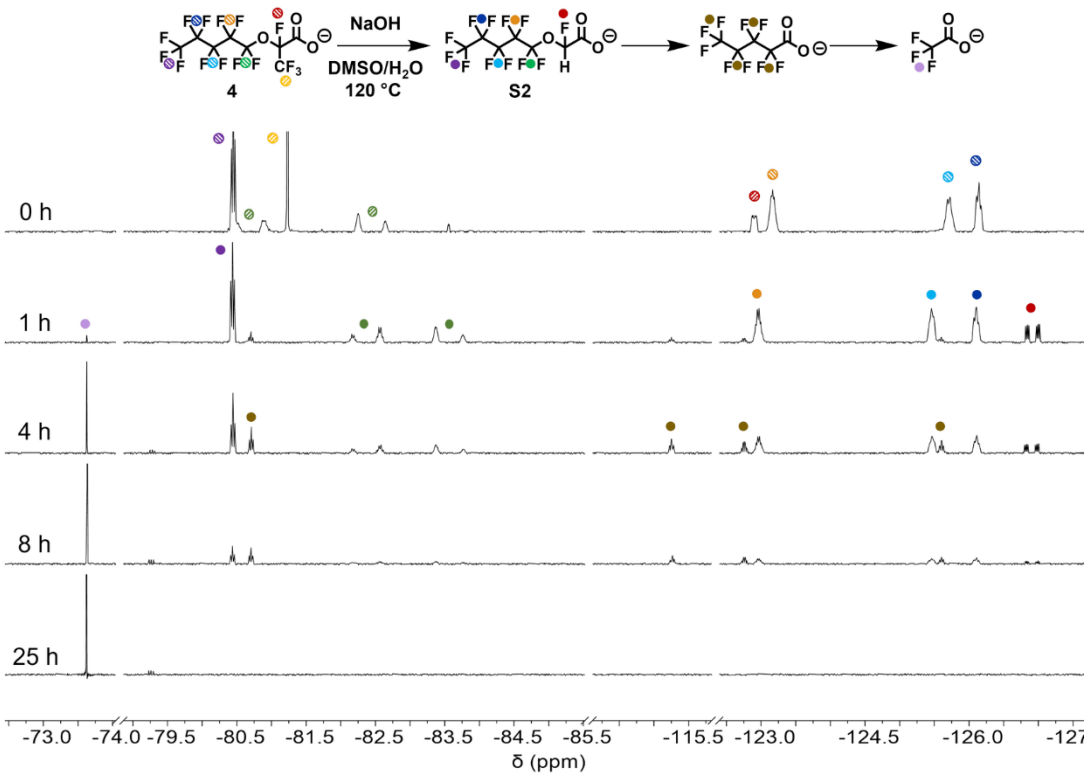

Figure 4.11. ^{19}F NMR spectra of **4** degradation reaction at 120 °C. The starting material (added as **4** ammonium salt) quickly decarboxylates and proto-de-trifluoromethylates to intermediate **S2**, which was also detected by APCI-MS (**Figure 4.13**). Over the course of several hours, **S2** degrades to PFPeA, which subsequently degrades further, mainly to fluoride and $CF_3CO_2^-$, as described for the degradation of PFPeA (**Figure 3.4**).

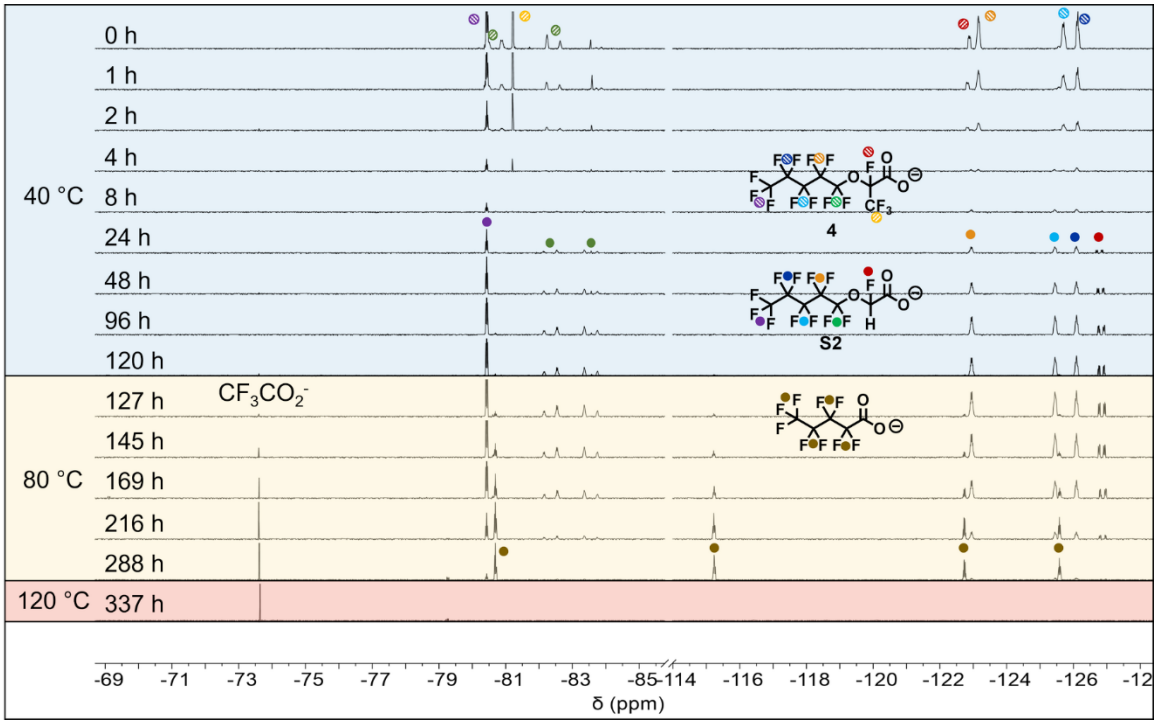

Figure 4.12. ^{19}F NMR spectra of degradation of **4** over time at increasing temperature stages. Starting material for **4** (top, shaded dots) disappear as **4** is converted to intermediate **S2** and falls out of solution, presumably because of an insoluble intermediate that is converted to intermediate **S2** over time, causing **S2** to slowly increase in concentration (brightly colored dots, until 120 h). When the temperature is increased to 80 °C (121 h), peaks corresponding to PFPeA (brown dots) and trifluoroacetate appear from **S2** degradation as predicted, then disappear more quickly after the temperature is increased to 120 °C (289 h).

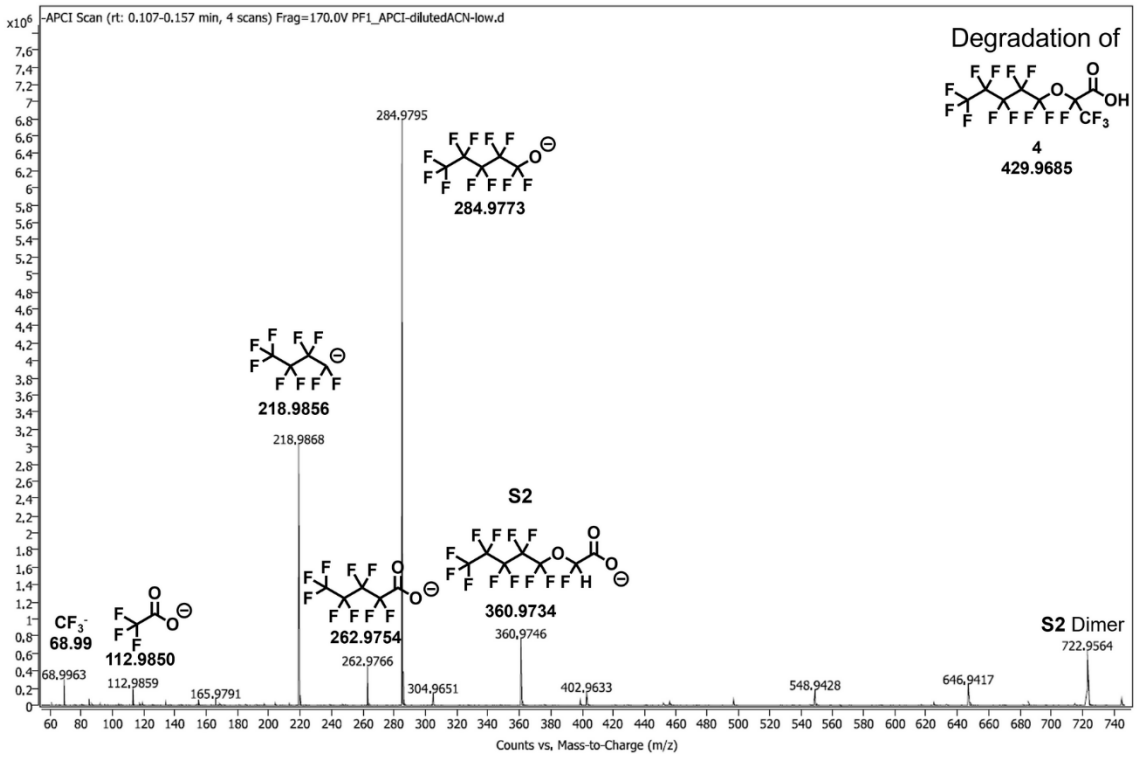

Figure 4.13. APCI-MS spectrum of an aliquot of **4** degradation reaction diluted in acetonitrile after 4 hours of heating at 120 °C. Molecular species identified from this reaction mixture are consistent with the proposed reaction mechanism, especially the **S2** and **S2** dimer peaks at 360.9746 m/z and 722.9564 m/z.

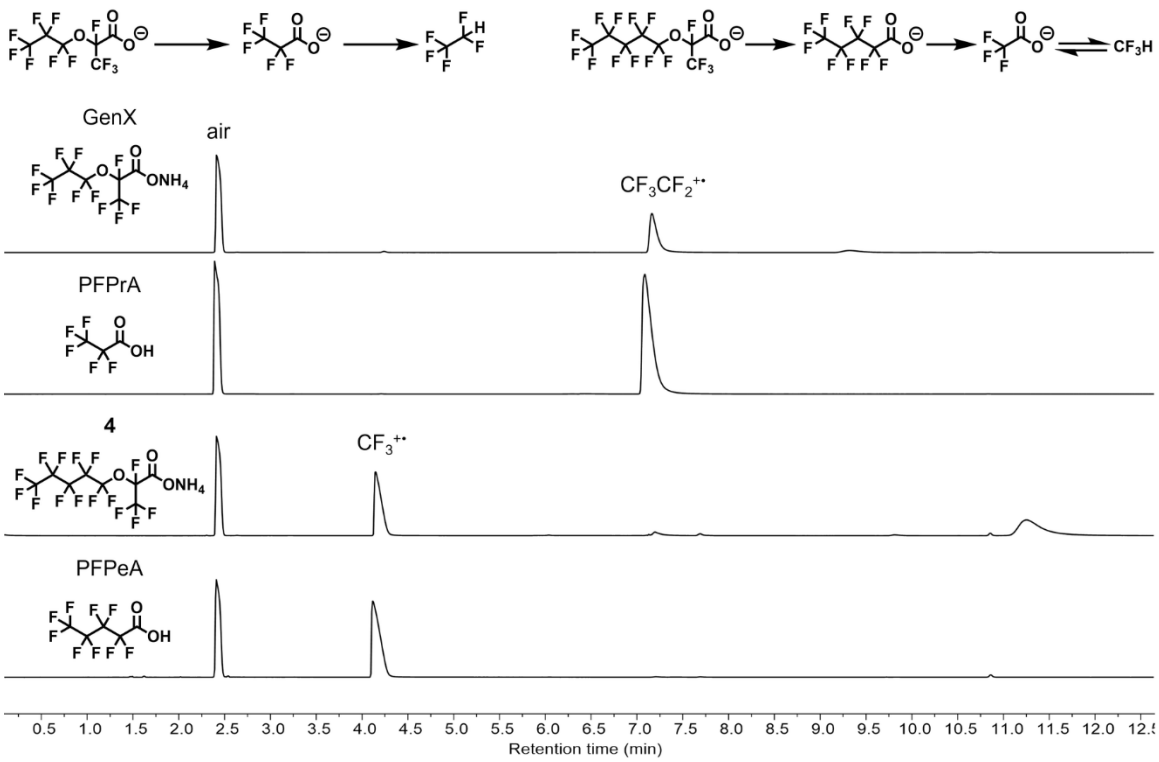

Figure 4.14. GCMS-headspace total ion chromatograms after 4 hours of reaction for GenX (top), perfluoropropionic acid (second from top), **4** (second from bottom), perfluoropentanoic acid (bottom). Both PFPrA and GenX show evidence of $CF_3CF_2^{+\bullet}$ gas fragments, presumably derived from CF_3CF_2H, whereas PFPeA and **4** show only $CF_3^{+\bullet}$ fragments, presumably from an equilibrium between CF_3COOH and CF_3H.

4.4. Conclusions

Two branched PFECAs of different tail lengths were degraded in DMSO with sodium hydroxide. The degradation occurred in three stages: 1) decarboxylation, de-trifluoromethylation, and protonation to Compound **5** / Compound **S2** at 40 °C, 2) S_N2 elimination and transformation for PFCA at 80 °C, 3) degradation of PFCA according to Chapter 3 at 120 °C. Observation of Compound **5** / Compound **S2** further supported the mechanism set forth in the previous chapter. Though the fluoride recovery for GenX was lower than desired, degradation of the longer-chain Compound **4**, in conjunction with the PFCA series degraded in Chapter 3, showed that the low fluoride recovery was not due to the nature of the ether but rather can be attributed to the tendency for the C3 PFCA to degrade to volatile CF_3CF_2H. The successful degradation of PFECAs shows that the low-temperature polar-aprotic-solvent-assisted alkaline degradation is competent to

degrade more than just straight-chain PFCAs and should be applicable to other PFAS as methods to activate their headgroups are developed.

4.5. Acknowledgements

We thank Dr. Yongrui Luo at Shanghai Institute of Organic Chemistry for helpful discussions about fluorine NMR, Saman Shafaie at Northwestern University's IMSERC facility for assistance with mass spectrometry, and Rebecca Sponenburg at Northwestern University's QBIC for ion chromatography.

Funding: BBT is supported by the National Science Foundation Graduate Research Fellowship Program (DGE-1842165). KNH is supported by National Science Foundation (CHE-1764328) and the Saul Winstein Chair in Organic Chemistry. Ion chromatography was performed at the Northwestern University Quantitative Bio-element Imaging Center generously supported by NASA Ames Research Center Grant NNA04CC36G. This work made use of the IMSERC at Northwestern University, which has received support from the NIH (1S10OD012016-01 / 1S10RR019071-01A1), Soft and Hybrid Nanotechnology Experimental (SHyNE) Resource (NSF ECCS-1542205), the State of Illinois, and the International Institute for Nanotechnology (IIN). GCMS was performed at the REACT Core Facility at Northwestern University; The REACT Core facility acknowledges funding from the U.S. Department of Energy, Office of Science, Office of Basic Energy Sciences, Catalysis Science program (DE-SC0001329) used for the purchase of the GC/MS analysis system.

4.6. Chapter 4 Appendix

A. Materials, Instrumentation, and Computational Methods

Materials. Reagents were purchased in reagent grade from commercial suppliers and used without further purification, unless otherwise described. Anhydrous DMSO was obtained by drying with activated 4Å molecular sieves. Reagents were purchased from Fisher or Sigma unless specified.

4,4′-difluorobenzophenone NMR standard (Merck) was prepared by diluting to 0.095 M in DMSO-d_6 and adding 60–80 µL of solution to a coaxial NMR tube insert (Wilmad-Lab Glass, WGS-5BL). Each ^{19}F NMR sample was referenced to 4,4′-difluorobenzophenone (-106.5 ppm) by inserting the coaxial tubes containing the external NMR standard into the NMR sample tube before NMR analysis. ^{13}C NMR samples were quantified using a sodium acetate standard in D_2O (50 µL, 5.33 M). ^{1}H NMR samples were quantified using 4,4′-dihydroxybiphenyl dissolved in DMSO-d_6 (0.68 M). Quantification of samples was conducted by integrating each NMR peak and normalizing with the external standard peak integration, then converting to molar concentration using the known molar amount of the external standard. 25 mL PTFE round bottom flasks were purchased from Ace Glass (United States, 13438-16).

PFCA degradation reactions were conducted on 0.5 mmol or 1 mmol scales.

Instruments

Proton nuclear magnetic resonance (^{1}H NMR) spectra and fluorine nuclear magnetic resonance (^{19}F NMR) spectra were recorded at 25 °C on a 400 MHz Bruker Avance III HD Nanobay equipped with a BBFO Smart probe w/ Z-Gradient (unless stated otherwise). Fluorine-decoupled carbon nuclear magnetic resonance (^{13}C NMR) spectra and two-dimensional C–F spectra were recorded on a Bruker Neo 600 MHz system with a QCI-F cryoprobe w/ Z-Gradient. Quantitative ^{13}C NMR

spectra were recorded on a Bruker Avance III 500 MHz system equipped with a 5mm DCH CryoProbe w/Z-Gradient using a 40 second D1 delay. Other spectra were recorded on a Bruker Avance III 600 MHz with a BBFO Smart Probe w/ Z-Gradient. Experiments used pulse programs adapted from standard Bruker pulses library.

Ion chromatography was performed using a Thermo Scientific Dionex ICS-5000+ equipped with a Dionex AS-DV autosampler and using a Dionex IonPac AS22 column (Product No. 064141, Thermo Scientific, California, USA). The analysis was run using an eluent of 4.5 mM sodium carbonate and 1.4 mM sodium bicarbonate (Product No. 063965 from Thermo Scientific, California, USA) and a Dionex AERS 500 Carbonate 4 mm Electrolytically Regenerated Suppressor (Product No 085029 from Thermo Scientific, California, USA). A flow rate of 1.2 mL/min was used, giving the following retention times: fluoride = 3.3 min; formate = 3.8 min. Elemental standards containing 1000 µg/mL F^-, and 1000 ug/mL $HCOO^-$ (ICF1, ICHCO1, respectively, from Inorganic Ventures, Christiansburg, VA, USA) were mixed to make quantitative standards consisting of 50, 25, 12.5, 6.25, 3.125, 1.56, 0.78 ug/mL of each anion in ultra-pure H_2O (18.2 MΩ·cm). Ultra pure H_2O was used as the calibration blank. Validation experiments indicated an error of approximately 10% for ion chromatography results.

APCI-MS was collected on an Agilent 6545 QTOF Mass Spectrometer equipped with Atmospheric Pressure Chemical Ionization (APCI) source coupled with Agilent 1200 series LC running in direct injection mode. Data acquisition and analysis were done on Agilent Mass Hunter software.

GC/MS analysis was performed in the Reactor Engineering and Catalyst Testing (REACT) core facility at Northwestern University using an Agilent 6850 GC system coupled to an Agilent

5975C MS system. Helium (Airgas, 99.999%) was purified using an Agilent "Big Universal Trap" (Model RMSH-2) and used as a carrier gas. Gas separation was performed using a HP-Plot Q column (19091P-Q04E, 30m x 0.320 mm x 20 um) starting at 50 °C for 4 minutes. The temperature was then ramped to 220 °C at 30 °C/min and held for 3 minutes. The flow rate of He was maintained at 1.2 mL/min (inlet split ratio of 10:1). The MS was operated in scan mode (Gain factor = 1, EM voltage = 2518, MS Source = 250 °C, MS Quad = 150 °C) from m/z = 5 to m/z = 300. A solvent delay was not used.

Geometry optimizations, frequency analyses, and single-point energies were calculated at the theoretical M06-2X/6-311+G(2d,p)-SMD-(DMSO) level (*171*, *172*) using the Gaussian 16 package (*173*) with default convergence criteria. M06-2X functional gives refined energies for organic systems (*174*). Frequency outcomes were examined to confirm stationary points as minima (no imaginary frequencies) or transition states (only one imaginary frequency). Paton's GoodVibes (*175*) was used to correct entropy and enthalpy by Grimme's quasi-harmonic approximation (*176*) and Head-Gordon's method (*177*). 3D structures of molecules were generated by CYL view (*178*). All energies are in kcal/mol if not labeled otherwise. All bond lengths are in Angstroms (Å).

4.6.1. Synthetic Procedures and NMR Characterization of Synthesized Compounds

General PFCA Destruction Procedure: Perfluorooctanoic acid (207 mg, 0.500 mmol) and sodium hydroxide (0.600 g, 15.0 mmol) were added to a 25 mL PTFE round bottom flask along with a PTFE-coated magnetic stirbar. 5 mL DMSO was added to the reaction vessel, followed by 0.625 mL distilled or de-ionized water. The vessel was sonicated for approximately 15 seconds, then the t = 0 aliquot was taken by diluting a 50 µL aliquot into 500 µL of deuterated solvent. The vessels were sealed with a rubber septum and pierced with a needle that was left in the septum to prevent overpressure. The vented vessels were then added to an oil bath preheated to 120 °C and stirred at 500 RPM for the specified time, usually 24 hours. Liquid aliquots for reactions monitored over time were taken using a syringe inserted through the rubber septum and diluted as above with solids removed by centrifugation if necessary. The reactions were removed from the heat and cooled for at least 40 minutes before workup. The entire contents of the reaction were diluted with distilled or deionized water until the solids at the bottom were completely dissolved (typically 20–40 mL water added) and were transferred to a polypropylene centrifuge tube. The resulting fluoride- and formate- containing solution was further diluted in water 100x–500x for ion chromatography analysis. For carbonaceous products quantification, the contents of the reaction were added to a 15 mL polypropylene centrifuge tube, centrifuged, and the DMSO solvent was decanted. The remaining solids were rinsed and centrifuged 2x with dichloromethane, then dried overnight at 120 °C on high vac. A portion of the solids (~30 mg) was dissolved (750 µL D_2O + 50 µL NaOAc standard in D_2O) for quantitative ^{13}C NMR analysis.

4.6.2. XYZ Coordinates of Optimized DFT Structures and Corresponding Energies

GenX
E(DMSO)[M06-2X/6-311++G(2d,p), SMD (DMSO)] = -2028.356103 a.u.
G_{corr}(DMSO)[M06-2X/6-311++G(2d,p)] = 0.051716 a.u.
H_{corr}(DMSO)[M06-2X/6-311++G(2d,p)] = 0.126659 a.u.
G = E(DMSO) + G_{corr} = -2028.304387 a.u.
H = E(DMSO) + H_{corr} = -2028.229444 a.u.

C	-4.44504000	0.10771900	-0.28358800
C	-3.14109700	-0.51613800	0.26092700
C	-1.88388600	0.33284700	-0.05068300
C	-0.57724800	-0.49189500	0.06187600
C	0.68547400	0.38509600	0.23210000
F	-4.50247900	1.39310600	0.03902600
F	-4.50683600	-0.01506400	-1.59956600
F	-5.48057000	-0.51918300	0.25314100
F	-3.00816500	-1.73291400	-0.28124500
F	-3.26176600	-0.63704300	1.58589100
F	-1.98057500	0.81600900	-1.29620000
F	-1.84742800	1.35907700	0.80758600
F	-0.45118500	-1.22633500	-1.04767500
F	-0.66606800	-1.31056800	1.11980400
F	0.61880300	1.39789200	-0.64747500
F	0.68221600	0.92261000	1.45818400
O	1.75341600	-0.41586800	0.02571000
C	3.04182000	0.08556100	0.30904600
F	3.23093000	0.02801100	1.65605900
C	3.33429100	1.53433000	-0.25749500
O	3.31654200	2.42905700	0.58914200
O	3.53674400	1.54111200	-1.47685400
C	3.98433000	-0.97672400	-0.27165200
F	5.24753400	-0.57037900	-0.14451800
F	3.86216300	-2.12392800	0.40834700
F	3.74726400	-1.24786900	-1.54549100

TS20
E(DMSO)[M06-2X/6-311++G(2d,p), SMD (DMSO)] = -2028.318027 a.u.
G_{corr}(DMSO)[M06-2X/6-311++G(2d,p)] = 0.046131 a.u.
H_{corr}(DMSO)[M06-2X/6-311++G(2d,p)] = 0.122854 a.u.
G = E(DMSO) + G_{corr} = -2028.271896 a.u.
H = E(DMSO) + H_{corr} = -2028.195173 a.u.

C	-4.39319500	0.23205400	-0.39490300
C	-3.17431800	-0.43710900	0.27884800
C	-1.83542900	0.26559700	-0.05632900
C	-0.60919000	-0.64468800	0.20270100
C	0.72273400	0.12654300	0.34367300
F	-4.33387600	1.54845100	-0.24010200
F	-4.42615600	-0.05339400	-1.68664400
F	-5.50334300	-0.21834800	0.16967900
F	-3.13005300	-1.71327500	-0.12518400
F	-3.36296400	-0.40251300	1.60123700
F	-1.84727100	0.61869000	-1.34977900
F	-1.74932500	1.37453800	0.68855500
F	-0.51345400	-1.50260900	-0.82065500
F	-0.82055500	-1.34156400	1.33171600
F	0.75790600	1.06039400	-0.63896500
F	0.69439000	0.80684000	1.50868000
O	1.72250000	-0.74704500	0.28102700
C	3.03126900	-0.13706400	0.43209100
F	3.42246700	-0.51526100	1.73993300
C	3.36540000	2.32149000	-0.15069900
O	3.08131200	2.77256400	0.88345000
O	3.70126300	2.16403800	-1.25396000
C	3.88900500	-1.00274200	-0.44275400
F	5.18251900	-0.65295000	-0.32815500
F	3.85534200	-2.33693700	-0.17921500
F	3.55012300	-0.87883500	-1.73331400

INT28

E(DMSO)[M06-2X/6-311++G(2d,p), SMD (DMSO)] = -1839.732628 a.u.

G_{corr}(DMSO)[M06-2X/6-311++G(2d,p)] = 0.039458 a.u.

H_{corr}(DMSO)[M06-2X/6-311++G(2d,p)] = 0.10878 a.u.

G = E(DMSO) + G_{corr} = -1839.69317 a.u.

H = E(DMSO) + H_{corr} = -1839.623848 a.u.

C	-4.02391400	-0.36619900	-0.10673400
C	-2.73116200	0.20918900	0.51308300
C	-1.48464300	0.00459000	-0.38299400
C	-0.16059400	0.12977000	0.41085200
C	1.07731200	0.40503200	-0.47282000
F	-4.12355500	0.00379200	-1.37677700
F	-4.02755600	-1.68768300	-0.03658000

F	-5.06893300	0.09943600	0.56085000
F	-2.54126700	-0.38823900	1.69635500
F	-2.91452700	1.51859000	0.70730000
F	-1.54507100	-1.21697000	-0.93243800
F	-1.52214200	0.91663700	-1.36209500
F	0.02387500	-1.01599600	1.07877900
F	-0.28227300	1.13132600	1.29787600
F	0.99834600	-0.41559300	-1.54983600
F	0.98036600	1.66406400	-0.95231100
O	2.16705200	0.21067300	0.26021900
C	3.40284000	0.53199500	-0.43922400
F	3.86334700	1.68585900	0.25162000
C	4.32659600	-0.53868600	0.06359000
F	5.58630100	-0.31234400	-0.34985000
F	4.41211500	-0.67473800	1.41270200
F	3.96374900	-1.74586600	-0.40073600

TS21

E(DMSO)[M06-2X/6-311++G(2d,p), SMD (DMSO)] = -1839.701735 a.u.

G_{corr}(DMSO)[M06-2X/6-311++G(2d,p)] = 0.037908 a.u.

H_{corr}(DMSO)[M06-2X/6-311++G(2d,p)] = 0.107841 a.u.

G = E(DMSO) + G_{corr} = -1839.663827 a.u.

H = E(DMSO) + H_{corr} = -1839.593894 a.u.

C	-4.03551600	-0.41415100	-0.11800400
C	-2.78242600	0.33257300	0.39004400
C	-1.47811300	-0.11668600	-0.31179900
C	-0.21129300	0.27973800	0.48792200
C	1.07061700	0.29725400	-0.37189100
F	-4.05642300	-0.41660100	-1.44418900
F	-4.04444300	-1.66209600	0.32124700
F	-5.11772700	0.20375500	0.33029300
F	-2.67984700	0.11680800	1.70754900
F	-2.96326300	1.63798900	0.17017600
F	-1.49517300	-1.44881800	-0.45181400
F	-1.44116600	0.44253000	-1.52725200
F	-0.05649100	-0.59963300	1.48302300
F	-0.38455600	1.50268900	1.01046700
F	1.08638200	-0.80641900	-1.14123000
F	1.02984300	1.35132800	-1.20086300
O	2.13321100	0.35160700	0.46174100
C	3.34553400	0.51262200	-0.18516000

F	3.77587300	1.79883100	-0.14941400
C	4.26494700	-0.47583700	-0.12867300
F	5.42768500	-0.29281800	-0.72165500
F	5.04939500	-0.69049600	1.55127700
F	3.85789100	-1.72659600	-0.18967900

INT29

E(DMSO)[M06-2X/6-311++G(2d,p), SMD (DMSO)] = -1739.723881 a.u.

G_{corr}(DMSO)[M06-2X/6-311++G(2d,p)] = 0.039301 a.u.

H_{corr}(DMSO)[M06-2X/6-311++G(2d,p)] = 0.107161 a.u.

G = E(DMSO) + G_{corr} = -1739.68458 a.u.

H = E(DMSO) + H_{corr} = -1739.61672 a.u.

C	3.79938800	0.13085900	-0.25179500
C	2.48718100	-0.49056800	0.27556200
C	1.22154800	0.22190400	-0.26101000
C	-0.03010400	-0.08038200	0.60177400
C	-1.35431500	0.20231500	-0.13915000
F	3.72098200	0.30493400	-1.56460000
F	4.02891700	1.29636100	0.33020000
F	4.80423400	-0.68775700	0.01654100
F	2.50290500	-0.42537900	1.61264400
F	2.45387300	-1.77059200	-0.10298500
F	1.42911700	1.54450100	-0.26150200
F	1.00820800	-0.18059300	-1.51891900
F	0.01811100	0.68201600	1.69672800
F	-0.02137200	-1.37005000	0.96150700
F	-1.28992700	1.40095200	-0.72961200
F	-1.54745000	-0.70981800	-1.09285200
O	-2.36018100	0.15486900	0.79000800
C	-3.59704400	0.44953600	0.31277300
F	-3.93042400	1.72884600	0.37281400
C	-4.43939100	-0.46460800	-0.11861500
F	-4.15136700	-1.73783500	-0.18310800
F	-5.65271200	-0.19261700	-0.51877800

TS22

E(DMSO)[M06-2X/6-311++G(2d,p), SMD (DMSO)] = -1815.633022 a.u.

G_{corr}(DMSO)[M06-2X/6-311++G(2d,p)] = 0.04642 a.u.

H_{corr}(DMSO)[M06-2X/6-311++G(2d,p)] = 0.11902 a.u.

G = E(DMSO) + G_{corr} = -1815.586602 a.u.

$H = E(DMSO) + H_{corr} = -1815.514002$ a.u.

C	-4.03659100	-0.42531600	-0.11705200
C	-2.79122200	0.33980100	0.38283300
C	-1.47975200	-0.12304100	-0.29666000
C	-0.22137600	0.29610300	0.50468300
C	1.06696800	0.28859900	-0.34518600
F	-4.04206900	-0.46575600	-1.44278600
F	-4.04577300	-1.66012300	0.35775700
F	-5.12568700	0.20126900	0.30087900
F	-2.69804100	0.15854300	1.70610700
F	-2.97426900	1.63823700	0.12776900
F	-1.49090300	-1.45785800	-0.40454700
F	-1.43081900	0.40725000	-1.52445200
F	-0.07196900	-0.55502300	1.52383400
F	-0.39679300	1.53297900	0.98971800
F	1.10264000	-0.83901900	-1.07249100
F	1.04208100	1.31378300	-1.20624400
O	2.12482300	0.37364900	0.50369800
C	3.33640800	0.52545200	-0.11352000
F	3.71957200	1.79892700	-0.25531400
C	4.17856500	-0.47239300	-0.30263000
F	5.32636300	-0.30848700	-0.91097000
F	3.81089700	-1.72566500	-0.21967800
O	5.26455600	-0.59648300	1.75651000
H	6.03990500	-1.14406400	1.91729300

INT30
E(DMSO)[M06-2X/6-311++G(2d,p), SMD (DMSO)] = -1815.715991 a.u.
G_{corr}(DMSO)[M06-2X/6-311++G(2d,p)] = 0.051117 a.u.
H_{corr}(DMSO)[M06-2X/6-311++G(2d,p)] = 0.121299 a.u.
$G = E(DMSO) + G_{corr} = -1815.664874$ a.u.
$H = E(DMSO) + H_{corr} = -1815.594692$ a.u.

C	-4.02018400	-0.36665900	-0.10709300
C	-2.72612500	0.20164600	0.51673900
C	-1.48238600	0.01048900	-0.38612400
C	-0.15583000	0.12476700	0.40507800
C	1.07867200	0.41538000	-0.47908100
F	-4.12242400	0.01836100	-1.37242900
F	-4.02324200	-1.68888500	-0.05272500

F	-5.06395900	0.09070300	0.56801400
F	-2.53152000	-0.41187600	1.69103500
F	-2.90983800	1.50802800	0.72968600
F	-1.54404600	-1.20297100	-0.95292900
F	-1.52258200	0.93660400	-1.35176000
F	0.03346100	-1.03111900	1.05429500
F	-0.27480000	1.11171000	1.30866000
F	0.99362500	-0.38371600	-1.57108400
F	0.98214600	1.68371000	-0.93226700
O	2.17268100	0.20528200	0.24178900
C	3.42406600	0.53309500	-0.45652800
F	3.85440400	1.68868200	0.25793600
C	4.33360000	-0.54853800	0.09657500
F	5.61274800	-0.29826300	-0.28892000
F	4.00565500	-1.73451600	-0.51240600
O	4.37213100	-0.74682700	1.44218100
H	3.52398700	-0.46679700	1.81489000

TS23

E(DMSO)[M06-2X/6-311++G(2d,p), SMD (DMSO)] = -1815.694019 a.u.

G_{corr}(DMSO)[M06-2X/6-311++G(2d,p)] = 0.049543 a.u.

H_{corr}(DMSO)[M06-2X/6-311++G(2d,p)] = 0.120059 a.u.

G = E(DMSO) + G_{corr} = -1815.644476 a.u.

H = E(DMSO) + H_{corr} = -1815.57396 a.u.

C	-4.04779700	-0.36684300	-0.15750000
C	-2.77170800	0.20803500	0.49579300
C	-1.50007800	-0.00443400	-0.36236900
C	-0.20089100	0.12190700	0.47151700
C	1.05981100	0.38251700	-0.38046800
F	-4.11162700	0.00072900	-1.43049800
F	-4.05476400	-1.68799800	-0.08421900
F	-5.10936400	0.10199700	0.48057700
F	-2.61679100	-0.38338500	1.68686100
F	-2.95530000	1.51897000	0.67726800
F	-1.54357800	-1.22744300	-0.90871400
F	-1.50289000	0.90441600	-1.34489700
F	-0.03686600	-1.01763400	1.15331200
F	-0.34057000	1.13333500	1.34255200
F	1.03330300	-0.45526500	-1.43639400
F	0.99641000	1.63104700	-0.87933800
O	2.13434500	0.20178700	0.40370900

C	3.35043200	0.51660700	-0.20997400
F	3.75718400	1.76612100	0.19435800
C	4.31688600	-0.46255700	-0.18032000
F	4.87659800	-0.91244300	1.47041500
F	5.53236800	-0.04947000	-0.57492000
O	3.99805600	-1.70038200	-0.56392400
H	4.38384500	-2.28939700	0.10438600

INT31
E(DMSO)[M06-2X/6-311++G(2d,p), SMD (DMSO)] = -1715.718778 a.u.
G_{corr}(DMSO)[M06-2X/6-311++G(2d,p)] = 0.050346 a.u.
H_{corr}(DMSO)[M06-2X/6-311++G(2d,p)] = 0.119337 a.u.
G = E(DMSO) + G_{corr} = -1715.668432 a.u.
H = E(DMSO) + H_{corr} = -1715.599441 a.u.

C	-3.76904300	0.40779900	0.17837300
C	-2.53593100	-0.42270200	-0.24184500
C	-1.19977400	0.18635200	0.24792000
C	0.01797000	-0.36809300	-0.53345600
C	1.35443600	-0.17463000	0.21357200
F	-3.68388400	0.72677700	1.46322600
F	-3.85049700	1.51511000	-0.54085100
F	-4.86234100	-0.31222300	-0.01756400
F	-2.52441600	-0.50476200	-1.57798900
F	-2.66512600	-1.64775800	0.27334500
F	-1.23808400	1.51509800	0.08854400
F	-1.05915900	-0.08802200	1.54985900
F	0.08958100	0.26478100	-1.70747000
F	-0.15077600	-1.67871900	-0.74823000
F	1.42425900	1.08178600	0.68037300
F	1.41843400	-0.99771800	1.26005900
O	2.36434900	-0.41826000	-0.67645400
C	3.61488600	-0.45453600	-0.12513400
F	3.99357500	-1.65328000	0.30897400
C	4.42175200	0.59232700	-0.10502700
F	5.64216900	0.46667800	0.37803800
O	4.19317200	1.83065900	-0.52140800
H	3.31044600	1.91197500	-0.91635600

INT32
E(DMSO)[M06-2X/6-311++G(2d,p), SMD (DMSO)] = -1791.697331 a.u.

G_{corr}(DMSO)[M06-2X/6-311++G(2d,p)] = 0.062912 a.u.
H_{corr}(DMSO)[M06-2X/6-311++G(2d,p)] = 0.134013 a.u.
G = E(DMSO) + G_{corr} = -1791.634419 a.u.
H = E(DMSO) + H_{corr} = -1791.563318 a.u.

C	-4.03339000	-0.34353900	-0.09695600
C	-2.73181900	0.21887000	0.51640100
C	-1.49103500	-0.00272800	-0.38368100
C	-0.16203100	0.11073900	0.40368400
C	1.07678300	0.36818300	-0.48430700
F	-4.13481800	0.02552400	-1.36717700
F	-4.05125400	-1.66487800	-0.02478600
F	-5.07051300	0.13428400	0.57445000
F	-2.54500600	-0.37704200	1.70091900
F	-2.89998600	1.53090100	0.70750800
F	-1.56822700	-1.22585100	-0.92806400
F	-1.52414800	0.90568100	-1.36646800
F	0.01036200	-1.03429500	1.07653100
F	-0.27049400	1.11735300	1.28737700
F	0.97987900	-0.45933500	-1.55894200
F	0.98465700	1.62537200	-0.97492600
O	2.16496300	0.16671000	0.24220300
C	3.40258300	0.47397000	-0.46257200
F	3.82517200	1.68489600	0.18517000
C	4.37883900	-0.55519800	0.06969900
F	4.26734800	-0.72490500	1.46163000
O	5.68127200	-0.18819600	-0.17124100
H	5.75307800	0.75879800	0.01469300
O	4.14325000	-1.79813900	-0.45388600
H	3.66472000	-1.66292000	-1.28390500

TS24
E(DMSO)[M06-2X/6-311++G(2d,p), SMD (DMSO)] = -1791.667119 a.u.
G_{corr}(DMSO)[M06-2X/6-311++G(2d,p)] = 0.061139 a.u.
H_{corr}(DMSO)[M06-2X/6-311++G(2d,p)] = 0.132465 a.u.
G = E(DMSO) + G_{corr} = -1791.60598 a.u.
H = E(DMSO) + H_{corr} = -1791.534654 a.u.

C	-4.05217100	-0.42067700	-0.07234500
C	-2.79349800	0.36393800	0.35898400
C	-1.49819600	-0.14058000	-0.32304800

C	-0.22179200	0.30575900	0.43303200
C	1.06254300	0.24453700	-0.42222700
F	-4.08106100	-0.54365700	-1.39270100
F	-4.06260100	-1.62396900	0.47829300
F	-5.13048400	0.23883900	0.32329600
F	-2.67601800	0.25394700	1.68848500
F	-2.97874900	1.64783700	0.03850800
F	-1.52522800	-1.47988200	-0.36725400
F	-1.47621800	0.32907700	-1.57605300
F	-0.07236200	-0.49578400	1.49513200
F	-0.38813300	1.56663200	0.86140400
F	1.06933900	-0.94085800	-1.07288800
F	1.00227200	1.20110400	-1.36511800
O	2.11329200	0.39207800	0.39591300
C	3.36528500	0.45899700	-0.27938500
F	3.72945300	1.79779900	-0.33733100
C	4.33953700	-0.34509800	0.35838800
F	5.17132900	-1.34134000	-0.98460300
O	3.95471800	-1.38997300	1.09633600
H	3.06049800	-1.65615100	0.83729400
O	5.47352200	0.22573700	0.75760300
H	6.16315900	-0.45554700	0.74095400

INT33

E(DMSO)[M06-2X/6-311++G(2d,p), SMD (DMSO)] = -1691.712462 a.u.

G_{corr}(DMSO)[M06-2X/6-311++G(2d,p)] = 0.062661 a.u.

H_{corr}(DMSO)[M06-2X/6-311++G(2d,p)] = 0.1321 a.u.

G = E(DMSO) + G_{corr} = -1691.649801 a.u.

H = E(DMSO) + H_{corr} = -1691.580362 a.u.

C	-3.77387500	0.41451300	0.18292700
C	-2.54372200	-0.41710300	-0.24333300
C	-1.20493400	0.18445400	0.24871900
C	0.01082200	-0.36656300	-0.53788100
C	1.34928000	-0.18335200	0.20828300
F	-3.68783200	0.72474000	1.46992600
F	-3.85263700	1.52690300	-0.52884900
F	-4.86982500	-0.30068800	-0.01730700
F	-2.53559600	-0.49196800	-1.57999600
F	-2.67723400	-1.64481200	0.26518200
F	-1.24195800	1.51490100	0.10011500
F	-1.06626900	-0.09985100	1.54903400

F	0.07791600	0.27431700	-1.70829400
F	-0.16602400	-1.67556400	-0.76384500
F	1.41072400	1.06149600	0.70090600
F	1.40310200	-1.02479400	1.24805100
O	2.35267000	-0.42524200	-0.67999000
C	3.60511500	-0.43794800	-0.13508900
F	4.00405100	-1.64938000	0.28861600
C	4.43767100	0.59425400	-0.11525200
O	5.68293400	0.54504000	0.38310000
H	5.83475900	-0.29820000	0.83765800
O	4.10156200	1.77480400	-0.64176700
H	4.60001800	2.47416600	-0.19049300

INT34

E(DMSO)[M06-2X/6-311++G(2d,p), SMD (DMSO)] = -1691.254953 a.u.

G_{corr}(DMSO)[M06-2X/6-311++G(2d,p)] = 0.05056 a.u.

H_{corr}(DMSO)[M06-2X/6-311++G(2d,p)] = 0.118592 a.u.

G = E(DMSO) + G_{corr} = -1691.204393 a.u.

H = E(DMSO) + H_{corr} = -1691.136361 a.u.

C	3.77541300	0.32838700	-0.12975000
C	2.48548000	-0.28098300	0.46284000
C	1.21633200	0.06619600	-0.35374800
C	-0.08378900	-0.13076000	0.46494400
C	-1.35515900	-0.27013500	-0.40146000
F	3.82136300	0.11560800	-1.43842900
F	3.82582600	1.63025000	0.10168400
F	4.82534100	-0.24669600	0.43745400
F	2.35594800	0.17114300	1.71667200
F	2.63270900	-1.60914000	0.48869000
F	1.29123000	1.34629100	-0.74519600
F	1.19726300	-0.71338200	-1.44199200
F	-0.21746500	0.92478500	1.27751500
F	0.04314100	-1.23857000	1.21477200
F	-1.29577600	0.67538100	-1.37053300
F	-1.30081700	-1.46062800	-1.03869200
O	-2.41645700	-0.15135700	0.39023100
C	-3.66620200	-0.37961800	-0.27164800
F	-4.06371100	-1.66518900	0.11409800
C	-4.65345000	0.58853600	0.10603300
O	-5.85655900	0.38684000	0.19869000
O	-4.15486900	1.84893800	0.22986300

H	-4.92413400	2.42621600	0.34206500

TS25
E(DMSO)[M06-2X/6-311++G(2d,p), SMD (DMSO)] = -1767.684371 a.u.
G_{corr}(DMSO)[M06-2X/6-311++G(2d,p)] = 0.069563 a.u.
H_{corr}(DMSO)[M06-2X/6-311++G(2d,p)] = 0.140758 a.u.
G = E(DMSO) + G_{corr} = -1767.614808 a.u.
H = E(DMSO) + H_{corr} = -1767.543613 a.u.

C	-3.90941700	0.17972700	-0.42937500
C	-2.68932700	-0.32777100	0.37072400
C	-1.34795400	0.26630900	-0.12665400
C	-0.12672900	-0.57042000	0.32950600
C	1.21590200	0.19244900	0.26652200
F	-3.84754100	1.49768000	-0.56674600
F	-3.94747000	-0.38187000	-1.62708400
F	-5.01761700	-0.13394300	0.22466400
F	-2.65885200	-1.66282000	0.27124100
F	-2.86541200	0.01257200	1.65090000
F	-1.36430100	0.30844100	-1.46652600
F	-1.24889500	1.51708000	0.33949800
F	-0.05163200	-1.64835800	-0.46046100
F	-0.32571300	-0.97313000	1.59463600
F	1.26559000	0.83757400	-0.92507300
F	1.20988500	1.15270400	1.21042600
O	2.20280200	-0.69709200	0.41967000
C	3.56805700	-0.23810300	0.55490800
F	3.67274700	0.33733200	1.81033700
C	3.91457200	0.79798600	-0.49280000
O	4.10686500	0.25673400	-1.69365200
H	4.23657100	-0.74060700	-1.57471700
O	4.63328100	-2.10661800	-0.81239800
H	4.25680800	-1.39766700	0.05772600
H	4.00531000	-2.83243800	-0.88764300
O	4.10250100	1.97201300	-0.28045300

5
E(DMSO)[M06-2X/6-311++G(2d,p), SMD (DMSO)] = -1691.303754 a.u.
G_{corr}(DMSO)[M06-2X/6-311++G(2d,p)] = 0.052111 a.u.
H_{corr}(DMSO)[M06-2X/6-311++G(2d,p)] = 0.119877 a.u.
G = E(DMSO) + G_{corr} = -1691.251643 a.u.

H = E(DMSO) + H_{corr} = -1691.183877 a.u.

C	3.79738100	-0.15087900	-0.08148100
C	2.44682600	0.59677500	-0.14187700
C	1.23756200	-0.30397900	0.21000100
C	-0.10203200	0.28641500	-0.29647900
C	-1.34436800	-0.30439000	0.40558100
F	3.87583900	-0.85944500	1.03724900
F	3.92794500	-0.96050000	-1.11984900
F	4.78228400	0.73427000	-0.10222400
F	2.30069200	1.08363300	-1.38063100
F	2.49696600	1.61089100	0.72654100
F	1.41547700	-1.50785700	-0.35075000
F	1.19809100	-0.45108800	1.53952600
F	-0.19056400	0.04419800	-1.60868200
F	-0.09606100	1.61298900	-0.09771300
F	-1.20350800	-1.64687500	0.46888800
F	-1.36971600	0.13146100	1.68104800
O	-2.42991200	0.07376500	-0.27711500
C	-3.66695000	-0.48020200	0.16197400
H	-3.60330300	-0.76457600	1.21183400
F	-3.86427500	-1.61984700	-0.57082700
C	-4.76725900	0.58770600	-0.07243200
O	-5.58519100	0.35528900	-0.97191200
O	-4.66766900	1.54962400	0.70818500

TS26
E(DMSO)[M06-2X/6-311++G(2d,p), SMD (DMSO)] = -1767.18454 a.u.
G_{corr}(DMSO)[M06-2X/6-311++G(2d,p)] = 0.059671 a.u.
H_{corr}(DMSO)[M06-2X/6-311++G(2d,p)] = 0.131506 a.u.
G = E(DMSO) + G_{corr} = -1767.124869 a.u.
H = E(DMSO) + H_{corr} = -1767.053034 a.u.

C	-4.07189600	-0.26333400	0.00627800
C	-2.76368300	0.55417600	-0.08191700
C	-1.49128700	-0.32925200	-0.08055500
C	-0.21492100	0.46166800	0.29673200
C	1.12072300	-0.20142100	-0.12552400
F	-4.03652400	-1.28043900	-0.84514200
F	-4.25031000	-0.72907000	1.23224900
F	-5.09445600	0.52066700	-0.30404500

F	-2.73841800	1.39590100	0.96016200
F	-2.80000500	1.26317500	-1.21520600
F	-1.66638100	-1.32254900	0.80588600
F	-1.36648100	-0.86574400	-1.30121500
F	-0.22456000	0.62032100	1.62946200
F	-0.28804200	1.68044600	-0.27281200
F	0.97361500	-1.55863600	0.13870100
F	1.15540600	-0.15176400	-1.50787800
O	2.12741900	0.34146100	0.44688300
C	3.66416200	-0.44252300	0.09152700
H	3.34157100	-1.02099600	-0.75331000
F	3.75094100	-1.10556400	1.23919900
C	4.46260300	0.85338500	-0.06608300
O	4.92434300	1.34055700	0.97872100
O	4.50246000	1.28912300	-1.23421200
O	5.44498900	-1.48349900	-0.59467900
H	5.69747700	-0.87703200	-1.29740100

INT35

E(DMSO)[M06-2X/6-311++G(2d,p), SMD (DMSO)] = -1364.208256 a.u.

G_{corr}(DMSO)[M06-2X/6-311++G(2d,p)] = 0.022959 a.u.

H_{corr}(DMSO)[M06-2X/6-311++G(2d,p)] = 0.079972 a.u.

G = E(DMSO) + G_{corr} = -1364.185297 a.u.

H = E(DMSO) + H_{corr} = -1364.128284 a.u.

C	-2.53042600	-0.26463400	0.07187500
C	-1.22385100	0.50964300	-0.21082600
C	0.05411100	-0.33545900	0.02199600
C	1.32433900	0.52800800	0.20000700
C	2.70507500	-0.16409500	-0.00665800
F	-2.49172600	-1.46278700	-0.49699200
F	-2.71762900	-0.40929800	1.37474300
F	-3.55464100	0.41303900	-0.42916900
F	-1.21847700	1.58923000	0.58386600
F	-1.25837900	0.90946800	-1.48779200
F	-0.13799700	-1.07603400	1.12834300
F	0.17740600	-1.16283800	-1.02446100
F	1.27509600	1.02699000	1.45247100
F	1.23059000	1.57411700	-0.65551700
F	2.49021600	-1.48193100	0.55556100
F	2.70524700	-0.48916700	-1.40679500
O	3.69089400	0.43526300	0.39916200

INT36
E(DMSO)[M06-2X/6-311++G(2d,p), SMD (DMSO)] = -1264.18692 a.u.
G_{corr}(DMSO)[M06-2X/6-311++G(2d,p)] = 0.021739 a.u.
H_{corr}(DMSO)[M06-2X/6-311++G(2d,p)] = 0.077517 a.u.
G = E(DMSO) + G_{corr} = -1264.165181 a.u.
H = E(DMSO) + H_{corr} = -1264.109403 a.u.

C	-2.34178700	-0.30707500	-0.02465800
C	-1.05494400	0.54737400	-0.02744700
C	0.23212200	-0.30353700	-0.15679300
C	1.49775600	0.44655400	0.31826800
C	2.77848200	-0.22473800	-0.20947400
F	-2.29281400	-1.19616900	-1.00848100
F	-2.47825800	-0.94021800	1.12878100
F	-3.38747300	0.48298800	-0.20700700
F	-1.01546600	1.25035800	1.11054700
F	-1.11831300	1.38997400	-1.06110500
F	0.10292400	-1.42542600	0.56081500
F	0.40157900	-0.62833800	-1.44582100
F	1.52251100	0.46538600	1.65576000
F	1.45306500	1.69674800	-0.14756500
F	2.96632800	-1.38730600	0.39580100
O	3.49293700	0.20956900	-1.02936200

S8
E(DMSO)[M06-2X/6-311++G(2d,p), SMD (DMSO)] = -403.090969 a.u.
G_{corr}(DMSO)[M06-2X/6-311++G(2d,p)] = 0.018354 a.u.
H_{corr}(DMSO)[M06-2X/6-311++G(2d,p)] = 0.053756 a.u.
G = E(DMSO) + G_{corr} = -403.072615 a.u.
H = E(DMSO) + H_{corr} = -403.037213 a.u.

C	-0.64585300	-0.20205800	0.39857500
F	-1.12899900	-1.11853300	-0.56843200
C	0.84299700	0.05474500	0.04981700
O	1.63777500	-0.86051000	0.30158900
O	1.04997300	1.17568600	-0.47033200
H	-0.79035100	-0.70028300	1.35655000
O	-1.37053300	0.94731000	0.32246600
H	-0.76924700	1.55106700	-0.16079500

INT37
E(DMSO)[M06-2X/6-311++G(2d,p), SMD (DMSO)] = -1791.697331 a.u.
G_{corr}(DMSO)[M06-2X/6-311++G(2d,p)] = 0.062912 a.u.
H_{corr}(DMSO)[M06-2X/6-311++G(2d,p)] = 0.134013 a.u.
G = E(DMSO) + G_{corr} = -1791.634419 a.u.
H = E(DMSO) + H_{corr} = -1791.563318 a.u.

C	-2.54150700	-0.26658600	0.05831300
C	-1.22853100	0.51108700	-0.18224300
C	0.04535600	-0.34922700	0.01484400
C	1.32226100	0.49940100	0.22466300
C	2.70656200	-0.18512400	-0.00816800
F	-2.51535700	-1.43283500	-0.57410900
F	-2.73333100	-0.47923100	1.35145000
F	-3.56006900	0.44639500	-0.40594300
F	-1.22434600	1.55176200	0.66365200
F	-1.25958400	0.97179400	-1.43935500
F	-0.15698900	-1.12966700	1.09272800
F	0.15394100	-1.13992000	-1.06140900
F	1.27093300	0.93673100	1.50511100
F	1.21587600	1.59344400	-0.56831600
F	2.65284300	-0.38315800	-1.49049700
O	3.69283100	0.48826700	0.35047000
O	2.57604200	-1.48878500	0.49742000
H	3.42891200	-1.67099000	0.91262400

INT28
E(DMSO)[M06-2X/6-311++G(2d,p), SMD (DMSO)] = -1502.648099 a.u.
G_{corr}(DMSO)[M06-2X/6-311++G(2d,p)] = 0.039227 a.u.
H_{corr}(DMSO)[M06-2X/6-311++G(2d,p)] = 0.10129 a.u.
G = E(DMSO) + G_{corr} = -1502.608872 a.u.
H = E(DMSO) + H_{corr} = -1502.546809 a.u.

C	3.92154100	-0.07225400	-0.44997100
C	2.69189400	-0.16657100	0.47967800
C	1.34517400	-0.01817200	-0.27069400
C	0.17883500	0.35861300	0.67779400
C	-1.22400500	0.05699600	0.09878000
F	3.75032200	-0.84431400	-1.51508400
F	4.11439400	1.17642600	-0.84325300
F	4.99418200	-0.48155500	0.21117800

F	2.80468400	0.79566000	1.40448400
F	2.72222300	-1.35934900	1.08181700
F	1.47165300	0.94139200	-1.19917100
F	1.08541800	-1.17686100	-0.88850600
F	0.27392100	1.66917900	0.93402600
F	0.32153300	-0.31772000	1.82990100
F	-1.23188400	0.47755700	-1.18551400
F	-1.36539800	-1.29053100	0.05899400
O	-2.12623700	0.64603700	0.88785700
C	-3.51351400	0.87554900	0.52566800
F	-3.47210400	1.76617800	-0.57925400
C	-4.11926300	-0.36723000	-0.06245900
F	-4.04466000	-1.39835200	0.79326400
F	-5.42719500	-0.14906200	-0.31089400
F	-3.62754400	-0.82752600	-1.24705700

TS27

E(DMSO)[M06-2X/6-311++G(2d,p), SMD (DMSO)] = -1767.149035 a.u.

G_{corr}(DMSO)[M06-2X/6-311++G(2d,p)] = 0.062824 a.u.

H_{corr}(DMSO)[M06-2X/6-311++G(2d,p)] = 0.132234 a.u.

G = E(DMSO) + G_{corr} = -1767.086211 a.u.

H = E(DMSO) + H_{corr} = -1767.016801 a.u.

C	-3.11871500	-1.11399600	0.10349100
C	-2.33131800	0.19477700	-0.13981300
C	-0.78212500	-0.01958500	-0.07919900
C	-0.03320200	1.31969400	0.20752200
C	1.52078700	1.45717800	0.05892600
F	-2.60450700	-2.10867300	-0.60875100
F	-3.10701200	-1.44585800	1.38562300
F	-4.38090200	-0.93397600	-0.26879100
F	-2.75321400	1.07967100	0.77390800
F	-2.68012300	0.63911900	-1.35461000
F	-0.57137900	-0.93016800	0.88158000
F	-0.45858500	-0.52251400	-1.27750100
F	-0.34590000	1.63700400	1.47559400
F	-0.66378000	2.16192300	-0.64744600
F	2.05003000	1.64007500	-1.17432600
F	2.30322600	1.52898500	1.15906800
O	1.72284100	-0.22639700	-0.00044300
C	2.94470600	-0.67121300	-0.33653100
H	3.74176400	0.05414100	-0.14420400

F	3.01144300	-0.88003400	-1.75583600
C	3.25497400	-2.01203600	0.37258900
O	3.95407100	-1.89189300	1.40314900
O	2.76698000	-3.04840200	-0.11600400
O	1.34368500	3.24565100	0.25248300
H	1.03331200	3.59527600	-0.58778600

References

1. E. Hammel, T. F. Webster, R. Gurney, W. Heiger-Bernays, Implications of PFAS definitions using fluorinated pharmaceuticals. *iScience*. **25**, 104020 (2022).

2. A. Kataria, H. Trachtman, L. Malaga-Dieguez, L. Trasande, Association between perfluoroalkyl acids and kidney function in a cross-sectional study of adolescents. *Environ. Heal.* **14**, 89 (2015).

3. V. Gallo, G. Leonardi, B. Genser, M.-J. Lopez-Espinosa, S. J. Frisbee, L. Karlsson, A. M. Ducatman, T. Fletcher, Serum Perfluorooctanoate (PFOA) and Perfluorooctane Sulfonate (PFOS) Concentrations and Liver Function Biomarkers in a Population with Elevated PFOA Exposure. *Environ. Health Perspect.* **120**, 655–660 (2012).

4. A. P. Starling, J. L. Adgate, R. F. Hamman, K. Kechris, A. M. Calafat, X. Ye, D. Dabelea, Perfluoroalkyl Substances during Pregnancy and Offspring Weight and Adiposity at Birth: Examining Mediation by Maternal Fasting Glucose in the Healthy Start Study. *Environ. Health Perspect.* **125**, 067016 (2017).

5. P. I. Johnson, P. Sutton, D. S. Atchley, E. Koustas, J. Lam, S. Sen, K. A. Robinson, D. A. Axelrad, T. J. Woodruff, The Navigation Guide—Evidence-Based Medicine Meets Environmental Health: Systematic Review of Human Evidence for PFOA Effects on Fetal Growth. *Environ. Health Perspect.* **122**, 1028–1039 (2014).

6. P. Grandjean, C. A. Gade Timmermann, M. Kruse, F. Nielsen, P. J. Vinholt, L. Boding, C. Heilmann, K. Mølbak, Severity of COVID-19 at elevated exposure to perfluorinated alkylates. *PLoS One*. **15**, 1–12 (2020).

7. V. Barry, A. Winquist, K. Steenland, Perfluorooctanoic Acid (PFOA) Exposures and Incident Cancers among Adults Living Near a Chemical Plant. *Environ. Health Perspect.* **121**, 1313–1318 (2013).

8. S. E. Fenton, A. Ducatman, A. Boobis, J. C. DeWitt, C. Lau, C. Ng, J. S. Smith, S. M. Roberts, *Environ. Toxicol. Chem.*, in press, doi:10.1002/etc.4890.

9. M. M. Administration, C-8 Medical Monitoring Program, (available at http://www.c-8medicalmonitoringprogram.com/).

10. C. Hogue, U.S. class-action case targets 9 PFAS makers. *Chem. Eng. News*. **96** (2018), pp. 15–15.

11. M. S. Reisch, DuPont, Chemours settle PFOA suits. *Chem. Eng. News*. **95** (2017), p. 5.

12. M. S. Reisch, Two firms sued over PFOA contamination. *Chem. Eng. News*. **94** (2016), p. 16.

13. A. M. Calafat, L.-Y. Wong, Z. Kuklenyik, J. A. Reidy, L. L. Needham, Polyfluoroalkyl Chemicals in the U.S. Population: Data from the National Health and Nutrition

Examination Survey (NHANES) 2003–2004 and Comparisons with NHANES 1999–2000. *Environ. Health Perspect.* **115**, 1596–1602 (2007).

14. J. M. Graber, T. M. Black, N. N. Shah, A. J. Caban-Martinez, S. E. Lu, T. Brancard, C. H. Yu, M. E. Turyk, K. Black, M. B. Steinberg, Z. Fan, J. L. Burgess, Prevalence and predictors of per-and polyfluoroalkyl substances (PFAS) serum levels among members of a suburban us volunteer fire department. *Int. J. Environ. Res. Public Health*. **18**, 1–13 (2021).

15. H. P. Susmann, L. A. Schaider, K. M. Rodgers, R. A. Rudel, Dietary habits related to food packaging and population exposure to PFASs. *Environ. Health Perspect.* **127** (2019), doi:10.1289/EHP4092.

16. D. Bond, J. Enck, "First in the Nation Testing Reveals Toxic Contamination in Soil and Water Near Norlite Incinerator" (Bennington, Vermont, 2020), (available at https://www.bennington.edu/sites/default/files/sources/docs/Norlite News Release %5Bdb final updated%5D.pdf).

17. J. E. Galloway, A. V. P. Moreno, A. B. Lindstrom, M. J. Strynar, S. Newton, A. A. May, A. A. May, L. K. Weavers, L. K. Weavers, Evidence of Air Dispersion: HFPO-DA and PFOA in Ohio and West Virginia Surface Water and Soil near a Fluoropolymer Production Facility. *Environ. Sci. Technol.* **54**, 7175–7184 (2020).

18. L. B. Cahoon, in *ACS Symposium Series* (2020; https://pubs.acs.org/sharingguidelines), pp. 91–103.

19. D. Q. Andrews, O. V. Naidenko, *Environ. Sci. Technol. Lett.*, in press, doi:10.1021/acs.estlett.0c00713.

20. USEPA, Announcement of Final Regulatory Determinations for Contaminants on the Fourth Drinking Water Contaminant Candidate List. *Fed. Regist.* **86**, 12272–12291 (2021).

21. G. B. Post, *Environ. Toxicol. Chem.*, in press, doi:10.1002/etc.4863.

22. B. Trang, So-called "forever chemicals" are polluting waterways. But regulating them is proving to be a long journey. *Milwaukee J. Sentin.* (2021), (available at https://www.jsonline.com/story/news/2021/07/30/forever-chemicals-causing-alarm-why-regulating-them-so-hard/8046915002/).

23. R. Fox, "Prepublication Federal Register Notice on Lifetime Drinking Water Health Advisories for Four Perfluoroalkyl Substances (PFAS)" (Washington, D.C., 2022), (available at https://www.epa.gov/system/files/documents/2022-06/prepublication-four-pfas-june-2022.pdf).

24. M. G. Evich, M. J. B. Davis, J. P. McCord, B. Acrey, J. A. Awkerman, D. R. U. Knappe, A. B. Lindstrom, T. F. Speth, C. Tebes-Stevens, M. J. Strynar, Z. Wang, E. J. Weber, W.

M. Henderson, J. W. Washington, Per- and polyfluoroalkyl substances in the environment. *Science (80-.).* **375** (2022), doi:10.1126/science.abg9065.

25. D. Dingell, *PFAS Action Act of 2019* (House of Representatives, 2019; https://debbiedingell.house.gov/sites/debbiedingell.house.gov/files/documents/190114_PFASActionAct.pdf).

26. C. Hogue, U.S. senators seek regulation of PFASs as a class in drinking water. *C&EN Glob. Enterp.* **96** (2018), pp. 16–16.

27. M. Brown, T. Brown, State Takes Action to Strengthen Environmental Criteria in Response to PFAS Contamination. *Michigan Deparment Environ. Qual.* (2019), (available at https://www.michigan.gov/deq/0,4561,7-135-3308-457220--,00.html).

28. W. J. Backe, T. C. Day, J. A. Field, Zwitterionic, Cationic, and Anionic Fluorinated Chemicals in Aqueous Film Forming Foam Formulations and Groundwater from U.S. Military Bases by Nonaqueous Large-Volume Injection HPLC-MS/MS. *Environ. Sci. Technol.* **47**, 5226–5234 (2013).

29. K. A. Barzen-Hanson, J. A. Field, Discovery and Implications of C_2 and C_3 Perfluoroalkyl Sulfonates in Aqueous Film-Forming Foams and Groundwater. *Environ. Sci. Technol. Lett.* **2**, 95–99 (2015).

30. D. O'Hagan, Understanding organofluorine chemistry. An introduction to the C–F bond. *Chem. Soc. Rev.* **37**, 308–319 (2008).

31. S. M. Mitchell, M. Ahmad, A. L. Teel, R. J. Watts, Degradation of Perfluorooctanoic Acid by Reactive Species Generated through Catalyzed H_2O_2 Propagation Reactions. *Environ. Sci. Technol. Lett.* **1**, 117–121 (2014).

32. S. Wang, Q. Yang, F. Chen, J. Sun, K. Luo, F. Yao, X. Wang, D. Wang, X. Li, G. Zeng, Photocatalytic degradation of perfluorooctanoic acid and perfluorooctane sulfonate in water: A critical review. *Chem. Eng. J.* **328**, 927–942 (2017).

33. N. J. Herkert, J. Merrill, C. Peters, D. Bollinger, S. Zhang, K. Hoffman, P. L. Ferguson, D. R. U. Knappe, H. M. Stapleton, Assessing the effectiveness of point-of-use residential drinking water filters for perfluoroalkyl substances (pfass). *Environ. Sci. Technol. Lett.* **7**, 178–184 (2020).

34. D. Zhang, Q. Luo, B. Gao, S.-Y. D. Chiang, D. Woodward, Q. Huang, Sorption of perfluorooctanoic acid, perfluorooctane sulfonate and perfluoroheptanoic acid on granular activated carbon. *Chemosphere*. **144**, 2336–2342 (2016).

35. M. F. Rahman, S. Peldszus, W. B. Anderson, Behaviour and fate of perfluoroalkyl and polyfluoroalkyl substances (PFASs) in drinking water treatment: A review. *Water Res.* **50**, 318–340 (2013).

36. Kerri Jansen, 'Forever chemicals' no more? *C&EN Glob. Enterp.* **97**, 28–32 (2019).

37. R. W. Coughlin, F. S. Ezra, Role of Surface Acidity in the Adsorption of Organic Pollutants the Surface of Carbon. *Environ. Sci. Technol.* **2**, 291–297 (1968).

38. Z. Jeirani, C. H. Niu, J. Soltan, Adsorption of emerging pollutants on activated carbon. *Rev. Chem. Eng.* **33**, 491–522 (2017).

39. V. Ochoa-Herrera, R. Sierra-Alvarez, Removal of perfluorinated surfactants by sorption onto granular activated carbon, zeolite and sludge. *Chemosphere*. **72**, 1588–1593 (2008).

40. Q. Yu, R. Zhang, S. Deng, J. Huang, G. Yu, Sorption of perfluorooctane sulfonate and perfluorooctanoate on activated carbons and resin: Kinetic and isotherm study. *Water Res.* **43**, 1150–1158 (2009).

41. New Jersey Department of Environmental Protection, Contaminants of Emerging Concern. *State New Jersey Website* (2018), (available at https://www.nj.gov/dep/srp/emerging-contaminants/).

42. US EPA Office of Water, "FACT SHEET: PFOA & PFOS Drinking Water Health Advisories" (2016), (available at https://www.epa.gov/sites/production/files/2016-06/documents/drinkingwaterhealthadvisories_pfoa_pfos_updated_5.31.16.pdf).

43. D. N. Kothawala, S. J. Köhler, A. Östlund, K. Wiberg, L. Ahrens, Influence of dissolved organic matter concentration and composition on the removal efficiency of perfluoroalkyl substances (PFASs) during drinking water treatment. *Water Res.* **121**, 320–328 (2017).

44. J. Yu, L. Lv, P. Lan, S. Zhang, B. Pan, W. Zhang, Effect of effluent organic matter on the adsorption of perfluorinated compounds onto activated carbon. *J. Hazard. Mater.* **225**–**226**, 99–106 (2012).

45. Calgon Carbon Corporation, FILTRASORB | Calgon Carbon Corporation (2022), (available at https://www.calgoncarbon.com/products/filtrasorb/).

46. S. B. Pillai, in *Handbook of Water and Used Water Purification* (Springer International Publishing, 2020; https://link.springer.com/referenceworkentry/10.1007/978-3-319-66382-1_4-1), pp. 1–22.

47. F. Dixit, R. Dutta, B. Barbeau, P. Berube, M. Mohseni, PFAS removal by ion exchange resins: A review. *Chemosphere*. **272**, 129777 (2021).

48. S. Liang, R. Mora, Q. Huang, R. Casson, Y. Wang, S. Woodard, H. Anderson, Field demonstration of coupling ion-exchange resin with electrochemical oxidation for enhanced treatment of per- and polyfluoroalkyl substances (PFAS) in groundwater. *Chem. Eng. J. Adv.* **9**, 100216 (2022).

49. P. Mccleaf, S. Englund, A. Ostlund, K. Lindegren, K. Wiberg, L. Ahrens, Removal efficiency of multiple poly- and per fluoroalkyl substances (PFASs) in drinking water using granular activated carbon (GAC) and anion exchange (AE) column tests. **120**, 77–87 (2017).

50. M. Ateia, A. Alsbaiee, T. Karanfil, W. Dichtel, Efficient PFAS Removal by Amine-Functionalized Sorbents: Critical Review of the Current Literature. *Environ. Sci. Technol. Lett.* **6**, 688–695 (2019).

51. E. Kumarasamy, I. M. Manning, L. B. Collins, O. Coronell, F. A. Leibfarth, Ionic Fluorogels for Remediation of Per- and Polyfluorinated Alkyl Substances from Water. *ACS Cent. Sci.* **6**, 487–492 (2020).

52. X. Liu, C. Zhu, J. Yin, J. Li, Z. Zhang, J. Li, F. Shui, Z. You, Z. Shi, B. Li, X.-H. Bu, A. Nafady, S. Ma, Installation of synergistic binding sites onto porous organic polymers for efficient removal of perfluorooctanoic acid. *Nat. Commun.* **13**, 1–10 (2022).

53. A. H. Karoyo, P. S. Sidhu, L. D. Wilson, P. Hazendonk, A. Borisov, Counterion Anchoring Effect on the Structure of the Solid-State Inclusion Complexes of β-Cyclodextrin and Sodium Perfluorooctanoate. *J. Phys. Chem. C*. **119**, 22225–22243 (2015).

54. R. Mukhopadhyay, B. Sarkar, K. N. Palansooriya, J. Y. Dar, N. S. Bolan, S. J. Parikh, C. Sonne, Y. S. Ok, Natural and engineered clays and clay minerals for the removal of poly- and perfluoroalkyl substances from water: State-of-the-art and future perspectives. *Adv. Colloid Interface Sci.* **297**, 102537 (2021).

55. K. A. Thompson, K. K. Shimabuku, J. P. Kearns, D. R. U. Knappe, R. S. Summers, S. M. Cook, Environmental Comparison of Biochar and Activated Carbon for Tertiary Wastewater Treatment. *Environ. Sci. Technol.* **50**, 11253–11262 (2016).

56. D. Li, K. Londhe, K. Chi, C. S. Lee, A. K. Venkatesan, B. S. Hsiao, Functionalized bio-adsorbents for removal of perfluoroalkyl substances: A perspective. *AWWA Water Sci.* **3** (2021), doi:10.1002/aws2.1258.

57. I. M. Militao, F. A. Roddick, R. Bergamasco, L. Fan, Removing PFAS from aquatic systems using natural and renewable material-based adsorbents: A review. *J. Environ. Chem. Eng.* **9** (2021), doi:10.1016/j.jece.2021.105271.

58. G. Crini, Review: A History of Cyclodextrins. *Chem. Rev.* **114**, 10940–10975 (2014).

59. K. Horikoshi, N. Nakamura, N. Matsuzawa, M. Yamamoto, in *Proceedings of the First International Symposium on Cyclodextrins* (Springer Netherlands, Dordrecht, 1982; http://link.springer.com/10.1007/978-94-009-7855-3_3), pp. 25–39.

60. T.-J. Kim, Y.-D. Lee, H.-S. Kim, Enzymatic production of cyclodextrins from milled corn starch in an ultrafiltration membrane bioreactor. *Biotechnol. Bioeng.* **41**, 88–94 (1993).

61. M. Matzuzawa, M. Kawano, N. Nakamura, K. Horikoshi, An Improved Method for the Preparation of Schardinger β-Dextrin on a Industrial Scale by Cyclodextrin Glycosyl Transferase of an AlkalophilicBacillus Sp. (ATCC 21783). *Starch - Stärke*. **27**, 410–413 (1975).

62. M. J. Weiss-Errico, K. E. O'Shea, Detailed NMR investigation of cyclodextrin-perfluorinated surfactant interactions in aqueous media. *J. Hazard. Mater.* **329**, 57–65 (2017).

63. N. Morin-Crini, G. Crini, Environmental applications of water-insoluble β-cyclodextrin–epichlorohydrin polymers. *Prog. Polym. Sci.* **38**, 344–368 (2013).

64. T. F. Cova, D. Murtinho, R. Aguado, A. A. C. C. Pais, A. J. M. Valente, Cyclodextrin Polymers and Cyclodextrin-Containing Polysaccharides for Water Remediation. *Polysaccharides*. **2**, 16–38 (2021).

65. G. Crini, M. Morcellet, Synthesis and applications of adsorbents containing cyclodextrins. *J. Sep. Sci.* **25**, 789–813 (2002).

66. A. H. Karoyo, L. D. Wilson, Tunable macromolecular-based materials for the adsorption of perfluorooctanoic and octanoic acid anions. *J. Colloid Interface Sci.* **402**, 196–203 (2013).

67. A. Alsbaiee, B. J. Smith, L. Xiao, Y. Ling, D. E. Helbling, W. R. Dichtel, Rapid removal of organic micropollutants from water by a porous β-cyclodextrin polymer. *Nature*. **529**, 190–194 (2016).

68. A. H. Karoyo, L. D. Wilson, Investigation of the Adsorption Processes of Fluorocarbon and Hydrocarbon Anions at the Solid–Solution Interface of Macromolecular Imprinted Polymer Materials. *J. Phys. Chem. C*. **120**, 6553–6568 (2016).

69. M. H. Mohamed, L. D. Wilson, J. V. Headley, Design and characterization of novel β-cyclodextrin based copolymer materials. *Carbohydr. Res.* **346**, 219–229 (2011).

70. D. Zhao, L. Zhao, C. Zhu, Z. Tian, X. Shen, Synthesis and properties of water-insoluble β-cyclodextrin polymer crosslinked by citric acid with PEG-400 as modifier. *Carbohydr. Polym.* **78**, 125–130 (2009).

71. F. Zhao, E. Repo, D. Yin, Y. Meng, S. Jafari, M. Sillanpää, EDTA-Cross-Linked β-Cyclodextrin: An Environmentally Friendly Bifunctional Adsorbent for Simultaneous Adsorption of Metals and Cationic Dyes. *Environ. Sci. Technol.* **49**, 10570–10580 (2015).

72. M. J. Klemes, L. P. Skala, M. Ateia, B. Trang, D. E. Helbling, W. R. Dichtel, Polymerized Molecular Receptors as Adsorbents to Remove Micropollutants from Water. *Acc. Chem. Res.* **53**, 2314–2324 (2020).

73. L. Xiao, Y. Ling, A. Alsbaiee, C. Li, D. E. Helbling, W. R. Dichtel, β-Cyclodextrin Polymer Network Sequesters Perfluorooctanoic Acid at Environmentally Relevant Concentrations. *J. Am. Chem. Soc.* **139**, 7689–7692 (2017).

74. L. Xiao, C. Ching, Y. Ling, M. Nasiri, M. J. Klemes, T. M. Reineke, D. E. Helbling, W. R. Dichtel, Cross-linker Chemistry Determines the Uptake Potential of Perfluorinated Alkyl Substances by β-Cyclodextrin Polymers. *Macromolecules*. **52**, 3747–3752 (2019).

75. M. J. Klemes, Y. Ling, M. Chiapasco, A. Alsbaiee, D. E. Helbling, W. R. Dichtel, Phenolation of cyclodextrin polymers controls their lead and organic micropollutant adsorption. *Chem. Sci.* **9**, 8883–8889 (2018).

76. M. J. Klemes, Y. Ling, C. Ching, C. Wu, L. Xiao, D. E. Helbling, W. R. Dichtel, Reduction of a Tetrafluoroterephthalonitrile-β-Cyclodextrin Polymer to Remove Anionic Micropollutants and Perfluorinated Alkyl Substances from Water. *Angew. Chemie Int. Ed.* **58**, 12049–12053 (2019).

77. A. Yang, C. Ching, M. Easler, D. E. Helbling, W. R. Dichtel, Cyclodextrin Polymers with Nitrogen-Containing Tripodal Crosslinkers for Efficient PFAS Adsorption. *ACS Mater. Lett.* **2**, 1240–1245 (2020).

78. R. Wang, Z. Lin, M. J. Klemes, M. Ateia, B. Trang, J. Wang, C. Ching, D. E. Helbling, W. R. Dichtel, A Tunable Porous β-Cyclodextrin Polymer Platform to Understand and Improve Anionic PFAS Removal. *ACS Cent. Sci.* (2022), doi:10.1021/acscentsci.2c00478.

79. Y. Ling, D. M. Alzate-Sánchez, M. J. Klemes, W. R. Dichtel, D. E. Helbling, Evaluating the effects of water matrix constituents on micropollutant removal by activated carbon and β-cyclodextrin polymer adsorbents. *Water Res.* **173** (2020), doi:10.1016/j.watres.2020.115551.

80. Y. Ling, M. J. Klemes, L. Xiao, A. Alsbaiee, W. R. Dichtel, D. E. Helbling, Benchmarking Micropollutant Removal by Activated Carbon and Porous β-Cyclodextrin Polymers under Environmentally Relevant Scenarios. *Environ. Sci. Technol.* **51**, 7590–7598 (2017).

81. C. Ching, Y. Ling, B. Trang, M. Klemes, L. Xiao, A. Yang, G. Barin, W. R. Dichtel, D. E. Helbling, Identifying the physicochemical properties of β-cyclodextrin polymers that determine the adsorption of perfluoroalkyl acids. *Water Res.* **209**, 117938 (2022).

82. C. Ching, M. J. Klemes, B. Trang, W. R. Dichtel, D. E. Helbling, β-Cyclodextrin Polymers with Different Cross-Linkers and Ion-Exchange Resins Exhibit Variable Adsorption of Anionic, Zwitterionic, and Nonionic PFASs. *Environ. Sci. Technol.* **54**, 12693–12702 (2020).

83. W. Ji, L. Xiao, Y. Ling, C. Ching, M. Matsumoto, R. P. Bisbey, D. E. Helbling, W. R. Dichtel, Removal of GenX and Perfluorinated Alkyl Substances from Water by Amine-Functionalized Covalent Organic Frameworks. *J. Am. Chem. Soc.* **140**, 12677–12681 (2018).

84. B. N. Nzeribe, M. Crimi, S. Mededovic Thagard, T. M. Holsen, Physico-Chemical Processes for the Treatment of Per- And Polyfluoroalkyl Substances (PFAS): A review. *Crit. Rev. Environ. Sci. Technol.* **49**, 866–915 (2019).

85. F. Xiao, P. C. Sasi, B. Yao, A. Kubátová, S. A. Golovko, M. Y. Golovko, D. Soli, Thermal Stability and Decomposition of Perfluoroalkyl Substances on Spent Granular

Activated Carbon. *Environ. Sci. Technol. Lett.* **7**, 343–350 (2020).

86. N. Watanabe, M. Takata, S. Takemine, K. Yamamoto, Thermal mineralization behavior of PFOA, PFHxA, and PFOS during reactivation of granular activated carbon (GAC) in nitrogen atmosphere. *Environ. Sci. Pollut. Res.* **25**, 7200–7205 (2018).

87. N. Watanabe, S. Takemine, K. Yamamoto, Y. Haga, M. Takata, Residual organic fluorinated compounds from thermal treatment of PFOA, PFHxA and PFOS adsorbed onto granular activated carbon (GAC). *J. Mater. Cycles Waste Manag.* **18**, 625–630 (2016).

88. K. P. Shine, W. T. Sturges, CO2 is not the only gas. *Science (80-.).* **315** (2007), pp. 1804–1805.

89. M. J. Bentel, Y. Yu, L. Xu, Z. Li, B. M. Wong, Y. Men, J. Liu, Defluorination of Per- and Polyfluoroalkyl Substances (PFASs) with Hydrated Electrons: Structural Dependence and Implications to PFAS Remediation and Management. *Environ. Sci. Technol.* **53**, 3718–3728 (2019).

90. M. J. Bentel, Y. Yu, L. Xu, H. Kwon, Z. Li, B. M. Wong, Y. Men, J. Liu, Degradation of Perfluoroalkyl Ether Carboxylic Acids with Hydrated Electrons: Structure–Reactivity Relationships and Environmental Implications. *Environ. Sci. Technol.* **54**, 2489–2499 (2020).

91. M. J. Bentel, Z. Liu, Y. Yu, J. Gao, Y. Men, J. Liu, Enhanced Degradation of Perfluorocarboxylic Acids (PFCAs) by UV/Sulfite Treatment: Reaction Mechanisms and System Efficiencies at pH 12. *Environ. Sci. Technol. Lett.* **7**, 351–357 (2020).

92. Z. Liu, M. J. Bentel, Y. Yu, C. Ren, J. Gao, V. F. Pulikkal, M. Sun, Near-Quantitative Defluorination of Perfluorinated and Fluorotelomer Carboxylates and Sulfonates with Integrated Oxidation and Reduction. *Environ. Sci. Technol.*, 7052–7062 (2021).

93. Y. Gu, T. Liu, H. Wang, H. Han, W. Dong, Hydrated electron based decomposition of perfluorooctane sulfonate (PFOS) in the VUV/sulfite system. *Sci. Total Environ.* **607**–**608**, 541–548 (2017).

94. Z. Song, H. Tang, N. Wang, L. Zhu, Reductive defluorination of perfluorooctanoic acid by hydrated electrons in a sulfite-mediated UV photochemical system. *J. Hazard. Mater.* **262**, 332–338 (2013).

95. R. Tenorio, J. Liu, X. Xiao, A. Maizel, C. P. Higgins, C. E. Schaefer, T. J. Strathmann, Destruction of Per-and Polyfluoroalkyl Substances (PFASs) in Aqueous Film-Forming Foam (AFFF) with UV-Sulfite Photoreductive Treatment. *Environ. Sci. Technol.* **54**, 6957–6967 (2020).

96. H. Hori, E. Hayakawa, H. Einaga, S. Kutsuna, K. Koike, T. Ibusuki, H. Kiatagawa, R. Arakawa, Decomposition of Environmentally Persistent Perfluorooctanoic Acid in Water

by Photochemical Approaches. *Environ. Sci. Technol.* **38**, 6118–6124 (2004).

97. B. Wu, S. Hao, Y. Choi, C. P. Higgins, R. Deeb, T. J. Strathmann, Rapid Destruction and Defluorination of Perfluorooctanesulfonate by Alkaline Hydrothermal Reaction. *Environ. Sci. Technol. Lett.* **6**, 630–636 (2019).

98. T. A. Bruton, D. L. Sedlak, Treatment of perfluoroalkyl acids by heat-activated persulfate under conditions representative of in situ chemical oxidation. *Chemosphere*. **206**, 457–464 (2018).

99. H. V Lutze, J. Brekenfeld, S. Naumov, C. Von Sonntag, T. C. Schmidt, Degradation of perfluorinated compounds by sulfate radicals - New mechanistic aspects and economical considerations. *Water Res.* **129**, 509–519 (2018).

100. Z. Sun, D. Geng, C. Zhang, J. Chen, X. Zhou, Y. Zhang, Q. Zhou, M. R. Hoffmann, Vitamin B12 (CoII) initiates the reductive defluorination of branched perfluor-ooctane sulfonate (br-PFOS) in the presence of sulfide. *Chem. Eng. J.* **423**, 130149 (2021).

101. V. Ochoa-Herrera, R. Sierra-Alvarez, A. Somogyi, N. E. Jacobsen, V. H. Wysocki, J. A. Field, Reductive Defluorination of Perfluorooctane Sulfonate. *Environ. Sci. Technol.* **42**, 3260–3264 (2008).

102. S. Park, C. De Perre, L. S. Lee, Alternate Reductants with VB12 to Transform C8 and C6 Perfluoroalkyl Sulfonates: Limitations and Insights into Isomer-Specific Transformation Rates, Products and Pathways. *Environ. Sci. Technol.* **51**, 13869–13877 (2017).

103. R. K. Singh, S. Fernando, S. F. Baygi, N. Multari, S. M. Thagard, T. M. Holsen, Breakdown Products from Perfluorinated Alkyl Substances (PFAS) Degradation in a Plasma-Based Water Treatment Process. *Environ. Sci. Technol.* **53**, 2731–2738 (2019).

104. G. R. Stratton, F. Dai, C. L. Bellona, T. M. Holsen, E. R. V Dickenson, S. M. Thagard, Plasma-Based Water Treatment: Efficient Transformation of Perfluoroalkyl Substances in Prepared Solutions and Contaminated Groundwater. *Environ. Sci. Technol.* **51**, 1643–1648 (2017).

105. M. Ateia, L. P. Skala, A. Yang, W. R. Dichtel, Product analysis and insight into the mechanochemical destruction of anionic PFAS with potassium hydroxide. *J. Hazard. Mater. Adv.* **3**, 100014 (2021).

106. G. Cagnetta, J. Robertson, J. Huang, K. Zhang, G. Yu, Mechanochemical destruction of halogenated organic pollutants: A critical review. *J. Hazard. Mater.* **313**, 85–102 (2016).

107. K. Zhang, J. Huang, G. Yu, Q. Zhang, S. Deng, B. Wang, Destruction of perfluorooctane sulfonate (PFOS) and perfluorooctanoic acid (PFOA) by ball milling. *Environ. Sci. Technol.* **47**, 6471–6477 (2013).

108. C. E. Schaefer, C. Andaya, A. Urtiaga, E. R. McKenzie, C. P. Higgins, Electrochemical treatment of perfluorooctanoic acid (PFOA) and perfluorooctane sulfonic acid (PFOS) in

groundwater impacted by aqueous film forming foams (AFFFs). *J. Hazard. Mater.* **295**, 170–175 (2015).

109. Q. Zhuo, S. Deng, B. Yang, J. Huang, G. Yu, Efficient electrochemical oxidation of perfluorooctanoate using a Ti/SnO2-Sb-Bi anode. *Environ. Sci. Technol.* **45**, 2973–2979 (2011).

110. A. M. Trautmann, H. Schell, K. R. Schmidt, K. M. Mangold, A. Tiehm, Electrochemical degradation of perfluoroalkyl and polyfluoroalkyl substances (PFASs) in groundwater. *Water Sci. Technol.* **71**, 1569–1575 (2015).

111. S. Garcia-Segura, A. B. Nienhauser, A. S. Fajardo, R. Bansal, C. L. Coonrod, J. D. Fortner, M. Marcos-Hernández, T. Rogers, D. Villagran, M. S. Wong, P. Westerhoff, Disparities between experimental and environmental conditions: Research steps toward making electrochemical water treatment a reality. *Curr. Opin. Electrochem.* **22** (2020), pp. 9–16.

112. M. Panizza, G. Cerisola, Direct and mediated anodic oxidation of organic pollutants. *Chem. Rev.* **109**, 6541–6569 (2009).

113. M. J. Krause, E. Thoma, E. Sahle-Damesessie, B. Crone, A. Whitehill, E. Shields, B. Gullett, Supercritical Water Oxidation as an Innovative Technology for PFAS Destruction. *J. Environ. Eng.* **148**, 05021006 (2022).

114. F. Wang, X. Lu, K. Shih, C. Liu, Influence of calcium hydroxide on the fate of perfluorooctanesulfonate under thermal conditions. *J. Hazard. Mater.* **192**, 1067–1071 (2011).

115. H. Javed, C. Lyu, R. Sun, D. Zhang, P. J. J. Alvarez, Discerning the inefficacy of hydroxyl radicals during perfluorooctanoic acid degradation. *Chemosphere*. **247**, 125883 (2020).

116. H. Javed, J. Metz, T. C. Eraslan, J. Mathieu, B. Wang, G. Wu, A.-L. Tsai, M. S. Wong, P. J. J. Alvarez, *Environ. Sci. Technol. Lett.*, in press, doi:10.1021/acs.estlett.0c00505.

117. J. Metz, H. Javed, J. Mathieu, M. Long, P. J. J. Alvarez, Comment on "Mechanistic Understanding of Superoxide Radical- Mediated Degradation of Perfluorocarboxylic Acids." *Environ. Sci. Technol.* **56**, 5287–5288 (2022).

118. H. Hori, A. Yamamoto, E. Hayakawa, S. Taniyasu, N. Yamashita, S. Kutsuna, H. Kiatagawa, R. Arakawa, Efficient Decomposition of Environmentally Persistent Perfluorocarboxylic Acids by Use of Persulfate as a Photochemical Oxidant (2005), doi:10.1021/ES0484754.

119. A. C. Parenky, N. G. de Souza, H. H. Nguyen, J. Jeon, H. Choi, Decomposition of Carboxylic PFAS by Persulfate Activated by Silver under Ambient Conditions. *J. Environ. Eng.* **146**, 06020003 (2020).

120. L. Yang, L. He, J. Xue, Y. Ma, Z. Xie, L. Wu, M. Huang, Z. Zhang, Persulfate-based

degradation of perfluorooctanoic acid (PFOA) and perfluorooctane sulfonate (PFOS) in aqueous solution: Review on influences, mechanisms and prospective. *J. Hazard. Mater.* **393** (2020), p. 122405.

121. A. Choudhary, D. Dong, M. Tsianou, P. Alexandridis, D. Bedrov, Adsorption Mechanism of Perfluorooctanoate on Cyclodextrin-Based Polymers: Probing the Synergy of Electrostatic and Hydrophobic Interactions with Molecular Dynamics Simulations. *ACS Mater. Lett.* **4**, 853–859 (2022).

122. T. Macbeth, in *2021 Global Summit on Environmental Remediation* (Pacific Northwest National Laboratory, 2021; https://www.pnnl.gov/projects/remplex/case-studies).

123. S. D. Richardson, T. A. Ternes, Water Analysis: Emerging Contaminants and Current Issues. *Anal. Chem.* **90**, 398–428 (2018).

124. C. G. Daughton, T. A. Ternes, Pharmaceuticals and personal care products in the environment: agents of subtle change? *Environ. Health Perspect.* **107**, 907–938 (1999).

125. L. Kovalova, D. R. U. Knappe, K. Lehnberg, C. Kazner, J. Hollender, Removal of highly polar micropollutants from wastewater by powdered activated carbon. *Environ. Sci. Pollut. Res.* **20**, 3607–3615 (2013).

126. Z.-X. Yang, Y. Chen, Y. Liu, Inclusion complexes of bisphenol A with cyclomaltoheptaose (β-cyclodextrin): solubilization and structure. *Carbohydr. Res.* **343**, 2439–2442 (2008).

127. H. Kitano, H. Endo, M. Gemmei-Ide, M. Kyogoku, Inclusion of Bisphenols by Cyclodextrin Derivatives. *J. Incl. Phenom.* **47**, 83–90 (2003).

128. G. Crini, C. Cosentino, S. Bertini, A. Naggi, G. Torri, C. Vecchi, L. Janus, M. Morcellet, Solid state NMR spectroscopy study of molecular motion in cyclomaltoheptaose (β-cyclodextrin) crosslinked with epichlorohydrin. *Carbohydr. Res.* **308**, 37–45 (1998).

129. E. Renard, A. Deratani, G. Volet, B. Sebille, Preparation and characterization of water soluble high molecular weight β-cyclodextrin-epichlorohydrin polymers. *Eur. Polym. J.* **33**, 49–57 (1997).

130. G. Mocanu, D. Mihai, D. LeCerf, L. Picton, M. Moscovici, Cyclodextrin-anionic polysaccharide hydrogels: Synthesis, characterization, and interaction with some organic molecules (water pollutants, drugs, proteins). *J. Appl. Polym. Sci.* **112**, 1175–1183 (2009).

131. Y. Ling, M. J. Klemes, S. Steinschneider, W. R. Dichtel, D. E. Helbling, QSARs to predict adsorption affinity of organic micropollutants for activated carbon and β-cyclodextrin polymer adsorbents. *Water Res.* **154**, 217–226 (2019).

132. H. Omorodion, M. Palenzuela, M. Ruether, B. Twamley, J. A. Platts, R. J. Baker, A rationally designed perfluorinated host for the extraction of PFOA from water utilising non-covalent interactions. *New J. Chem.* **42**, 7956–7968 (2018).

133. Y. Liu, G. Su, F. Wang, J. Jia, S. Li, L. Zhao, Y. Shi, Y. Cai, H. Zhu, B. Zhao, G. Jiang, H. Zhou, B. Yan, Elucidation of the Molecular Determinants for Optimal Perfluorooctanesulfonate Adsorption Using a Combinatorial Nanoparticle Library Approach. *Environ. Sci. Technol.* **51**, 7120–7127 (2017).

134. L. Xiao, C. Ching, Y. Ling, M. Nasiri, M. J. Klemes, T. M. Reineke, D. E. Helbling, W. R. Dichtel, Crosslinker Chemistry Determines the Uptake Potential of Perfluorinated Alkyl Substances by β-Cyclodextrin Polymers. *ChemRxiv* (2018) (available at https://chemrxiv.org/articles/Crosslinker_Chemistry_Determines_the_Uptake_Potential_of_Perfluorinated_Alkyl_Substances_by_-Cyclodextrin_Polymers/7492631).

135. C. Yang, H. Huang, T. Ji, K. Zhang, L. Yuan, C. Zhou, K. Tang, J. Yi, X. Chen, A cost-effective crosslinked β-cyclodextrin polymer for the rapid and efficient removal of micropollutants from wastewater. *Polym. Int.* **68**, 805–811 (2019).

136. H. Li, B. Meng, S.-H. Chai, H. Liu, S. Dai, Hyper-crosslinked β-cyclodextrin porous polymer: an adsorption-facilitated molecular catalyst support for transformation of water-soluble aromatic molecules. *Chem. Sci.* **7**, 905–909 (2016).

137. Y. Tu, G. Xu, L. Jiang, X. Hu, J. Xu, X. Xie, A. Li, Amphiphilic hyper-crosslinked porous cyclodextrin polymer with high specific surface area for rapid removal of organic micropollutants. *Chem. Eng. J.* **382**, 123015 (2020).

138. N. W. Sach, D. T. Richter, S. Cripps, M. Tran-Dubé, H. Zhu, B. Huang, J. Cui, S. C. Sutton, Synthesis of Aryl Ethers via a Sulfonyl Transfer Reaction. *Org. Lett.* **14**, 3886–3889 (2012).

139. B. Phillips, C. Wang, X. Tu, S. Banerjee, M. Al-hashimi, Cyclodextrin-derived polymer networks for selective molecular adsorption. *Chem. Commun.* **56**, 11783–11786 (2020).

140. A. Leeson, T. Thompson, H. F. Stroo, R. H. Anderson, J. Speicher, M. A. Mills, J. Willey, C. Coyle, R. Ghosh, C. Lebrón, C. Patton, Identifying and Managing Aqueous Film-Forming Foam-Derived Per- and Polyfluoroalkyl Substances in the Environment. *Environ. Toxicol. Chem.* **40**, 24–36 (2021).

141. Persistent Organic Pollutants Review Committee, "Report of the Persistent Organic Pollutants Review Committee on the work of its thirteenth meeting Addendum Risk management evaluation on pentadecafluorooctanoic acid (CAS No: 335-67-1, PFOA, perfluorooctanoic acid), its salts and PFOA-related compounds" (2017), (available at http://chm.pops.int/Implementation/Alternatives/AlternativestoPOPs/ChemicalslistedinAnnexA/PFOA/tabid/8292/Default.aspx).

142. International Pollutants Elimination Network, "PFAS Pollution Across the Middle East and Asia" (2019), (available at https://ipen.org/sites/default/files/documents/pfas_pollution_across_the_middle_east_and_asia.pdf).

143. N. Rich, Rob Bilott v. DuPont. *N. Y. Times Mag.* (2016), p. 36.

144. C. M. Glover, O. Quiñones, E. R. V. Dickenson, Removal of perfluoroalkyl and polyfluoroalkyl substances in potable reuse systems. *Water Res.* **144**, 454–461 (2018).

145. A. Maimaiti, S. Deng, P. Meng, W. Wang, B. Wang, J. Huang, Y. Wang, G. Yu, Competitive adsorption of perfluoroalkyl substances on anion exchange resins in simulated AFFF-impacted groundwater. *Chem. Eng. J.* **348**, 494–502 (2018).

146. M. Inyang, E. R. V. Dickenson, The use of carbon adsorbents for the removal of perfluoroalkyl acids from potable reuse systems. *Chemosphere*. **184**, 168–175 (2017).

147. C. D. Vecitis, H. Park, J. Cheng, B. T. Mader, M. R. Hoffmann, Kinetics and Mechanism of the Sonolytic Conversion of the Aqueous Perfluorinated Surfactants, Perfiuorooctanoate (PFOA), and Perfluorooctane Sulfonate (PFOS) into Inorganic Products. *J. Phys. Chem. A*. **112**, 4261–4270 (2008).

148. J. Cheng, C. D. Vecitis, H. Park, B. T. Mader, M. R. Hoffmann, Sonochemical degradation of perfluorooctane sulfonate (PFOS) and perfluorooctanoate (PFOA) in groundwater: Kinetic effects of matrix inorganics. *Environ. Sci. Technol.* **44**, 445–450 (2010).

149. X. Liang, J. Cheng, C. Yang, S. Yang, Factors influencing aqueous perfluorooctanoic acid (PFOA) photodecomposition by VUV irradiation in the presence of ferric ions. *Chem. Eng. J.* **298**, 291–299 (2016).

150. D. Kong, P. J. Moon, E. K. J. J. Lui, O. Bsharat, R. J. Lundgren, Direct reversible decarboxylation from stable organic acids in dimethylformamide solution. *Science (80-.).* **369**, 557–561 (2020).

151. S. Zhou, B. T. Nguyen, J. P. Richard, R. Kluger, J. Gao, Origin of Free Energy Barriers of Decarboxylation and the Reverse Process of CO 2 Capture in Dimethylformamide and in Water. *J. Am. Chem. Soc.* **143**, 137–141 (2021).

152. H. K. Liberatore, S. R. Jackson, M. J. Strynar, J. P. McCord, *Environ. Sci. Technol. Lett.*, in press, doi:10.1021/acs.estlett.0c00323.

153. C. Zhang, A. C. Mcelroy, H. K. Liberatore, N. L. M. Alexander, D. R. U. Knappe, Stability of Per- and Poly fl uoroalkyl Substances in Solvents Relevant to Environmental and Toxicological Analysis (2021), doi:10.1021/acs.est.1c03979.

154. D. A. Dixon, T. Fukunaga, B. E. Smart, Structures and Stabilities of Fluorinated Carbanions: Evidence for Anionic Hyperconjugation. *J. Am. Chem. Soc.* **108**, 4027–4031 (1986).

155. T. M. Rangarajan, S. Sathyamoorthi, D. Velayutham, M. Noel, R. P. Singh, R. Brahma, Products formed at intermediate stages of electrochemical perfluorination of propionyl and n-butyryl chlorides. Further evidence in support of NiF 3 mediated free radical

pathway. *J. Fluor. Chem.* **132**, 107–113 (2011).

156. L. V. Saloutina, A. Y. Zapevalov, V. I. Saloutin, M. I. Kodess, V. E. Kirichenko, M. G. Pervova, O. N. Chupakhin, Synthesis of 2,3-bis(perfluoroalkyl)quinoxalines and 2,3-bis(perfluoroalkyl)-1,4-benzoxazines from oxides of internal perfluoroolefins. *J. Fluor. Chem.* **126**, 976–983 (2005).

157. A. Foris, 19F and1H NMR spectra of halocarbons. *Magn. Reson. Chem.* **42**, 534–555 (2004).

158. T. Hogan, A. Sen, High-yield, radical-initiated oxidative functionalization of ethane by perfluorocarboxylic acid anhydrides. Role of metal ions in catalytic alkane oxidations in the presence of perfluorocarboxylic acid anhydrides. *J. Am. Chem. Soc.* **119**, 2642–2646 (1997).

159. C. Dai, L. Sun, H. Liao, B. Khezri, R. D. Webster, A. C. Fisher, Z. J. Xu, Electrochemical production of lactic acid from glycerol oxidation catalyzed by AuPt nanoparticles. *J. Catal.* **356**, 14–21 (2017).

160. T. Chatterjee, E. Boutin, M. Robert, Manifesto for the routine use of NMR for the liquid product analysis of aqueous CO2 reduction: formaldehyde quantification in water, 4257–4265 (2020).

161. J. D. LaZerte, L. J. Hals, T. S. Reid, G. H. Smith, Pyrolyses of the Salts of the Perfluoro Carboxylic Acids. *J. Am. Chem. Soc.* **75**, 4525–4528 (1953).

162. T. Hudlicky, R. Fan, J. W. Reed, D. R. Carver, Practical preparation of some potentially anesthetic fluoroalkanes: regiocontrolled introduction of hydrogen atoms. *J. Fluor. Chem.* **59**, 9–14 (1992).

163. R. N. Haszeldine, 817. The reactions of metallic salts of acids with halogens. Part III. Some reactions of salts of fluorohalogenoacetates and of perfluoro-acids. *J. Chem. Soc.*, 4259 (1952).

164. D. A. Hercules, C. A. Parrish, T. S. Sayler, K. T. Tice, S. M. Williams, L. E. Lowery, M. E. Brady, R. B. Coward, J. A. Murphy, T. A. Hey, A. R. Scavuzzo, L. M. Rummler, E. G. Burns, A. V. Matsnev, R. E. Fernandez, C. D. McMillen, J. S. Thrasher, Preparation of tetrafluoroethylene from the pyrolysis of pentafluoropropionate salts. *J. Fluor. Chem.* **196**, 107–116 (2017).

165. L. J. Hals, T. S. Reid, G. H. Smith, The preparation of terminally unsaturated perfluoro olefins by the decomposition of the salts of perfluoro acids. *J. Am. Chem. Soc.* **73** (1951), p. 4054.

166. X. Zhang, K. Seppelt, Fluorocarbonate, [FC02] - : Preparation and Structure, 32–34 (1995).

167. M. Iznaden, C. Portella, Hydro-2-oxo-3-perfluoroesters. Synthese et Properties

Remarquables: Hydrate, equilibre cent-enolique. *J. Fluor. Chem.* **43**, 105–118 (1989).

168. M. J. Pellerite, Unusual reaction chemistry in thermal decomposition of alkali metal 2-alkoxy-2,3,3,3-tetrafluoropropionate salts. *J. Fluor. Chem.* **49**, 43–66 (1990).

169. Y. Ge, Z. Liu, H. Liu, J.-K. Feng, D. Liu, X. Ge, Theoretical study on the degradation reaction mechanism of elimination hydrogen fluoride from perfluoropropionic acid. *Comput. Theor. Chem.* **1029**, 33–40 (2014).

170. E. F. Houtz, D. L. Sedlak, Oxidative conversion as a means of detecting precursors to perfluoroalkyl acids in urban runoff. *Environ. Sci. Technol.* **46**, 9342–9349 (2012).

171. Y. Zhao, D. G. Truhlar, The M06 suite of density functionals for main group thermochemistry, thermochemical kinetics, noncovalent interactions, excited states, and transition elements: Two new functionals and systematic testing of four M06-class functionals and 12 other function. *Theor. Chem. Acc.* **120**, 215–241 (2008).

172. A. V. Marenich, C. J. Cramer, D. G. Truhlar, Universal solvation model based on solute electron density and on a continuum model of the solvent defined by the bulk dielectric constant and atomic surface tensions. *J. Phys. Chem. B*. **113**, 6378–6396 (2009).

173. M. J. Frisch, G. W. Trucks, H. B. Schlegel, G. E. Scuseria, M. A. Robb, J. R. Cheeseman, G. Scalmani, V. Barone, G. A. Petersson, H. Nakatsuji, X. Li, M. Caricato, A. V. Marenich, J. Bloino, B. G. Janesko, J. V. O. R. Gomperts, B. Mennucci, H. P. Hratchian, A. F. Izmaylov, J. L. Sonnenberg, D. Williams-Young, F. Ding, F. Lipparini, F. Egidi, J. Goings, B. Peng, A. Petrone, D. R. T. Henderson, V. G. Zakrzewski, J. Gao, N. Rega, G. Zheng, W. Liang, M. Hada, M. Ehara, K. Toyota, R. Fukuda, J. Hasegawa, M. Ishida, T. Nakajima, Y. Honda, O. Kitao, H. Nakai, T. Vreven, K. Throssell, J. J. A. Montgomery, J. E. Peralta, F. Ogliaro, M. J. Bearpark, J. J. Heyd, E. N. Brothers, K. N. Kudin, V. N. Staroverov, T. A. Keith, R. Kobayashi, J. Normand, K. Raghavachari, A. P. Rendell, J. C. Burant, S. S. Iyengar, J. Tomasi, M. Cossi, J. M. Millam, M. Klene, C. Adamo, R. Cammi, J. W. Ochterski, R. L. Martin, K. Morokuma, O. Farkas, J. B. Foresman, D. J. Fox, Gaussian 16 A.03 (2016).

174. N. Mardirossian, M. Head-Gordon, How Accurate Are the Minnesota Density Functionals for Noncovalent Interactions, Isomerization Energies, Thermochemistry, and Barrier Heights Involving Molecules Composed of Main-Group Elements? *J. Chem. Theory Comput.* **12**, 4303–4325 (2016).

175. G. Luchini, J. Alegre-Requena, IFunes, J. Rodríguez-Guerra, J. Chen, R. Paton, bobbypaton/GoodVibes: GoodVibes v3.0.0 (2019), doi:10.5281/ZENODO.3346166.

176. S. Grimme, Supramolecular binding thermodynamics by dispersion-corrected density functional theory. *Chem. - A Eur. J.* **18**, 9955–9964 (2012).

177. Y. P. Li, J. Gomes, S. M. Sharada, A. T. Bell, M. Head-Gordon, Improved force-field parameters for QM/MM simulations of the energies of adsorption for molecules in zeolites

and a free rotor correction to the rigid rotor harmonic oscillator model for adsorption enthalpies. *J. Phys. Chem. C*. **119**, 1840–1850 (2015).

178. C. Y. Legault, CYLview20 (2020), (available at http://www.cylview.org).

179. F. Xiao, P. C. Sasi, B. Yao, A. Kubátová, S. A. Golovko, M. Y. Golovko, D. Soli, *Environ. Sci. Technol. Lett.*, in press, doi:10.1021/acs.estlett.0c00114.

180. S. Hao, Y.-J. Choi, B. Wu, C. P. Higgins, R. Deeb, T. J. Strathmann, Hydrothermal Alkaline Treatment for Destruction of Per- and Polyfluoroalkyl Substances in Aqueous Film-Forming Foam. *Environ. Sci. Technol.* **55**, 3283–3295 (2021).

181. M. Strynar, S. Dagnino, R. McMahen, S. Liang, A. Lindstrom, E. Andersen, L. McMillan, M. Thurman, I. Ferrer, C. Ball, Identification of Novel Perfluoroalkyl Ether Carboxylic Acids (PFECAs) and Sulfonic Acids (PFESAs) in Natural Waters Using Accurate Mass Time-of-Flight Mass Spectrometry (TOFMS). *Environ. Sci. Technol.* **49**, 11622–11630 (2015).

182. G. McGrath, NC activists hope Biden EPA will force 'forever chemical' study. *Fayettev. Obs.* (2021), (available at https://www.fayobserver.com/story/news/2021/01/27/denied-by-trump-epa-nc-activists-hope-biden-epa-force-forever-chemical-study/4265453001/).

183. M. Sun, E. Arevalo, M. Strynar, A. Lindstrom, M. Richardson, B. Kearns, A. Pickett, C. Smith, D. R. U. Knappe, Legacy and Emerging Perfluoroalkyl Substances Are Important Drinking Water Contaminants in the Cape Fear River Watershed of North Carolina. *Environ. Sci. Technol. Lett.* **3**, 415–419 (2016).

184. C. Hogue, PFAS-making plant wasn't inspected for years, US EPA watchdog says. *Chem. Eng. News* (2020), (available at https://cen.acs.org/environment/persistent-pollutants/PFAS-making-plant-wasnt-inspected/98/web/2020/05).

185. S. Davidson, J. Harris, N. Henry, C. Kincheloe, B. Parker, "EPA Toxic Substances Control Act Consent Orders Need Better Coordination" (Washington, D.C., 2020).

186. U. EPA, Chemours Toxic Substances Control Act Notice of Violation -February 14, 2019 (2019), (available at https://www.epa.gov/nc/chemours-toxic-substances-control-act-notice-violation-february-14-2019).

187. J. W. Washington, C. G. Rosal, J. P. McCord, M. J. Strynar, A. B. Lindstrom, E. L. Bergman, S. M. Goodrow, H. K. Tadesse, A. N. Pilant, B. J. Washington, M. J. Davis, B. G. Stuart, T. M. Jenkins, Nontargeted mass-spectral detection of chloroperfluoropolyether carboxylates in New Jersey soils. *Science (80-.).* **368**, 1103–1107 (2020).

188. M. G. Evich, M. Davis, E. J. Weber, C. Tebes-Stevens, B. Acrey, W. M. Henderson, S. Goodrow, E. Bergman, J. W. Washington, Environmental Fate of Cl-PFPECAs: Predicting the Formation of PFAS Transformation Products in New Jersey Soils. *Environ. Sci. Technol.* **in press** (2022), doi:10.1021/acs.est.1c06126.

Vita

Brittany Trang is from Peoria, Illinois and completed her bachelor's degree in chemistry and English at the Ohio State University, where she studied the synthesis of organic dyes for p-type dye-sensitized solar cells with Dr. Yiying Wu. During her undergraduate degree, she was a DAAD RISE intern with Dr. Anne Staubitz at Christian-Albrechts-Universität zu Kiel in Germany where she studied cross-couplings for integrating spiropyran molecular switches into conducting polymers. She also was a Berkeley Lab Undergraduate Research intern at the Molecular Foundry at Lawrence Berkeley National Lab with Dr. Nate Hohman, where she researched bulk 2D hybrid chalcogenide semiconductor materials. After receiving a National Science Foundation Graduate Research Fellowship in 2017, she began her chemistry PhD at Northwestern University, where she worked with Prof. William Dichtel on PFAS remediation. In 2021, she earned a AAAS Mass Media Fellowship and worked as a science reporter intern at the Milwaukee Journal Sentinel. After earning her PhD, she will be a 2022–2023 Sharon Begley Science Reporting Fellow at STAT News in Boston.